DYNAMICS OF A SMALL SURGE-TYPE GLACIER, ST. ELIAS MOUNTAINS, YUKON TERRITORY, CANADA: CHARACTERIZATION OF BASAL MOTION USING 1-D GEOPHYSICAL INVERSION

by

Laetitia M.J. De Paoli
BSc. Equivalent, Université de Reims-Champagne-Ardenne, France, 2005

A THESIS SUBMITTED IN PARTIAL FULFILLMENT
OF THE REQUIREMENTS FOR THE DEGREE OF
MASTER OF SCIENCE
in the Department
of
Earth Sciences

SIMON FRASER UNIVERSITY
Spring 2009

APPROVAL

Name: **Laetitia De Paoli**

Degree: **Master of Science**

Title of Thesis: **Dynamics of a small surge-type glacier, St. Elias Mountains, Yukon Territory, Canada: Characterization of basal motion using 1-D geophysical inversion**

Examining Committee:

Chair: **Dr. Dan Gibson**
Assistant Professor, Department of Earth Sciences

Dr. Gwenn Flowers
Senior Supervisor
Assistant Professor, Department of Earth Sciences

Dr. Andrew Calvert
Supervisor
Professor, Department of Earth Sciences

By written/email consultation from Alaska
Dr. Martin Truffer
External Examiner
Associate Professor, University of Alaska Fairbanks

Date Defended/Approved: March 25, 2009

SFU SIMON FRASER UNIVERSITY
LIBRARY

Declaration of Partial Copyright Licence

The author, whose copyright is declared on the title page of this work, has granted to Simon Fraser University the right to lend this thesis, project or extended essay to users of the Simon Fraser University Library, and to make partial or single copies only for such users or in response to a request from the library of any other university, or other educational institution, on its own behalf or for one of its users.

The author has further granted permission to Simon Fraser University to keep or make a digital copy for use in its circulating collection (currently available to the public at the "Institutional Repository" link of the SFU Library website <www.lib.sfu.ca> at: <http://ir.lib.sfu.ca/handle/1892/112>) and, without changing the content, to translate the thesis/project or extended essays, if technically possible, to any medium or format for the purpose of preservation of the digital work.

The author has further agreed that permission for multiple copying of this work for scholarly purposes may be granted by either the author or the Dean of Graduate Studies.

It is understood that copying or publication of this work for financial gain shall not be allowed without the author's written permission.

Permission for public performance, or limited permission for private scholarly use, of any multimedia materials forming part of this work, may have been granted by the author. This information may be found on the separately catalogued multimedia material and in the signed Partial Copyright Licence.

While licensing SFU to permit the above uses, the author retains copyright in the thesis, project or extended essays, including the right to change the work for subsequent purposes, including editing and publishing the work in whole or in part, and licensing other parties, as the author may desire.

The original Partial Copyright Licence attesting to these terms, and signed by this author, may be found in the original bound copy of this work, retained in the Simon Fraser University Archive.

Simon Fraser University Library
Burnaby, BC, Canada

Last revision: Spring 09

Abstract

The dynamics of a small surge-type glacier are investigated as part of a study to characterize glacier response to climate in southwest Yukon Territory, Canada. DEMs of the glacier surface and bed are constructed from surface elevation and ice thickness data. Measured surface velocities are higher than expected for a surge-type glacier in its quiescent phase over the upper 3500 m of the 5 km-long glacier, but much lower than typical surge velocities. Flowline basal velocities are reconstructed from the measured surface velocities using a 1-D geophysical inverse model. Control tests are used to validate the inversion scheme, and sensitivity tests are performed to evaluate the influence of uncertain parameters. Inversion of the measured surface velocities reveals an unusually high contribution of basal motion to the overall motion. Based on these results and several other lines of evidence, we suggest that the glacier may be undergoing a slow surge.

Executive summary

The dynamics of a small surge-type valley glacier are investigated as part of a study to evaluate the modulating role of glacier dynamics on the glacier response to climate in the Donjek Range of the St. Elias Mountains, Yukon Territory, Canada. Surface elevation and ice thickness data were collected on the study glacier between 2006 and 2008 using kinematic global positioning system (GPS) techniques and ice-penetrating radar. These data were used to construct digital elevation models (DEMs) of the glacier surface and bed by kriging. A velocity pole survey was also conducted during three consecutive summer field seasons. The displacements of 12 poles located along an approximate flowline were recorded over a one-month period each year using kinematic GPS techniques. Measured surface velocities range from less than $10\,\mathrm{m\,a^{-1}}$ over the lowermost 1500 m of the 5 km-long glacier to a maximum of $\sim$25–35 $\mathrm{m\,a^{-1}}$ over the upper 3500 m. The velocities over this upper zone are higher than expected for a surge-type glacier of this size in its quiescent phase, but much lower than typical surge velocities.

Basal velocities along an approximate flowline are reconstructed from the measured surface velocities using a 1-D geophysical inverse model. An analytical relationship between the basal velocity, deformational velocity and surface velocity of an ice body flowing in a channel defines the forward model, which is subsequently linearized using a method of longitudinal averaging for variable ice thickness and surface slope. To perform the inversion itself, two different methods are tested through a set of control tests using synthetic input data. The singular value decomposition method (SVD), identified as the most accurate, is subsequently used to invert the measured surface velocities, and sensitivity tests are performed to evaluate the influence of the shape factor, the flow-law coefficient, the longitudinal averaging length and the errors on the data.

Inversion of the measured surface velocities yields results that are reasonably robust with respect to uncertain parameters, and shows that basal motion accounts for roughly 50–100% of the total surface motion along the flowline. Such a high contribution of basal motion is characteristic of surging glaciers. The high modelled contribution of basal motion above 1700 m along the flowline, the undulation of the glacier surface, the observation of many crevasses, and the fact that the subglacial drainage system appears to be strongly influenced by factors other than topography in this region suggest that the glacier is not in a state of quiescence. In addition, to sustain the measured surface velocities would require a more positive mass balance than has likely been obtained in recent years. Based on the evidence presented in this thesis, we suggest that the glacier may be undergoing a slow surge.

Acknowledgments

First of all, I would like to thank my supervisor, Gwenn Flowers, for her guidance and support during the three years I spent at SFU. Gwenn not only taught me a great deal about glaciology, she also has been a great advisor and friend. I am grateful for her outstanding guidance in all academic matters, and for the friendly and stimulating environment she has created throughout my studies. Her constant encouragements, her constructive criticism and her open-door policy were very much apreciated. I am also grateful to my other comittee member, Andrew Calvert, for his time and his constructive feedback on my work and to Martin Truffer for reviewing this thesis. I would like to thank all members of the SFU glaciology group for their advice on matters ranging from programming to conference presentations and for creating an enjoyable work atmosphere. Special thanks to Jennifer Owen and Patrick Belliveau, who made valuable contributions to this thesis.

This work would not have been possible without the efforts of the people who conducted field work, while I was enjoying the Vancouver summer weather. I am especially grateful to Brett Wheler, who played a major role in the field. I am also indebt to Gwenn Flowers, Jessica Logher, Chris Doughty, Patrick Belliveau and Alex Jarosh for collecting and sometime processing field data.

My graduate studies were supported by Gwenn Flowers through grants from the Natural Sciences and Engineering Research Council of Canada (NSERC), the Canada Foundation for Innovation (CFI) and the Canada Research Chairs (CRC) Program. I am also grateful to Simon Fraser University for providing funding through teaching assistantships.

Finally, I would like to thank my parents for being available whenever I need advice or encouragements. Thank you for your selfless support in each and every one of my endeavours, whether they involve writing a thesis or moving to another continent.

Contents

List of Tables

List of Figures

Chapter 1

Introduction

Mountain glaciers and ice caps represent only 3% of all glacierized area on Earth (e.g. Bamber and Payne, 2004), yet being sensitive to climate fluctuations, they can have a significant impact on sea level. Transfer of ice from the continents to the ocean is the most important contributor to sea-level rise after the thermal expansion of the ocean itself (e.g. Solomon et al., 2007). A number of recent studies have established that small mountain glaciers and ice caps are making a greater contribution to total global ice loss than Greenland and Antarctica together (e.g. Braithwaite and Raper, 2002; Kaser et al., 2006; Meier et al., 2007; Solomon et al., 2007), and that the contribution of these smaller ice masses has increased over the last decade (e.g. Meier et al., 2007). Glaciers are also important as sources of freshwater in many regions of the world, and changes in glacier volumes have implications for regional hydrology (e.g. Kaser et al., 2004). It is therefore essential to understand the response of mountain glaciers to climate fluctuations in order to predict global changes in sea level and regional changes in water quality and quantity.

1.1 Background and statement of the problem

Glaciers are related to climate through their mass balance. Mass balance is a measure of the total mass change of a glacier over a certain period of time, usually taken as one year. Mass balance can be defined over the whole surface of a glacier, or at a given location. By definition, the accumulation area is the zone over which the net annual mass balance is positive, while the ablation area is the zone over which the net annual mass balance is negative. An accumulation area ratio (the fraction of the glacier area occupied by the accumulation zone) of 2/3 is often quoted for glaciers that are in balance with climate (Paterson, 1994). In practice this ratio depends on glacier hypsometry, among other quantities. Fluctuations in precipitation cause variations in the amount of snow accumulation on a glacier, while fluctuations in air temperature cause variations in the amount of ice lost by surface melting (Paterson, 1994) and affect the amount of precipitation that falls as rain as opposed to snow. Local or global changes in climate thus translate into mass balance changes, to which glaciers ultimately respond by advancing or retreating.

1.1.1 Mass balance and glacier dynamics

Under near steady-state conditions, changes in glacier geometry, such as ice thickness and glacier length, result directly from changes in mass balance. Glaciers typically respond to a decrease in net balance by retreating and thinning until a new equilibrium volume is reached. This results in a reduction of the surface area located at low elevations where mass balance is negative, and thus in a reduction in loss of ice through melting. Glaciers respond to an increase in net balance by advancing and thickening, thus increasing the surface area over which ablation occurs to compensate for the higher net accumulation. When fluctuations in mass balance occur rapidly, the glacier geometry cannot maintain a steady-state. Furthermore, changes in subglacial mechanics can complicate the relationship between glacier geometry and mass balance. In this case, geometric transitions can be the result of spatial and temporal changes in velocity rather than direct consequences of changes in mass balance (e.g. Meier et al., 2007).

1.1.2 Basal dynamics and subglacial hydrology

Small valley glaciers typically respond to changes in mass balance over time scales of several years to several decades (Jóhannesson et al., 1989). However, small but sudden changes in the local climate can potentially have direct and rapid impacts on the dynamics of a glacier. By quickly increasing or decreasing surface melting, and thus the amount of water available at the bed, basal motion can be affected over relatively short timescales, influencing the total motion of the glacier as well as the amount of mass turnover. An example of this phenomenon is the characteristic seasonal cycle in flow speed experienced by many alpine glaciers (Paterson, 1994).

The overall motion of a glacier can be separated into two distinct components: the motion due to the internal deformation of ice under its own weight, and the motion taking place at the ice-bed interface, referred to here as basal motion. Basal motion can be due to sliding of the glacier over its bed, to the deformation of underlying sediments or to a combination of these processes. Basal motion can be an important process for many glaciers (e.g. Clarke, 2005), with basal flow rates sometimes accounting for more than half the total motion of a glacier (e.g. Paterson, 1994).

Basal motion is linked to the amount of water available at the bed and to the subglacial drainage system structure (e.g. Iken, 1981; Clarke, 2005; Bartholomaus et al., 2008). Decades of field observations and theoretical analyses have lead to the classification of subglacial drainage systems as “fast” or “slow” (e.g. Raymond et al., 1995; Fountain and Walder, 1998). Both types of drainage systems can coexist beneath a glacier, and seasonal, or even diurnal, switches between the two types may be common (e.g. Björnsson, 1998). In a fast, channelized system (e.g. Röthlisberger, 1972; Shreve, 1972; Kamb, 1987; Raymond et al., 1995), water travels through a few tunnels within the ice or at the ice-bed interface. The steady-state water pressure in the channels varies inversely with the water flux, and tunnels transporting large amounts of water grow at the expense of smaller tunnels (Kamb, 1987). The size of the tunnels adjusts to the water flux and is a function of the melting enlargement induced by frictional heating and the closure caused by ice deformation (Nye, 1953; Röthlisberger, 1972). A channelized drainage system therefore requires sufficient injection of water to be sustained. For this reason, temperate alpine glaciers typically have a relatively inefficient (distributed) drainage system during the winter, and switch to a more efficient (channelized) drainage system in the spring or early summer, when water volumes increase due to surface melting (e.g. Nienow et al., 1998). There are several forms of “slow” drainage systems, however only the linked-cavity drainage system is described here because it is the best described of all slow drainage systems. In a slow or distributed linked-cavity drainage system, hydraulically connected water-filled cavities form behind protuberances in the glacier bed (e.g. Kamb, 1987; Iken, 1981). Because the connections between cavities are narrow orifices, the flow of water is restricted and an increase in water flux results in a direct increase in water pressure (Kamb, 1987). In a distributed drainage system, water emerges from the glacier through many small outlet streams (Björnsson, 1998).

Because the contribution of basal motion is linked to the amount of water available at the bed and to the subglacial drainage system structure (e.g. Iken, 1981), the surface velocity of a typical alpine glacier varies seasonally. Glacier surface velocities commonly peak in late spring/early summer, when surface melting increases basal water pressure and an efficient channelized drainage system is not yet established (e.g. Nienow et al., 1998). High basal water pressures promote sliding by decoupling the ice from the bed and causing partial or total flotation of the ice mass. High basal water pressures also promote weakening of saturated subglacial sediments, enhancing deformation and increasing basal motion (e.g. Iverson et al., 1998; Clarke, 2005).

Processes operating at the ice-bed interface can thus have a very strong influence on the overall glacier dynamics. Moreover, changes in surface conditions can in some cases directly and rapidly affect the glacier flow regime through changes in basal motion. Characterization of basal motion is therefore an important component of this study, particularly for surge-type glaciers as we will see in the next section.

1.1.3 Glacier surges in western North America

Glacier surges, as defined by Meier and Post (1969), are quasi-periodic events, generally lasting for 2-3 years, characterized by a considerable increase in flow velocity over part or the whole area of a glacier. Only a small percentage of all glaciers surge and these glaciers, commonly referred to as surge-type glaciers, exhibit an irregular geographical distribution, forming clusters in some regions and being absent in other regions. According to Clarke et al. (1986), surge-type glaciers can mainly be found in the mountain ranges of western North America, Svalbard, Iceland and East Greenland, the Pamirs, the Karakorum, the Caucasus, the Tien-Shan and the Andes. The 204 surge-type glaciers identified by Post (1969) in North America are located in the Alaska Range, the Chigmit, eastern Wrangell, eastern Chugach and St. Elias Mountains.

Surging glaciers commonly exhibit chaotically crevassed surfaces, with a high rate of crevasse opening, sheared margins and tributaries, and propagating bulges. Surge-type glaciers in their quiescent phase may present loops or folds in the medial moraines, or distinctively large areas of nearly stagnant ice (Meier and Post, 1969).

Parameters influencing surges

The periodicity of surges suggests that they are not triggered directly by irregular events such as earthquakes or climatic fluctuations, though it has been suggested that landslides can indirectly trigger surges (e.g. Gardner and Hewitt, 1990; Barrand and Murray, 2006).

Despite correlations between surging and glacier length or surface slope (e.g. Clarke et al., 1986; Jiskoot et al., 2000; Björnsson et al., 2003), there are surge-type glaciers of all sizes, shapes, slopes and thicknesses. Surge-type glaciers can be subpolar, temperate or polythermal and are found in both continental and marine climates, which suggests that the ability to surge is independent of climatic environment or thermal regime. However, the irregular geographic distribution of surge-type glaciers suggests that specific environmental conditions are required. The geologic setting seems to have an influence on the surge potential of a glacier. Clarke et al. (1984) speculated that beds made of unconsolidated glacial sediments (till) are permeable and easily deformable and may enable surging. According to Harrison and Post (2003), all drilling done on surge-type glaciers to date has revealed subglacial till.

Although the ability of glaciers to surge does not seem to depend on the climate setting, climate has a definite influence on surge behaviour through control of the glacier thermal regime. The surges of subpolar glaciers in Svalbard are longer and slower than surges of temperate glaciers in western North America (e.g. Dowdeswell et al., 1991; Harrison and Post, 2003). Climate also has an influence on the triggering of surges, and on the time interval between surges. A correlation exists between cumulative mass balance and surge intervals for Variegated Glacier, Alaska (Eisen et al., 2001) and Medvizhiy Glacier, Russia (Dyurgerov et al., 1985). However, the periodicity of surges suggests that the geometrical evolution of the glacier is the primary control on surge initiation, as we will see below, and year-to-year fluctuations in external conditions are only of secondary importance (e.g. Lingle and Fatland, 2003; Post, 1969).

Water stored englacially and subglacially plays an important role by interacting with the subglacial till to generate high basal water pressures which enhance bed deformation and promote sliding of the ice over its bed (e.g. Harrison and Post, 2003). Water pressures well above ice overburden pressure were measured during the 1982-1983 surge of Variegated Glacier, while pressures dropped well below overburden after the surge termination (Kamb et al., 1985).

The surge cycle

The surge cycle comprises the surging or active phase, and the non-surging or quiescent phase. The active phase usually lasts 1 to 6 years for western North American glaciers, and more commonly 2-3 years. It is always much shorter than the quiescent phase, which lasts from 15 to 100 years, more commonly 20-30 years for glaciers in western North America

(Meier and Post, 1969).

Ice reservoir and receiving areas can be defined for surge-type glaciers and usually differ from the accumulation and ablation zones. Reservoir and receiving areas arise due to a downstream resistance to sliding, thought to result from the glacier thermal structure for subpolar glaciers and from spatial variation in the efficiency of the subglacial drainage system for temperate glaciers (Clarke et al., 1984). During the quiescent phase, ice accumulates in the reservoir area causing thickening and the longitudinal profile in the lower part of the reservoir area steepens. The receiving area is located directly downslope from the reservoir area, and usually undergoes thinning during the quiescent phase because it is out of balance with climate and does not receive sufficient supply of ice to maintain a constant profile. Ice velocities during the quiescent phase are usually comparable to or lower than velocities in non-surge-type glaciers having the same geometrical characteristics (size, slope, ice thickness) and are often lower than the climate-dependent balance velocity required for the glacier to maintain a constant profile (e.g. Bindschadler et al., 1977; Raymond, 1987). Examples of reported quiescent-phase glacier surface velocities include: 3.2 m/a on the centerline of Konsvegen Glacier, a 25 km-long subpolar glacier in Svalbard (Melvold and Hagen, 1998); $\sim$ 14 m/a for Tungnaárjökull, a warm-based 40 km-long outlet glacier of Vatnajökull, Iceland; about 8 m/a in 2005 for Trapridge Glacier (Frappé and Clarke, 2007), a mid-sized polythermal glacier located in the St. Elias Mountains, and up to 200 m/a for Variegated Glacier, a 20 km-long temperate glacier located in the coastal St. Elias Mountains.

In the late stages of the quiescent phase, the thickening of the reservoir area and thinning of the receiving area are accompanied by increased velocity in the reservoir area. A threshold is reached when the glacier has accumulated enough mass in the reservoir area to surge again. The surge is initiated with rapid movement in the lower part of the reservoir area. The surge can propagate upglacier to higher reaches of the reservoir area due to stress redistribution and downglacier to the receiving area due to mass redistribution (Raymond, 1987). This causes vertical lowering of the ice surface in the reservoir area and vertical rise in the receiving area. The active phase is characterized by a 10- to 100-fold increase in velocity, with average surge velocities ranging from 100 m/a to over 1000 m/a for small glaciers in Alaska and south-western Yukon (Meier and Post, 1969). In many cases, the increase in flow velocity is accompanied by an advance of the terminus on the scale of hundreds of meters to several kilometers. Surges of the “Alaskan type” (Murray et al., 2003) are usually characterized by surge onsets lasting a few months and very rapid terminations, sometimes as short as a few hours.

Surging mechanism

Glacier surges in western North America are thought to occur when the normal, efficient channelized subglacial drainage system is disrupted and switches to a relatively inefficient linked-cavity drainage system (e.g. Clarke et al., 1984; Kamb, 1987; Raymond, 1987). Clarke et al. (1984) suggest the following mechanism for "Alaskan-type" surges of temperate or polythermal glaciers:

1. During the quiescent phase, the receiving area is more resistant to sliding than the reservoir area, possibly due to a more efficient drainage system near the terminus. This would reduce water pressure in the lower reaches of the glacier and decrease sliding. This resistance to sliding causes the reservoir area to thicken without flowing.
2. Thickening of the reservoir area is accompanied by an increase in shear stress, leading to enhanced ice deformation. The increasing ice deformation greatly reduces the efficiency of the channelized drainage system.
3. Water quickly accumulates at the glacier bed, which increases the subglacial water pressure and decreases basal shear stress, resulting in faster sliding. The high water pressure also weakens the subglacial sediments, thus increasing motion through bed deformation.
4. At the end of the surge, ice thickness and glacier slope are reduced, which results in a decrease in the shear stress, leading to a decrease in deformation. This allows the channels to regenerate and basal sliding to decrease.

Kamb (1987) suggested that the high sliding velocities occurring during the surge enhance cavitation and may thus facilitate the establishment and persistence of a linked-cavity drainage system. In addition, the fast sliding counteracts the melt-enlargement of the orifices connecting the cavities, thus sustaining the distributed system.

"Alaskan-type" versus "Svalbard-type" surges

The classic surge-type behaviour has been defined from observations of glacier surges in Alaska and the Yukon. Polar glaciers are also known to surge, but are less well documented than North-American surge-type glaciers. Dowdeswell et al. (1991) compared glacier surges in Svalbard to surges in other parts of the world (mainly western North America) and established that Svalbard glaciers exhibit a different type of surge behaviour. They found that "Svalbard-type" surges are characterized by (1) a longer active phase (3-10 years compared to 1-3 years for other glaciers), (2) a longer quiescent phase (50-500 years), (3) much lower ice velocities during the active phase, and (4) a gradual surge termination spanning several years (instead of several days for "Alaskan-type" surges). Murray et al. (2003) suggest that the surges of the polythermal subpolar glaciers of Svalbard are controlled by a thermal mechanism (Fowler et al., 2001), while "Alaskan-type" surges of mostly temperate glaciers in other parts of the world are controlled by the hydraulical mechanism proposed by Kamb et al. (1985).

1.1.4 Statement of the problem

Glaciers in Alaska and western Yukon Territory represent nearly 13% of all mountain glaciers on Earth (Arendt et al., 2002), and their current contribution to rising sea level is significant. Because they are located at high latitudes, many glaciers in western North America are especially sensitive to global warming. The dynamics of some of these glaciers can be complex (especially for tidewater and surge-type glaciers) making their response highly nonlinear. This work is part of a broader study, one of whose aims is to evaluate the modulating role of glacier dynamics on the response of glaciers to the regional climate in the St. Elias Mountains. The high proportion of surge-type glaciers in the St. Elias Mountains make a consideration of glacier dynamics essential in an evaluation of regional glacier-climate response.

The present work focuses on one of two study glaciers in the Donjek Range selected for their similar geometries and regional climate setting and their contrasting orientations and dynamic regimes. The dynamics of the glacier under consideration are examined in this thesis in order to distinguish between internal and external factors influencing the glacier flow regime and ultimately the glacier mass balance.

1.2 Study site

The study glacier is a small unnamed surge-type valley glacier situated at about 60°49' N and 139°07' E in Kluane National Park and Reserve (KNPR), south-west Yukon Territory, Canada. More precisely, it is located on the south side of the Donjek Range in the St. Elias Mountains which is flanked by the Kluane and Kaskawulsh outlet glaciers (Figure 1.1). The study glacier is south facing and occupies a tributary valley of the Kaskawulsh Glacier (Figure 1.1). It is about 5 km long and 1 km wide and spans an elevation of about 2000 m to 2800 m above sea level. It has two steep tributaries that join the main trunk about mid-glacier. The western tributary terminates in an ice-cored moraine and the eastern tributary is dynamically detached from the main trunk of the glacier. A contour map of the study glacier is shown in Figure 1.2. A 1951 aerial photograph shows the glacier during what appears to be a surge (P. G. Johnson, personal communication, 2006), with the terminus located about 1 km further down-valley than at present. Another surge in the late 1980s has also been reported. Nothing definitive is known about the glacier thermal regime except what is presented in this thesis.

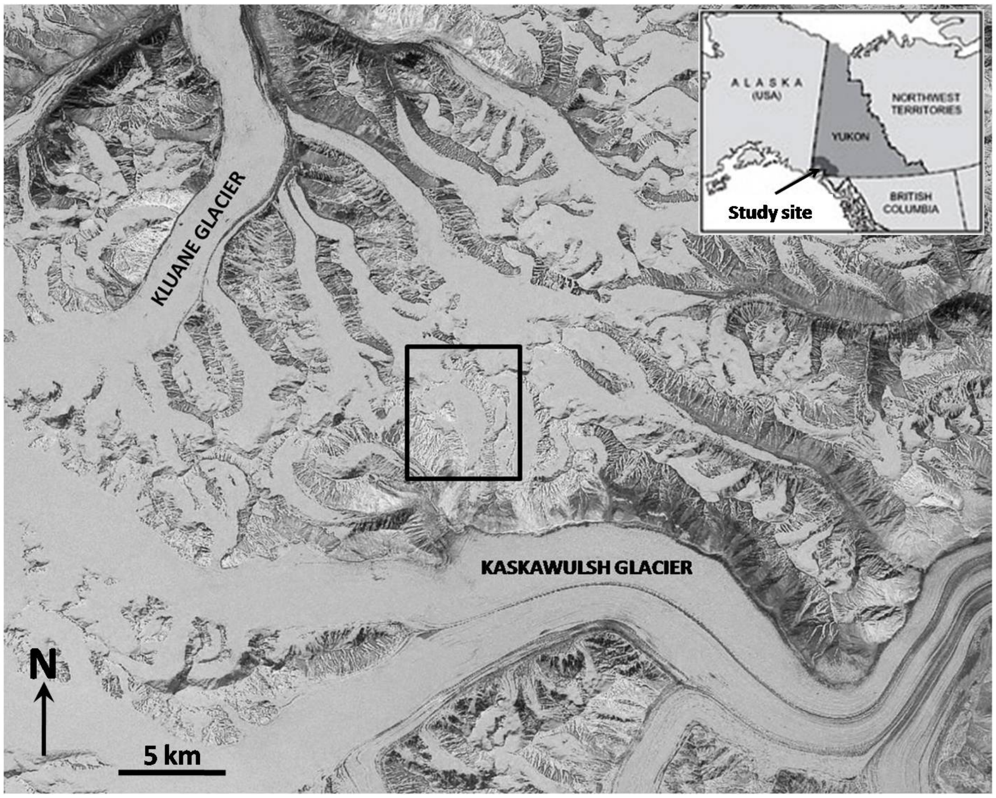

Figure 1.1: Landsat image of the Donjek Range. The black box indicates the location of the study glacier

1.3 Thesis outline, goals and objectives

The long-term goal of this study is to assess the importance of glacier dynamics in modulating glacier-climate sensitivity on a regional scale. The overall goal of this thesis is to characterize the dynamics of the study glacier toward identifying the processes responsible for its current flow regime. My objectives are to answer the following questions: (1) What do the bed topography and the distribution of ice thickness look like and how might they influence the distribution and flow of subglacial water? (2) What is the basal velocity profile and what fraction of the observed surface velocity does it account for? (3) What factors control the current glacier flow regime and is this regime characteristic of a surge-type glacier in its quiescent phase? To answer these questions, the present study is organized around three main tasks:

1. Construct digital elevation models of the glacier surface and bed and calculate the distribution of upstream drainage area;

2. Evaluate the contribution of basal motion to the overall glacier motion using geophysical inversion methods;

3. Evaluate whether the results are consistent with what is expected from a surge-type glacier in its quiescent phase, and identify the main controls on the current flow regime.

This thesis is divided into four main chapters. In Chapter 2, the datasets used to generate the surface and bed DEMs, as well as those used as input to the inverse model are presented. In Chapter 3, the construction of DEMs of the glacier surface and bed by kriging is detailed, and flowline profiles of glacier geometry are derived. In Chapter 4, inversion methods are presented and used to recover a longitudinal basal velocity profile. Control tests of the inversion algorithm are performed to evaluate the validity of the method, after which the real data are inverted. The sensitivity of the inversion results to four parameters is also tested and results are discussed from a methodological point of view. In Chapter 5, I discuss the inversion results and their implications from a glaciological point of view. Chapter 6 provides a brief summary and conclusion.

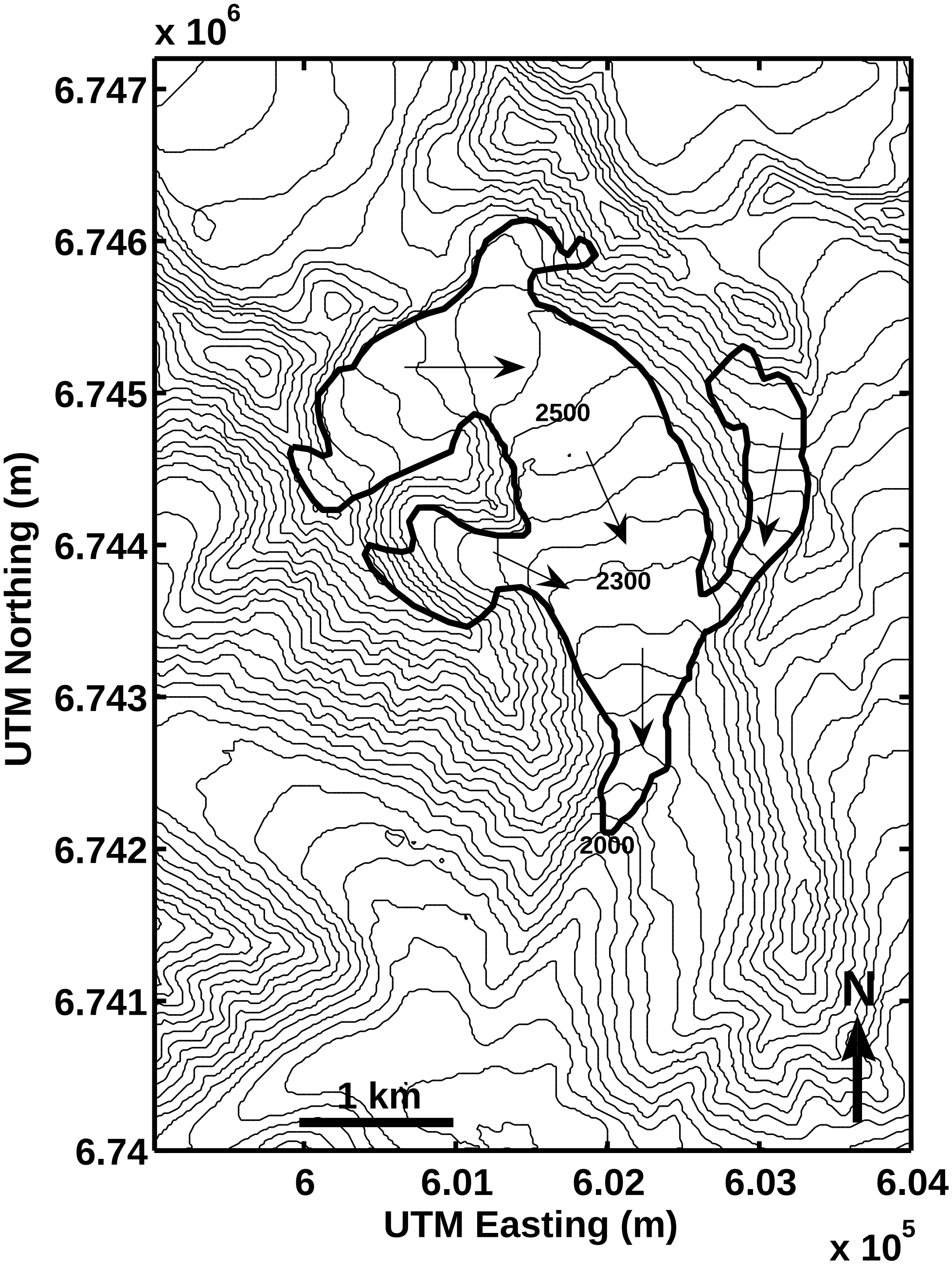

Figure 1.2: Contour map of the study glacier and its surroundings. Contour interval is 50 m. The fine arrows indicate the direction of ice flow

Chapter 2

Data, errors and model inputs

Data have been collected on the study glacier during three consecutive summer field seasons from 2006 to 2008. The model presented in Chapter 4 requires specification of the surface velocity along an approximate flowline, as well as parameters characterizing the glacier geometry, such as ice thicknesses and surface slope. This chapter describes the data collection and the derivation of several model inputs. Other model inputs require construction of a digital elevation model (DEM) of the surface and the bed of the glacier and will be presented in Chapter 3. The data presented here were collected by various members of the SFU field crew. I did not take part in either the acquisiton or the processing of these data.

2.1 Surface Elevation

Ice-surface elevations over most of the main trunk of the glacier were obtained by real-time kinematic GPS surveying using Trimble R7 receivers with Zephyr geodetic antennas and a temporary local base station situated ∼200 m from the glacier (Figure 2.1). In 2008, a permanent base station was established at the Kluane Lake Research Station about 40 km from the field site. The temporary station has now been referenced to this new station. The distribution of the glacier surface elevation data collected during the 2006 and 2007 surveys is shown in Figure 2.1, along with the location of the temporary base station. The data were collected following transect paths on the glacier surface and dense spatial coverage was achieved over most of the main trunk of the glacier, except for in a few areas including (1) an ice-cored moraine between the trunk and west tributary glacier, (2) a heavily crevassed region over a bedrock ridge and (3) a prominent icefall below the glacier headwall. Two steep tributaries to the main trunk of the glacier were not surveyed (the eastern tributary is effectively disconnected from the main trunk). Parts of these tributaries are nearly vertical and the west tributary has a hanging glacier just below the ridge crest.

Changes in surface geometry, primarily due to ablation, occurred over the one-month survey period in 2006 and between the two consecutive surveys in 2006 and 2007, so the DEM created from these data is a blend of the July 2006 and August 2007 geometries. The fact that the ice surface elevation at a given location can vary from one year to the next or within the period of one survey constitutes a source of uncertainty in the DEM. Based on

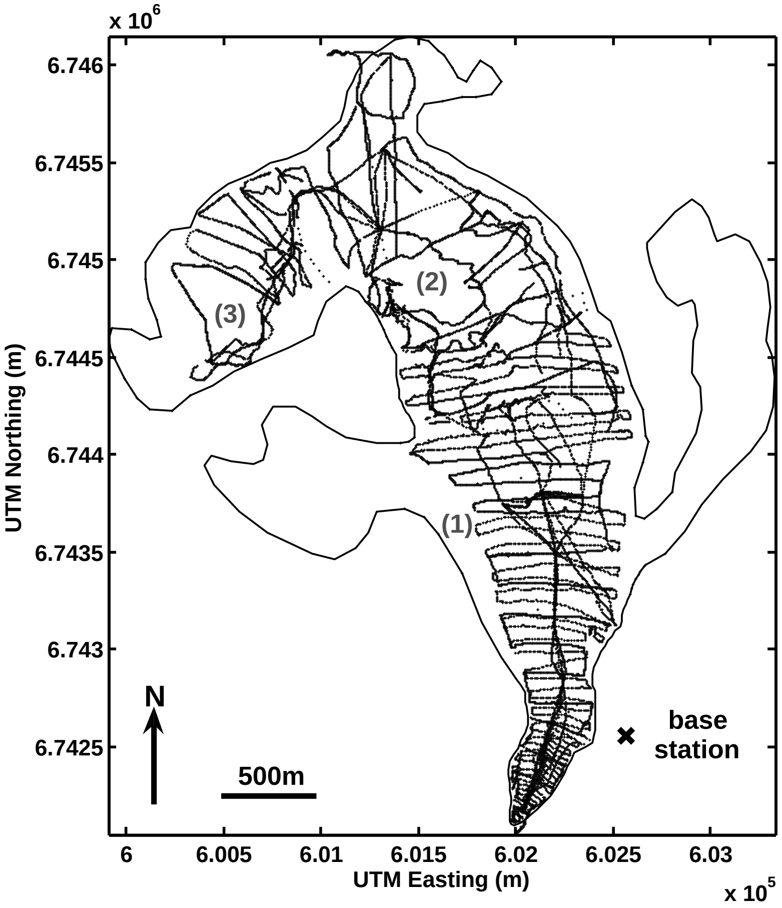

Figure 2.1: Spatial distribution of raw glacier surface elevation data with the glacier outline (solid line). A few areas were avoided, including (1) an ice-cored moraine between the trunk and west tributary glacier, (2) a heavily crevassed region over a bedrock ridge and (3) a prominent icefall below the glacier headwall. Glacier tributaries have not been surveyed

the survey methodology and the different time periods over which the data were collected, the surface elevation errors are estimated to be $\sim \pm 1\,\mathrm{m}$.

2.1.1 Glacier outline and flowline

The glacier outline is first estimated from the 1977 map of the area of Kluane Glacier (Dept of Energy, Mines and Resources Canada, Map 115 B/14, 1987). The outline is then updated by using the 2006-2007 survey data points that are located outside the 1977 outline to define a new ice margin. An approximate flowline was mapped during the 2006 GPS survey by taking measurements along the direction of steepest slope.

2.2 Ice thickness

Ground-based ice-penetrating radar data were collected during the summer 2007 and spring 2008 field seasons. A high-power impulse transmitter identical to that described by Narod and Clarke (1994) was used along with resistively-loaded transmitting and receiving antennas fabricated by Icefield Instruments Inc. Each antenna is composed of two 4 m-long sections. The impulse transmitter operates with a pulse rate of 512 Hz and the transmitting antenna produces a centre frequency of 8 MHz. A National Instruments USB-5133 2CH $100\,\mathrm{MS\,s^{-1}}$ digitizer is used in place of an oscilloscope to capture the receiver signal which is displayed on a miniature laptop computer (ASUS eeePC with solid-state hard drive). Data acquisition and simple processing software were custom-designed by Blue System Integration Ltd. and include GPS capability (Rikaline SiRF III USB GPS receiver). The radar survey geometry is shown in Figure 2.2.

Data were collected at 10 s intervals while the equipment was towed on skis along survey transects. Antennas were oriented parallel to the direction of motion for ease of travel. Each saved trace comprised a stack of 50 traces acquired at the same location and subsequently averaged in order to increase the signal-to-noise ratio. Over the lower two-thirds of the glacier, the spacing between transect paths was approximately 200 m and clear bed reflections were achieved over much of this area. Adverse travelling conditions and frequent clutter in the radar returns resulted in patchy coverage over the upper one-third of the glacier. Moreover, several inacessible or highly crevassed areas were not surveyed. The spatial distribution of the radar data is shown in Figure 2.3.

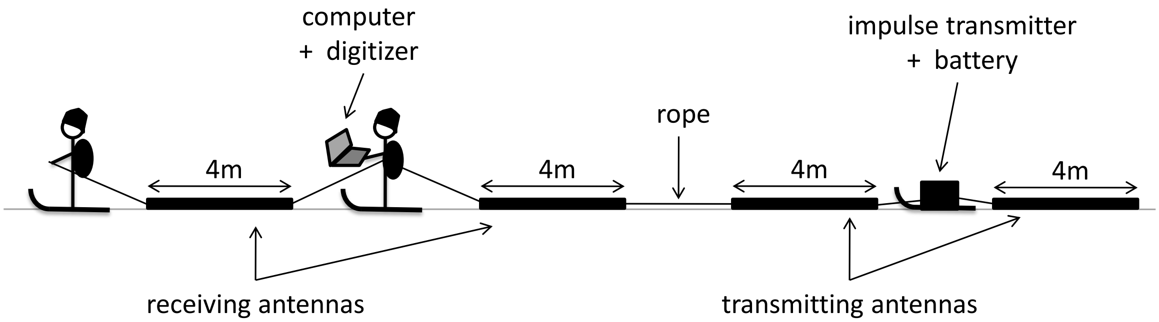

Figure 2.2: Radar survey equipment geometry

To derive ice-thicknesses, the arrival times of the direct air wave and of the bed reflection are manually identified on the radar traces. To minimize errors associated with data of variable amplitude, we attempt to pick arrival times corresponding to the first incidence of energy (as opposed to the peak). Travel times for the direct and reflected wave are thus extracted from each radar trace and ice thickness is computed from the travel-time difference, with the assumption that the ice surface and bed are parallel in the vicinity of the measurement. A homogenous ice velocity of $1.68 \times 10^8\,\mathrm{m\,s^{-1}}$ is assumed. Englacially reflected wave arrivals are common, but the high resolution of the survey usually allows one to follow the bed profile along a transect and discriminate between bed and englacial reflections.

The data quality was assessed for each radar trace and recorded as a quality index. Quality indices were assigned depending on the clarity of the bed reflection, with a quality index of 1 corresponding to a very poor reflection and 5 to an excellent reflection. In Chapter 3, quality indices are used to filter the ice-thickness data as a precursor to interpolation by kriging.

2.3 Surface velocity

A network of 10 velocity stakes (10 ft-long metal or PVC conduits) was established along the glacier flowline in the summer 2006. Two additional poles were installed in the summer 2007. The locations of the 12 poles, labelled S1 to S12, are shown in Figure 2.4. These poles were

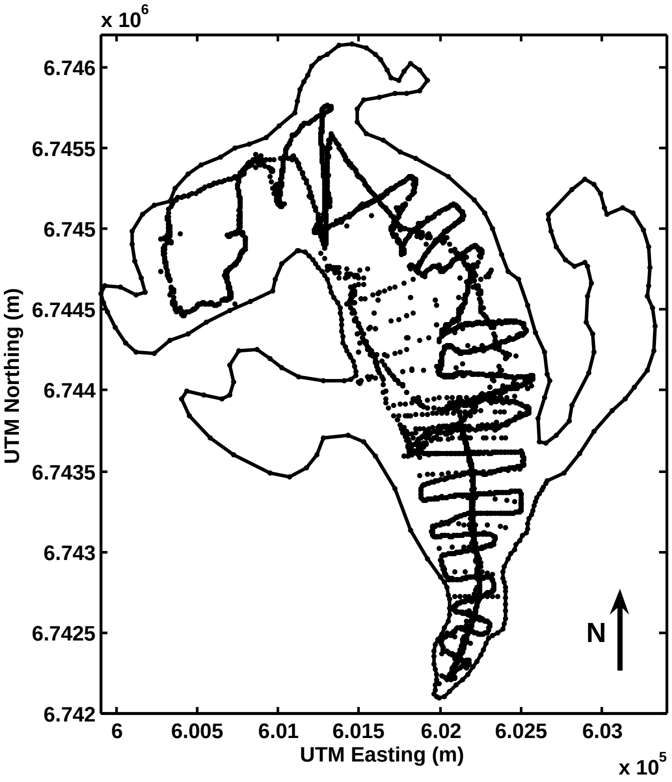

Figure 2.3: Spatial distribution of ice-penetrating radar data

surveyed weekly during the periods listed in Tables 2.1 and 2.2 using real-time kinematic (RTK) GPS in 2006 and 2007 and post-processing kinematic (PPK) GPS in 2008. The equipment and methodology are as described in Section 2.1. Methodological uncertainties in the position measurements of the poles were estimated empirically by having different team members measure the location of the same pole in succession. An uncertainty of ±5 cm in the pole horizontal coordinates was estimated based on the instrumental uncertainty and our methodology.

Surface velocities are calculated using the total pole displacement between the first and the last day of survey for a given pole. Vertical displacement of the pole during the survey period is not taken into account, thus the calculated surface velocities are strictly horizontal.

The resulting velocities can be expressed mathematically as

$$u_s = \frac{\sqrt{(E_f - E_i)^2 + (N_f - N_i)^2}}{N_d}, \tag{2.1}$$

where E_i and N_i are the initial Easting and Northing coordinates, E_f and N_f are the final Easting and Northing coordinates, and N_d is the length of the survey in days. Standard error propagation is used to assign errors to the surface velocities (Appendix A).

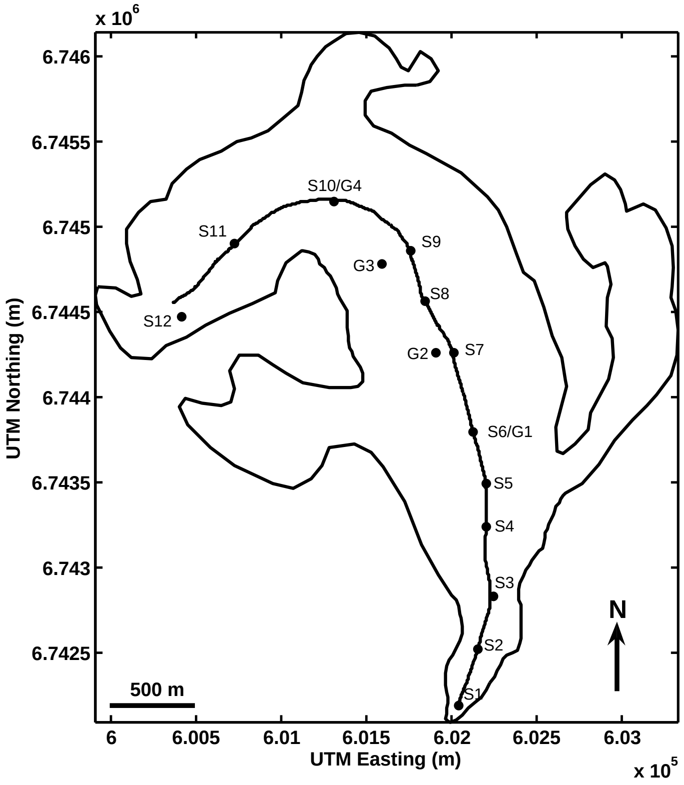

Figure 2.4: Spatial distribution of ice-velocity survey poles used in this study. Poles labelled S1 to S12 are velocity stakes that were surveyed intermittently. Poles G1 to G4 have GPS antennas mounted on them and data were collected at 15 s to 2 min intervals. Note that both simple ice stakes (S6,S10) and poles with mounted GPS (G1,G4) occupy the sites labelled S6/G1 and S10/G4

2.3.1 Poles with fixed GPS

An additional set of four velocity poles was installed between 2006 and 2008. These poles differ from those velocity poles described above in that a GPS antenna is attached to the pole for the duration of the measurement period. The displacements of these poles, labelled G1 to G4 in Figure 2.4, were determined using post-processing kinematic (PPK) GPS. The GPS equipment, shown in Figure 2.5, is identical to that described in Section 2.1, except for the antennas, which are larger than those used with the roving GPS receiver. Positions of these poles are measured every 15 s to 2 minutes for a period of three to six weeks. Because the GPS receiver is attached to the poles, we only include the instrumental uncertainty of ±1 cm on the positions measured this way. This gives rise to errors on the velocity calculations that are much lower than those for poles S1 to S12.

The periods over which these poles locations were measured is different from the periods over which the poles S1 to S12 were surveyed. For consistency, the velocities derived using measurements from these four poles need to be calculated over a period that is similar to the period over which the other pole velocities are derived. Periods roughly coinciding with the pole surveys described above are therefore chosen to calculate the velocities associated with poles G1–G4. The surface velocities and associated errors are computed in the same manner as for the other poles, using the total displacement occurring between the first and the last day of the chosen period. The periods over which velocities are computed, along with the resulting surface velocities and associated errors are presented in Tables 2.1 and 2.2.

2.3.2 Post-processing kinematic (PPK) GPS processing

Post-processing kinematic (PPK) GPS is used to determine the locations of poles with fixed GPS receivers (poles G1–G4) from 2006 to 2008, as well as for surveying all velocity poles (S1–S12) in 2008. Because there is no radio link between the base station and the roving receiver, the processing of the raw GPS data is done after the survey using the commercial software Trimble Geomatics Office. Raw GPS data are mainly a record of tracked phase, but also contains Keplerian parameters characterizing the satellites orbits. The main steps of the processing of raw GPS data are the following:

- satellite orbits are generated from the Keplerian parameters;
- possible cycle slips are detected and repaired (cycle slips occur when the receiver temporarily loses track of the satellite signal);

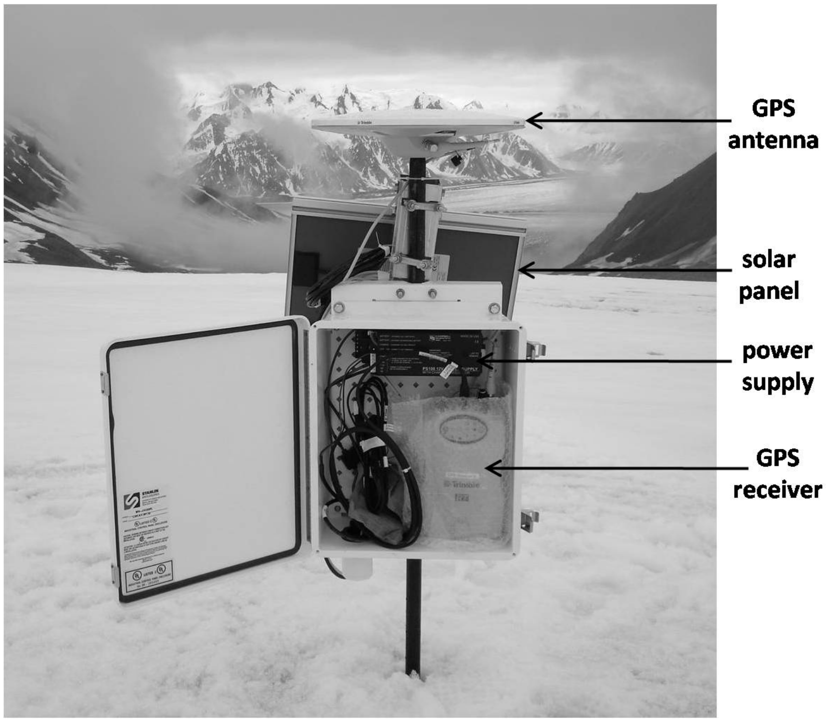

Figure 2.5: Equipment attached to a velocity survey pole to measure horizontal displacements using post-processing kinematic GPS

- a first approximation of the roving receiver position is computed using the pseudoranges between the receivers (roving receiver and base station) and at least three satellites;
- raw carrier phase data is transformed and differentiated;
- an initial calculation of the baseline vector between the roving receiver and the base station is carried out;
- ambiguities associated with the phase of the signal are resolved and the baseline vector is recalculated;
- the position of the roving receiver is calculated using the known coordinates of the base station;
- Elevation measurements are expressed using the WSG84 geoid as a reference for sea level (instead of the WGS84 geocentric ellipsoid).

2.3.3 Surface velocity datasets

Four datasets are defined from the measurements presented in Tables 2.1 and 2.2: Summer 2006, Summer 2007, Annual 2006-2007 and Annual 2007-2008. It is important to note that the "summer" velocity data cover only one to two weeks in the middle of the melt season, but are referred to as "summer" for convenience. A number of poles had melted out between the 2006 and 2007 field seasons and were re-set in the summer 2007. For this reason, the annual 2006-2007 dataset contains only 8 poles, while the three other datasets contain 11 poles.

Before describing these four datasets the question of short-term variability in summer surface velocity must be addressed. The surface velocity data are values averaged over the measurement period (usually ∼2–3 weeks) and are taken as representative of this period. Short-term speed-up events may take place that are not captured in the datasets presented here. Such events cannot be identified from regular pole survey measurements, as poles are only surveyed weekly, but may be identified in measurements from poles with attached GPS (poles G1–G4), for which daily and even hourly displacement records exist. To this end, daily velocities are extracted from the raw GPS data for poles G1 to G4 and searched for short-term speed-up events. We find that the average velocities used in the datasets presented here are fairly representative of the overall velocity during the measurement period, with few and only small deviations from the average value for most datasets, as shown in Figure 2.6 for pole G1 in Summer 2007.

Figures 2.7 and 2.8a show that the flowline velocity structure is similar for the four datasets, with velocities less than 10 m/a over the lower 1500 m of the glacier, and velocities greater than 10 m/a over the upper 3500 m. Figure 2.8a also reveals a distinct difference between the summer and annual velocities, with an offset of ∼10 m/a above 2000 m from the terminus. Since the measurements of "summer" velocity do not include the late spring and early summer, the true seasonality of the velocity profile may be stronger than indicated by these data.

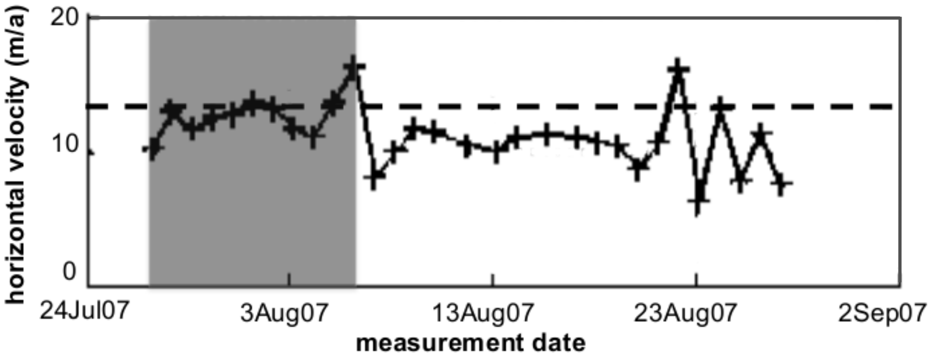

Figure 2.6: Surface velocity measured in Summer 2007 for pole G1 is plotted as a function of time to assess short-term variability. Velocity time series were obtained from static daily position solutions processed using Trimble Office software. The surface velocity is shown to be representative of the value used in the Summer 2007 dataset (Table 2.1), represented by the bold dashed line, over the period used to derived it (gray area)

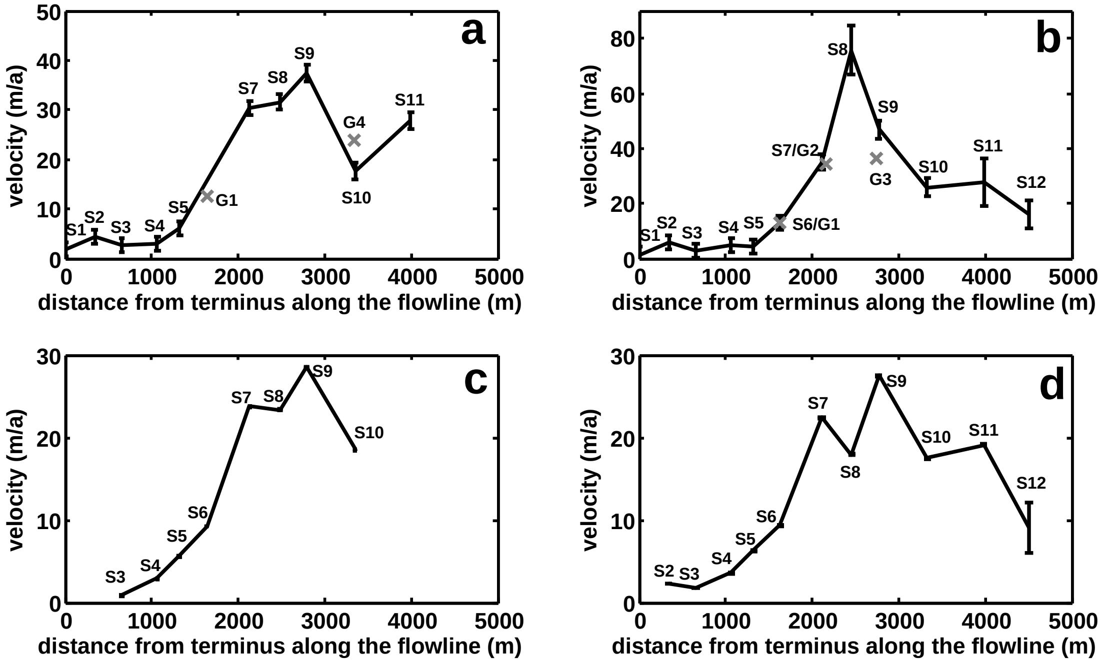

Figure 2.7: Measured surface velocities with associated errors plotted as a function of distance from the glacier terminus along the flowline for the (a) Summer 2006, (b) Summer 2007, (c) Annual 2006-2007 and (d) Annual 2007-2008 datasets. The gray crosses correspond poles G1 and G4 in (a) and poles G1, G2, and G3 in (b)

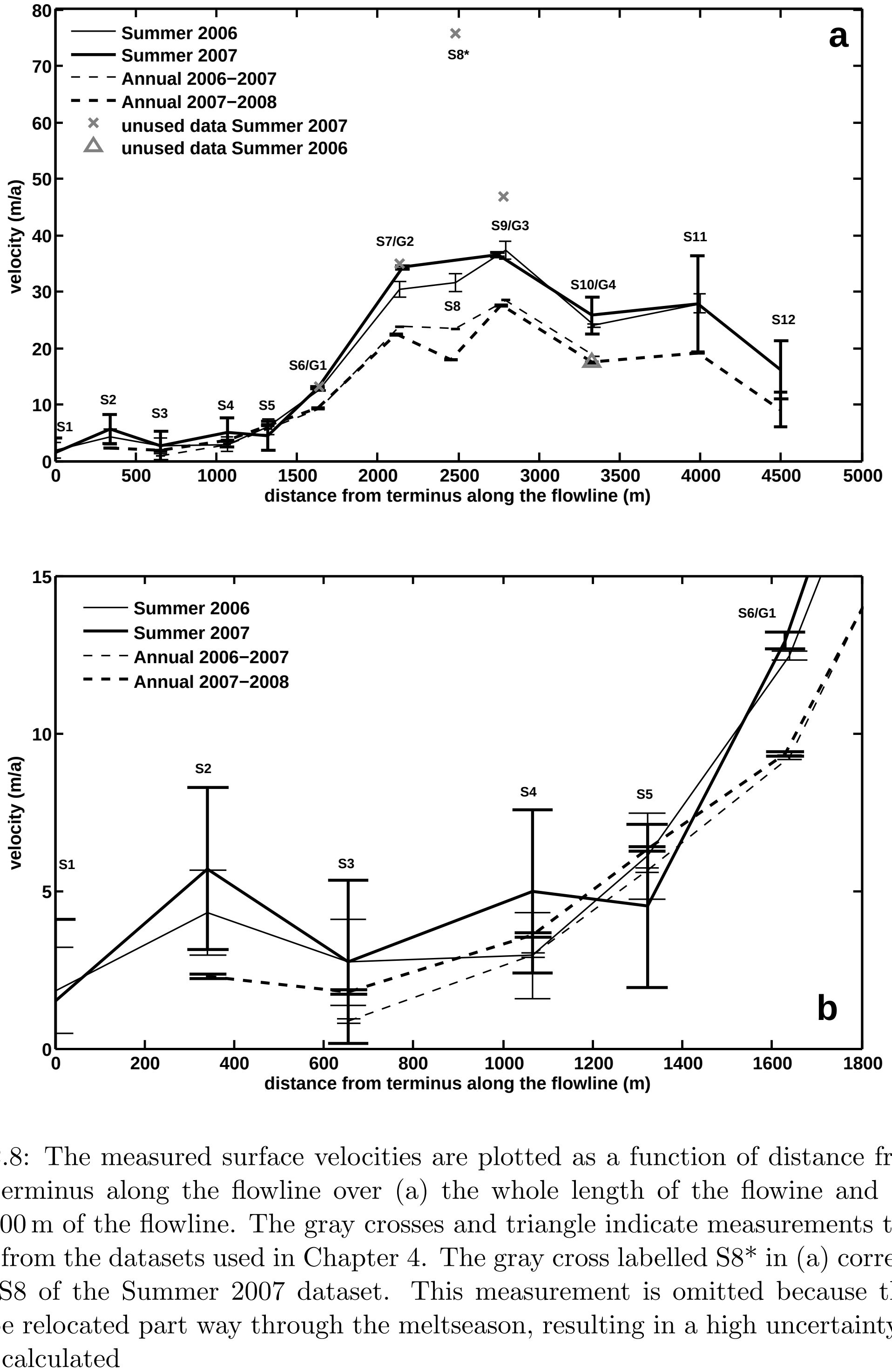

Figure 2.8: The measured surface velocities are plotted as a function of distance from the glacier terminus along the flowline over (a) the whole length of the flowine and (b) the lower 1500 m of the flowline. The gray crosses and triangle indicate measurements that are omitted from the datasets used in Chapter 4. The gray cross labelled S8* in (a) corresponds to pole S8 of the Summer 2007 dataset. This measurement is omitted because the pole had to be relocated part way through the meltseason, resulting in a high uncertainty in the velocity calculated

		Summer 2006					**Summer 2007**				
Pole name	Distance from terminus along flowline (m)	start date	end date	number of days	velocity (m/a)	error (m/a)	start date	end date	number of days	velocity (m/a)	error (m/a)
S1	0	11Jul06	30Jul06	19	1.8	1.4	27Jul07	6Aug07	10	1.5	2.5
S2	342	11Jul06	30Jul06	19	4.3	1.4	27Jul07	6Aug07	10	5.7	2.5
S3	655	11Jul06	30Jul06	19	2.7	1.4	27Jul07	6Aug07	10	2.7	2.5
S4	1067	11Jul06	30Jul06	19	2.9	1.4	27Jul07	6Aug07	10	5.0	2.5
S5	1321	11Jul06	30Jul06	19	6.1	1.4	27Jul07	6Aug07	10	4.5	2.5
G1	1629	10Jul06	23Jul07	13	1.2	0.1	27Jul07	6Aug07	10	12.9	0.3
S6	1639	-	-	-	-	-	27Jul07	6Aug07	10	13.2	2.6
S7	2135	14Jul06	30Jul06	19	30.4	1.4	27Jul07	5Aug07	9	35.0	2.9
G2	2157	-	-	-	-	-	28Jul07	6Aug07	9	34.3	0.3
S8	2482	14Jul06	30Jul06	16	31.6	1.6	28Jul07	5Aug07	8	75.7	9.1
G3	2745	-	-	-	-	-	30Jul07	6Aug07	7	36.5	0.4
S9	2792	14Jul06	30Jul06	16	37.4	1.6	28Jul07	5Aug07	8	46.9	3.2
S10	3331	14Jul06	29Jul06	15	17.6	1.6	28Jul07	5Aug07	8	25.8	3.2
G4	3340	13Jul06	23Jul07	10	24.0	0.3	-	-	-	-	-
S11	3985	14Jul06	29Jul06	15	27.9	1.7	2Aug07	5Aug07	3	27.7	8.6
S12	4506	-	-	-	-	-	31Jul07	5Aug07	5	16.0	5.2

Table 2.1: Pole survey data for the summer 2006 and summer 2007 periods. Note that the distances from terminus along the flowline are measured at the start of the 2006 survey and are therefore not exactly accurate for subsequent years

Pole name	Distance from terminus along flowline (m)	**Annual 2006-2007**					**Annual 2007-2008**				
		start date	end date	number of days	velocity (m/a)	error (m/a)	start date	end date	number of days	velocity (m/a)	error (m/a)
S1	0	-	-	-	-	-	-	-	-	-	-
S2	342	-	-	-	-	-	27Jul07	15Jul08	353	2.30	0.07
S3	655	30Jul06	27Jul07	362	0.90	0.07	27Jul07	15Jul08	353	1.80	0.07
S4	1067	30Jul06	27Jul07	362	2.90	0.07	27Jul07	15Jul08	353	3.60	0.07
S5	1321	30Jul06	27Jul07	362	5.60	0.07	27Jul07	15Jul08	353	6.30	0.07
S6	1639	30Jul06	27Jul07	362	9.20	0.07	27Jul07	15Jul08	353	9.30	0.07
S7	2135	30Jul06	27Jul07	362	23.80	0.07	27Jul07	5Jul08	343	22.40	0.08
S8	2482	30Jul06	28Jul07	363	23.40	0.07	28Jul07	7Jul08	344	17.90	0.08
S9	2792	30Jul06	28Jul07	363	28.50	0.07	28Jul07	7Jul08	344	27.50	0.08
S10	3331	29Jul06	28Jul07	364	18.50	0.07	28Jul07	7Jul08	344	17.40	0.08
S11	3985	-	-	-	-	-	2Aug07	14Jul08	359	19.10	0.08
S12	4506	-	-	-	-	-	31Jul07	14Jul08	357	9.00	3.10

Table 2.2: Pole survey data for the years 2006-2007 and 2007-2008. Note that the distances from terminus along the flowline are measured at the start of the 2006 survey and are therefore not exactly accurate for subsequent years

Chapter 3

Digital elevation models and flowline profiles

3.1 Generating a surface DEM by kriging in Matlab

Digital elevation models (DEMs) are constructed by interpolating a set of data points onto a regular grid. Many different methods exist to interpolate data which yield results of varying quality. Results arising from different methods are briefly compared in section 3.3.3. The method of kriging, sometimes referred to as optimal interpolation, is used for generating both glacier surface and bed DEMs. The theory of kriging was first introduced by Matheron (1963) and was then widely used in geology and the mineral industry. This method of interpolation has also proved useful in other disciplines of Earth Science such as hydrology and glaciology (e.g. Flowers and Clarke, 1999; Hock and Jensen, 1999).

Kriging is an exact interpolator, which means that when estimating a value at a point for which a measured datum is available, the value of the data point is respected and thus the expected interpolation error is zero. Through geostatistical analysis of the data, kriging also takes into account distances between data points, according more weight to points located close to the estimated point than to points situated further apart. The interpolation is rendered optimal by minimizing the variance of the estimation error. In addition, the statistical analysis quantifies spatial anisotropy in the dataset and allows this information to be taken into account in the interpolation process. For all these reasons, kriging often leads to better results than other common interpolation methods.

3.1.1 Input data

The inputs to the surface DEM are the GPS-measured surface elevations presented in Chapter 2. Only measured data points situated on the ice are considered at this stage. The surrounding terrain is not included in the kriging interpolation because its morphology prevents its preconditioning in the same manner as the glacier surface. The surrounding terrain topography, in the form of contour lines digitized from the Kluane Glacier area map (115 B/14), are added to the glacier surface DEM at a later stage. However, a few data points digitized from the map, all situated on the glacier outline, are added to the GPS measured dataset. This is done to ease the later juxtaposition of the surrounding terrain and krigged glacier surface, and make this transition more faithful to reality in zones where measured data are scarce. The spatial distribution of input data, including points added from the outline, is shown in Figure 2.1 in Chapter 2.

3.1.2 Data preconditioning

Interpolation using ordinary kriging is most efficient when the input dataset has a normal or Gaussian distribution. In addition, data points occupying the same location give rise to singularities in the statistical calculations. Therefore, the raw data need first to be preconditioned in order to optimize kriging. This preconditioning takes the form of two transformations: first, the raw data are averaged over the interpolating grid, then they are detrended.

Data averaging

The raw data are in some places heavily clustered, with measurements taken very close to one another. Such close measurements show surface structure that is too fine to be adequately resolved by the kriging algorithm, and is thus likely to be translated into surface artefacts by the kriging. The raw data also present many occurrences of measurements taken at the same location. These “doubles” produce singularities in the variogram calculations and therefore would be problematic in the geostatistical analysis. Indeed, the statistical calculations include division of quantities by the distance between two data pairs, resulting in a singularity when the two data points have the same location. Thus, the raw data need to be stripped of “doubles” and very close data points.

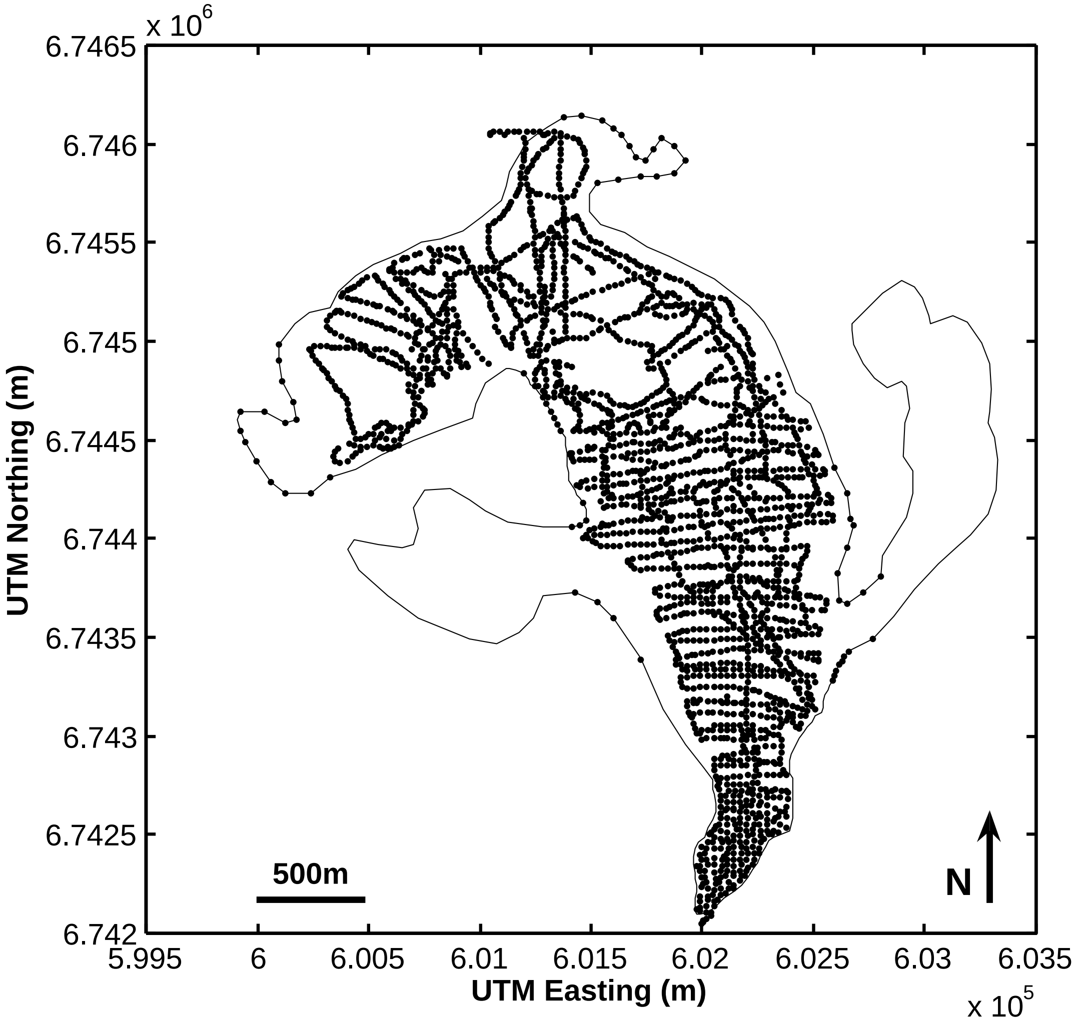

Figure 3.1: Spatial distribution of averaged glacier surface elevation data and glacier outline (solid line). Glacier tributaries have not been GPS surveyed and contain no data.

The problem described above is resolved by combining data points that are situated in the same 30 m grid cell. We combine data by taking the respective averages of the Easting, Northing and elevation of every data point situated in the same 30 m grid cell. The variability of the errors between data points is small, so data are all of comparable quality, and therefore are weighted equally. The spatial distribution of averaged glacier surface elevation data is shown in Figure 3.1.

Data detrending

The input data must be characterized by an approximately normal distribution for the kriging interpolation to be performed correctly (Carr, 1995). This is not the case for the raw glacier surface elevation data, as can be seen in Figure 3.2a. Over most of the length of the glacier the surface slopes in a roughly north-south direction, which is the direction of flow. Therefore we expect the data to have a trend in this direction. This is apparent when plotting the surface elevation component of the dataset as a function of Northing (Figure 3.3). This spatial trend constitutes a statistical bias and therefore must be removed.

Although the variation of elevation with Northing is approximately linear, removing the trend by simply subtracting a best-fit line does not yield the best results. Indeed, the direction of ice flow changes from north-south over most of the glacier to west-east over the

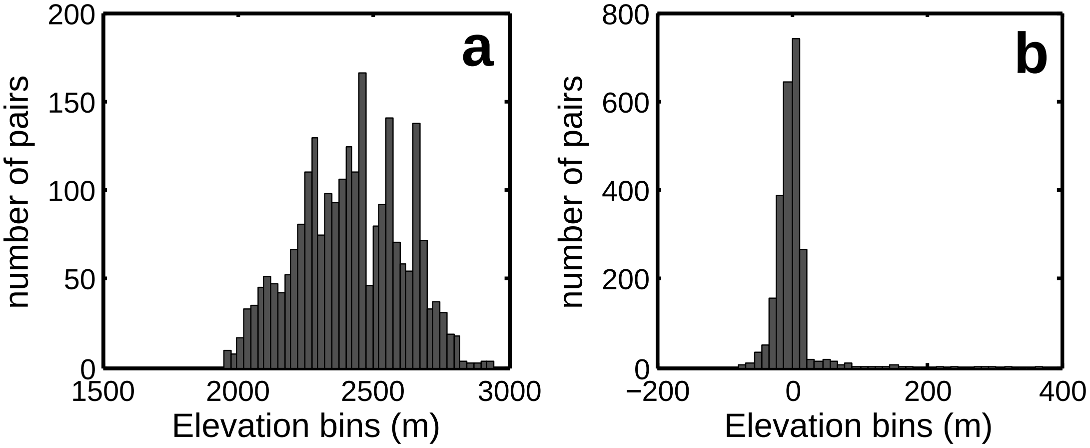

Figure 3.2: Histograms of (a) averaged and (b) transformed ice surface elevations. The transformation results in an approximately normal distribution.

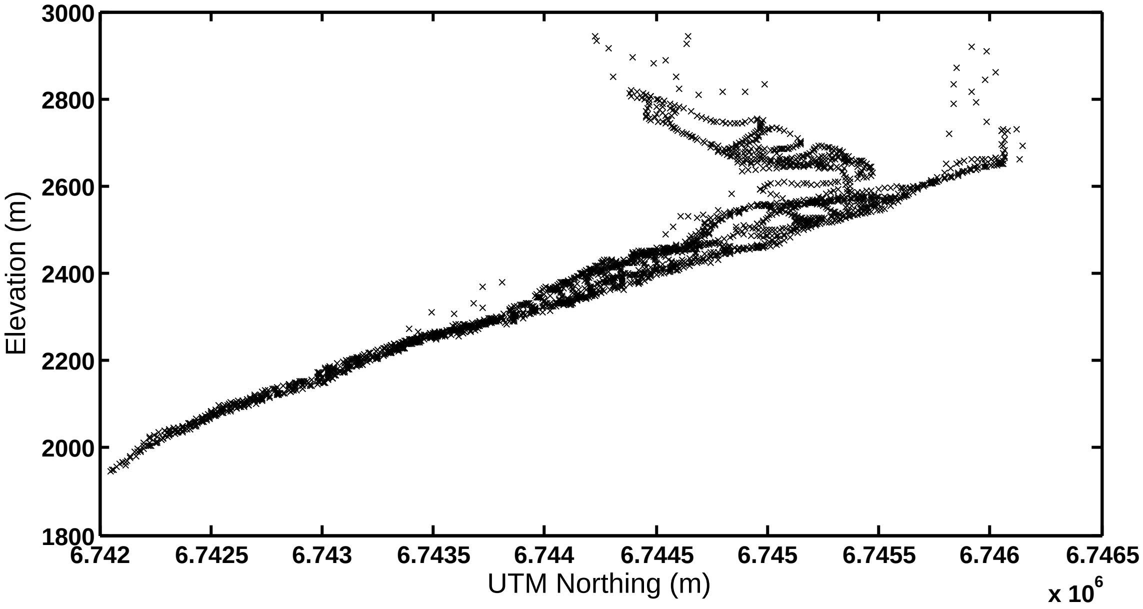

Figure 3.3: Projection of glacier surface elevation data onto the Northing coordinate to illustrate dominant spatial trend.

upper portion of the glacier. This situation forces such a linear transformation to be realized in two stages, with a best-fit line defined for both the south-sloping lower part and the east-sloping upper part of the glacier. This two-zone transformation is easily implemented but results in inconsistencies in the region where the two different sections meet.

A data transformation that is continuous over the whole length of the glacier is therefore adopted. I choose a transformation that I refer to as flowline detrending which uses an approximate flowline situated near the centerline of the glacier. This transformation is carried out in four steps:

1. Points along the flowline, previously identified by their Northing and Easting UTM coordinates, are given a flowline coordinate, which corresponds to their distance from the glacier terminus along the flowline itself.

2. For each glacier surface elevation datum, the closest point on the flowline is identified and its flowline coordinate assigned to the data point. Thus every data point now possesses four coordinates: Northing, Easting, elevation, and distance from terminus along the flowline (this distance actually corresponds to the distance from terminus of

the associated flowline point).

3. Using least-squares regression, a best-fit line is calculated for the elevation data as a function of distance from terminus. The equation of the best-fit line is

$$E = 0.2\,s + 2025.5, \tag{3.1}$$

   where E is the elevation is meters and s the distance from the terminus along the flowline in meters.

4. The value of elevation corresponding to its flowline coordinate on the best-fit line is subtracted from the actual elevation of each data point.

The resulting transformed data set has a mean of nearly zero and an approximately normal distribution (Figure 3.2b).

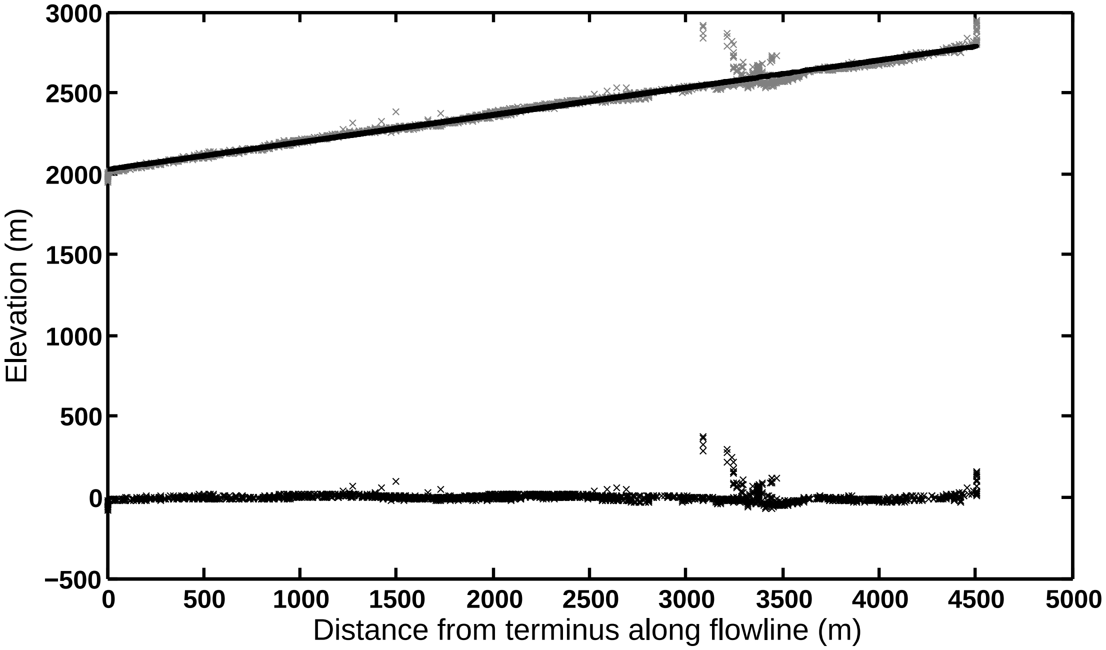

Figure 3.4: Glacier surface elevation values from averaged dataset along with best-fit line (top) and elevations values from transformed dataset (bottom). The transformation shifts the data mean to approximately zero.

3.1.3 Geostatistical analysis

As mentioned above, kriging is an interpolation method that incorporates information about the data through statistical analysis. Before kriging can be applied, the spatial autocovariance of the elevation data must be calculated. This is done by calculating the semivariogram, which is directly related to the autocovariance function.

Experimental semivariogram

A fundamental assumption of kriging is that values of data points separated by a short distance (small lag) have a greater probability of being similar than values further apart, and that this similarity does not depend on absolute location (Carr, 1995). The semivariogram is thus used to characterize how the data (here elevations) change as the distance between data points increases. The semivariogram depends only on lag distance h, or distance between two data points. Following Carr (1995), the semivariogram is defined analytically as

$$\gamma(h) = \frac{1}{2N} \sum_{i=1}^{N} [Z(x_i) - Z(x_{i+h})]^2, \tag{3.2}$$

where N is the total number of data considered, $Z(x_i)$ is the elevation of a data point at position x_i and $Z(x_{i+h})$ is the elevation of a data point situated at a distance h from the first data point.

Semivariogram models

Once the semivariogram is computed, it is modelled and the statistical parameters describing the dataset are extracted. The most common model functions of semivariograms are the Gaussian and spherical models. The equation for an idealized spherical model is (David, 1977)

$$\gamma(h) = \begin{cases} CO + C\left(\dfrac{3h}{2a} - \dfrac{h^3}{2a^3}\right), & 0 < h \leq a, \\ CO + C = \text{sill}, & h > a, \\ 0, & h = 0, \end{cases} \tag{3.3}$$

where the parameter CO is the “nugget” value, a is the range and C is equal to the sill minus the nugget value. The sill is the constant value reached by the semivariogram when the lag h becomes large and is related to the variance of the data. The range a is defined mathematically as $a = a'/\sqrt{3}$ with $\gamma(a') = 0.95(\text{sill})$ and marks the lag distance at which the sill value is reached. In statistical terms, the range value defines the maximum lag at which correlation is significant (Carr, 1995). Another common semivariogram model is the Gaussian model, defined by Journel and Huijbregts (1978),

$$\gamma(h) = \begin{cases} CO + C\left[1 - \mathrm{e}^{-\frac{h^2}{a^2}}\right], & h > 0, \\ 0, & h = 0, \end{cases} \tag{3.4}$$

where the nugget value, the sill and the range are defined as for the spherical model. The covariance is directly related to the semivariogram by the relation

$$\text{covariance} = \text{sill} - \gamma(h). \tag{3.5}$$

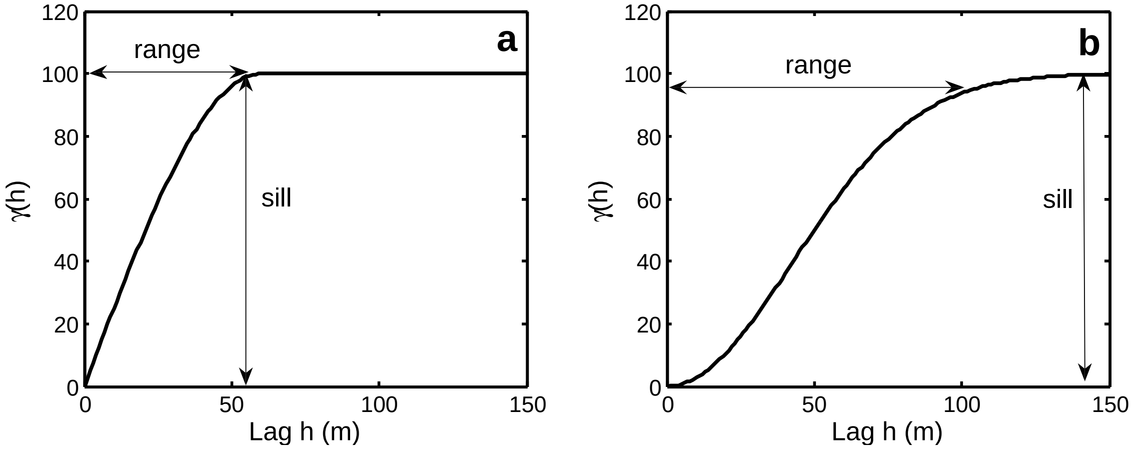

Figure 3.5: Two semivariogram models: (a) spherical and (b) Gaussian.

Omnidirectional semivariogram

The omnidirectional semivariogram is generated using data pairs that are oriented in any direction. The experimental omnidirectional semivariogram of the transformed data is computed using the algorithm presented in Carr (1995). The class size is the quantity added to the lag at each increment and is an important parameter to determine. Selection of an appropriate class size is done empirically and depends mainly on the spatial sampling of the dataset. A class size value that is too small could result in too few data pairs for small lags. A class size value that is too large may result in an excessive number of pairs for small lags while depleting larger lags. Experimentation led me to choose a class size of 30 m carried over 60 increments. The semivariogram thus spanned lags of 30 to 1800 m. Figure 3.6 shows the resulting variogram along with its best-fit model. Comparison of the experimental semivariogram with the spherical and Gaussian models presented above shows that the shape of the experimental semivariogram is best approximated using a Gaussian model. Nugget, range and sill values are determined graphically and presented in Table 3.1.

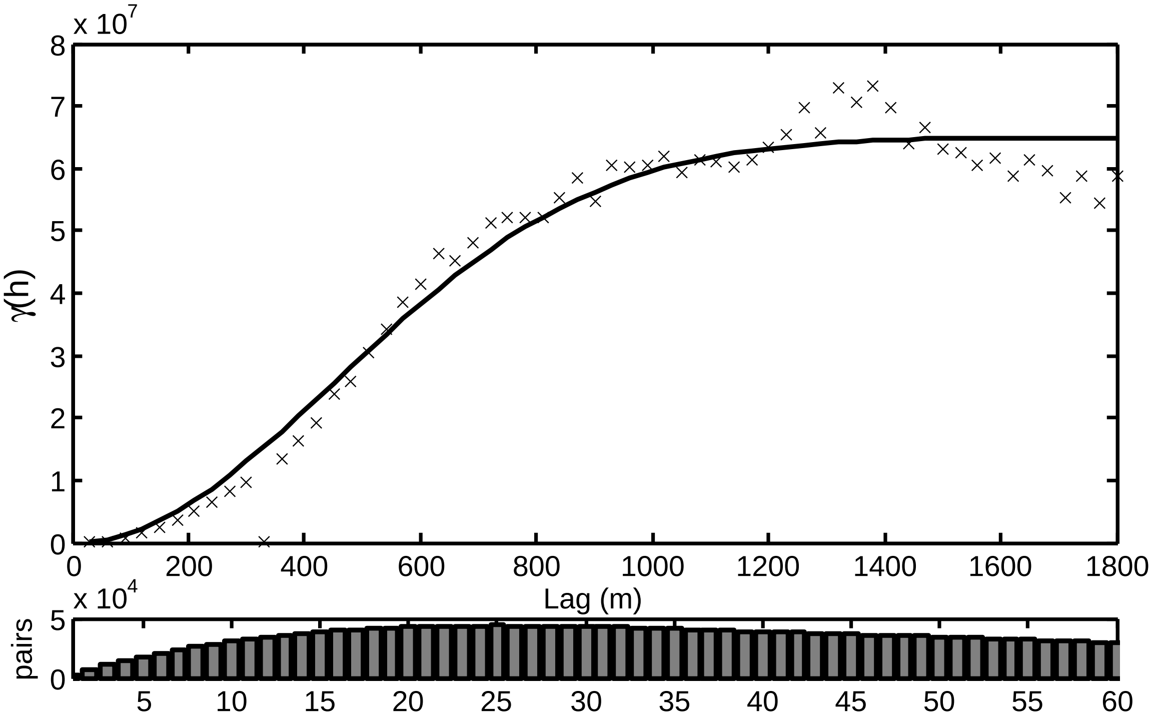

Figure 3.6: Experimental omnidirectional semivariogram. The semivariogram function (top) and number of pairs (bottom) are represented as a function of lag h. The crosses correspond to the experimental values while the solid line is the idealized Gaussian model.

Parameter name	**Value**
Type of model	Gaussian
Nugget (m^2)	0
Range (m)	1100
Sill (m^2)	6.5×10^7

Table 3.1: Statistical parameters derived from the omnidirectional semivariogram in Figure 3.6.

Directional semivariogram and anisotropy

Directional semivariograms allow us to put an additional constraint on the dataset by calculating its anisotropy. Directional semivariograms are calculated by isolating groups of data pairs having a particular orientation. The directional semivariograms are computed for four orientations. The four resulting directional variograms can be fitted with Gaussian models and are plotted in Figure 3.7. The associated angles between the semivariogram direction and North as well as the associated statistical parameters are presented in Table 3.2.

	Angle of semivariogram (°)			
Parameter name	**0**	**45**	**90**	**135**
Type of model	Gaussian	Gaussian	Gaussian	Gaussian
Nugget (m^2)	0	0	0	0
Range (m)	1100	1000	1700	700
Sill (m^2)	1.4×10^7	2.3×10^7	3.0×10^7	7.2×10^6

Table 3.2: Statistical parameters derived from the directional semivariograms analysis. Specified angles are angles between the considered direction and North.

Estimating the direction and magnitude of the anisotropy is the last step of geostatistical analysis. This is done by plotting the four range values obtained from the four semivariograms as vectors having a magnitude corresponding to the range value and orientation of the associated semivariogram angle. Figure 3.8 shows the resulting anisotropy "ellipse" for our dataset. The plot shows an ellipse striking north-south, thus indicating an anisotropy angle of 90° from the North. This means that the spatial correlation is greater in the north-south direction than in the east-west direction. The magnitude of the anisotropy is calculated by dividing the range of the major axis of the ellipse by the range of the minor axis and is found to have a value of 2.43.

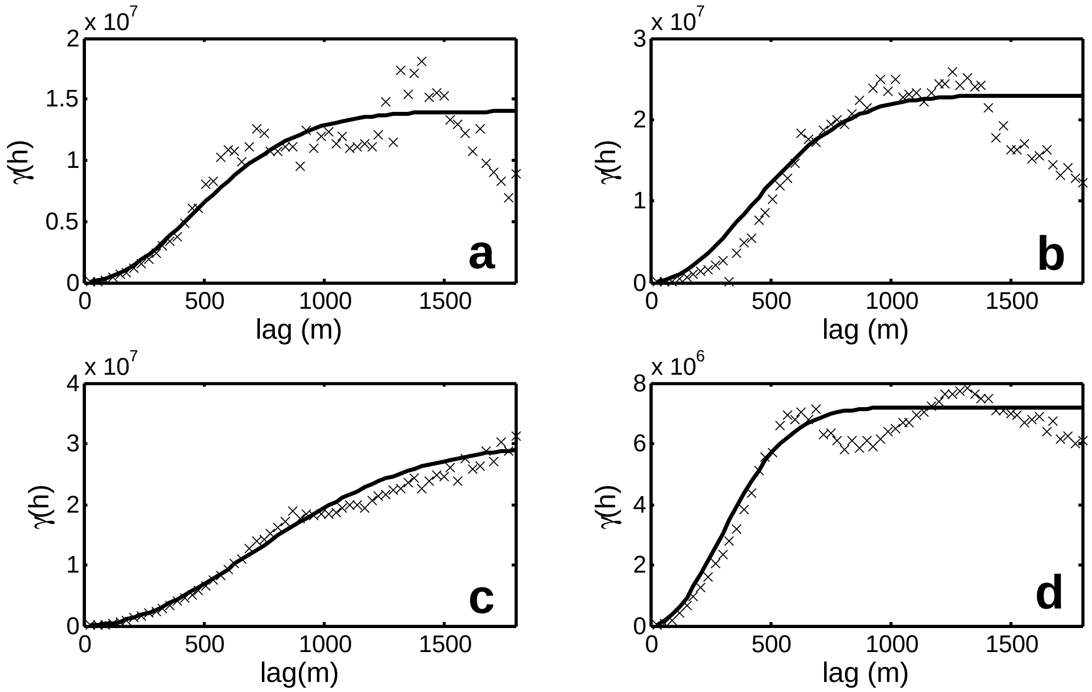

Figure 3.7: Experimental directional semivariograms. Direction makes angles of (a) 0°, (b) 45°, (c) 90°, (d) 135° to the north, respectively. For each angle, the semivariogram function is represented as a function of the lag h. The crosses correspond to the experimental values and the solid line is associated the Gaussian model.

3.1.4 Anisotropic kriging using the VEBYK routine

The anisotropic parameter values derived through the geostatistical analysis of the data can now be used in the interpolation of the data. The interpolation is performed in Matlab using a published routine (Sidler, 2003) and associated package of Matlab scripts called "Value Estimation By Kriging"(VEBYK). A few modifications have been made to adapt the original routine to our kriging needs. These are presented below.

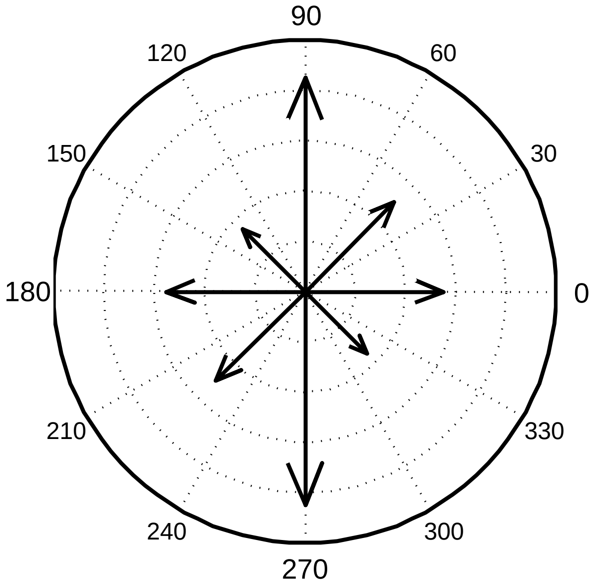

Figure 3.8: Anisotropy ellipse constructed from ranges of directional semivariograms (Table 3.2).

Inputs and grid

Inputs to the routine are the transformed dataset, the desired resolution, the statistical parameters resulting from the geostatistical analysis and the number of points to be included in the search neighbourhood. Detailed inputs are presented in Table 3.3. The grid used to interpolate the data with VEBYK is staggered with respect to the averaging grid: the interpolated points are located on the grid nodes while the averaged data are located within the cells defined by the interpolated grid. The interpolated grid along with the averaged data are illustrated in Figure 3.9.

Steps of the VEBYK routine

The VEBYK algorithm to perform interpolation by ordinary kriging is similar to the algorithm presented in Carr (1995). Here we summarize the main steps of the routine:

1. Calculate grid node coordinates. Grid limits are automatically defined by the coordinates of points located at the edges of the dataset, but can also be specified manually. A value of 30 m was chosen for the grid spacing.

Name	**Description**
coord	Transformed dataset containing coordinates and values of sampled points
dgrid	Resolution of the interpolating grid
points	Number of neighbours used in the interpolation
nugget	Statistical parameter obtained from omnidirectional semivariogram
range	Statistical parameter obtained from omnidirectional semivariogram
sill	Statistical parameter obtained from omnidirectional semivariogram
anisotropy	Magnitude of anisotropy obtained from directional semivariograms
alpha	Angle of anisotropy obtained from directional semivariograms
crossv	Logical value used to switch cross-validation mode on or off
verbose	Logical value used to switch the waitbar on or off

Table 3.3: General inputs to the VEBYK routine

2. Rotate coordinate system to account for anisotropy angle.
3. Calculate the covariance function using the values of sill, range and nugget and the specified semivariogram model (Gaussian model in our case).
4. For each point of the interpolated grid:
    (a) Identify the closest neighbouring points to be used in the interpolation, later referred to as "sample points". The number of sample points considered is specified by the parameter `points`.
    (b) Calculate the distance (or lags) between pairs of sample points.
    (c) Calculate matrix of covariances (referred to as C) between pairs of sample points. Covariances are derived from the covariance function using the lags calculated in the previous step.
    (d) Calculate the distance (or lag) between the grid point under consideration and each of the sample points.
    (e) Calculate matrix of covariances (referred to as c) between the grid point under consideration and the sample points. Covariances are again derived from the covariance function using calculated lags.
    (f) Calculate the ratio of c to C to obtain a vector of kriging coefficients or kriging weights

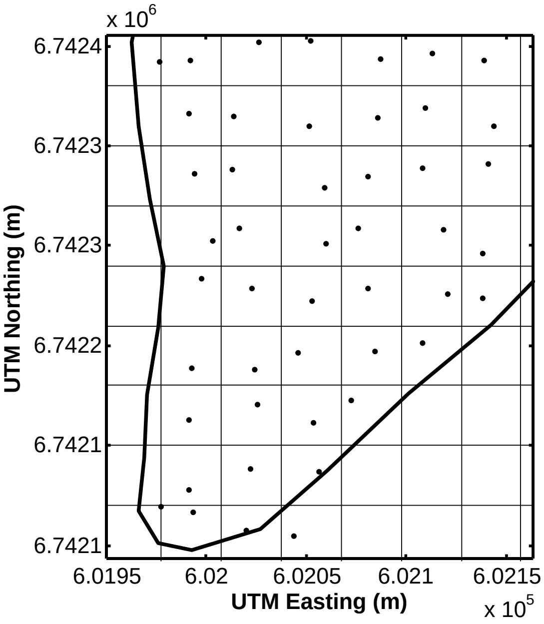

Figure 3.9: Close up plot of an area near the terminus of the glacier. The grid used to interpolate the data using VEBYK is presented along with the averaged data (dots) and the glacier outline (thick black line). The grid is staggered with respect to the averaged data, as the krigged elevations are computed on the grid nodes while the averaged data lies within the cells.

(g) Compute the variance of the error using the covariance function and the kriging coefficients.

(h) Derive the estimated value of the grid point under consideration by calculating a weighted average of the sample point values (the weights being the kriging coefficients).

5. When the previous loop has been repeated for each of the grid points, the transformation introduced when rotating the coordinate system is reversed.

The geostatistical parameters obtained from the experimental semivariogram and used in this algorithm are listed in Table 3.4.

Anisotropy is used in kriging to suppress the effect of small-scale trends that may remain after data preconditioning. According to Sidler (2003), kriging weights at the border of the search neighbourhood can become excessively large if anisotropy is not taken into account, which can produce artefacts in the resulting DEM. Anisotropy is taken into account in the kriging interpolation by rotating both the grid of estimated values and the coordinates of all data points, so that the main axis points in the direction of anisotropy. After rotation, the main axis thus points in the direction of the longest range in Figure 3.8. This rotation is equivalent to an eigenvalue transformation. The axis corresponding to the smallest range in Figure 3.8 (now the y-axis) is subsequently dilated by a factor equal to the magnitude of the anisotropy. Unlike the rotation described above, the dilatation of the y-axis is not carried out on the coordinates of all data points. Instead, it is implemented in the calculation of the lags between pairs of sample points (point 4(b) above), by multiplying the y-coordinates by the anisotropy magnitude. The search for the closest neighbouring points is then carried out in the transformed coordinate system using a circular search neighbourhood. In the untransformed coordinate system, this search neighbourhood is an ellipse whose long axis points in the direction of anisotropy.

Outputs of the VEBYK routine are two three-column matrices, called `output` and `errorvariance`. The three columns of the `output` matrix contain the Northing coordinates, the Easting coordinates and the estimated elevation of the grid points respectively. The three columns of the `errorvariance` matrix contain the Northing coordinates, the Easting coordinates and the variance of the kriging error associated to each of the grid points. The elevation data contained in the `output` file is referred to as *krigged* data, as opposed to the *measured* data used as input.

Parameter name	**Type of parameter**	**Value**
Class size (m)	Input	30
Number of increments	Input	60
Nugget (m^2)	Output	0
Range (m)	Output	1100
Sill (m^2)	Output	6.5×10^7
Anisotropy angle (°)	Output	90
Anisotropy magnitude	Output	2.429

Table 3.4: Summary of geostatistical parameters. The second column indicates whether the parameter in an input or an output of the geostatistical analysis.

Adaptation of the original routine

One major modification was done to adapt the routine to our specific needs. The original VEBYK algorithm uses the von Kármán covariance model as the only model to compute covariances for increasing lags. This type of covariance function was originally introduced to “characterise the seemingly chaotic, random velocity fields observed in turbulent media” (Sidler, 2003). For a specific value of the von Kármán parameter ν, the von Kármán covariance model is identical to the exponential model. However, we have shown above that the semivariogram, and thus the covariance function, for our dataset is best characterized by a Gaussian model. There is no combination of parameters which would allow a von Kármán covariance model to be equivalent to a Gaussian model. As a consequence, the component of the routine computing the covariance function was adapted to use a Gaussian model instead of a von Kármán model.

3.1.5 Parameter selection for VEBYK

In addition to the modification described above, several parameters must be specified to optimize kriging. The values of the parameters described below are summarized in Table 3.5.

Importance of the search neighbourhood

While experimenting with the parameter controlling the type and size of the search neighbourhood, expressed as a list of point coordinates in the variable `points`, I noticed that the interpolation results are sensitive to these parameters. The VEBYK routine allows for two types of neighbourhood search: “a simple search and a quadrant search”. In the simple search, the algorithm selects the specified number of points with the smallest lags. In a quadrant search, the algorithm searches for one fourth of the points in each quadrant. For example, if the total number of neighbours to search for is 12, the algorithm searches for three points in each quadrant. By considering neighbours out of each of the four quadrants, the “quadrant” search option helps prevent situations where sample points used to estimate the value of a grid point are located exclusively in a small portion of space. This additional constraint is particularly useful in the case of clustered data, and can help in reducing the occurrence of unrealistic artefacts (Sidler, 2003). Experimentation showed that our kriging results improve when this type of neighbourhood search is enabled.

In addition, the radius of the search neighbourhood, controlled by the number of sample points used in the interpolation, is an especially important parameter. In theory, with data values that are known exactly, using all data values would lead to the optimal result, but this in not true in practice. First, CPU time and memory usage are factors to be considered for any computation. Considering the whole dataset would considerably increase computing time and memory usage. Secondly, it is worth noting that the spatial correlation between data points decreases when the lag between them increases. This is easily verified by looking at the shape of the covariance function: it decreases for increasing lags. The further away a point is located from the estimated grid point, the smaller the associated kriging weight. Therefore, considering a high number of points in the interpolation does not particularly improve the result. Moreover, using too many points can result in the covariance matrix becoming quasi-singular, and thus difficult or impossible to invert. This was a recurring issue in my work and led me to reduce the search neighbourhood below the recommended 12 to 32 sample points (Sidler, 2003). Choosing a small search neighbourhood can however result in high frequency artefacts (Sidler, 2003). We chose to consider a 4-point neighbourhood, which allowed us to avoid major artefacts while keeping the covariance matrix invertible.

Cross validation

The VEBYK routine also allows the user to enable or disable cross-validation. When cross-validation is enabled the closest neighbour is skipped so that the value of an eventual sampled data point coinciding with the estimation point is not used. Since we want kriging to work as an exact interpolator and reflect the value of data points that are situated on grid nodes, we choose to disable cross-validation.

Parameter	**Value**
Type of neighbourhood search	Quadrant search
Number of sample points	4
Cross-validation	off
Covariance model	Gaussian

Table 3.5: Value of specific input parameters to the VEBYK routine

3.1.6 Data post-processing

Data transformations

The interpolated data obtained from the raw kriging reflects the detrending transformation applied when preconditioning the measured data. These transformations must be removed to recover the desired krigged glacier surface elevation data. The steps followed to “re-trend” the data are the following:

- Each krigged point is associated with the flowline coordinate (or distance from the terminus) of the closest flowline point.
- The equation of the best-fit line used to detrend the data (see section 3.1.2 page 28) describes a linear transformation associating elevations to flowline coordinates. The value of elevation corresponding to the flowline coordinate of each krigged point is identified using the equation of the best-fit line (equation 3.1) and added to the “raw” krigged elevation.

Figure 3.10 presents the krigged data before and after re-trending.

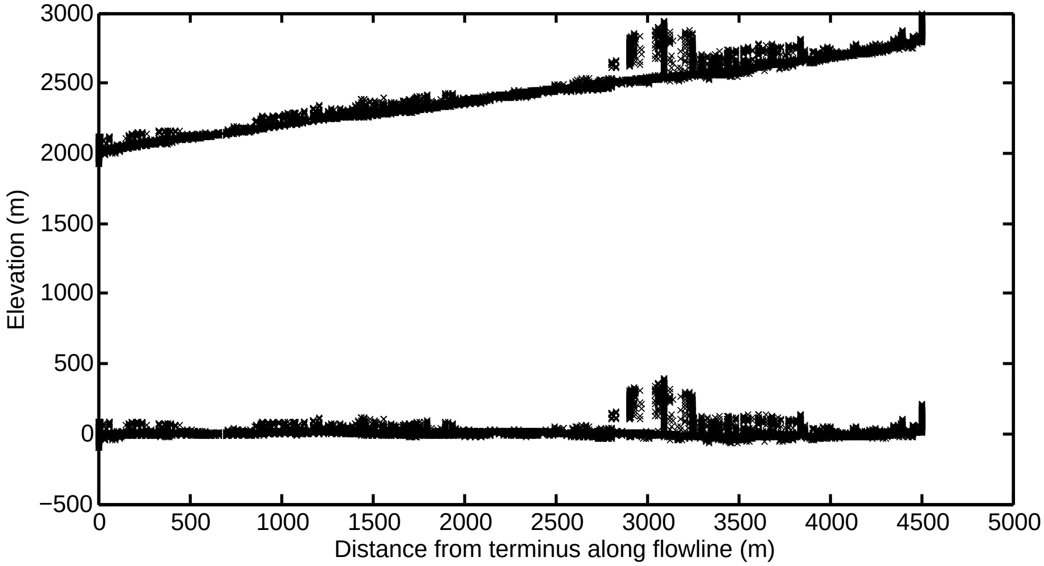

Figure 3.10: Krigged data before (bottom) and after (top) re-trending.

Ice mask

The VEBYK kriging routine performs the interpolation on a rectangular grid and the output is a rectangular surface including the glacier and the surrounding terrain. However, the surrounding terrain topography was not included in the interpolation at this stage, because it could not be detrended using the same transformation used for the glacier surface. Therefore, the krigged data situated outside of the glacier correspond to areas where the were no input data.

The glacier itself must therefore be isolated from the rectangular grid, and all points situated outside of the glacier outline ignored. This is done using a glacier mask, shown in Figure 3.11, defined by an array of ones and zeros corresponding respectively to points situated on or off the ice. The resolution at which the mask is generated is chosen to match the resolution of the krigged data, and the grid boundaries are specified so that the coordinates of the points generated by the mask coincide with the coordinates of the krigged data. Element-by-element multiplication of the digital mask and the krigged data then isolates the glacier.

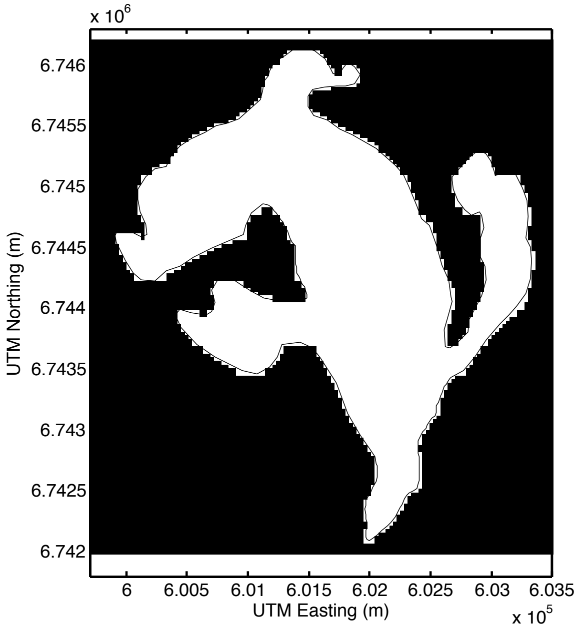

Figure 3.11: Ice mask. Ones, in white, represent areas with ice.

Glacier tributaries

The two glacier tributaries have not been surveyed due to their difficulty of access (vertical headwalls, ongoing rockfall, hanging glaciers and cornices) and they are not represented in the raw dataset. Surface elevations of these tributaries have been extracted from the Kluane Glacier area map but were not included in the kriging interpolation because of the detrending issues mentioned above. Both tributaries are steeper than the main trunk of the glacier, and as a result, their associated elevation trends differ from the trend of the trunk glacier. Tributaries are therefore given the same treatment as the surrounding topography and are added in a later stage. Since the ice mask includes both tributaries, these are removed in a separate step.

Surrounding topography

Finally, the surrounding topography, including the two tributaries, is merged with the krigged glacier trunk data. The surrounding topography and tributary elevations were digitized from the map in the form of elevation contours with a 40 m interval (Jennifer Owen, personal communication).

After eliminating those terrain points that overlap with the krigged data, the surrounding terrain and krigged data were merged and interpolated onto a regular grid using a linear interpolation method in Matlab. The interpolation grid was chosen so that its nodes coincide with the krigged data points and a Matlab interpolation routine was selected that respects the values of the data located on the grid nodes. This helped ensure that the ice surface obtained by kriging was not altered by merging with the surrounding topography.

3.2 Generating a surface DEM by kriging in Surfer

In addition to generating a surface DEM using kriging in Matlab, we use the surface mapping software Surfer 8, from Golden Software, to compute different versions of the surface DEM. Surfer computes the geostatistics of the dataset, fits a semivariogram and interpolates the data using ordinary kriging. As for the DEM generated with VEBYK, a resolution of 30 m is chosen. Surfer does not allow the user to perform complex data transformations, like the flowline detrending described in Section 3.1.6. It also does not allow the user to import custom semivariograms. As a consequence, I did not attempt to exactly reproduce the

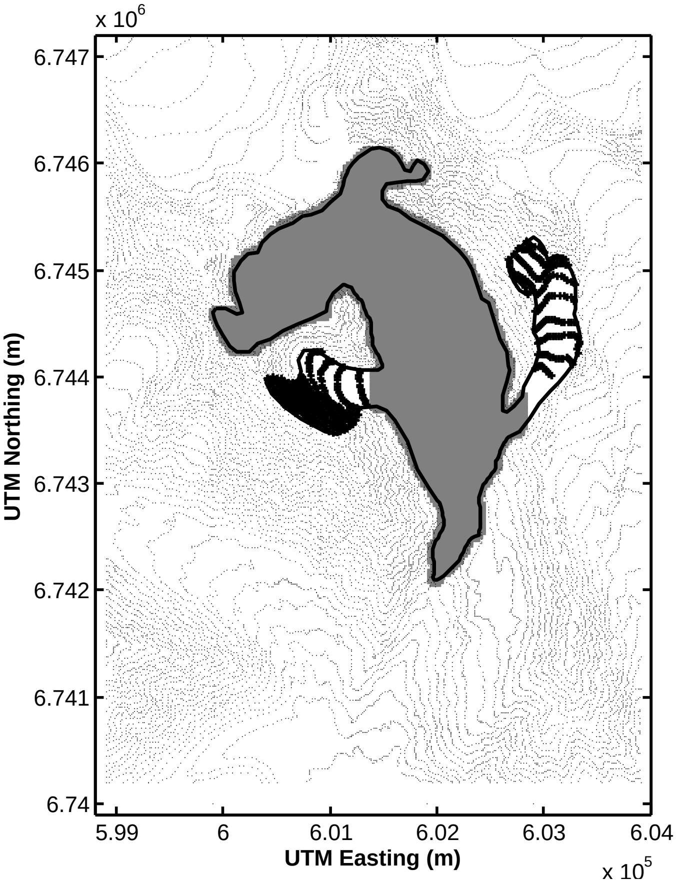

Figure 3.12: Basin-scale topographic data. The gray area represents the glacier area krigged using the VEBYK routine, the bold black points are the tributary data, digitized from the Kluane Glacier area map and the light black points are the surrounding terrain data, also digitized from the map.

kriging procedure performed in Matlab and used the recommended default settings instead. I computed versions of the surface DEM in a slighty different manner using three methods: (1) kriging of the raw dataset, (2) kriging of the spatially averaged dataset and (3) kriging of the transformed dataset.

3.2.1 Interpolation of the raw dataset by kriging

Since Surfer does not require that the data be normally distributed prior to kriging, I interpolate the entire basin-scale dataset, containing the ice-surface GPS measurements as well as the digitized surrounding topography. The default settings of Surfer are used, as experimentation showed that they produce better results than when other statistical or kriging parameters are manually selected. Table 3.6 lists these default settings.

Parameter description	**Value**
Covariance model	linear
Kriging type	ordinary point kriging
Cross-validation	off
Type of neighbourhood search	quadrant
Maximum number of data to use	64

Table 3.6: Value of default parameters for kriging in Surfer

3.2.2 Interpolation of the averaged dataset by kriging

Some data points are very close to each other and are likely to produce artefacts when krigged. This is the reason the data were averaged prior to kriging with the VEBYK routine. This consideration still holds, and we expect the interpolation of a spatially averaged dataset in Surfer to yield more realistic results than the kriging of raw data. A dataset comprising the averaged data (see the first step of data preconditioning described in Section 3.1.6) and the surrounding topography (not averaged) is compiled and gridded in Surfer. The default settings presented in Table 3.6 are used and the procedure used to interpolate the raw dataset is repeated.

3.2.3 Interpolation of the transformed dataset by kriging

As a third exercise, we use Surfer to krig the ice surface dataset transformed in Matlab. The method used to detrend the data is described in Section 3.1.2. Unlike the two previous exercises, the surrounding topography is not incorporated into the dataset for kriging, as it cannot be detrended in the same manner as the ice surface data. Since the dataset krigged in Surfer is transformed (both spatially averaged and detrended), it will later need to be re-trended to obtain true surface elevations. The DEM is thus obtained in several steps:

1. The raw ice-surface elevation dataset is averaged and detrended in Matlab following the procedure outlined in Section 3.1.6.

2. The transformed dataset is then krigged in Surfer using the default settings listed in Table 3.6.

3. The krigged data are then re-trended in Matlab using the procedure presented in Section 3.1.6. The glacier is isolated using the ice mask.

4. The re-trended data contain true ice surface elevations interpolated on a regular grid. To obtain a rectangular DEM spanning the whole basin, the krigged and re-trended data are merged with the raw surrounding topography data.

5. Finally, we krig these combined data in Surfer using default parameters. The resolution used is 30 m and the boundaries are chosen so that the nodes of the new grid and the nodes of the previously krigged ice surface data coincide. This is done to ensure that the elevation value from the first round of kriging (point 2 above) is respected.

3.3 Results

This section presents the DEMs obtained by kriging using the VEBYK routine in Matlab and using Surfer and quantifies the error associated with each method. Results from methods other than kriging are also presented for comparison.

3.3.1 DEM generated by kriging using VEBYK in Matlab

The results obtained after post-processing of the data krigged using VEBYK are shown in Figures 3.13 and 3.14. Specific areas of the glacier, described below, are annoted by numbered circles (1, 2 and 3) in both figures, and an aerial photograph of the glacier is presented in Figure 3.15 for comparison. The krigged ice surface qualitatively reproduces the topography observed in the field. However, there is a ridge-like feature present in the north-eastern region of the modelled glacier that is not present in reality. This feature (labelled 1 in Figures 3.13 and 3.14) is an artefact most likely occurring as a result of the detrending/re-trending transformation. This assumption is supported by the fact that the feature does appear in the DEM generated by kriging the detrended data in Surfer, but not in the DEM generated by kriging the untransformed data in Surfer. The ice surface also appears unrealistically perturbed in the area west of the ridge-like feature where the glacier curves along its length (labelled 2 in Figures 3.13 and 3.14) and two smaller ridge-like perturbations are visible in the area where the western tributary merges with the main body of the glacier (label 3). Although observations indicate an uneven surface in this area, the effect is likely emphasized by the method for detrending the data.

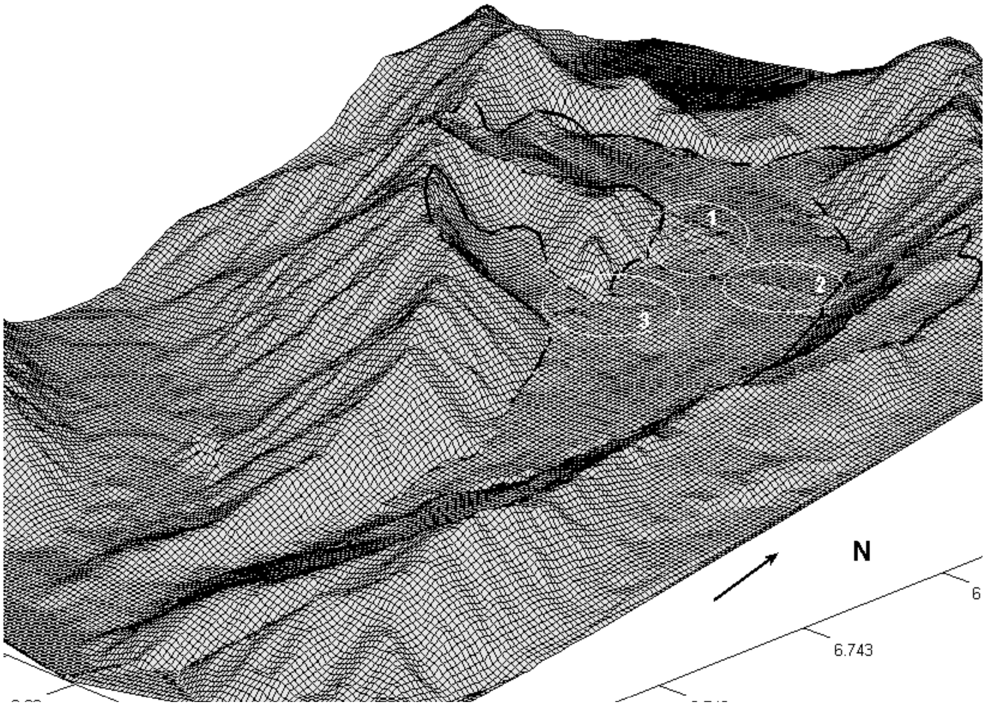

Figure 3.13: 3D basin-scale view of the surface DEM generated by kriging in Matlab. Areas circled represent (1) an artificial ridge-like feature, (2) an unrealistically irregular ice surface and (3) two smaller artificial ridge-like features.

Performance analysis

In addition to the qualitative assessment above, two performance metrics are computed to quantify the error associated with kriging in several different ways. The `errorvariance` output of the VEBYK routine is the variance of the error associated with kriging at each grid node. When the variance of the error is high, the interpolated value is less reliable. Figure 3.16 shows a two dimensional map of the glacier with the variance of the kriging error represented in shades of gray. Light areas situated within the outline of the glacier correspond to regions having a relatively high kriging error, thus making the krigged elevations

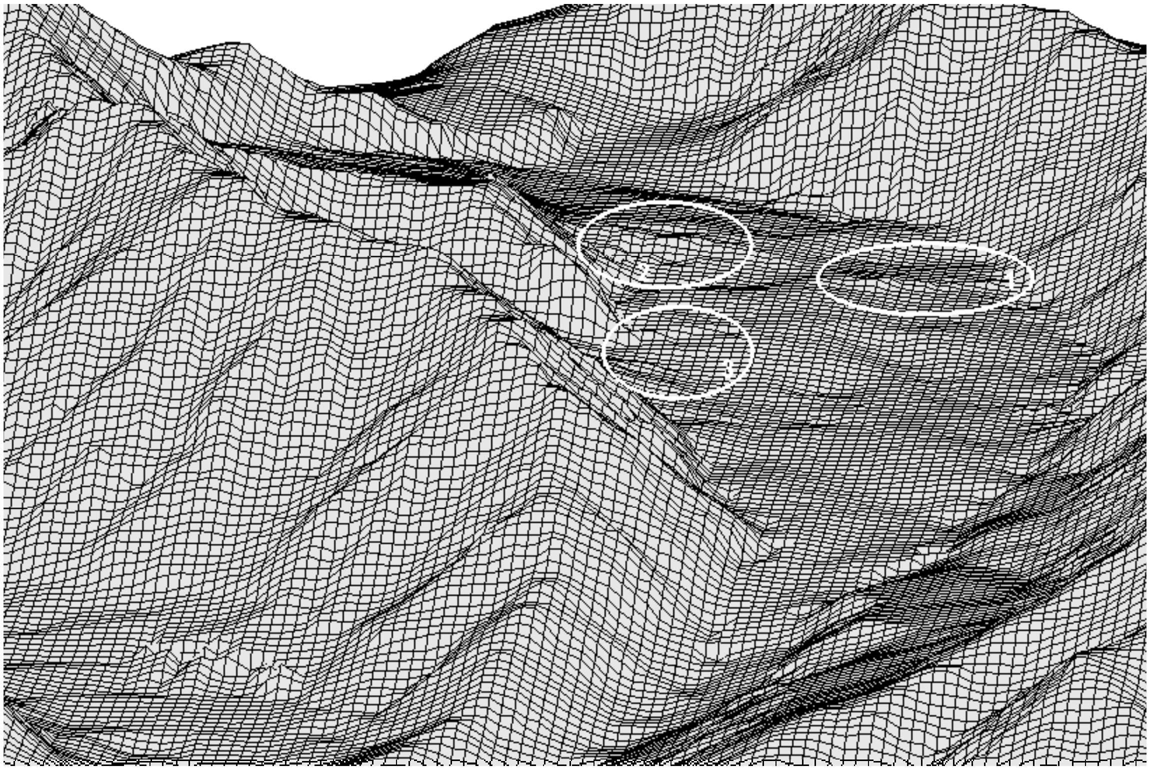

Figure 3.14: 3D view of the surface DEM generated by kriging in Matlab. Areas circled represent (1) an artificial ridge-like feature, (2) an unrealistically irregular ice surface and (3) two smaller artificial ridge-like features.

less reliable in these regions. There are three major areas where the variance is high. The first is situated in the north-western corner where the glacier originates. A hanging glacier at the headwall makes this location difficult of access to ground surveys, thus there are few data available in this region. The second area is located in the north part of the glacier close to where it curves along its length. Large crevasses have formed in that area, thus making it hazardous to access and thus difficult to survey. Finally the third zone is located on the eastern margin, about mid-glacier where the western tributary merges. This area is separated from the main trunk of the glacier by a large moraine and has not been surveyed. The fact that all three areas correspond to zones where the data are sparse supports the

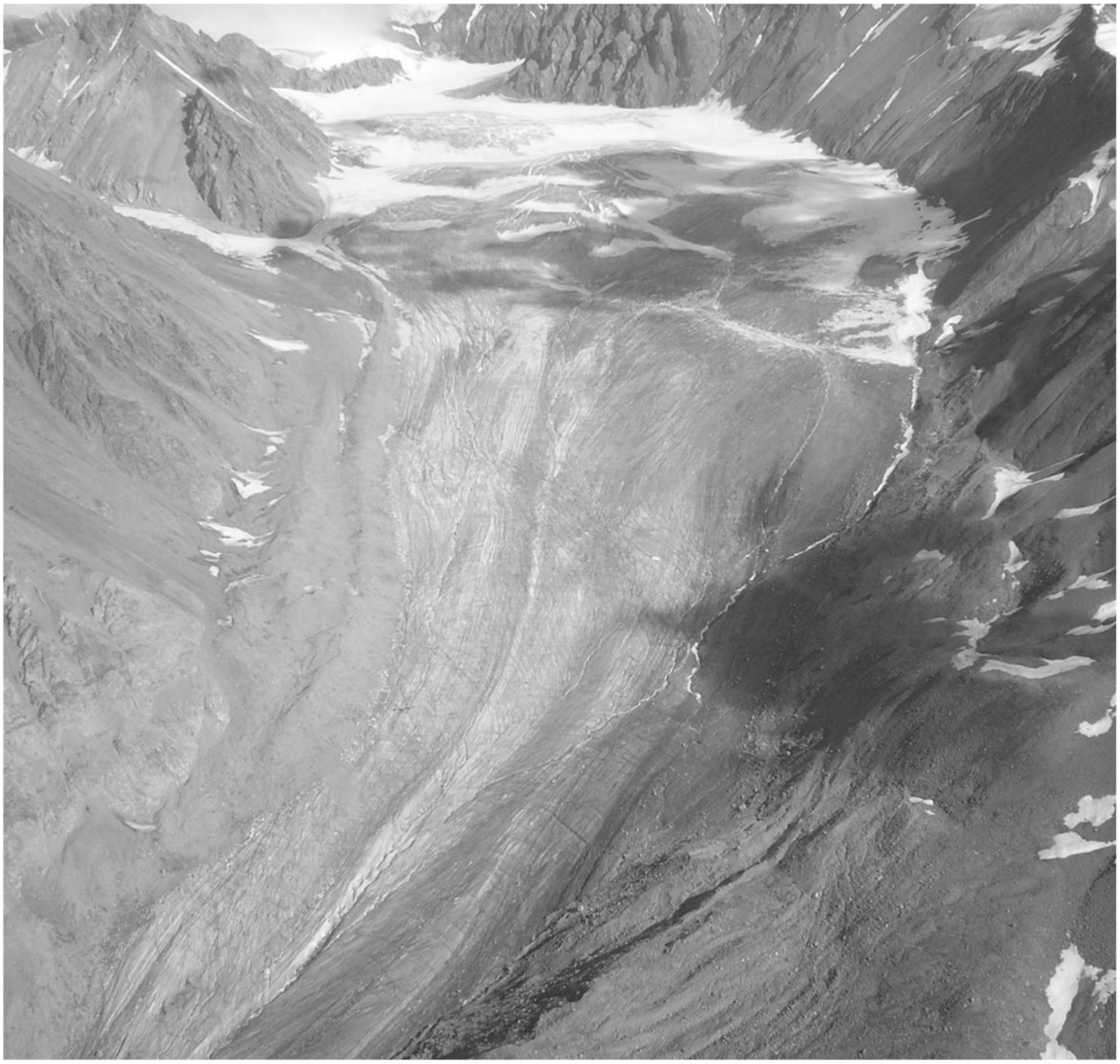

Figure 3.15: Aerial photograph of study glacier, 2005 (G. Flowers)

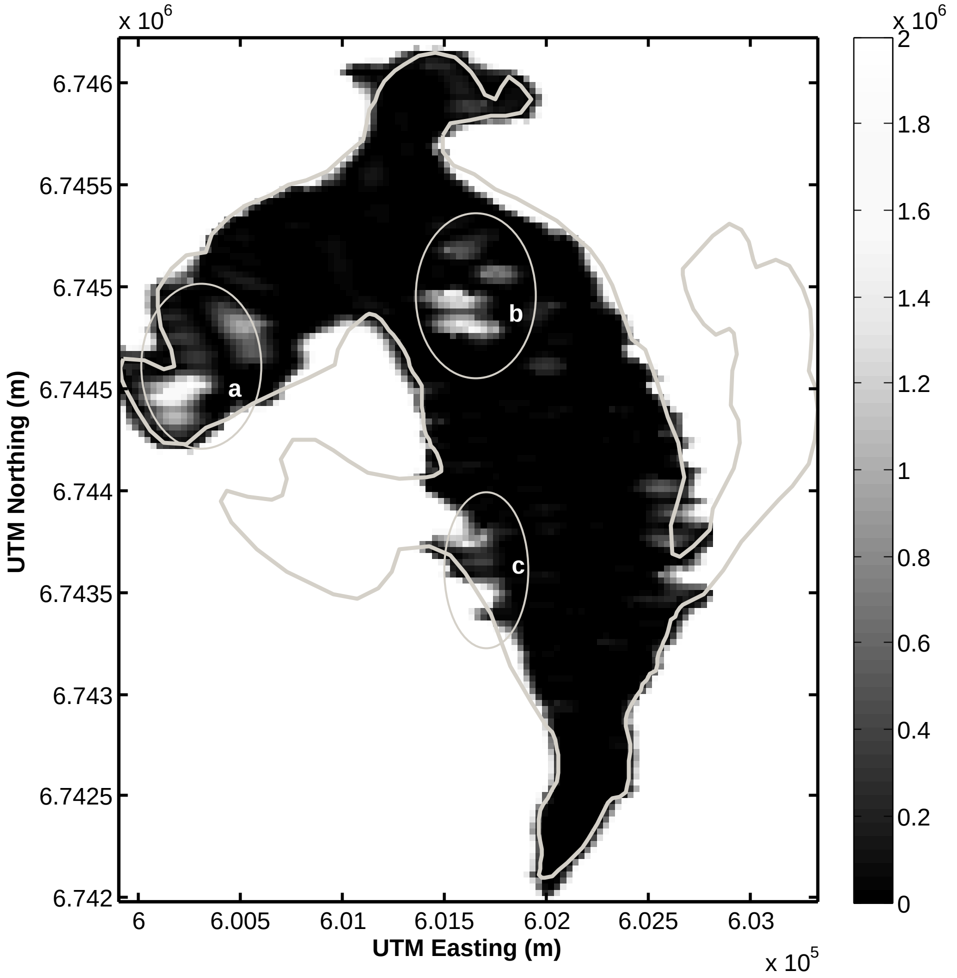

Figure 3.16: Surface DEM performance plot representing the distribution of the variance of the kriging error. Light areas represent areas where the variance of the kriging error is relatively higher than in other areas. Krigged elevations are less reliable in these areas. Areas circled are of interest and correspond to regions where measured data are especially sparse or nonexistent.

idea that the kriging algorithm is performing well.

Another way of assessing the quality of the surface DEM is to compare the krigged elevations with the measured elevations. Data preconditioning ensured that each cell contains no more than one data point by averaging the raw data. The krigged values are located at the intersection of grid edges rather than at the gridcell centers, and there are four data values associated with each cell. In order to compare the krigged and measured elevations, the krigged elevations are plotted as a function of the measured elevations, where data exist. Because the number of measured data and krigged data needs to be the same in order to plot one as a function of the other, the four corners of each cell are averaged to obtain one value of krigged elevation per cell. Figure 3.17 shows the krigged elevations plotted against the measured elevations for the cells that contain data. This process might introduce small errors in addition to the errors attributable to kriging, and Figure 3.17 should therefore not be interpreted as giving a strict measure of the kriging error. All points cluster closely along the one-to-one line, which shows that measured and krigged values are nearly identical in every cell and, therefore, that the kriging result accurately represents the measured data.

In addition to the visual assessment provided by the performance plot presented above, we want to quantify the error between krigged and measured data. To this end we calculate the root mean square error, or RMSE, defined by

$$\mathrm{RMSE} = \sqrt{\frac{1}{N} \sum \left(E_m - E_k\right)^2}, \tag{3.6}$$

where N is the total number of data. The RMSE quantifies the deviation of the krigged elevations E_k from their expected values, expressed as the measured elevations E_m. The value of the kriging error calculated using Equation 3.6 is shown in Figure 3.17.

3.3.2 DEM generated by kriging using Surfer

In this section, results for the three surface DEMs computed using kriging in Surfer are presented. The procedure used to compute these DEMs is described in section 3.2.

DEM computed from the raw dataset

Figure 3.18 shows a three dimensional view of the glacier surface computed from the raw dataset. This method gives good results but produces a large artefact (Figure 3.18) that

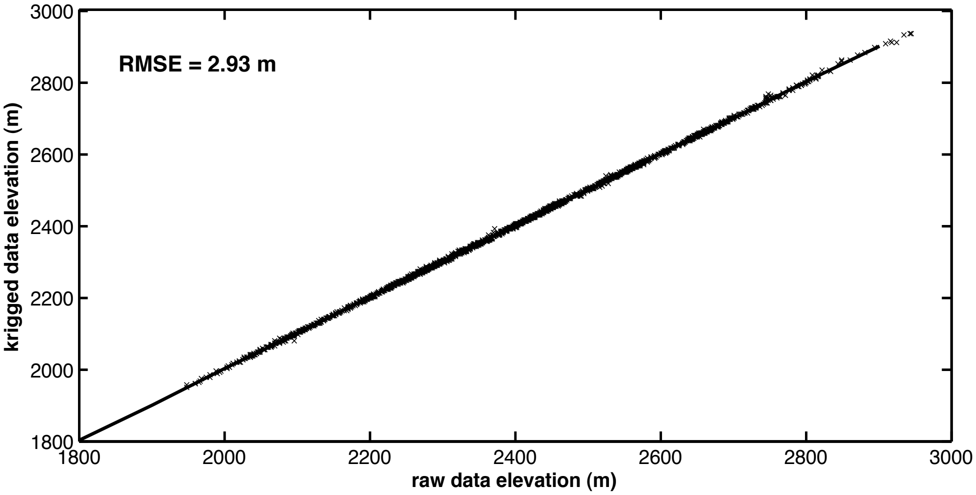

Figure 3.17: Matlab surface DEM performance plot. Krigged elevations are plotted against measured elevations for all cells containing data. All points gather in a narrow band along the line of slope 1. The value of the root mean square error (RMSE), calculated from Equation 3.6, is shown in the top left corner.

can be seen in the center of the glacier. The actual ice surface presents a few depressions in this area, but the degree of structure shown in Figure 3.18 is less pronounced in reality. This effect could be due to the fact that the raw data is heavily clustered in this area, with measurements separated by only a few meters.

DEM computed from the averaged dataset

The glacier surface modelled from the averaged dataset is shown in Figure 3.19. Visual inspection of the DEM shows a good agreement with observations. The irregular structure of the mid-glacier depression observed in the DEM generated from raw data is not as pronounced here and is closer to the real observed topography. However, the lowermost depression is still slightly exaggerated.

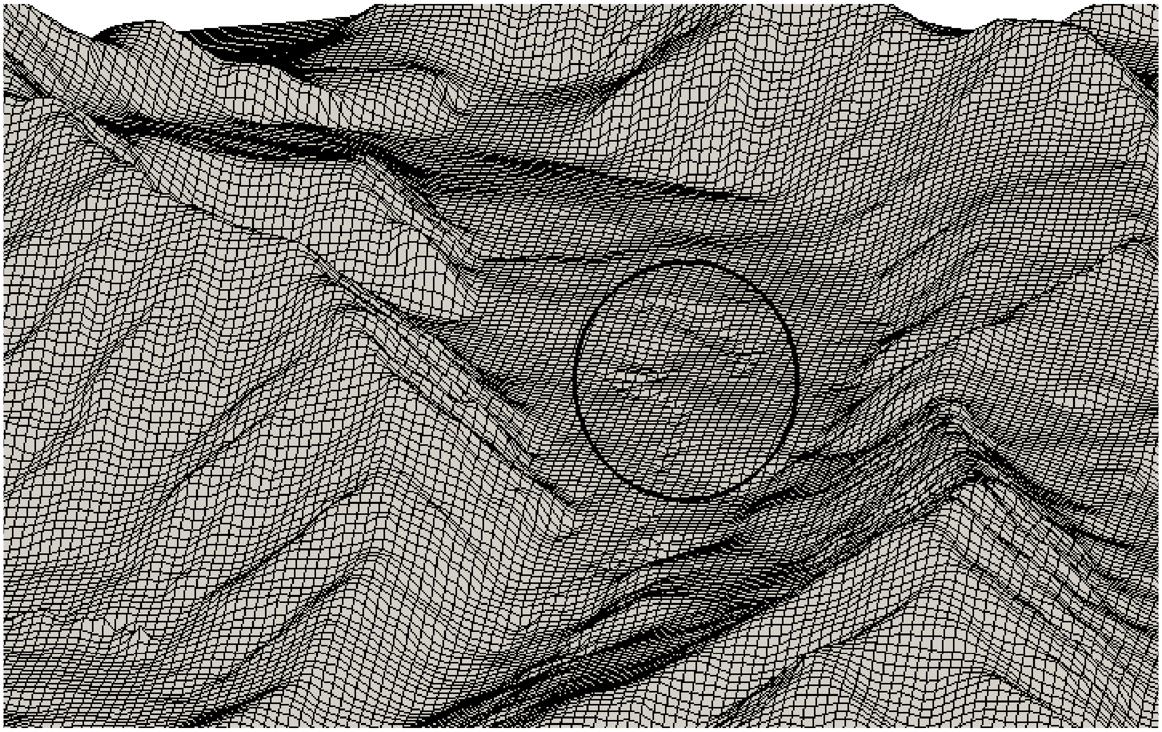

Figure 3.18: Surfer surface DEM generated from the raw dataset by kriging. The degree of structure of the depressions outlined in the circle is less pronounced in reality.

DEM computed from the transformed dataset

The DEM computed from transformed data is shown in Figure 3.20. The ice surface is also well represented and the central set of depressions is reproduced more realistically than in the two previous DEMs. However, a few unrealistic features appear. A ridge-like feature can be seen in the north-east sector of the glacier, and several smaller ridge-like perturbations are visible in the area where the western tributary merges with the main body of the glacier. These features, circled in Figure 3.20, are also present in the surface DEM generated from the transformed data using the VEBYK routine, but they do not appear in the DEMs generated from raw or averaged data. This leads me to conclude that the ridge-like features are products of the detrending/re-trending process.

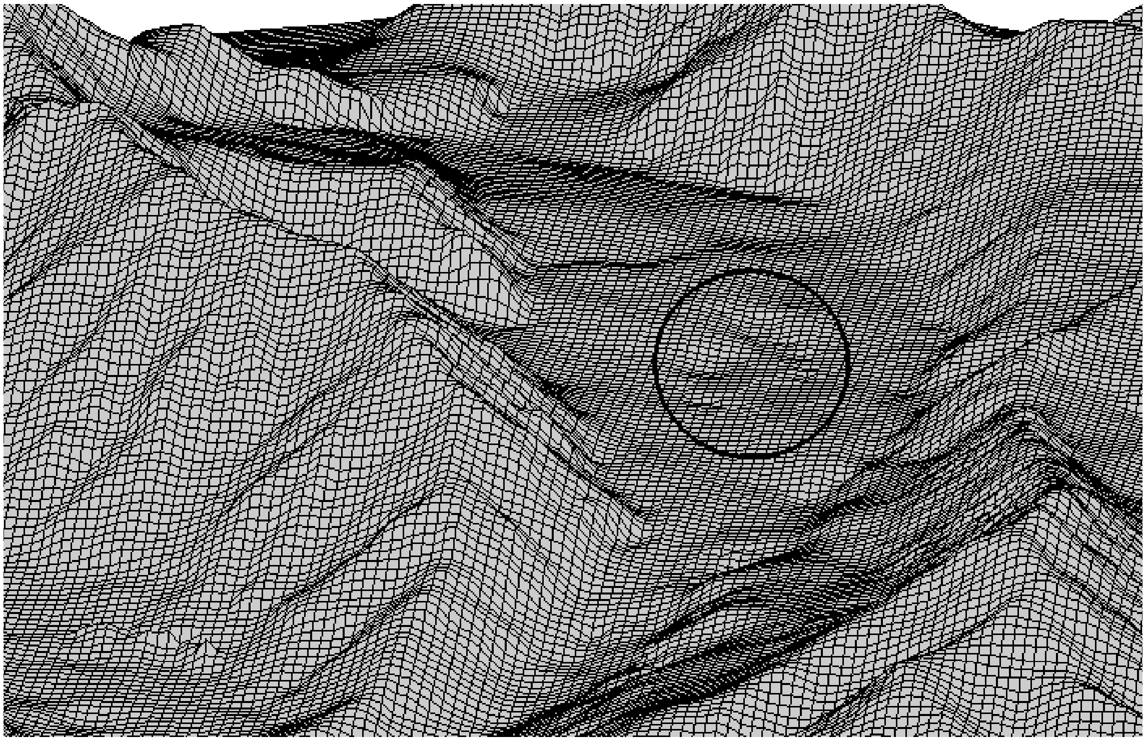

Figure 3.19: Surfer surface DEM generated from the averaged dataset by kriging. The degree of structure of the lowermost depression outlined in the circle is less pronounced in reality

Performance analysis

To assess and compare the quality of each of the three DEMs, I conduct a performance analysis as described in Section 3.3.1. For each of the DEMs, the error is quantified through calculation of the root mean square error. The computed error values are shown in Table 3.7. For the three DEMs, the points gather in a narrow band along a line of slope 1 as in Figure 3.17, which means that the kriging method respects the measured data. The measure of the kriging error can be used to rank the DEMs obtained by the different methods according to how well they represent the measured data. Based on the error metric, the DEM computed in Surfer from averaged data is the best, with a root mean squared error

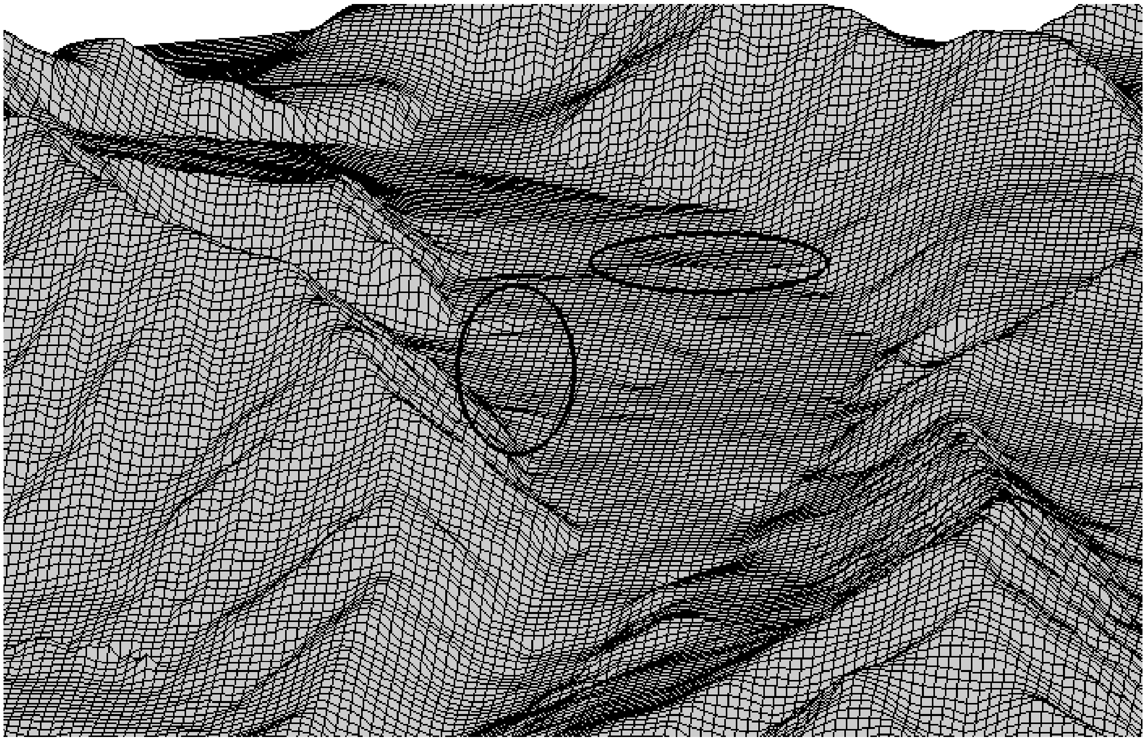

Figure 3.20: Surfer surface DEM generated from the transformed dataset by kriging. The two circled areas show artificial ridge-like features resulting from the detrending/re-trending process.

(RMSE) of 2.53 m. The DEM computed from the raw data ranks second, with a root mean squared error of 2.54 m, but the exaggerated degree of structure in the mid-glacier depressions is problematic. The DEMs computed from transformed data using Surfer and the VEBYK routine in Matlab rank last, with root mean squared errors of 2.80 m and 2.93 m, respectively. It is important to note that the method used to estimate errors also accounts for errors introduced while detrending and retrending the data. This could be a reason why both DEMs generated from transformed data seem to be of lower quality.

DEM	**RMSE**
DEM modelled from transformed data using VEBYK	2.93 m
DEM modelled from raw data in Surfer	2.54 m
DEM modelled from averaged data in Surfer	2.53 m
DEM modelled from transformed data in Surfer	2.80 m
Final surface DEM	2.57 m

Table 3.7: Surfer surface DEM performance is evaluated using the root mean square error (RMSE) and compared to the performance of the DEM modelled from transformed data in VEBYK and of the final DEM (presented in Section 3.3.4).

3.3.3 DEMs generated in Surfer using other methods

In addition to kriging, Surfer supports a variety of interpolation methods. For comparison, we show results of interpolation using three of these methods.

Nearest neighbour

Nearest neighbour interpolation is a method that assigns the value of the nearest point to each grid node. Not surprisingly, this results in a coarse terrace-like surface, as shown in Figure 3.21.

Minimum curvature

The minimum curvature method, widely used in the earth sciences, generates the smoothest possible surface while attempting to match the data as closely as possible. It is not an exact interpolator. Qualitative inspection of the DEM obtained with this method (Figure 3.22) shows good agreement with field observations for the ice surface. However the surrounding topography is not recovered very well, especially at the northern edge of the DEM where wave-like bulges are produced where none are present in reality.

Radial basis

The radial basis method is an exact interpolator and is usually considered very effective in fitting the data and producing a smooth surface. However, it does not seem to be a good method for our purpose, as the resulting ice surface, shown is Figure 3.23, is especially perturbed.

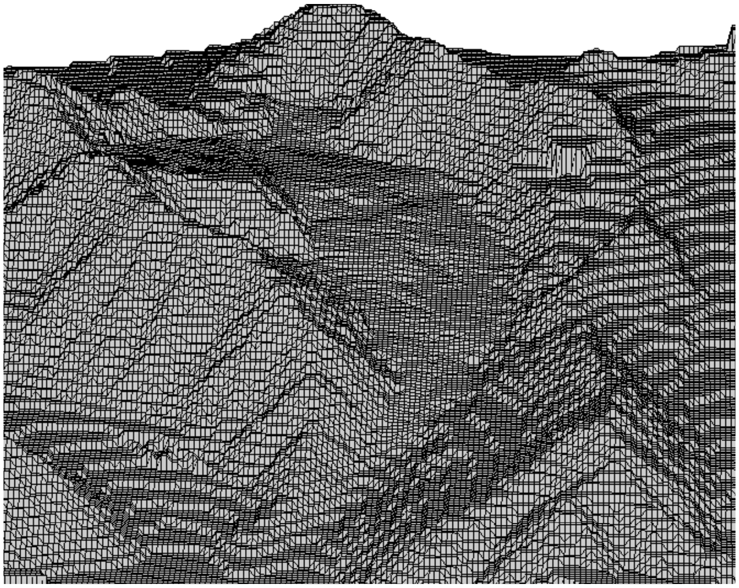

Figure 3.21: Surfer surface DEM generated from raw data using the nearest neighbour method.

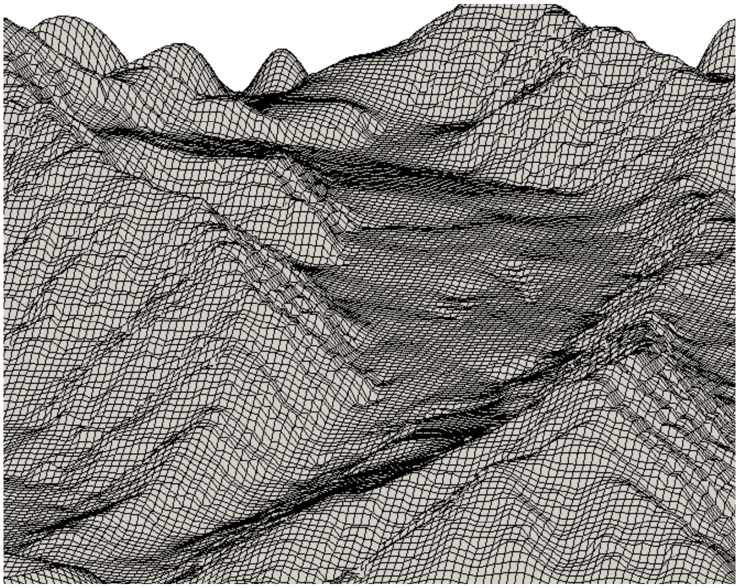

Figure 3.22: Surfer surface DEM generated from raw data using the minimum curvature method.

These three examples illustrate the importance of choosing an accurate interpolation method and further justify the choice of kriging.

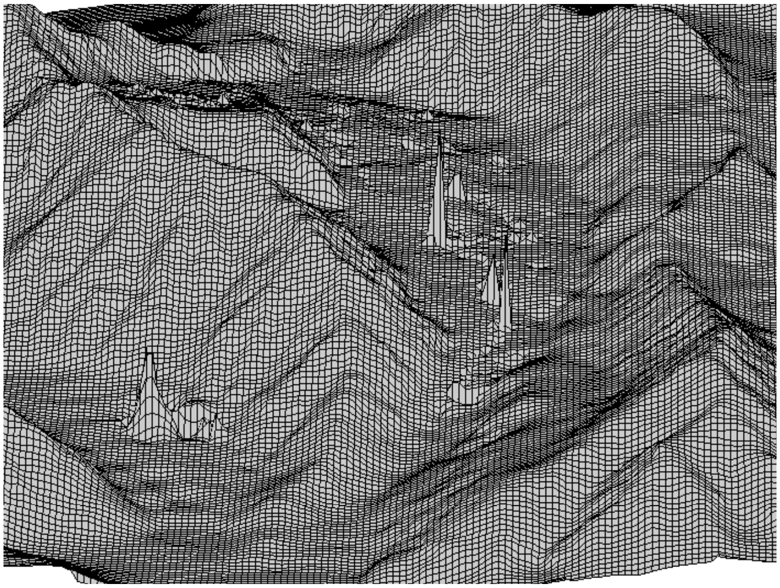

Figure 3.23: Surfer surface DEM generated from raw data using the radial basis method.

3.3.4 Final surface DEM

Of the four surface DEMs computed using kriging, each had at least one major defect. By quantifying how well the data are represented by the four DEMs, the error metric indicates that the three DEMs generated in Surfer are superior in quality to the DEM generated in Matlab. The DEM generated in Surfer from the averaged data has the best quality. The only major shortcoming of this DEM is that the central reaches of the glacier where prominent depressions occur are not reproduced in a realistic manner (box 'b' in Figure 3.24). This area is modelled in a much more realistic fashion in the DEM computed from transformed data using the VEBYK routine, but this DEM shows a ridge-like defect in another area (box 'a' in Figure 3.24). Because these defects are located in different areas, we choose to combine these two DEMs to construct a final surface DEM.

Because the DEM generated in Surfer appears reliable in all areas except the mid-glacier depression zone (box 'b' in Figure 3.24), and the DEM generated in Matlab appears

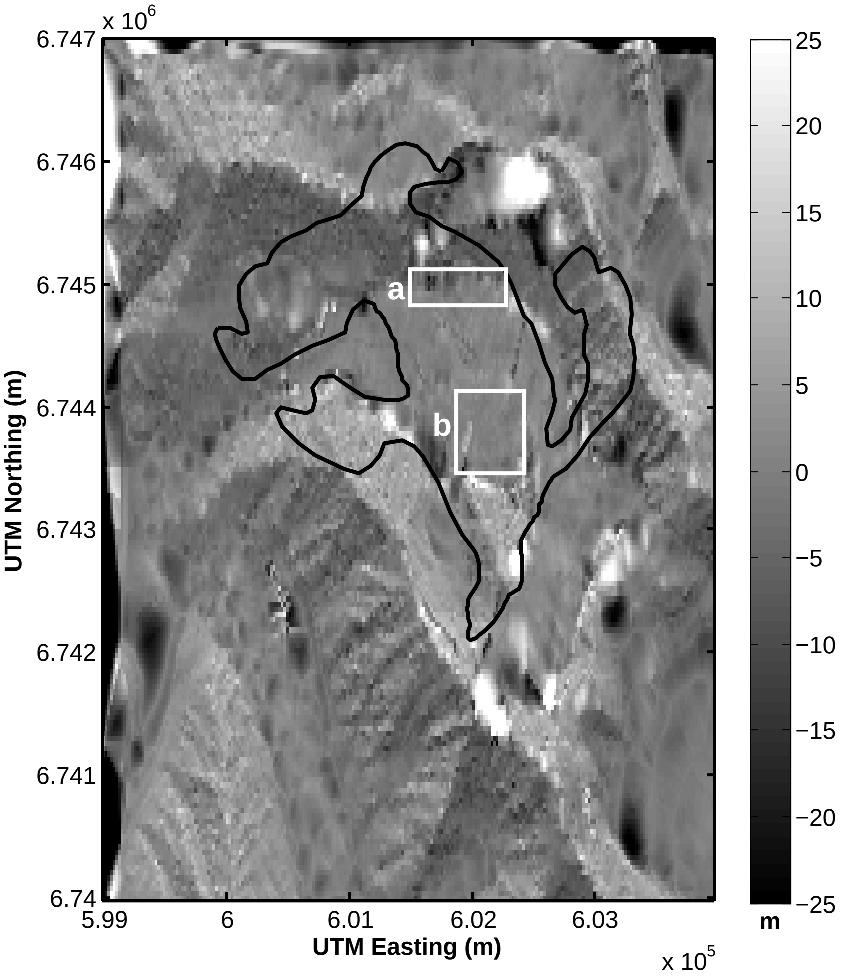

Figure 3.24: Comparison of Surfer and Matlab DEMs. Elevations from the DEM generated by kriging of averaged data in Surfer are subtracted from elevations from the DEM computed by kriging of transformed data in Matlab. The vertical bar on the left indicates the elevation difference between the two DEMs in meters. Boxes outline (a) the area where the ridge-like feature is visible in the Matlab DEM but not in the Surfer DEM, (b) the area patched from the Matlab DEM into the Surfer DEM. The difference between the two DEMs is scarcely visible in this plot, but visual inspection of the 3D map indicates that this area is better represented in the Matlab DEM.

reliable in this same area, a hybrid DEM is constructed by patching this area. To this end, the area of interest is isolated on both DEMs. The point locations and elevations of the Surfer DEM are then replaced by the point locations and elevations from the Matlab DEM. The area patched is shown by the lower rectangle (labeled 'b') in Figure 3.24. The hybrid DEM is then interpolated again on a regular grid, as the patching process introduces some irregularities. The interpolation is done using a nearest neighbour method. This method is valid here because the DEM points are located on the nodes of the grid, so the elevation of each point is reproduced and any deviation to the grid pattern in the patched area is corrected.

The resulting DEM, shown as a 3D mesh in Figures 3.25 and 3.26, presents a smooth surface, and accurately reproduces the observed ice surface. A performance analysis is conducted using the procedure described above, and results are presented in Table 3.7. The root mean squared error between krigged and averaged datasets is 2.57 m. This value is higher than the best DEM obtained by kriging with Surfer because the area patched comes from the DEM generated from the transformed data in Matlab, which has the highest root mean squared error. The lower part of the glacier presents a smooth, regular surface, with a few depressions visible along the centerline. On the higher part of the glacier, on the other hand, the surface presents undulations, and the modelled result reproduces the observations fairly well. The final 30 m DEM is resampled using linear interpolation, and two additional DEMs are created with resolutions of 20 and 50 m. These are presented in Figure 3.27.

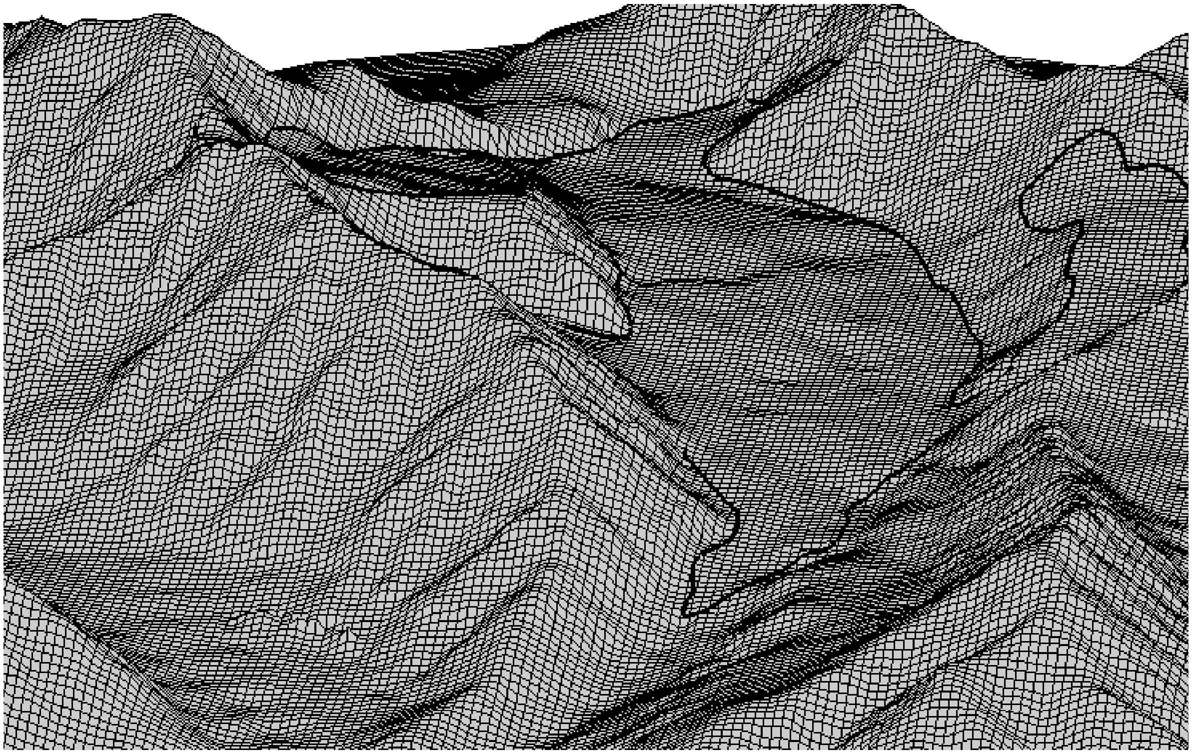

Figure 3.25: Final surface DEM with 30 m resolution. The thick black line defines the glacier outline.

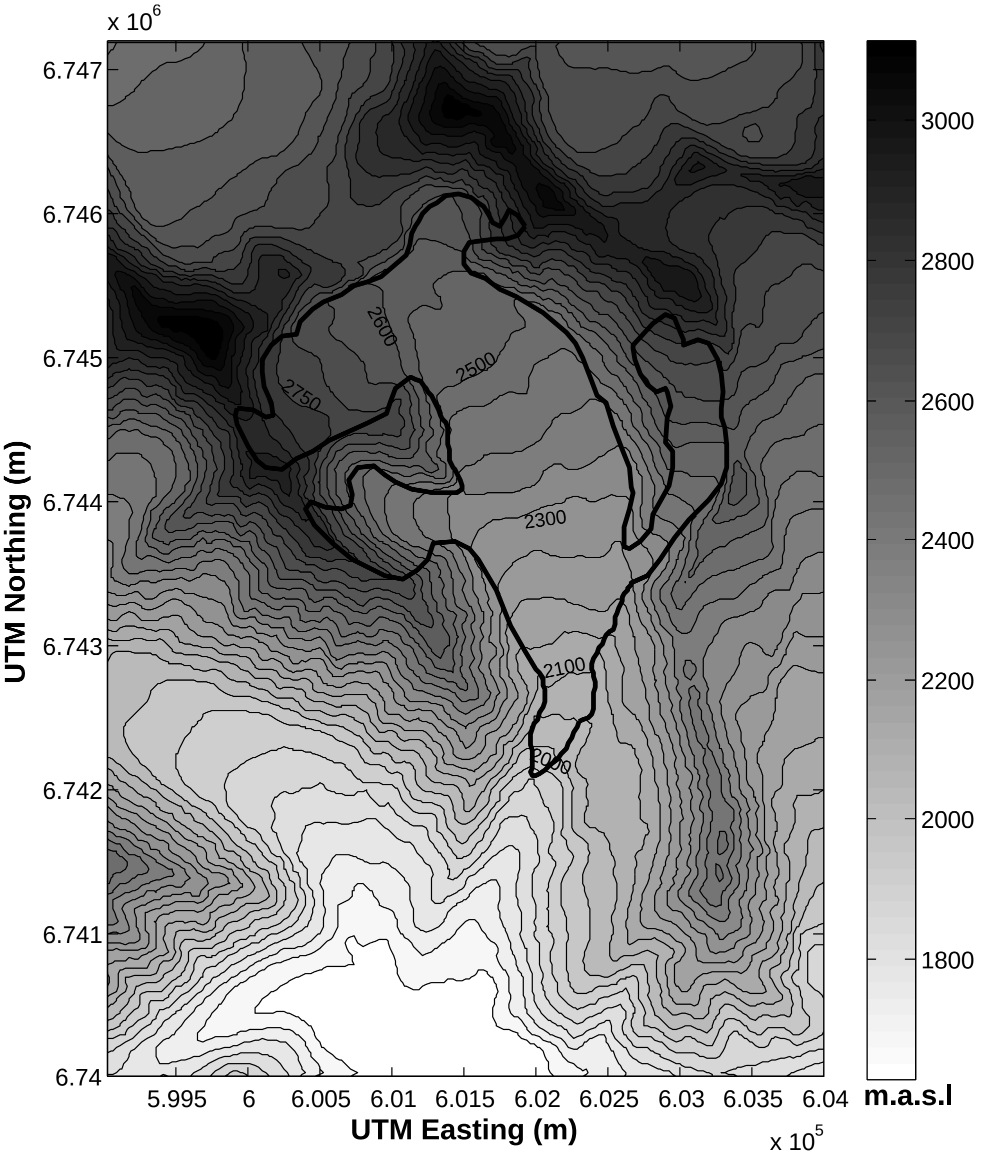

Figure 3.26: Final surface DEM: basin-scale contour map. Elevation contour interval is 50 m, DEM resolution is 30 m.

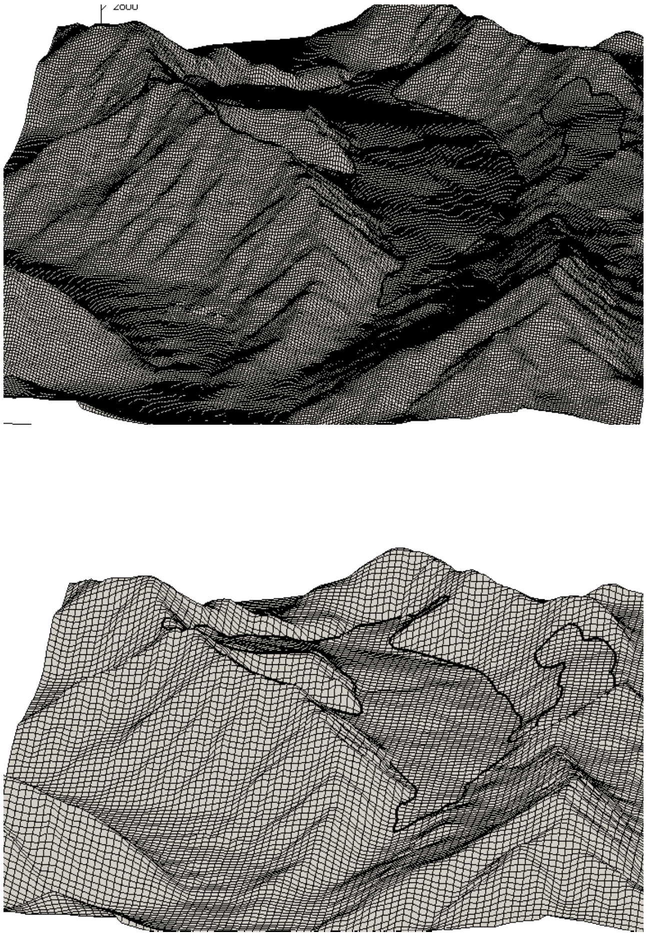

Figure 3.27: Final surface DEMs resampled at a resolution of 20 m (top) and 50 m (bottom). The thick black line defines the glacier outline.

3.4 Bed DEM generated by kriging in Surfer

A digital elevation model of the bed of the glacier is generated using Surfer 8. The ice thickness dataset presented in Chapter 2 is interpolated using ordinary kriging, and then subtracted from the surface DEM to obtain bed elevations.

3.4.1 Methods

Data preconditioning

To each of the ice thickness measurements, presented in Chapter 2, a quality index is assigned. This index describes the reliability of the reflection picked during the processing of the radar data. Quality indices vary from 1, describing a very poor reflection, to 5, for an excellent reflection. The reliability of the final DEM is directly linked to both the quality and the quantity of the original data. The quality of the interpolation indeed deteriorates when the number of data drops. The optimal interpolation is thus achieved by balancing the quality and the quantity of the data. The dataset is filtered and data with quality indices of 1 and 2, corresponding to “poor” and “very poor” reflections, are discarded.

To further improve the result, we added points from the glacier outline to the dataset, with associated ice thicknesses of zero. These additional data, digitized from the map, are a great help in defining the limits of the glacier and contribute to a more realistic tapering of ice thickness at the margins of the glacier. Figure 3.28 shows the spatial distribution of the filtered ice thickness data, including outline points.

Kriging of ice thicknesses in Surfer

The filtered ice thickness dataset is then interpolated at a resolution of 30 m using the default parameters for ordinary kriging in Surfer. These parameters are presented in Table 3.6 in Section 3.2. Because the ice thickness grid nodes must coincide with the surface elevation grid nodes in a later step, the same spatial limits and resolution as for the surface DEM are specified.

Data post-processing

After kriging in Surfer, the interpolated ice thicknesses are imported into Matlab and the glacier is isolated using the ice mask described in Section 3.1.6. Tributaries are also cut

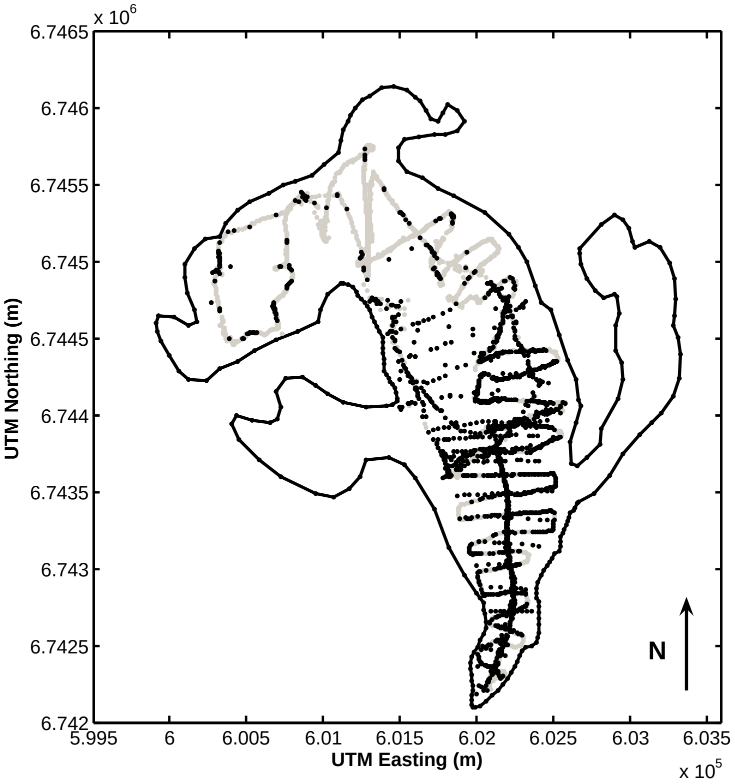

Figure 3.28: Spatial distribution of ice thickness data. The grey dots represent all measured data while the black dots represent the subset of data used in the interpolation based on their quality indices.

out, because they have not been surveyed and ice thicknesses are most likely innacurate in these areas. Moreover, the eastern tributary is detached from the trunk glacier and is therefore not dynamically important. The western tributary flows into the trunk glacier, creating a moraine, but the flow remains confined near the eastern margin of the trunk glacier. Therefore, the contribution of the western tributary to the overall dynamics of the glacier is not especially important.

From ice thicknesses to bed elevations

To derive bed elevations, the krigged ice thicknesses are subtracted from the ice surface elevations obtained from the final surface DEM. To this end, points from both DEMs must coincide and both models need to contain the same number of points. In anticipation of that issue, the spatial limits and resolution were specified in the kriging routine so that both DEM grids coincide. The surface DEM is also passed through the ice mask to eliminate terrain points and tributaries are cut out in order to obtain two sets of data of the same size and for which point locations coincide. The ice thicknesses are then subtracted from the surface elevations to generate bed elevations. Finally, the new bed elevation data are merged with the surrounding topography and the complete dataset is reinterpolated onto a regular grid. This is done following the same procedure used for the surface DEM in Section 3.1.6.

3.4.2 Results

Ice thickness map

The ice thickness data, interpolated at a resolution of 30 m using ordinary kriging in Surfer, is presented in Figure 3.30. Ice thicknesses range from ∼0–20 m downglacier to a maximum of ∼150 m upglacier, with an average thickness of 78 m. The performance analysis, illustrated in Figure 3.29, shows that measured values are well reproduced by kriging, with a root mean squared error of 4.1 m.

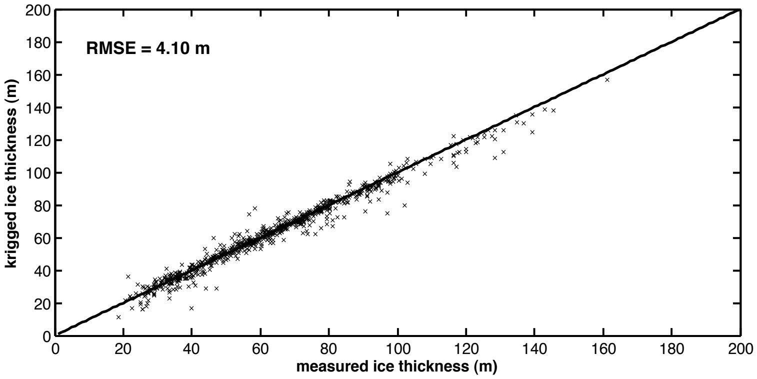

Figure 3.29: Ice thickness DEM performance plot. Krigged ice thicknesses are plotted against measured ice thicknesses for all cells containing data. The value of the root mean square error is shown in the top left corner.

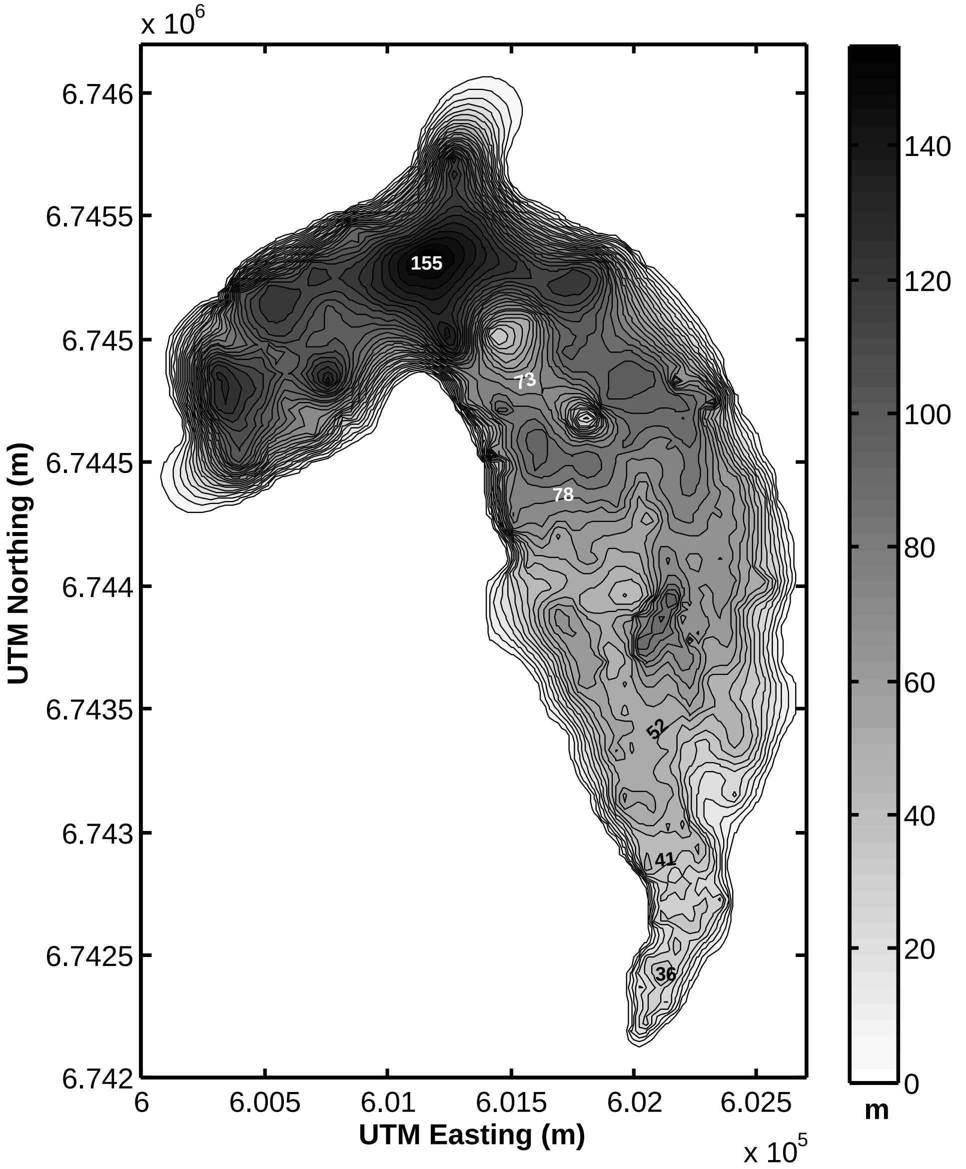

Figure 3.30: Ice thickness contour map. Since they have not been surveyed, tributaries have been cut out. Contour interval is 6 m

Bed elevation map

The bed DEM, derived from the krigged ice thickness and surface DEMs, is presented in Figures 3.31 and 3.32. The bed topography shows a few depressions mid-glacier around the centerline (box a in Figure 3.32) and a large asperity is visible in the north-west where the glacier curves along its length (box b in Figure 3.32).

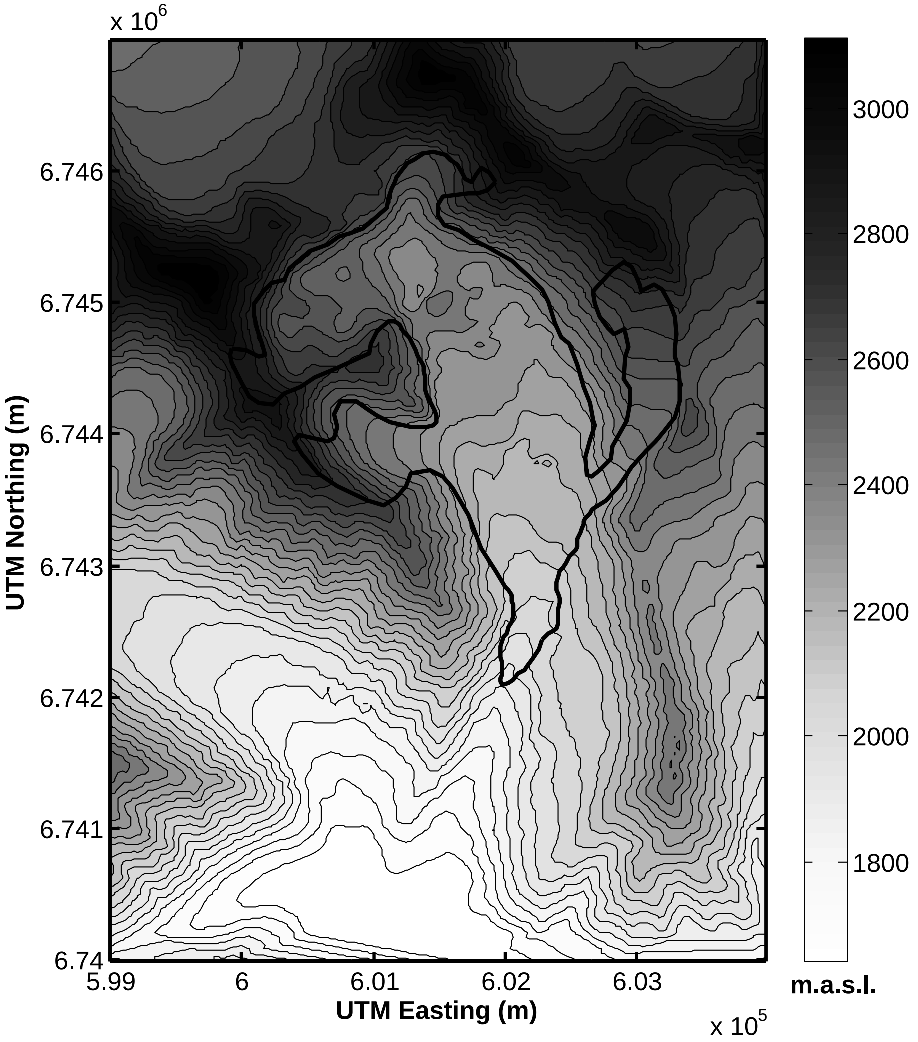

Figure 3.31: Bed DEM: basin-scale contour map. Elevation contour interval is 50 m, DEM resolution is 30 m.

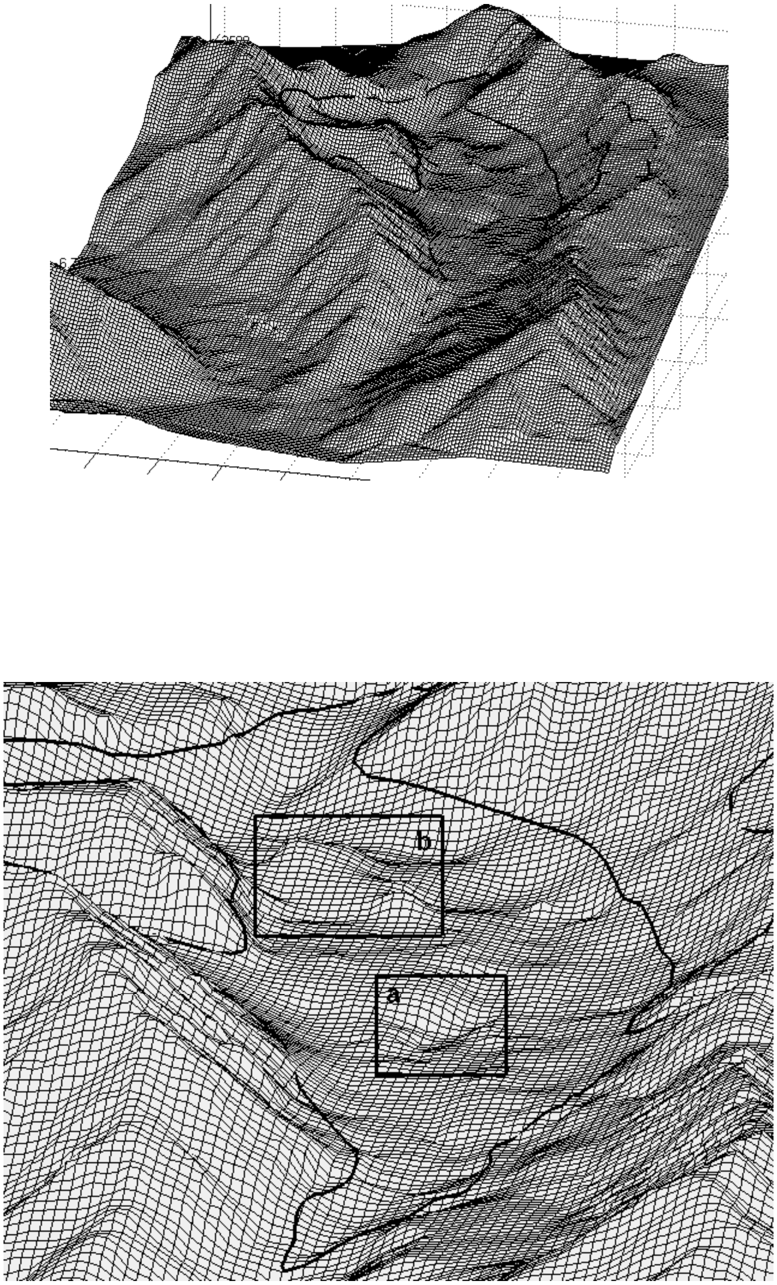

Figure 3.32: Bed DEM: basin-scale (top) and glacier-scale (bottom) 3D views. Boxes outline (a) a set of depressions and (b) a large asperity.

3.5 Flowline profiles

Flowline profiles are derived from the surface and bed DEMs and from the ice thickness map. The flowline used to compute the profiles is the high resolution flowline presented in Chapter 2.

3.5.1 Surface elevation, bed elevation and ice thickness profiles

Surface and bed elevation profiles are computed from the surface and bed DEMs, respectively. For each flowline point, all points within a prescribed radius are identified and their distances to the nearest point on the flowline are computed. An inverse distance average of their elevations is then computed and attributed to the flowline point. For both surface and bed profiles, a search radius of 50 m was used. The value of 50 m was chosen so that at least one point in each of the 8 directions of the 30 m DEM grid is included in the calculation of the inverse distance average. The thickness along the flowline is derived from the krigged ice thicknesses in a similar manner using a search radius of 50 m. Profiles of surface elevation, bed elevation and ice thickness are presented in Figure 3.34a and b.

3.5.2 Slope profile

The local slope is derived directly from the surface profile. First, the surface elevation profile is fitted with a polynomial. To be able to fit the surface more closely, the profile is divided into four sections and the best-fit polynomial is calculated for each section. Experimentation shows that the closest fits are obtained using polynomials of order 20 to 25. Then the derivatives of each of the four polynomials are computed, evaluated at each flowline point and slope values are extracted. Because the polynomials do not fit the surface elevation closely enough at the junction between zones, the two first and last points located at the junction between polynomials are not taken into account in the calculation of slope. Since the distance associated with these ignored points is very small, this omission does not have a noticeable impact on the resulting slope. The few missing points are then recovered by interpolation. Finally, because the local slope calculated with this method presents unrealistic high frequency oscillations, it is averaged over a distance of two ice thicknesses. The averaged value of 78 m is used at all points for the ice thickness and, as a final step, the slope is interpolated at a 1 m resolution using a cubic spline method. The resulting slope profile is shown in Figure 3.34c.

3.5.3 Shape factor profile

Shape factors are dimensionless quantities used to characterize the shape of a glacier's bed. They depend on the ratio of the half-width of the glacier to the ice thickness on the centerline:

$$W = \frac{w}{h}, \tag{3.7}$$

where w is the half-width of the glacier and h is the local ice thickness along the centerline. Shape factors are assigned using the W-dependent values advocated in Paterson (1994); these values are reproduced in Table 3.8. The flowline ice thickness profile can be used here to calculate W, but the half-width of the glacier at each flowline point must be estimated. To do this the surface DEM as well as the flowline are used. First, the angle made by the flowline direction with respect to North is computed for each flowline point. The surface DEM is passed through the ice mask as described in Section 3.1.6 to isolate the ice from the surrounding terrain. Then, for each flowline point, a line perpendicular to the local orientation of the flowline is defined in the form of an array of points located 20 m from each other. For each of the points of the line thus defined, the algorithm searched for surface DEM points situated within a 40 m radius. If such points are found, the algorithm jumps to the next point of the array. When no DEM points are found within 40 m, it means that we have reached the edge of the glacier, and the location of the last point in the array is recorded. The procedure is repeated along the line defined in the other direction to record the location of the opposite glacier edge. Once both edges have been located, the algorithm jumps to the next flowline point and repeats the procedure. The half-width of the glacier is derived from the two locations recorded for each flowline point. Finally, the shape factor ratio W is calculated according to Equation 3.7, and the shape factor for each flowline point

W	**Parabola**	**Semi-ellipse**	**Rectangle**
1	0.445	0.500	0.558
2	0.646	0.709	0.789
3	0.746	0.799	0.884
4	0.806	0.849	1.000
∞	1.000	1.000	1.000

Table 3.8: Values of shape factors (Paterson, 1994)

is estimated using the values in Table 3.8. Because the bed shape revealed in the bed DEM is closest to a semi-ellipse, values of shape factors corresponding to a semi-ellipse are used to derive the profile presented in Figure 3.34d.

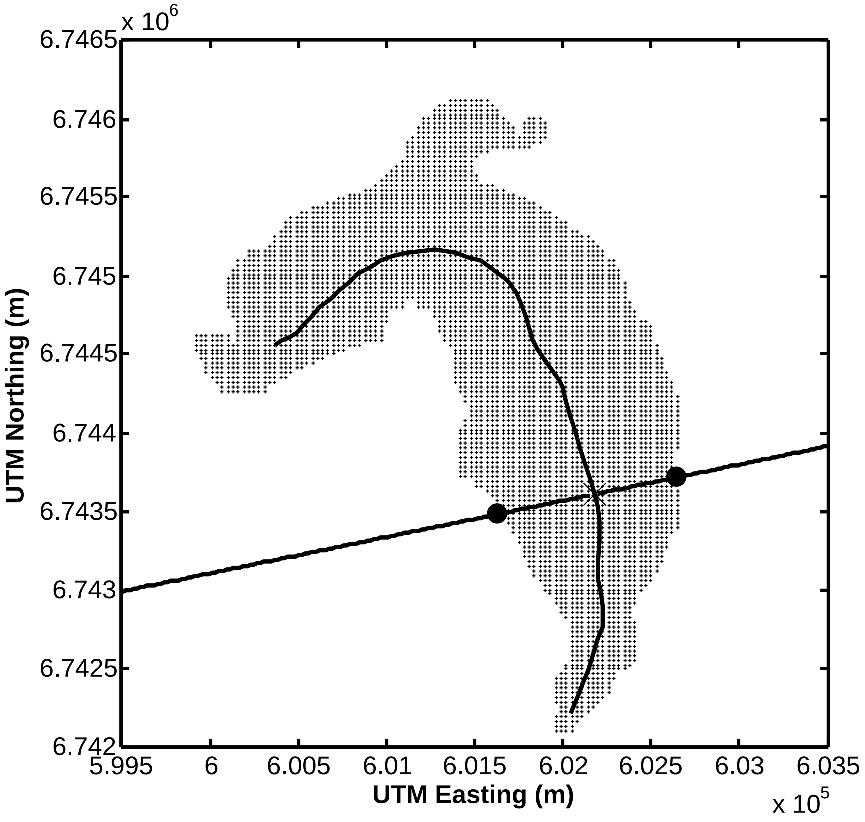

Figure 3.33: Glacier half-width calculation. Surface DEM points are plotted along with the flowline. The straight line is perpendicular to the local flowline direction. The two black circles correspond to the detected glacier margins, the distance between them defines the local width of the glacier.

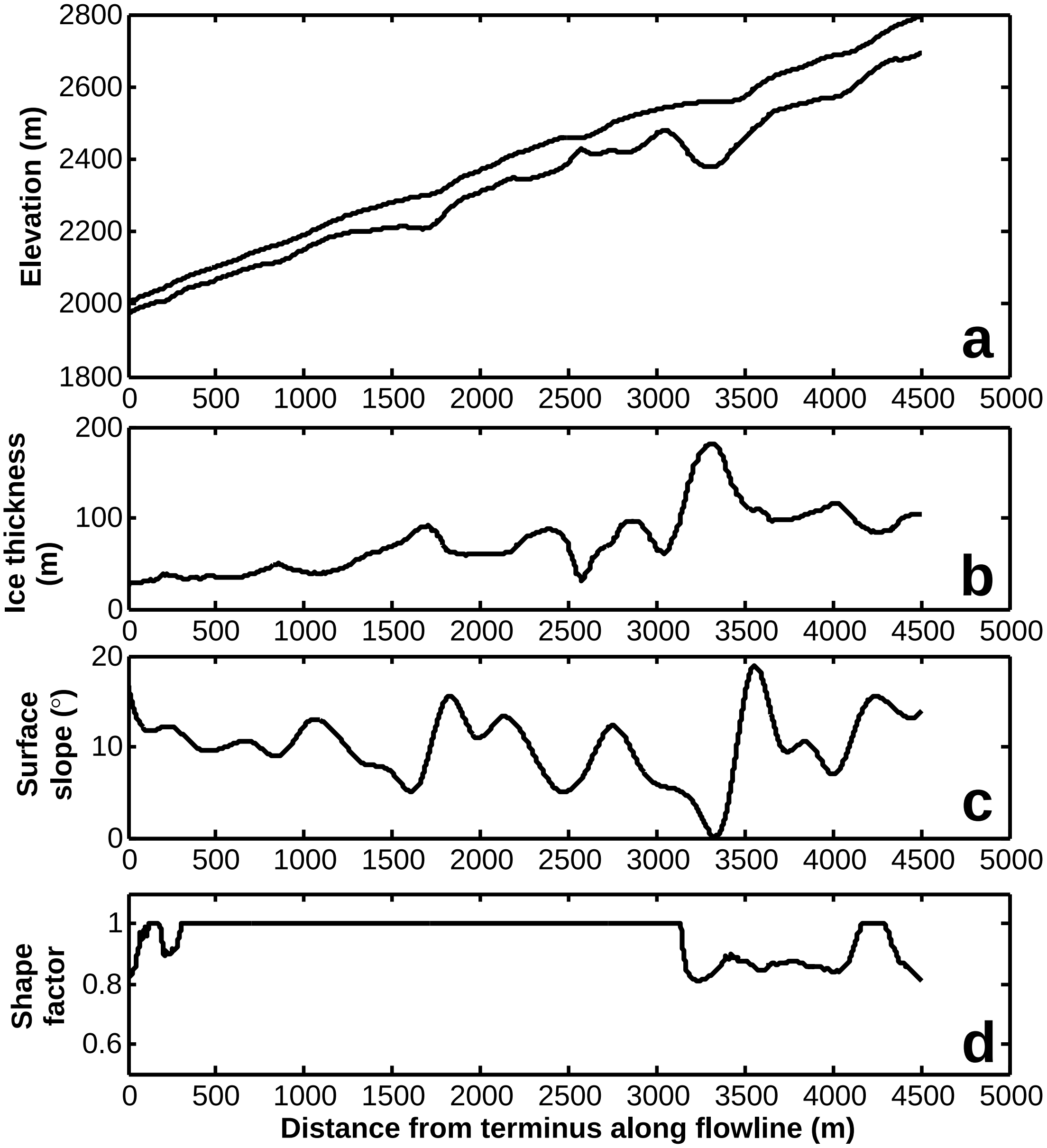

Figure 3.34: Flowline profiles. (a) Surface elevation (top line) and bed elevation (bottom line), (b) ice thickness, (c) local surface slope and (d) shape factor (using an semi-elliptical bed shape) are plotted as a function of distance from the glacier terminus along the flowline.

Chapter 4

Linear geophysical inversion

Geophysical inverse theory describes a set of statistical methods to estimate unknown geophysical parameters from measured data. There are many inverse methods, which are adapted to different problems. For example, parameter estimation is a method used to estimate a number of discrete parameters from a set of measured data, while inversion aims to estimate a continuous model from a set of measurements. Note that the term "inversion" is commonly used to refer to the set of methods gathered in inverse theory, but is also used to refer to a specific inverse method. Geophysical inversion also features two different approaches, frequentist or Bayesian, corresponding to two different views of statistics. Here we use a frequentist inversion method as described in Parker (1994), and we will simply call it inversion in the rest of this work.

Geophysical inverse theory was originally developed to construct models of the Earth and is widely used in seismology and mineral exploration. It has also gained popularity among hydrologists and glaciologists. Recently, Bayesian inversion methods have been used by Parrenin et al. (2001) to assess the quality of the Vostok glaciological timescale and by Gudmundsson and Raymond (2008) to determine basal slipperiness and basal topography from surface velocity and topography variations along the flowline of ice streams. Maxwell et al. (2008) used a Kozlov-Maz'ya iteration method to determine basal velocities and stresses. Frequentist inversion has been used by Truffer (2004), whose inverse approach to estimate the basal speed of valley glaciers is the basis for the work described here.

As we will see in more detail in Section 4.2.1, glacier models have been developed that calculate surface velocities from basal and deformational velocities. Such models establish a mathematical relationship between parameters (basal velocities) and data (surface velocities) and are referred to as *forward* models. The inverse problem consists of estimating the parameters (here basal velocities) from the data (surface velocities). It is important to note that the vocabulary of inverse theory is slightly different than that of other disciplines. The term *model* as used in inverse theory does not refer to the mathematical relationship between data and parameter, but to the parameters themselves. The mathematical relationship is called the *forward model*. In other words, *model* is the term for the quantity being estimated by the inverse problem, while the *forward model* is the mathematical relationship between the model and the data. These concepts are illustrated in Figure 4.1.

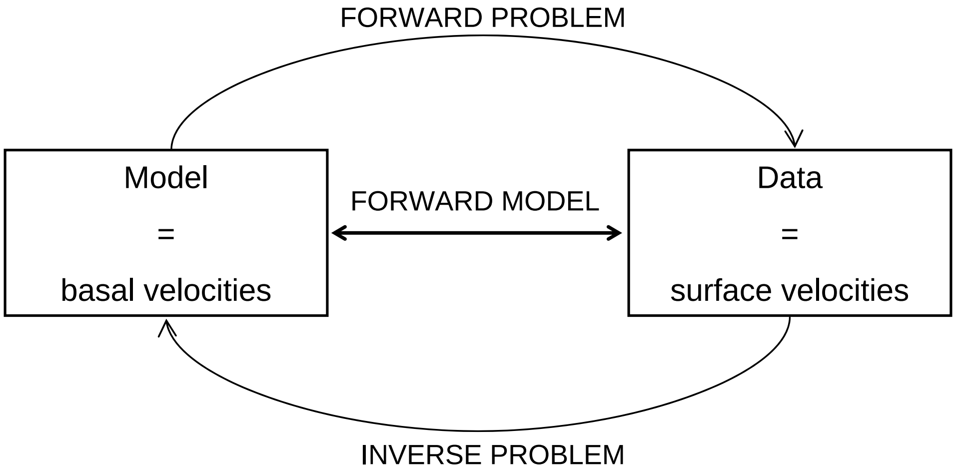

Figure 4.1: Forward and inverse problem diagram

4.1 Input data

This section presents the data to be used as input to the forward model and the inversion. The acquisition and processing of these data are discussed in more detail in previous chapters.

4.1.1 Surface velocity data

The surface velocity data used in the inversion are presented in detail in Chapter 2. The surface velocities were measured during three consecutive summers, yielding four datasets:

Summer 2006 surface velocities, summer 2007 surface velocities and annual surface velocities for the periods 2006-2007 and 2007-2008. Some of the velocity measurements presented in Chapter 2 were discarded in favour of nearby measurements with lower errors. Table 4.1 indicates which of the measurements presented in Chapter 2 were used in the datasets mentioned above. The "summer" season here is not defined in a traditional sense as the melt season, but corresponds to the periods of study-site occupation: from the 11th to the 30th of July for 2006 and from the 27th of July to the 6th of August for 2007. The annual velocities are calculated from measurements ranging from July 11, 2006 to July 27, 2007 for the first dataset and from July 27, 2007 to July 15, 2008 for the second dataset. The four datasets, along with associated errors are presented in Figure 4.2.

Poles	**Summer 2006**	**Summer 2007**	**Annual 2006-2007**	**Annual 2007-2008**
S1	✓	✓	N/A	N/A
S2	✓	✓	N/A	✓
S3	✓	✓	✓	✓
S4	✓	✓	✓	✓
S5	✓	✓	✓	✓
G1	✓	✓	N/A	N/A
S6	N/A	×	✓	✓
S7	✓	×	✓	✓
G2	N/A	✓	N/A	N/A
S8	✓	×	✓	✓
G3	N/A	✓	N/A	N/A
S9	✓	×	✓	✓
S10	×	✓	✓	✓
G4	✓	N/A	N/A	N/A
S11	✓	✓	N/A	✓
S12	N/A	✓	N/A	✓

Table 4.1: Poles used in the inversion of surface velocity

4.1.2 Ice thickness, surface slope and shape factors

Ice thicknesses, surface slopes and shape factors are inputs required in the forward model. They were derived from the surface DEM and the ice thickness map, using a procedure described in Chapter 3, Section 3.5. Ice thickness, slope and shape factor profiles are presented in Figure 3.34.

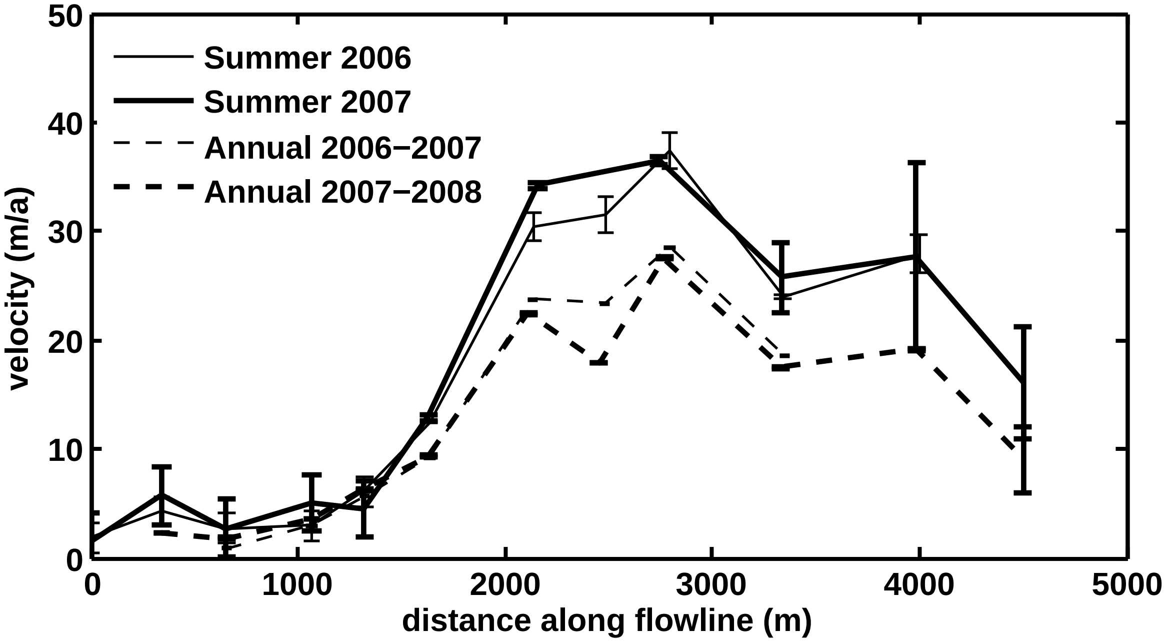

Figure 4.2: Surface velocities measured at pole locations along the glacier flowline, presented with associated uncertainties, are plotted as a function of distance from the glacier terminus for the four datasets.

4.2 Methods

This section deals with the methods used to derive basal velocities from surface velocity measurements. It presents the forward model, as well as the two inverse methods used to compute basal velocities. The forward model is one dimensional over the length of the glacier and requires as input a flow-law coefficient, whose value depends on depth. A transient temperature model, described at the end of this section, is therefore used to calculate an effective temperature over the thickness of the glacier. Appendix B presents the main equations governing ice flow and details the background and derivation of several equations introduced in this section.

4.2.1 Forward model

The first step of the inversion procedure is to define the model used to describe the physics of the problem, referred to as forward model. A forward model is a mathematical relationship linking parameters characterizing the system under investigation to quantities being measured. In our case, the forward model links the basal velocity to the measured surface velocity. Inverting the forward model consists of using the actual measurements to infer the values of the parameters characterizing the system. In our case, inverting the forward model is estimating the basal velocity from surface velocity measurements. The forward model used here is identical to the one used in Truffer (2004), which itself uses the model developed by Kamb and Echelmeyer (1986).

Laminar flow of ice down an inclined channel

A starting point of the forward model is to express the velocity due to the deformation of ice flowing down an inclined channel (subsequently referred to as deformational velocity or creep velocity). The relationship between observed surface velocity, deformational velocity and basal velocity is illustrated in Figure 4.3. Ice is treated as a non-linear viscous fluid and its rheology is characterized by a power law linking stress to strain rate. This flow law, known as Glen's flow law (Glen, 1955), includes two parameters: the flow-law coefficient A and the flow-law exponent n. The value $n = 3$, widely used by glaciologists to describe the rheology of glacier ice, will be used in the rest of this work (Glen's flow law is described in more detail in Appendix B, Section B.2). An idealized glacier in the form of a slab of uniform thickness h along the flowline and uniform bed inclination α is considered. The glacier assumes a laminar flow regime, in which all flowlines are parallel to the surface. This corresponds to a simple-shear stress regime, which means that all but one stress component are zero; the only non-zero stress component is situated in the plane defined by the direction of glacier flow and the direction perpendicular to the channel. It follows that the vertical component of velocity is zero. Using this glacier geometry and the assumption of laminar flow, Paterson (1994) showed that the deformational velocity at the surface of the glacier can be expressed analytically as

$$u_c = \frac{2A}{n+1} \left(\rho g \sin\alpha\right)^n h^{n+1}, \tag{4.1}$$

where ρ is the ice density, g is the gravitational acceleration and other parameters are as defined above (Equation 4.1 is derived in Appendix B, Section B.3). This expression is valid for a slab glacier of infinite extent both in the direction parallel to the flow and in the horizontal direction perpendicular to the flow. Realistically, glaciers usually flow down valleys in confined channels and the drag exerted by the valley walls onto the ice mass reduces the velocity along the centerline of the glacier. The shape of the channel can be accounted for by introducing a shape factor f in the expression for the creep velocity (Nye, 1965). The shape factor depends on the ratio of glacier width to ice thickness, and values differ depending on whether we consider a parabolic, semi-elliptical or rectangular channel (see Section 3.5 for more details). For a semi-elliptical channel, values range from 0.5 for a narrow channel to 1 for a wide channel for which the drag from the valley walls has no effect

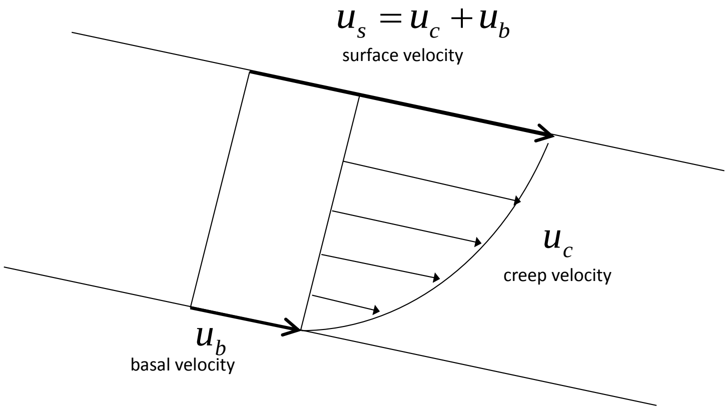

Figure 4.3: Relationship between the observed surface velocity, the creep (or deformational) velocity and the basal velocity for an idealized slab glacier

on the velocity on the centerline. Adapting the previous equation, the surface velocity due to ice deformation on the centerline of the glacier becomes

$$u_c = \frac{2A}{n+1} \left(\rho g f \sin\alpha\right)^n h^{n+1}, \tag{4.2}$$

where h is the ice thickness at the center of the channel. It is important to note that the velocity u_c presented here is the surface velocity resulting only from the deformation of ice, and does not include slip at the ice-bed interface or deformation of the bed itself.

Case of variable ice thickness and surface slope

We thus need a model that links the total surface velocity to the creep and basal velocities. For an idealized slab glacier, surface velocity is simply the sum of the local deformational and basal velocities, but this is no longer true for real glaciers. Real glaciers have variable slopes and ice thicknesses, and not all locations on the glacier can be described by laminar flow and simple shear regime. Because the slope of the glacier bed varies over the length of the flowline, there is longitudinal compression or extension that varies over the length of the glacier (Nye, 1952), giving rise to non-zero longitudinal stress gradients. The coupling introduced by the longitudinal stress gradients can considerably modify the velocity from that calculated using local slope and thickness (Equation 4.2).

Kamb and Echelmeyer (1986) developed a model that describes how the longitudinal stress gradients act in an ice body to create a particular velocity distribution along the length of the glacier that depends on the longitudinal profile of ice thickness and surface slope. From the longitudinal stress balance, they derive an equation that quantifies the longitudinal averaging of local slope and thickness by the longitudinal stress-gradient coupling. They found that the creep velocity $u(x)$ at any point of horizontal coordinate x located along the length of the glacier can be expressed as

$$u(x) = u_{obs}(x_0) e^{T(x) - T(x_0)}, \tag{4.3}$$

where x_0 is an arbitrary reference point along the flowline and T is defined as

$$T(x) = \int_{x-2l}^{x+2l} \left(n \ln \alpha f + (n+1) \ln h\right) W_l(x' - x) \, \mathrm{d}x'. \tag{4.4}$$

The term W_l is a weighting function and l, called the longitudinal coupling length, depends on rheological parameters and is generally about one to three times the ice thickness (Kamb and Echelmeyer, 1986). Equations 4.3 and 4.4 correspond to Kamb and Echelmeyer's Equations 35a and 35b.

Truffer (2004) combined and adapted these equations into the following form:

$$\ln u_s(x) = \int_0^L g(x' - x) \ln \left(u_c(x') + u_b(x') \right) \mathrm{dx}', \tag{4.5}$$

where u_s is the observed surface velocity, u_b is the basal velocity along the centerline of the glacier, L is the total length of the glacier and x is the glacier longitudinal coordinate, measuring a distance from the terminus along the flowline. The weighting function g corresponds to the function W_l of Kamb and Echelmeyer (1986). Although the notation g overlaps with the acceleration of gravity, it is appropriate to keep this notation because the weighting function g is used below to generated the Gram matrix G, which will replace it. The weighting function g is defined as

$$g(x' - x) = C\, e^{-\frac{|x'-x|}{l}}, \tag{4.6}$$

where l is the longitudinal coupling length as in Kamb and Echelmeyer (1986). A value of three times the local ice thickness will be used in the rest of this work, following Truffer (2004). The term C is a normalizing factor, whose purpose is to ensure that

$$\int_0^L g(x' - x)\mathrm{dx}' = 1. \tag{4.7}$$

The relationship expressed in Equation 4.5 can be used to calculate surface velocities, given an appropriate boundary condition at the bed of the glacier. In words, Equation 4.5 expresses that the observed surface velocity is not equal to the local sum of basal and deformational velocities. Instead, it is equal to a weighted average of this sum over a prescribed averaging distance. The averaging distance and weights are prescribed by the weighting function W. An idealized normalized weighting function is shown in Figure 4.4. The length $4\,l$ is called the averaging length and provides a measure of the distance over which the effects of varying slope and thickness are averaged. The relationship between basal and surface velocities, described in Equation 4.5, constitutes the foundation of the forward model.

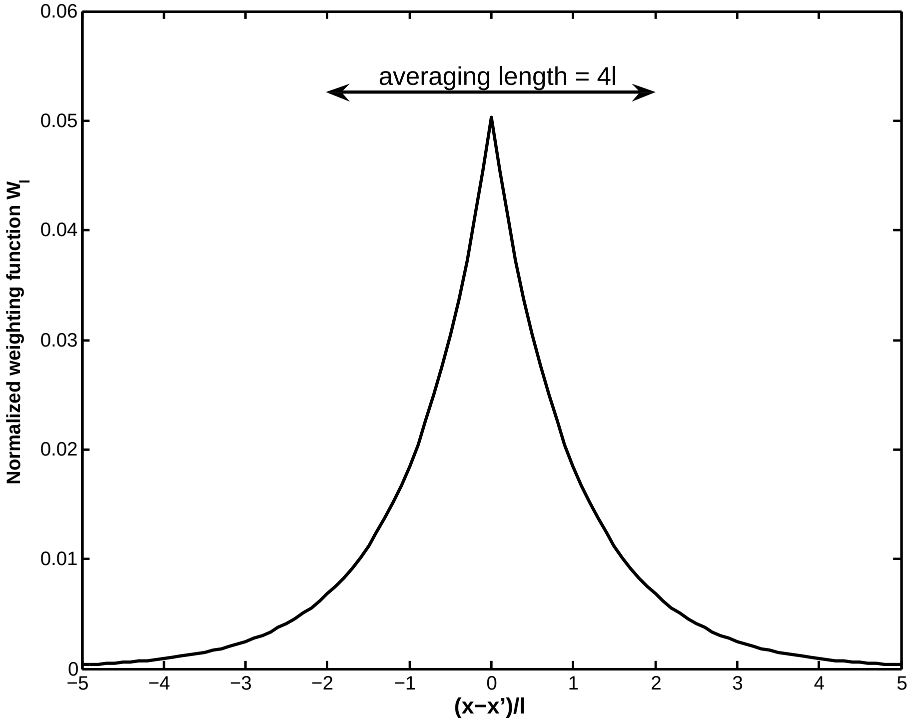

Figure 4.4: Idealized normalized weighting function W_l for a synthetic glacier of length 10. Weighting function is evaluated in the middle of the glacier and longitudinal coupling length is set to 1. The averaging length is four times the longitudinal coupling length l.

4.2.2 Linear inverse problem

Definition

Now that the forward problem is defined, the inverse problem can be formulated. A forward problem is a well-posed problem and can be written, in mathematical terms, as an inner product:

$$d_j = [g_j, m], \quad j = 1, ...N, \tag{4.8}$$

where d_j are the data, m is the model and g_j are continuous Kernel functions. In this case, the Kernel functions are calculated using the weighting function g. Using this notation, the forward model can be written as the following inner product:

$$\ln u_s = \left[g, \ln(u_c + u_b)\right]. \tag{4.9}$$

In Equation 4.9, the data $d_j = \ln u_s$ are N discrete real numbers, while the model $m = \ln(u_c + u_b)$ is a function of a Hilbert space H. Following the approach of Truffer (2004), we rewrite Equation 4.9 as:

$$\ln u_s - [g, \ln u_c] = \left[g, \ln(1 + \frac{u_b}{u_c})\right]. \tag{4.10}$$

With this notation, the data become $d_j = \ln u_s - [g, \ln u_c]$ and the model $m = \ln(1 + u_b/u_c)$. Equation 4.10 is linear, which leads to a relatively simple linear inverse problem. Using the surface velocity measurements as well as measurements of local slope and ice thickness, the data d_j can be evaluated at each of the N points of longitudinal coordinate x_j for which measurements of surface velocity exist.

Model discretization and Gram matrix

Although inverse theory considers the model m to be a continuous function of the longitudinal coordinate x, numerical treatment of the inverse problem requires that the model be evaluated at a finite number of locations. As a consequence, the model must be discretized in space. The longitudinal coordinate x is discretized into a vector of M components. The components x_i are real numbers quantifying the distance from the glacier terminus along the flowline and locating the centers of the M cells of discretized space. The model m is also discretized into an M-component vector and will be evaluated at each point x_i along the discretized flowline. The resolution at which both longitudinal coordinate and model are discretized is chosen so that $M > N$, thus defining an underdetermined problem.

The discretization of the model produces an underdetermined inverse problem. As a consequence, an infinite number of solutions exists for m that will produce the same predicted distribution of data and there exists no unique solution to the inverse problem. This concept is illustrated in Figure 4.5. A well-posed problem is defined by three conditions: existence, uniqueness and stability of the solution. Here the uniqueness condition is violated, and the inverse problem is ill-posed. Such problems are typically solved by inverse methods using the process of regularization, which will be explained in a subsequent section.

The Kernel functions g_j are equal to the weighting function of Equation 4.6. The weighting function g is in turn a function of the relative coordinate $x' - x$. The coordinate x' corresponds to the data locations x_j in discretized space. Thus there is one weighting (or Kernel) function g_j for each of the N data locations. Because the longitudinal space has been discretized into an M-component vector, the Kernel functions are not continuous in space, but are also discretized into M-component vectors. To summarize, there are N discretized Kernel functions $g_j(x_i)$, each of them having M spatial components. Computation of the N Kernel functions at each point of the discretized space thus creates a matrix having N lines and M columns. This matrix is called the Gram matrix and is usually denoted G (Parker, 1994). It links the data to the model so that

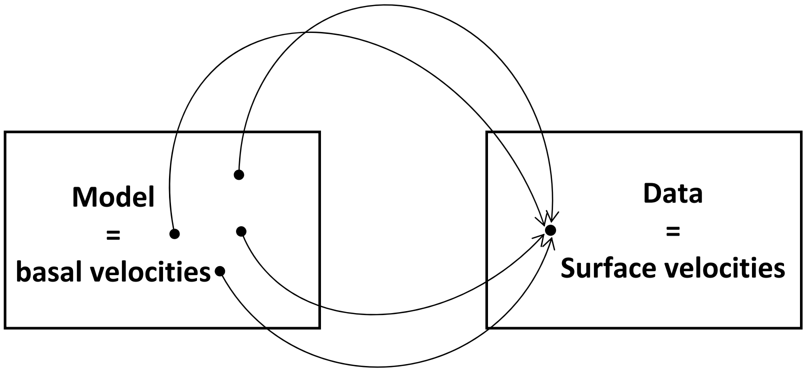

Figure 4.5: Illustration of an underdetermined inverse problem. While the forward problem is deterministic, the inverse problem is not, and many solutions for the model can produce the same data.

$$\ln u_s - [g, \ln u_c] = G \ln \left(1 + \frac{u_b}{u_c} \right). \tag{4.11}$$

In matrix notation, this is equivalent to $d = G\,m$, where d is an $N \times 1$ vector containing the data, m is a $M \times 1$ vector containing the discretized model and G is a $N \times M$ matrix containing the discretized Kernel functions. Finding an accurate model m will involve inverting the Gram matrix G. In most underdetermined problems, G is singular and a special technique is needed to perform the inversion.

Model norm and model objective function

As mentioned above, the solution to the inverse problem is non-unique and an infinite number of models m honour the data perfectly. Among these models that satisfy Equation 4.10, one that is deemed "best", or most realistic from a glaciological point of view must be selected. This process is called optimization and is usually carried out by minimizing a model norm (Parker, 1994). The choice of an appropriate norm is important and allows the incorporation of some a-priori knowledge about the solution. Following a method called Occam's inversion (Constable et al., 1987), we choose a model norm that selects the smoothest model by minimizing its second derivative. The principle behind Occam's inversion is that the best model should be the simplest model that fits the data. Constable et al. (1987) note that features appearing in the model that are not necessary to fit the observed data may not reflect reality and instead may result from an arbitrary starting guess or from an instability of the numerical method. On the other hand, a feature appearing in the most simple solution must be significant. The smoothest model is therefore a simplified representation of reality, deprived of any structure that cannot be verified in reality. According to Constable et al. (1987), the method ensures that "the real profile must be at least as rich in structure as the profile found, but never less complex in structure". The norm selecting the smoothest model is a measure of the second derivative of m. It is expressed in terms of a weighting matrix W_m containing coefficients of a second order finite-difference scheme:

$$W_m = \frac{1}{\mathrm{dx}^2} \begin{bmatrix} 0 & 0 & 0 & & & & & & \\ 1 & -2 & 1 & & & & & 0 & \\ & 1 & -2 & 1 & & & & & \\ & & & \cdots\cdots & & & & & \\ & & & & & 1 & -2 & 1 & \\ & 0 & & & & & 1 & -2 & 1 \\ & & & & & & 0 & 0 & 0 \end{bmatrix}, \tag{4.12}$$

where dx is the spatial resolution of the model. The first and last lines have coefficients reflecting boundary conditions adapted to the problem. The choice of the boundary condition has a physical meaning for the model and should take into consideration the requirement that W_m be invertible. The choice of boundary conditions is specific to the inversion method that is used and will be discussed below.

The weighting matrix W_m is applied to the model m to form a quantity known as the model objective function ϕ_m. The model objective function can be expressed as a norm or in a matrix form:

$$\phi_m = \|W_m\, m\|^2 = m W_m^T W_m m, \tag{4.13}$$

where W_m^T is the transpose of the weighting matrix. The inversion process known as optimization finds smooth models that fit the data by minimizing the model objective function ϕ_m, subject to the condition $d = G\, m$.

Misfit function

Measurements of glacier surface velocity have errors associated with them. It is very important to take these uncertainties into account in the inversion. Because the data have associated errors, it would be misguided to select a model that fits the data perfectly. Instead one wants to choose a model that allows the data to be recovered within the associated uncertainties. The quantity measuring how well the data are reproduced is called the misfit or the misfit function. Like the model objective function, it is expressed as a norm and is parameterized using a weighting matrix:

$$W_d = \begin{bmatrix} \frac{1}{\sigma_1} & & & & 0 \\ & \frac{1}{\sigma_2} & & & \\ & & \ddots & & \\ & & & \frac{1}{\sigma_{N-1}} & \\ 0 & & & & \frac{1}{\sigma_N} \end{bmatrix}, \tag{4.14}$$

where σ_j are the standard deviations of the errors. In this case, there is only one measurement (and thus only one associated error) per location x_j, thus the standard deviation is the value of the error scaled by the measured value. To translate errors on the measured surface velocities to errors on the data, as defined in Equation 4.10, the standard rules for propagating errors, presented in Appendix A, are applied. The misfit function ϕ_d can then be written:

$$\phi_d = \|W_d(d - G\, m)\|^2, \tag{4.15}$$

where the product $G\, m$ is the predicted data, that is to say the data that are obtained when the model resulting from the inversion is used as input to the forward model. The misfit function is the basic tool used to formulate the criterion for solving the inverse problem within a tolerance. It has been shown that in most cases the criterion $\phi_d = N$ yields models that fit the data within the error (Parker, 1994). However, in some cases no models that satisfy this criterion can be found and the criterion can be relaxed to $\phi_d - N \leq$ tol, where tol is an appropriate tolerance value. The inverse problem now becomes:

$$\text{minimize} \qquad \phi_m = \|W_m m\|^2 = mW_m^T W_m m \tag{4.16}$$

$$\text{subject to} \qquad \phi_d = \|W_d(d - Gm)\|^2 \leq N. \tag{4.17}$$

Regularization

The best solution should result from a balance between finding a smooth model and fitting the data closely. The process of balancing these two requirements is called regularization and how regularization is accomplished depends on the method of inversion. If a deterministic approach is taken, the inverse problem is solved numerically and regularization is performed by introducing a trade-off parameter that acts as a weight between misfit and model objective function. In the case of a singular value decomposition method (SVD) or spectral method, the regularization intervenes in the truncation of the SVD. The regularization process specific to each of these methods will be addressed in detail in the following sections.

4.2.3 Inversion using Tikhonov regularisation and a deterministic approach

The inversion method using a deterministic approach involves numerically solving the regularized inverse problem. A Tikhonov-type regularization of the inverse problem is done by introducing a trade-off parameter β. The trade-off parameter is a Lagrange multiplier and allows one to give different weight to the model objective function and to the misfit. In other words, the trade-off parameter is a tool used to vary the relative importance of fitting the data closely and finding a smooth model. Solving the regularized inverse problem is thus done by minimizing the function

$$\phi = \phi_d + \beta\, \phi_m, \tag{4.18}$$

under the condition that $(\phi_d - N) \leq \text{tol}$, where tol is an appropriate tolerance level. In our case the tolerance level is chosen so that the algorithm yields at least one solution. Choice of an appropriate solution involved experimenting with the tolerance level. We found that specifying too small a tolerance level would result in models that fit the data closely but have unrealistic oscillations.

Inversion without a reference model

With the parametrization described in Equation 4.18, minimizing the objective function ϕ is equivalent to equating its first derivative to zero, that is to say to solving $\partial\phi/\partial m = 0$. Replacing ϕ_d and ϕ_m by their matrix notations and developing the equation, it follows that the model m can be expressed as

$$m = (G^T\, W_d^T\, W_d\, G \,+\, \beta\, W_m^T\, W_m)^{-1}(G^T\, W_d^T\, W_d\, d_{\text{obs}}), \tag{4.19}$$

where d_{obs} are the data derived from observations, m is the model recovered from the inversion and all other terms are as defined above. The data predicted by the recovered model are then obtained by $d_{\text{pred}} = G\, m$ and can be compared to the observed data.

Inversion with a reference model

A reference model is a predefined model (in our case a predefined basal velocity profile) that allows one to incorporate a-priori knowledge about the model. It helps to constrain the solution when the structure of the expected model is known. In this case, introducing a reference model helps constrain the solution by avoiding models that have too much structure, as we will see in the results section. When using a reference model m_{ref}, the model objective function is formulated so as to minimize the difference between the model and the reference model:

$$\phi_m = \|W_m\,(m - m_{\text{ref}})\|^2, \tag{4.20}$$

and the recovered model becomes

$$m = (G^T\, W_d^T\, W_d\, G \,+\, \beta\, W_m^T\, W_m)^{-1}(G^T\, W_d^T\, W_d\, d_{\text{obs}}) \,+\, \beta\, W_m^T\, W_m\, m_{\text{ref}}. \tag{4.21}$$

Finding the optimal trade-off parameter

The optimal model is selected by finding the optimal trade-off parameter β. This is done by calculating the recovered model m for many values of the trade-off parameter and then selecting the models that satisfy the condition expressed in Equation 4.17. This condition states that the optimal models are those for which $\phi_d = N$ or alternatively for which $\phi_d - N \leq$ tol. I found that using a tolerance tol = N/100 yields the best results for this specific problem. The inversion algorithm was set up to find the minimum value of β producing a misfit that satisfies the criterion. When the optimal value of the trade-off parameter is found, m is computed for this specific value of β. The optimal basal velocity profile v_b is then recovered from the optimal model m using Equation 4.10. This type of regularization, called Tikhonov regularization and illustrated in Figure 4.6, is equivalent to a conditional minimization with a Lagrange parameter.

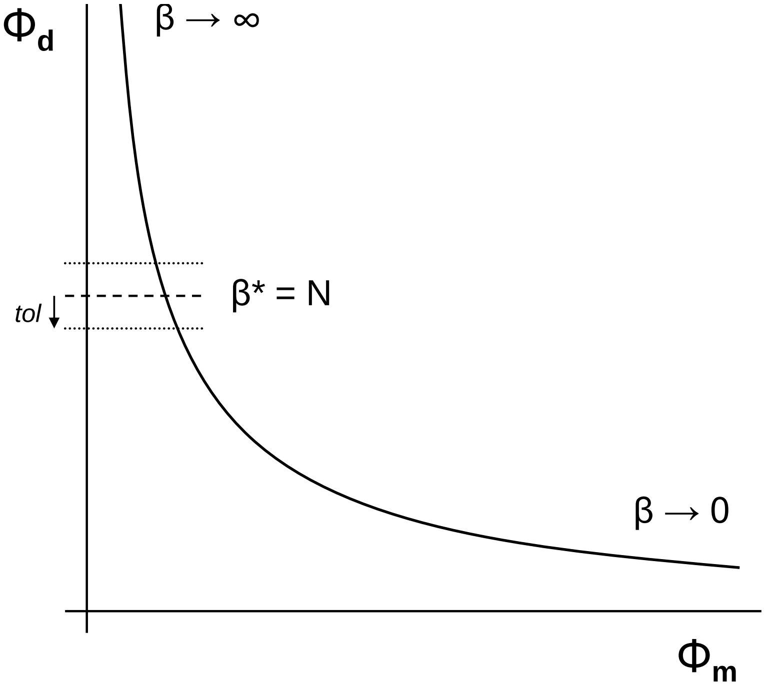

Figure 4.6: Ideal Tikhonov curve. The misfit function ϕ_d is plotted as a function of the model objective function ϕ_m. The optimal trade-off parameter β^* is either equal to the number of data N or situated in the interval defined by the tolerance level *tol*.

4.2.4 Inversion using a spectral decomposition method

The spectral method or singular value decomposition (SVD) method is a powerful method to solve inverse problems, and more broadly, a large number of matrix inversion problems. Although it gives only an approximate solution and cannot be implemented with all types of forward models, the spectral method is numerically simpler and faster than the deterministic approach. It is based on the mathematical notion of the spectrum of a linear transformation.

Any linear forward or inverse problem, when expressed in a matrix form, can be assimilated to a linear transformation A, expressed as an $N \times N$ matrix. Parker (1994) defines the spectrum of a linear transformation A as the N real numbers λ_n, called eigenvalues, that permit the equation

$$A\,\mathbf{u_n} \;=\; \lambda_\mathbf{n}\,\mathbf{u_n}, \tag{4.22}$$

to have a solution, where $\mathbf{u_n}$ is a non-zero vector of N real numbers, called the eigenvector, and $n = 1, 2, ..., N$. The eigenvalues λ_n are positive numbers decreasing from λ_1 to λ_n. The property expressed in Equation 4.22 allows any symmetric and positive definite matrix A to be written as a matrix product in a process called "spectral factorisation":

$$A = U\,\Lambda\,U^T. \tag{4.23}$$

In Equation 4.23, U and Λ are matrices containing the eigenvectors and the eigenvalues, respectively. This expression is valid for a determined problem ($N = M$).

Truncated singular value decomposition

In this specific case, we saw that the inverse problem can be written as a linear transformation

$$d = G\,m, \tag{4.24}$$

where d is an $N \times 1$ vector containing the data, m is an $M \times 1$ vector containing the unknown model and G is the $N \times M$ Gram matrix. The matrix G is rectangular and can be written in the form of a spectral factorization, also called singular value decomposition (SVD):

$$G = U\,\Lambda\,V^T, \tag{4.25}$$

where U and V are matrices containing the eigenvectors of $A\,A^T$ and Λ is the matrix containing the eigenvalues of $A\,A^T$ (eigenvalues of $A\,A^T$ are singular values of A). Because the problem is underdetermined, the Gram matrix G is not square. The matrices U and V are square and have respectively N and M components, but the eigenvalue matrix Λ is a non-square $N \times M$ matrix and is therefore singular. Because the purpose of the inversion process is to invert the Gram matrix to recover the model m from Equation 4.24, Λ must be rendered square. This is done by noting that there is a large range of eigenvalues and many of them are zero. Thus Λ is truncated to keep only the first p non-zero eigenvalues. In practice, this is usually done by rejecting all eigenvalues smaller than 10^{-12} (Parker, 1994). Figure 4.7 shows an example of truncated spectral expansion. To be consistent, eigenvectors are truncated accordingly, so that G is the product of three matrices of the following sizes:

- U is an $N \times p$ matrix,
- Λ is a $p \times p$ matrix,
- V is an $M \times p$ matrix.

The Gram matrix, expressed as a spectral expansion (Equation 4.25) or SVD, is now invertible. As mentioned above, this inversion is carried out by minimizing a model norm, subject to a misfit criterion. To optimize the result, a balance should be sought between the two processes in the form of regularization. This is done by truncating the SVD, or discarding a certain number of eigenvalues (in practice, replacing them by zeros). The number J of singular values to retain is understood as a sort of regularization parameter. The reason that truncating the SVD helps achieve a balance between finding a smooth model and fitting the data lies in the fact that the range of eigenvalues obtained in most practical problems is very large. Parker (1994) notes that the great majority of eigenvalues are smaller than the first eigenvalues by factors of at least 10^6. As a result a term corresponding to an eigenvalue situated at the begining of the spectral expansion makes the same contribution to the misfit, but a smaller contribution to the model norm, than a term situated further. On the other hand, terms located towards the end of the expansion, corresponding to very small eigenvalues, make only a small contribution to reducing the misfit while considerably increasing the model norm. Since the purpose of regularization is to minimize the model norm while keeping the misfit small, truncating the spectral expansion seems to be an appropriate regularization technique.

Inversion with reference model

Here we present the equations for an inversion with a reference model, however introducing $m_{\text{ref}} = 0$ in the following equations is enough to adapt the technique for an inversion without a reference model. As detailed in Section 4.2.2, inversion of uncertain data involves minimizing a model norm subject to a misfit criterion:

$$\text{minimize} \qquad \phi_m = \|W_m\,(m - m_{\text{ref}})\|^2 \tag{4.26}$$

$$\text{subject to} \qquad \phi_d = \|W_d(d - Gm)\|^2 \leq N. \tag{4.27}$$

In the spectral approach, the misfit and model norm are transformed via a variable transformation. First, one can define x such that

$$x = W_m\,(m - m_{\text{ref}}). \tag{4.28}$$

With this notation the misfit criterion can be written

$$\phi_d = \|Ax - b\|^2, \tag{4.29}$$

where A is a $N \times M$ matrix such that $A = W_d\,G\,W_m^{-1}$, and b is a $N \times 1$ vector such that $b = W_d\,d_{\text{obs}} - W_d\,G\,m_{\text{ref}}$. With this notation, the inverse problem becomes

$$\text{minimize} \qquad \phi_m = \|x\|^2 \tag{4.30}$$

$$\text{subject to} \qquad \phi_d = \|Ax - b\|^2 \leq N. \tag{4.31}$$

The matrix A, as shown for the Gram matrix G above, can be written in the form of a spectral decomposition as in Equation 4.25. Introducing a Lagrange multiplier β and minimizing the function $\phi = \phi_m + \beta\,\phi_d$ (as for the Tikhonov regularisation), it can be shown that the variable x becomes

$$x = V\,F\,\Lambda^{-1}\,U^T\,b, \tag{4.32}$$

where F is the identity matrix for now, and will become important later during the regularization process. Once the matrix A and b, as well as the eigenvectors and eigenvalues of the SVD are computed, the model m can be recovered from x using Equation 4.28. The misfit, given by

$$\phi_d = \|(F - I_p)\, U^T b\|^2 + \|(I_N - U\, U^T)\, b\|^2, \tag{4.33}$$

where I_p and I_N are respectively $p \times p$ and $N \times N$ identity matrices, as well as the model norm, given by

$$\phi_m = (U^T b)^T\, (L^{-1}\, T)^2\, (U^T b), \tag{4.34}$$

are also computed.

Regularization

Computing the misfit and model norm is useful in the regularization process. As mentioned above, the inverse problem is regularized by truncating the spectral expansion. The appropriate number of eigenvalues to discard must be determined that allows the misfit to be close to the prescribed value of N while minimizing the model norm. The appropriate number J of eigenvalues that should be retained is determined by identifying the point where the misfit reaches the value of N. All smaller eigenvalues are then ignored. This is done by using the matrix F introduced above. While having $F = I$ when computing the full SVD, we now alter F so that its first J values are ones and the rest are zeros. The effect of this is to set all eigenvalues $\lambda_{i>J}$ to zero when multiplying the eigenvalue matrix Λ by F. This regularization procedure is summarized in Figure 4.7. The regularized model m is then computed using Equations 4.28 and 4.32, and finally the basal velocity profile v_b is recovered from the model m using the relationship in Equation (4.10).

4.2.5 Transient temperature model

We have seen in Sections 4.2.1 and 4.2.2 that basal velocities and observed surface velocities are linked by a forward model and that estimating one from the other, using either a forward or inverse method, requires knowledge of the theoretical deformational velocity. The deformational, or creep, velocity, expressed theoretically in Equation 4.2, depends on the geometry of the glacier and on the mechanical properties, or rheology, of the ice. The flow law of ice, an empirical relationship between the shear strain rate and the shear stress, is a power law depending on the flow-law coefficient A and the flow-law exponent n (the flow law is derived in Appendix B, Section B.2). While a fixed value of $n = 3$ is used in most glacier studies, the value of A depends mainly on the ice temperature, and to a lesser extent

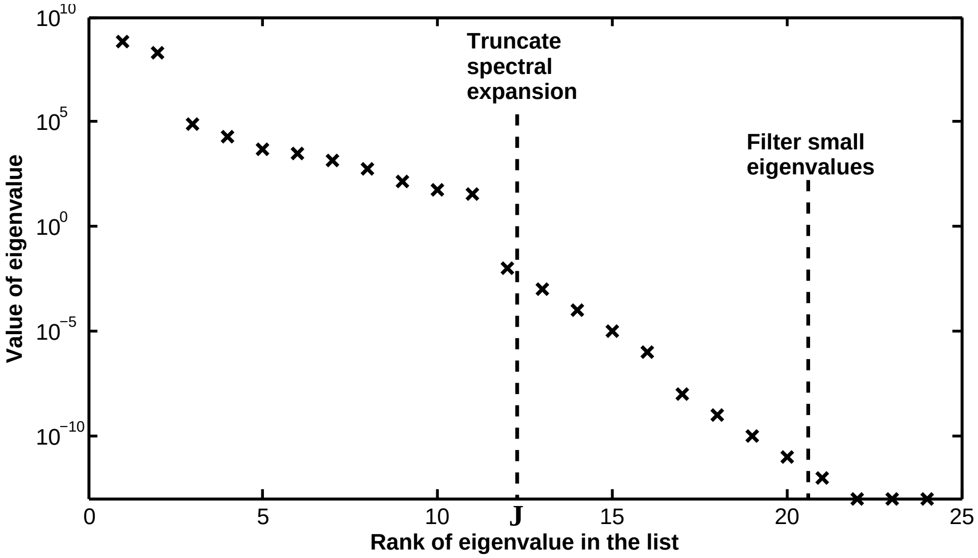

Figure 4.7: Example of spectral expansion. Eigenvalues are plotted as a function of their rank in the list. First, all eigenvalues smaller than 10^{-12} are filtered. Then all eigenvalues having a rank higher than J are discarded and the recovered model is computed using only these first J eigenvalues. This process is called regularization and helps balance fitting the data and finding a smooth model. The value J is chosen so that the misfit obtained with this truncation is close to the number of data N.

on many other factors such as crystal orientation or impurity content (Paterson, 1994). It is therefore important to use a value of A that is adapted to the particular problem.

A difficulty arises from the fact that the forward model is one dimensional and cannot take into account possible variations of temperature with depth. The model uses a theoretical expression for the surface velocity due to creep, which depends on the velocities of underlying layers of ice and thus on internal ice temperatures. As a consequence, a value of A that is representative of the whole thickness of the glacier, and not just the surface layer, must be used. In other words, an effective value of A, and thus an effective value of ice temperature, must be calculated. To this end, digital temperature sensors were installed at 5 m intervals over the thickness of the glacier in 2008, but a complete dataset is not yet available. Thus a transient model is constructed to compute a theoretical distribution of temperature with depth. Although a general approach is adopted here by using a transient temperature-depth model, a steady-state model would yield equally valid results.

The thermal equation

A fictitious slab glacier of constant thickness, slope and ice density is considered. The values of thickness and slope are averages of the study-glacier thickness and slopes along the flowline. The common density value of 917 kg/m^3 for ice is used. The thermal equation is derived from the energy balance equation using several constitutive relationships. The energy balance equation,

$$\rho \frac{\mathrm{du}}{\mathrm{dt}} = \sigma_{\mathrm{xz}}\, \dot{\epsilon}_{\mathrm{xz}} + \rho\, a - \frac{\partial q_{\mathrm{i}}}{\partial \mathrm{x}_{\mathrm{i}}}, \tag{4.35}$$

where u is the internal energy, ρ the ice density, σ_{xz} the shear stress, $\dot{\epsilon}_{\mathrm{xz}}$ the shear strain rate, a the energy supply term and q_{i} the energy flux, relates the total internal energy of the glacier (left-hand side in Equation 4.35) to the heat produced by ice deformation (first term on the right-hand side of Equation 4.35), the energy supply (second term on the right-hand side) and the loss of energy by conduction (third term of right-hand side). For ice, the energy supply term a is usually assumed to be zero. Using constitutive relationships, the internal energy u and the energy flux q_{i} are linked to the ice temperature. The shear strain rate $\dot{\epsilon}_{\mathrm{xz}}$ is also linked to the shear stress σ_{xz} using Glen's flow law as a constitutive relationship (These two steps are detailed in Appendix B). It follows that the temperature distribution with depth z and with time t can be described by a non-linear second-order partial differential equation (first order in time and second order in space):

$$\frac{\partial T}{\partial t} = \frac{1}{\rho c(T)} \left[K(T) \frac{\partial^2 T}{\partial z^2} + \frac{\partial K(T)}{\partial T} \left(\frac{\partial T}{\partial z} \right)^2 + \Phi \right], \tag{4.36}$$

where $c(T)$ is the heat capacity, $K(T)$ is the thermal conductivity and Φ is

$$\Phi = \sigma_{\mathrm{xz}} \dot{\epsilon}_{\mathrm{xz}} = 2\, A_0\, \exp\left[-\frac{Q}{RT} \right] \left(\rho\, g\, (h - z)\, \sin\theta \right)^{n+1}. \tag{4.37}$$

Parameters in Equation 4.37 are presented in Table 4.2 along with their numerical values. The derivation of Equation 4.36 is detailed in Appendix B, Section B.3.

Input data and types of temperature profiles

To solve the temperature equation in space and time, boundary conditions at the surface and the bed of the glacier must be provided for each timestep, as well as an initial condition for each spatial grid node. The surface temperature boundary condition is provided by a surface temperature dataset from Wheler (2009). Two automatic weather stations using temperature and relative humidity probes (HMP 45C212) equipped with radiation shields were set to record 2 m air temperatures (precision ±0.28°C) every five minutes on a Campbell Scientific CR1000 data logger. From daily temperature measurements over a period of over a year, mean annual surface temperature as well as average seasonal temperatures are extracted; they are presented in Table 4.2. The surface temperatures are measured at a fixed location near the middle of the flowline. Because surface temperature measurements are not available for many points along the flowline, this location, which is taken to be representative of the whole glacier, is used.

It is important to keep in mind that the purpose of this temperature model is to derive an effective temperature over the thickness of the ice in order to calculate the value of the flow-law coefficient used in the inversion. The temperature calculation is therefore to be viewed as a simple tool to help in choosing a reasonable and realistic flow-law coefficient. A possible way to improve the forward model in future research would be to compute temperature profiles at many locations along the flowline and derive effective values of the flow-law coefficient for each of these locations. This would allow a more realistic estimation of the deformational velocity by including spatial variation of the flow-law coefficient in the same way as for the slope and ice thickness.

While we have measurements of the surface temperature, we do not have any information on the bed temperature (temperature sensors at the bed were installed in 2008, but were not yet equilibrated), and so two hypothetical cases are considered: the bed is at the pressure melting point or the bed is frozen. In the first case, the basal boundary condition for the temperature is the pressure melting point during the simulated time period. This type of boundary condition, a known temperature, is a Dirichlet boundary condition. In the second case, the bed temperature is below the pressure melting point and the bed temperature is controlled by the temperature of the overlying ice and by the geothermal flux. Here it is not the bed temperature itself but rather a temperature gradient (in the form of the geothermal flux) that is specified, making it a Neumann-type boundary condition.

With these surface and basal boundary conditions, the simulation is run to generate four temperature profiles differing by their boundary conditions:

1. Constant mean annual temperature on the surface (Dirichlet condition) and constant pressure melting point temperature at the bed (Dirichlet condition),

2. Linearly varying seasonal temperatures on the surface (Dirichlet condition) and constant pressure melting point temperature at the bed (Dirichlet condition),
3. Constant mean annual temperature on the surface (Dirichlet condition) and temperature gradient depending on the geothermal flux at the bed (Neumann condition),
4. Linearly varying seasonal temperature on the surface (Dirichlet condition) and temperature gradient at the bed (Neumann condition).

Spatial and temporal discretization

In order to solve Equation (4.36) for the time-dependent temperature distribution, both spatial and temporal domains must be discretized. If one pictures time as a horizontal coordinate and space as a vertical coordinate, discretization produces a two-dimensional grid. The thermal equation is then to be solved for each grid node. The vertical coordinate z (the thickness of the glacier) is discretized into 1 m adjacent layers and the "horizontal coordinate" t (the time span of the simulation) is discretized into timesteps of 0.1 month. The choice of temporal resolution is justified below.

The temperature equation is a partial differential equation with derivatives in both time and space. A common technique to solve such an equation is to discretize the spatial derivatives using a finite difference scheme and solve the resulting ordinary differential equations in time. Applying this technique, often referred to as the method of lines, the spatial derivatives of temperature at each grid node are approximated as a function of the temperature at adjacent grid nodes. We use a forward finite difference scheme for the first-order derivative:

$$\frac{\partial T}{\partial z} \approx \frac{T(z_{i+1}, t) - T(z_i, t)}{\Delta z}, \tag{4.38}$$

where Δz is the spatial gridcell size, and a centered finite difference for the second-order derivative (applying a backward finite difference on the first-order finite difference derivative results in a centered finite difference for the second order):

$$\frac{\partial^2 T}{\partial z^2} \approx \frac{T(z_{i+1}, t) + T(z_{i-1}, t) - 2T(z_i, t)}{\Delta z^2}. \tag{4.39}$$

symbol	**name**	**value**	**unit**
Temperature-independent constants			
ρ	ice density	917	$\mathrm{kg\,m^{-3}}$
g	gravitional acceleration	9.8	$\mathrm{m\,s^{-2}}$
Q	creep activation energy	60700	$\mathrm{J\,mol^{-1}}$
R	Universal gas constant	8.31424	$\mathrm{J\,mol^{-1}\,K^{-1}}$
T_m	melting temperature of ice at atmospheric pressure	273.15	K
β'	pressure melting point coefficient	8.7×10^{-4}	$\mathrm{K\,m^{-1}}$
A_0	temperature-independent flow-law coefficient	8.75×10^{-13}	$\mathrm{Pa^{-3}\,s^{-1}}$
n	flow-law exponent	3	-
q_G	geothermal flux	0.07	$\mathrm{W\,m^{-2}}$
Temperature-dependent quantities			
$c(T)$	heat capacity of ice	$7.7929\,T - 13.331$	$\mathrm{J\,kg^{-1}\,K^{-1}}$
$K(T)$	thermal conductivity of ice	$9.085 \times 10^{-5}\,T^2 - 0.053\,T + 10.4204$	$\mathrm{W\,m^{-1}\,K^{-1}}$
Glacier geometry parameters			
θ	glacier surface slope	10.08	degrees
h	glacier thickness	78	m
Spatial and temporal grid parameters			
Δz	spatial resolution	1	m
Δt	temporal resolution	0.1	month
Surface boundary conditions			
	Mean annual temperature	-8.58	°C
	Mean winter temperature	-14.81	°C
	Mean spring temperature	-11.48	°C
	Mean summer temperature	$+3.13$	°C
	Mean fall temperature	-10.16	°C

Table 4.2: Input parameters to the temperature model

The index i refers to the grid node being evaluated, with $i = 1, \ldots, N$, where N is the number of horizontal ice layers. Substituting the discretized derivatives of Equations (4.38) and (4.39) into Equation (4.36), the spatially discretized form of the thermal equation can be written

$$\frac{\partial T_i}{\partial t} = \frac{1}{\rho c(T_i)} \left[K(T_i) \left(\frac{T_{i+1} + T_{i-1} - 2T_i}{\Delta z^2} \right) + \frac{\partial K(T_i)}{\partial T_i} \left(\frac{T_{i+1} - T_i}{\Delta z} \right)^2 + \Phi(T_i) \right], \tag{4.40}$$

where $T_i = T(z_i, t)$, $T_{i+1} = T(z_{i+1}, t)$ and $T_{i-1} = T(z_{i-1}, t)$.

The partial differential equation (PDE) in time and space of Equation (4.36) has been transformed into an ordinary differential equation (ODE) in time. Such an equation can be solved using a simple Matlab ODE solver, when appropriate boundary and inital conditions are specified. However after experimenting with several Matlab ODE solvers, I found that the algorithm becomes unstable or even does not converge at all for glacier slopes steeper than 0.3°. This is indeed problematic since the mean glacier slope used in this model is around 10°. An alternative approach is therefore taken: the temperature equation is discretized in time as well and solved by iterations in both space and time. To this end I express the time derivative in Equation 4.40 using a forward difference scheme:

$$\frac{\partial T(z_i, T_j)}{\partial t} = \frac{T(z_i, t_{j+1}) - T(z_i, t_j)}{\Delta t}, \tag{4.41}$$

where j is the temporal index, varying between 1 and the total number of time steps. With this notation, the temperature at each internal grid node (excluding the surface and bed boundaries and the initial temperature profiles that need to be specified) can be evaluated by iterations using the following relationship:

$$T(z_i, t_{j+1}) = \frac{\Delta t}{\rho c(T_i)} \left[K(T_i) \left(\frac{T_{i+1} + T_{i-1} - 2T_i}{\Delta z^2} \right) + \frac{\partial K(T_i)}{\partial T_i} \left(\frac{T_{i+1} - T_i}{\Delta z} \right)^2 + \Phi(T_i) \right] + T(z_i, t_j). \tag{4.42}$$

Equation (4.42) is the final temperature equation, to be solved by iterations from an initial temperature profile. It is important to note that this type of discretization for the time derivative can prevent numerical convergence in certain conditions. Indeed, the algorithm solving Equation (4.42) by iterations becomes unstable when the quantity

$$r_i = \frac{K(T_i)\, \Delta t}{\rho c(T_i)\, \Delta z^2} \tag{4.43}$$

is greater than 1/2. The maximum timestep for which r_i is smaller than 1/2 and therefore for which the algorithm is stable is determined experimentally to be $\Delta t = 0.1\,\text{month}$. Such a small time step makes the routine slightly more time consuming, but is an acceptable compromise to using a more complex temporal discretization scheme that would be stable for larger timesteps.

Numerical solution

As mentioned above, solving the temperature equation requires the specification of both boundary and initial conditions. The boundary conditions are either a fixed mean annual temperature or varying seasonal temperatures on the surface, and either fixed basal temperature (equal to the pressure melting point) or a fixed temperature gradient (depending on the geothermal flux) at the bed of the glacier. In the case of a fixed temperature gradient basal boundary condition, the temperature at the bed is

$$T_{M,j+1} = T_{M,j} + \frac{\Delta t}{\rho c(T_{M,j})}\left[2K(T_{M,j})\frac{T_{M-1,j} - T_{M,j} - \Delta z\, G}{\Delta z^2} + \frac{\partial K(T_{M,j})}{\partial T}\,\frac{G^2}{\Delta z^2} + \Phi_{M,j}\right], \tag{4.44}$$

where G is a coefficient defined as $G = -q_G/K(T_{M,j})$ and $T_{M,j} = T(z_M, t_j)$ is the temperature at the bed at time t_j. The value $q_G = 70\,\text{mW/m}^2$ is chosen for the geothermal flux. This value lies within the range $65 - 75\,\text{mW/m}^2$ documented for the location of the study glacier in the Alaska insert of the Geothermal Map of North America (AAPG, 2004). In the case of a fixed temperature gradient, the temperature at the bed varies in time and, for this reason, a switch is incorporated in the algorithm that prevents the temperature from rising above the pressure melting point. Such a switch is also in effect at each internal grid node. The pressure melting temperature is calculated using the relationship

$$T_{PMP} = T_0 - \beta' z_i, \tag{4.45}$$

where $T_0 = 275.15\,\text{K}$ is the melting temperature at atmospheric pressure, z_i is the depth within the ice in meters and $\beta' = 8.1 \times 10^{-4}\,\text{K}\,\text{m}^{-1}$ of ice is the pressure melting coefficient (Paterson, 1994).

Numerical solution of the temperature equation also requires an initial temperature-depth profile to be specified. A profile of temperature linearly interpolated between the surface and basal boundary conditions is used to initialize the iteration. Such a profile may not be realistic, especially in the case of varying surface temperature or when the basal temperature is controlled by the geothermal flux. For this reason, the model is first run for 300 years, a period long enough for the temperature profile to reach steady-state. This steady-state temperature profile is then taken as the initial condition. Finally, the algorithm is run for one year to generate mean annual or seasonal temperature profiles.

Strain rate profile and effective temperature

The purpose of the temperature model is to determine effective temperatures over the thickness of the ice. The temperature-depth profiles must therefore be averaged to obtain a value of temperature representative of the whole ice layer. In doing so, it is worth keeping in mind that the effective temperature is to be used to choose an effective flow-law coefficient. This effective flow-law coefficient will in turn be used to calculate the creep velocity for the forward model of the inversion. Therefore it is important to note that not all ice layers contribute equally to the deformational velocity. Indeed, each ice layer is advected on the layer situated beneath it, so that its creep velocity depends on the deformation rate of the lower layers. The deformational velocity is thus controlled by the deformation rate, or strain rate of the ice. As a consequence, the distribution of strain rate with depth must be considered when calculating an effective temperature. The effective temperature is therefore calculated as a weighted average with depth of the temperature profile, with weights depending on the strain rate. The shear strain rate of an inclined slab glacier is defined by

$$\dot{\epsilon}_i = A_0 \exp\left(-\frac{Q}{RT_i}\right) [\rho g z_i \sin\theta]^n , \tag{4.46}$$

where z_i is the distance from the bed at which the strain rate is evaluated ($z = 0$ at the bed and $z = h$ at the surface). The strain rate is a function of depth and is evaluated at the same spatial resolution as the calculated temperature profile. The strain rate profile is then scaled to 1 so that its values can be used as weights. The effective temperature is finally computed as a weighted average of the temperature profile, with the scaled strain rate used as a weighting coefficient for each layer of ice.

4.3 Results

In this section, results of the temperature model as well as results from the geophysical inversion are presented. The first section deals with the temperature profiles and derived effective temperatures. The three subsequent sections present control tests of the inversion and results from the geophysical inversion of the four datasets using the two methods presented above. The last section explores the sensitivity of the inversion routine to three model parameters.

4.3.1 Temperature profiles

The temperature profiles obtained using the four sets of boundary conditions described in section 4.2.5 differ widely. The first two consider a bed at the pressure melting point at all times, while the last two consider a frozen bed with a temperature controlled by the geothermal flux.

Temperature at the base of the glacier is controlled by geothermal heat and friction. Glaciers are divided into three main categories according to their thermal regime. Paterson (1994) defines these categories as (1) cold, when all the ice is below the melting point, (2) temperate, when all the ice is at the pressure melting point, except for a 10-20 m surface layer subject to seasonal temperature variations, and (3) polythermal, when both cold and temperate ice is present. For example, some polythermal glaciers have a basal layer of ice at the pressure melting point while the rest of the glacier is below freezing. Some glaciers may exhibit several thermal regimes at once. For example the bed may be frozen in some areas and at the pressure melting point in others.

Most glaciers located south of the arctic circle are thought to be either polythermal or temperate over most of their area (Paterson, 1994), although they may be frozen at the bed in some places. The relatively high surface velocities observed on the study glacier suggest that there may be a substantial amount of sliding and thus, that melting may be taking place at the bed.

Model 1: Mean annual temperature at the surface and pressure melting point at the base

For the first profile, shown in Figure 4.8, temperature is held constant at the mean annual temperature of $-8.5°\mathrm{C}$ at the surface. Temperature is also held constant at the pressure melting point of $-0.068°\mathrm{C}$ at the bed. Note that the temperature-depth profiles generated here are assumed to be representative of the whole glacier, and thus the averaged ice thickness along the glacier flowline is used to calculate the pressure melting point. Since both surface and bed temperatures are held constant over the length of the simulation and because heat sources are negligible, the steady-state profile is identical to the initial condition.

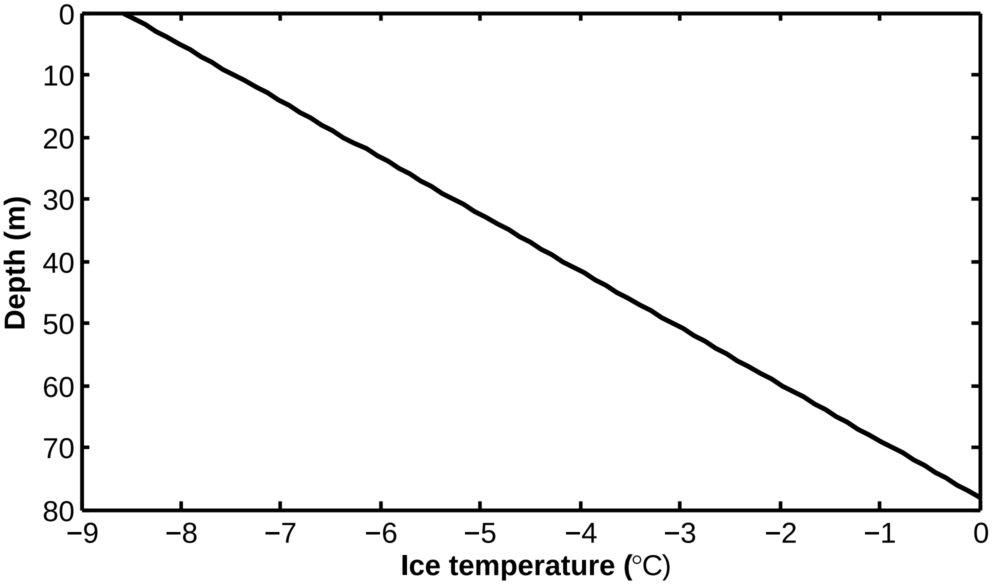

Figure 4.8: Temperature profile derived from Model 1. Ice temperature in degrees Celsius is plotted as a function of depth. The total depth of the glacier is 78 m. Temperature is maintained constant at the mean annual temperature at the surface and at the pressure melting point at the bed.

Model 2: Seasonal variations of temperature at the surface and pressure melting point at the base

In the second profile, the bed temperature is again fixed at the pressure melting point, while the surface temperature is allowed to vary seasonally. This temperature forcing applied to the surface is extracted from surface temperature measurements. Data acquisition methods, data processing and the final surface temperature dataset are presented in Chapter 2. Temperatures for the surface boundary condition vary linearly from −14°C in winter, to −12°C in the spring, +3°C in summer and −10°C in the fall. Although the average surface temperature in summer is positive, the value of 0°C is used in the model since the temperature of ice cannot rise above this limit without the ice melting (positive surface temperatures are recorded because temperature is measured at 2 m height above the surface). In this simulation, we extracted four profiles corresponding to the four seasons, winter ranging from January to March, spring from April to June, summer from July to September and fall from October to December. These four profiles are presented in Figure 4.9. The profiles clearly show that a layer of ice about 20 m thick is subject to seasonal temperature variations. When considering one particular season, we can see that the surface temperature of the previous season (whether warmer or cooler than the season considered) is propagated deeper in the ice, resulting in a hook-like feature in the temperature profile. This effect is mostly visible in the summer and fall profiles.

Model 3: Mean annual temperature at the surface and geothermal flux at the base

The third profile, shown in Figure 4.10, features the same surface boundary condition as the first profile, in other words, surface temperature is maintained constant at the mean annual value of −8.5°C. The treatment of the bottom boundary condition, however, differs from the two previous profiles. Instead of considering a fixed basal temperature (Dirichlet condition), we consider a fixed temperature gradient at the bed (Neumann condition). The temperature of the lower ice layer is obtained using the relationship in Equation (4.44). This type of boundary condition presupposes a frozen bed. The initial temperature of the bed must still be specified, and the value of −1°C is chosen. Because a-priori knowledge of the glacier hints at a melting bed, this value close to the pressure melting point seems appropriate. Unlike the first profile, this third profile changes substantially during the 300 year period used to reach steady-state. The balance between the geothermal heat at the bed and the cold temperature forcing at the surface causes the bed temperature to slide from its original value of −1°C to around −6.5°C over a period of about 200 years.

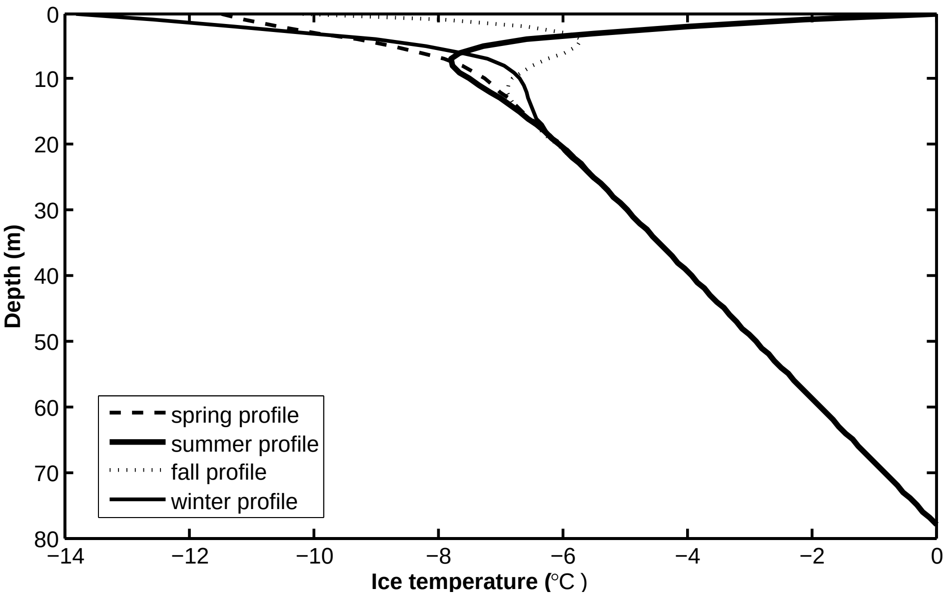

Figure 4.9: Temperature profile derived from Model 2. Ice temperature in degrees Celsius is plotted as a function of depth. Surface temperature is allowed to vary seasonally between −14°C in winter and 0°C in summer. The bed temperature is held constant at the pressure melting point. After the ice below the seasonal layer reaches steady-state, the simulation is run for a period of one year to generate four seasonal profiles.

Model 4: Seasonal variations of temperature at the surface and geothermal flux at the base

In the fourth and last profile, temperature at the surface is allowed to vary seasonally as described in the second profile and the bed boundary condition is coded by specifying a temperature gradient in the same fashion as for the third profile. The bed temperature drops from −1°C to −6°C during the 300 year period to reach steady-state. Near the surface, the same features as in the second profile are observed. The Model 4 profile is presented in Figure 4.11.

Strain rate profile and effective temperatures

For each of the four profiles, a strain rate profile is computed using the relationship of Equation 4.46 and then scaled to 1. A typical scaled strain rate profile is shown in Figure 4.12.

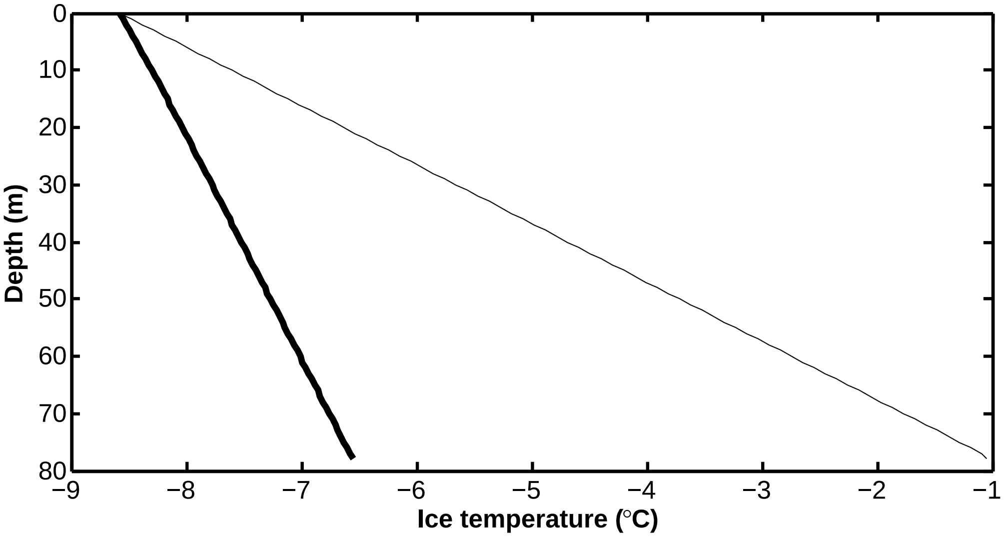

Figure 4.10: Temperature profile derived from Model 3. Ice temperature in degrees Celsius as a function of depth. Temperature is maintained constant at the mean annual temperature at the surface and temperature gradient is specified as a function of the geothermal flux at the bed. The thin line represents the arbitrary starting profile and the thick line is the final steady-state profile. The bed temperature decreases gradually over a 300 year period to reach steady-state.

The strain rate is highest near the bed and close to zero near the surface, indicating that the amount of ice deformation is greater in the basal layers. Depth-integrated effective temperatures are calculated from each temperature profile, and for each season (for the profiles featuring several seasons) using the method presented above. The resulting effective temperatures are presented in Table 4.3.

The effective temperatures resulting from temperature models 1 and 2 are much higher than effective temperatures resulting from temperature models 3 and 4. This effect has already been observed on the temperature profiles and results from the fact that the bed is allowed to freeze with this type of boundary condition, while it is kept at the pressure melting point with the Dirichlet-type condition.

In addition, the effective temperatures obtained using the mean annual temperature at the surface (temperature models 1 and 3) are slightly lower than the temperatures obtained using a seasonal forcing on the surface (temperature models 2 and 4). This is true for

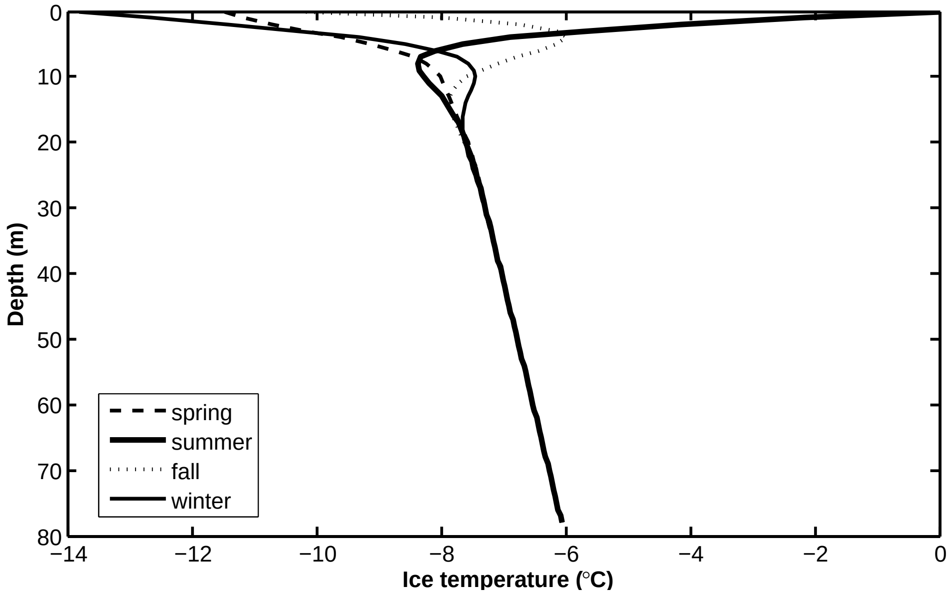

Figure 4.11: Temperature profile derived from Model 4. Ice temperature in degrees Celsius is plotted as a function of depth. Surface temperature is allowed to vary seasonally between −14°C in winter and 0°C in summer. The bed temperature is controlled by a temperature gradient at the bed. After the ice below the seasonal layer reaches steady-state, the simulation is run for a period of one year to generate four seasonal profiles.

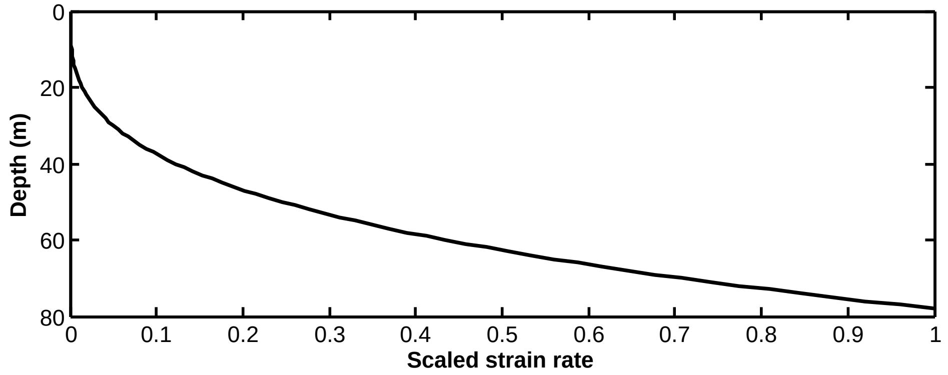

Figure 4.12: Relative strain rate as a function of depth

both basal boundary conditions. This difference results from the fact that the mean annual temperature used in temperature models 1 and 3 is lower than the average of the seasonal temperatures used in models 2 and 4 (−8.58°C versus −8.33°C). The reason for this is that the period used to calculate the mean annual temperature is longer and differently centered than the four seasonal periods. Also, for the Neumann-type boundary condition in models 3 and 4, the steady-state temperature reached at the bed is about a half degree lower for the mean annual surface temperature than for the seasonal forcing, yielding slightly different strain rate profiles; because the strain rate is more important near the bed, the effective temperature is affected.

In regard of these results and because a melting bed is a plausible scenario, I choose to adopt an effective temperature of −2°C as a reference model and to use a flow-law coefficient of $2.4 \times 10^{-24}\,\mathrm{s}^{-1}\mathrm{Pa}^{-3}$ in the inversion, as this is the value corresponding to a temperature of −2°C as advocated by Paterson (1994). The possibility that the bed is frozen is explored in the sensitivity tests by using a flow-law coefficient corresponding to lower effective temperatures.

Temperature model	**Period**	**Effective temperature**
Model 1	Annual	−1.89°C
Model 2	Winter	−1.74°C
	Spring	−1.74°C
	Summer	−1.74°C
	Fall	−1.74°C
Model 3	Annual	−6.96°C
Model 4	Winter	−6.46°C
	Spring	−6.46°C
	Summer	−6.46°C
	Fall	−6.46°C

Table 4.3: Effective temperatures

4.3.2 Control tests of the inversion

The methods used for the geophysical inversion (including the inversion algorithm) of the surface velocities are described in sections 4.2.2, 4.2.3 and 4.2.4. In order to verify that the algorithm works properly and to validate the inversion methods, we perform control tests of the inversion algorithm. In a successful control test, a synthetic basal velocity profile would be recovered accurately by the inversion procedure. The main steps of the control test routine are the following:

1. a synthetic basal velocity profile (or synthetic model) is chosen,
2. the synthetic basal velocity profile is used as input to the forward model to generate a set of synthetic surface velocities,
3. the set of synthetic velocities is perturbed by adding a small random component of "noise" having a mean value of 1% of the mean surface velocity,
4. the perturbed dataset is computed from the perturbed synthetic surface velocities using the relationship in Equation (4.10),
5. the perturbed synthetic data is run through the inversion algorithm and a recovered basal velocity profile is extracted,
6. the basal velocity profile resulting from the inversion is again run through the forward model to generate a set of predicted surface velocities.

Comparing the synthetic and recovered models, as well as the synthetic and predicted data, is a helpful tool to assess the quality of the algorithm and inversion method. Both deterministic and spectral inversion methods are tested. Each method is tested using two different basal velocity profiles and three glacier geometries, leading to six control tests for each method:

- Test 1: Slab-like glacier and sinusoidal basal velocity profile,
- Test 2: Slab-like glacier and rectangular basal velocity profile,
- Test 3: Wedge-shaped glacier and sinusoidal basal velocity profile,
- Test 4: Wedge-shaped glacier and rectangular basal velocity profile,
- Test 5: Real glacier geometry and sinusoidal basal velocity profile,

- Test 6: Real glacier geometry and rectangular basal velocity profile.

Parameters for the sinusoidal and rectangular velocity profiles and for the three glacier geometries are presented in Table 4.4.

Two separate geophysical inversion methods are presented in Section 4.2.3 and 4.2.4.

Parameter	**TEST 1**	**TEST 2**	**TEST 3**
Synthetic glacier geometry	slab	slab	wedge
Ice thickness type	constant	constant	variable
Ice thickness (m)	100	100	10 to 200
Slope type	constant	constant	constant
Slope (°)	5	5	2.54
Shape factor	1	1	1
Synthetic model	sinusoidal	rectangular	sinusoidal
Minimum basal velocity (m/yr)	0	4.0	0
Maximum basal velocity (m/yr)	2.0	4.8	2.0
Wavelength of basal velocity (m)	3000	–	3000
Step location along flowline (m)	–	2250	–
	TEST 4	**TEST 5**	**TEST 6**
Synthetic glacier geometry	wedge	real	real
Ice thickness type	variable	variable	variable
Ice thickness (m)	10 to 200	78*	78*
Slope type	constant	variable	variable
Slope (°)	2.54	10.08*	10.08*
Shape factor	1	0.96*	0.96*
Synthetic model	rectangular	sinusoidal	rectangular
Minimum basal velocity (m/yr)	4.0	0	4.0
Maximum basal velocity (m/yr)	4.8	2.0	4.8
Wavelength of basal velocity (m)	–	3000	–
Step location along flowline (m)	2250	–	2250

Table 4.4: Glacier geometry and synthetic model parameters for the inversion control tests. Values for the real glacier geometry, followed by an asterisk, are averages. The thickness and slope profiles used for the real glacier geometry are presented in Figure 3.34. All shape factors are calculated for semi-elliptical beds.

In order to assess the quality of each of the two methods, the six tests presented above are performed for each method. Inversion using both methods can be carried out with or without a reference model. Both cases are tested for each method, leading to four sets of control tests, each featuring six individual tests. The results of these 24 tests are presented below.

Using a deterministic approach with a reference model

The methodology of employing a deterministic approach is detailed in section 4.2.3. Results of the six tests described above, performed with this method and using a reference model, are presented in Figure 4.13. In the case when a deterministic method and a reference model are used, as for all of the 12 tests featuring a reference model, the synthetic basal velocity profile, or synthetic model is taken as the reference model.

While the perturbed surface velocities are almost perfectly predicted in the six tests, the basal velocity profile is less well recovered. In the case of a sinusoidal synthetic model (tests 1, 3 and 5), the basal velocities are well recovered for low corresponding surface velocities, but as the amplitude between minimum and maximum surface velocity increases, the recovered model shows unrealistic oscillations. Thus the synthetic basal velocity profile is well recovered in test 1, but only the principal trend of the model is recovered in tests 3 and 5. In the case of a rectangular synthetic velocity profile, the quality of the inversion is even lower, and oscillations of large amplitude are observed (tests 2, 4 and 6). In test 6, the synthetic basal velocity seems to be recovered better than in tests 2 and 4. This might result from the fact that the rectangular step is substantially higher than in the two other tests.

Using a spectral approach with a reference model

Results of the control tests performed using the spectral approach described in section 4.2.4 are presented in Figure 4.14. Here again, the synthetic basal velocity profile is taken as the reference model. The spectral method appears to perform better than the deterministic approach in recovering the synthetic basal velocities. Not only are the synthetic data matched closely, but the synthetic model is also recovered fairly well. In the case of test 1, the model is recovered so well that the recovered and synthetic model curves are superimposed in Figure 4.14a. In tests 2, 4 and 6, the rectangular basal velocity profile is less well reproduced than in tests 1, 3 and 5, and the solution oscillates slightly, although the oscillations are far less significant than those observed in control tests using the deterministic approach. This oscillation effect is likely due to the fact that the algorithm solves for the smoothest model.

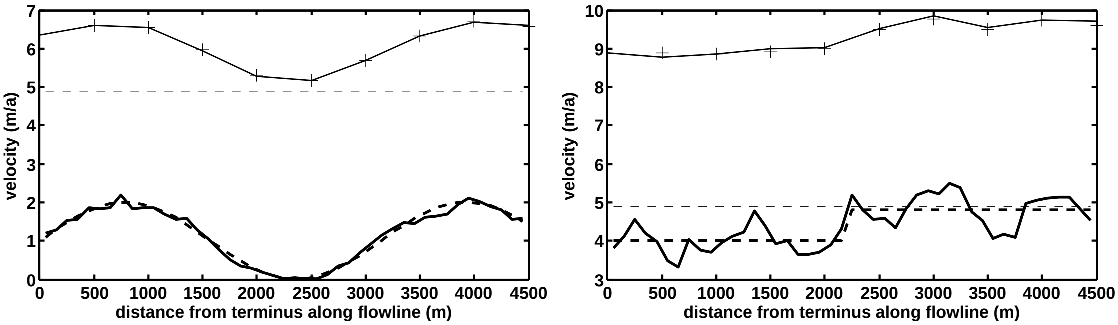

(a) Test1: slab geometry/sinusoidal basal velocity (b) Test2: slab geometry/step basal velocity

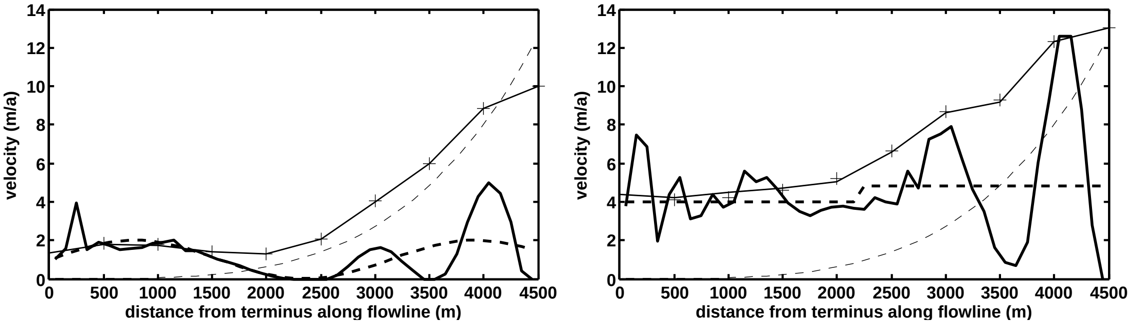

(c) Test3: wedge geometry/sinusoidal basal velocity (d) Test4: wedge geometry/step basal velocity

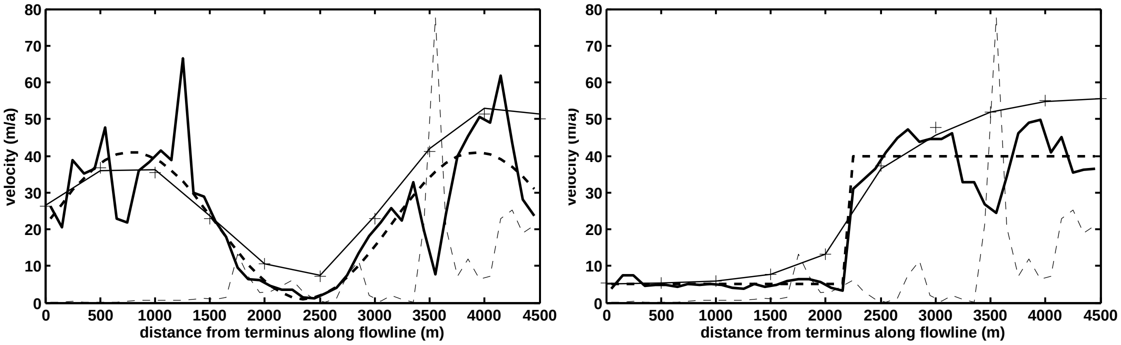

(e) Test5: real geometry/sinusoidal basal velocity (f) Test6: real geometry/step basal velocity

Figure 4.13: Control test results using a deterministic approach and a reference model. For each of the six tests (a) to (f), ice velocity is plotted against the distance from the glacier terminus along the flowline. The thick dashed line and the thick full line are respectively the synthetic and recovered basal velocity profiles. The crosses are the synthetic perturbed velocities, the thin full line is the predicted velocity profile and the thin dashed line represents the deformational velocity.

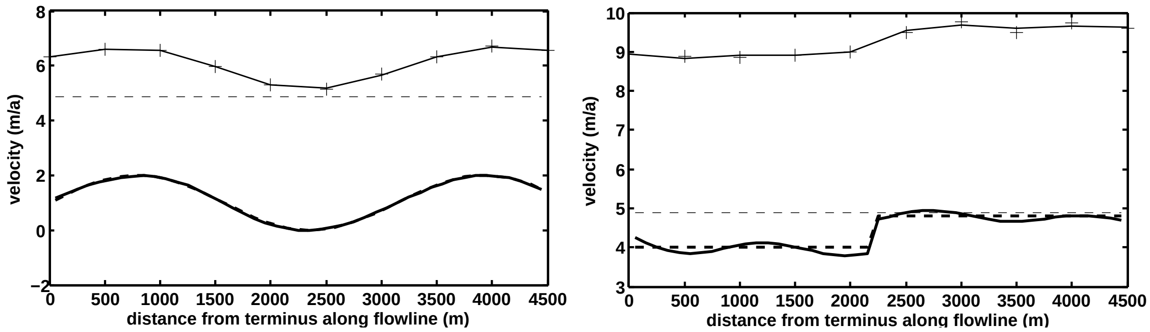

(a) Test1: slab geometry/sinusoidal basal velocity

(b) Test2: slab geometry/step basal velocity

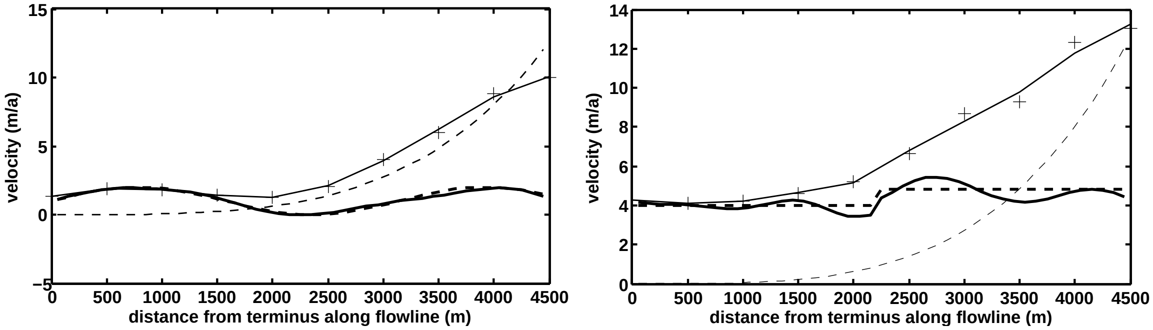

(c) Test3: wedge geometry/sinusoidal basal velocity

(d) Test4: wedge geometry/step basal velocity

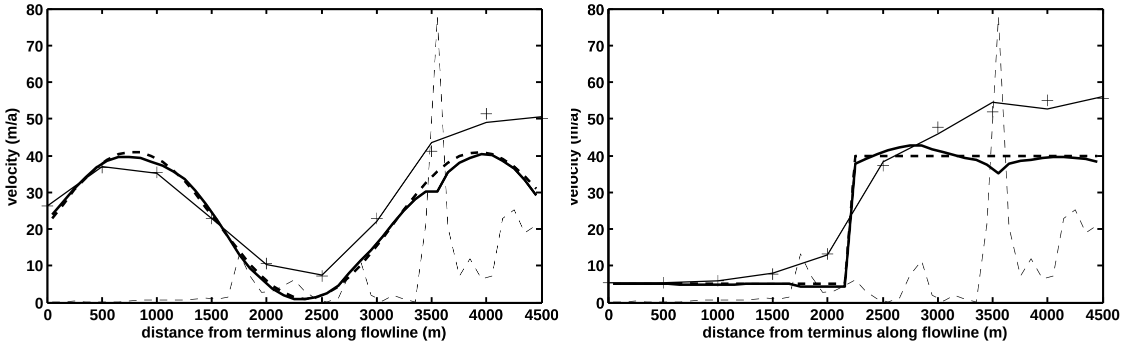

(e) Test5: real geometry/sinusoidal basal velocity

(f) Test6: real geometry/step basal velocity

Figure 4.14: Control test results using a spectral approach and a reference model. For each of the six tests (a) to (f), ice velocity is plotted against the distance from the glacier terminus along the flowline. The thick dashed line and the thick full line are respectively the synthetic and recovered basal velocity profiles. The crosses are the synthetic perturbed velocities, the thin full line is the predicted velocity profile and the thin dashed line represents the deformational velocity.

Step functions cannot be reproduced by smoothest models, and therefore the oscillations are not a shortcoming of the spectral method.

Inversion without a reference model

Results from inversion control tests performed without a reference model are shown in Figure 4.15 for the deterministic approach and in Figure 4.16 for the spectral approach. Omitting a reference model amounts to setting $\mathrm{m}_{\mathrm{ref}} = 0$. Removing the reference model reduces the constraints on the solution.

As can be observed in Figure 4.15 and 4.16, the recovered basal velocity profile shows far more instability than in the previous cases when a reference model was used. The synthetic model seems to be reproduced fairly well in one case only (test 1 in both Figure 4.15 and Figure 4.16), but the solution is erratic in all other tests. Although it can be argued that the trend of the oscillations follows the pattern of the synthetic velocity profile, these control tests show that the inversion is simply not successful using either the deterministic or spectral inversion method without a reference model (except for test 1).

Influence of noise

An additional test is conducted to examine the influence of variable amounts of noise on the inversion. This test is conducted for a slab-like glacier with a sinusoidal synthetic basal velocity profile (test 1) using the spectral decomposition method and a reference model. Synthetic surface velocity data generated from the synthetic model are perturbed with noise amouting to 2%, 5%, 10% and 20% of the mean synthetic surface velocity and then inverted. The result of the same test performed with the default noise of 1% of the mean surface data is shown in Figure 4.14a. The results of the elevated noise test, presented in Figure 4.17, show the reduction in accuracy of the recovered model with increasing noise. Qualitative inspection of the plots indicates that the main pattern of the synthetic model is recovered for up to 20% noise, though substantial oscillations arise with this noise level. These results are discussed in Section 4.4.

Concluding remarks on the control tests

It is important to keep in mind that the same amount of noise (1% of the mean surface velocity) has been used to perturb the data in all four sets of control tests. This considered,

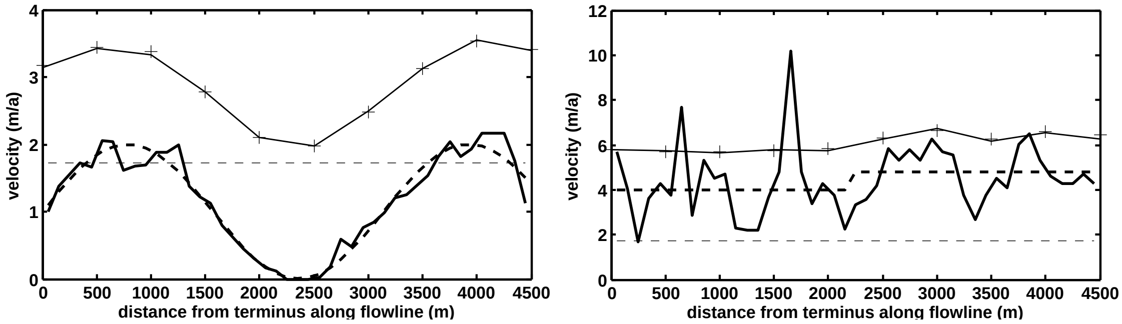

(a) Test1: slab geometry/sinusoidal basal velocity (b) Test2: slab geometry/step basal velocity

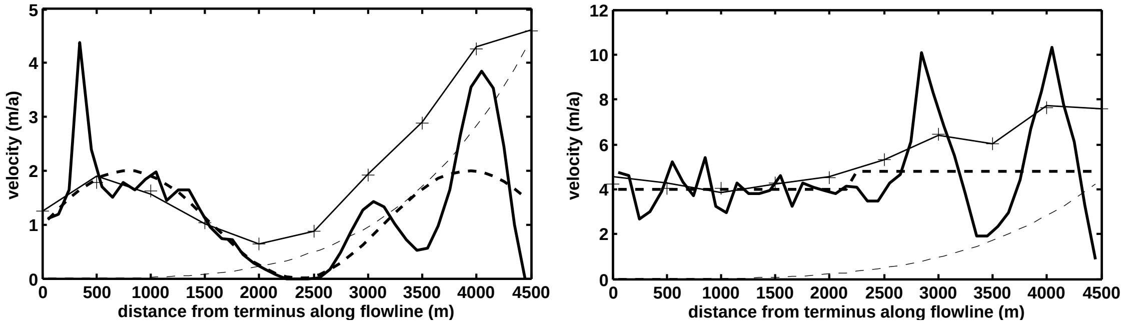

(c) Test3:wedge geometry/sinusoidal basal velocity (d) Test4: wedge geometry/step basal velocity

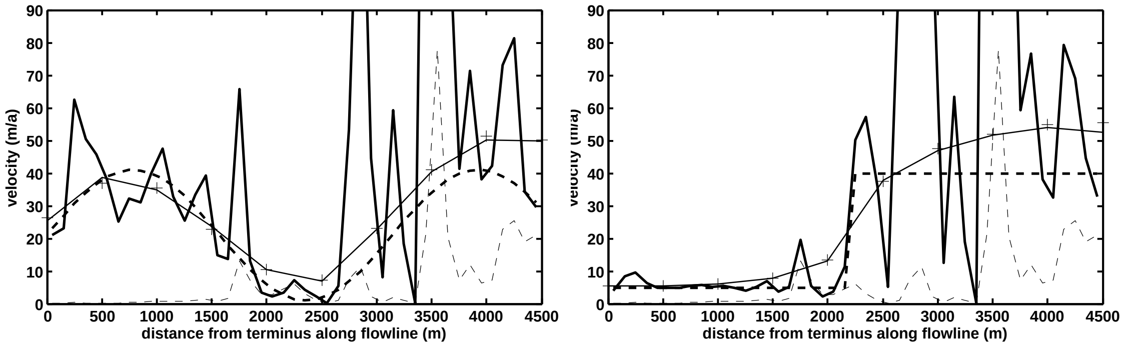

(e) Test5: real geometry/sinusoidal basal velocity (f) Test6: real geometry/step basal velocity

Figure 4.15: Control test results using a deterministic approach without a reference model. For each of the six tests (a) to (f), ice velocity is plotted against the distance from the glacier terminus along the flowline. The thick dashed line and the thick full line are respectively the synthetic and recovered basal velocity profiles. The crosses are the synthetic perturbed velocities, the thin full line is the predicted velocity profile and the thin dashed line represents the deformational velocity.

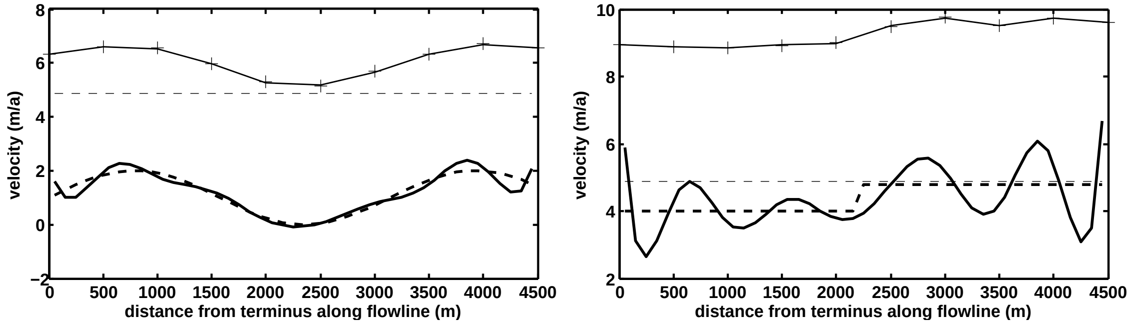

(a) Test1: slab geometry/sinusoidal basal velocity (b) Test2: slab geometry/step basal velocity

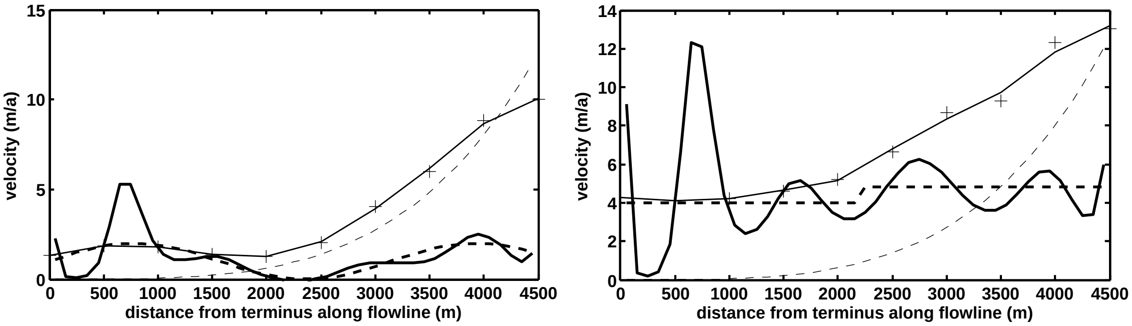

(c) Test3: wedge geometry/sinusoidal basal velocity (d) Test4: wedge geometry/step basal velocity

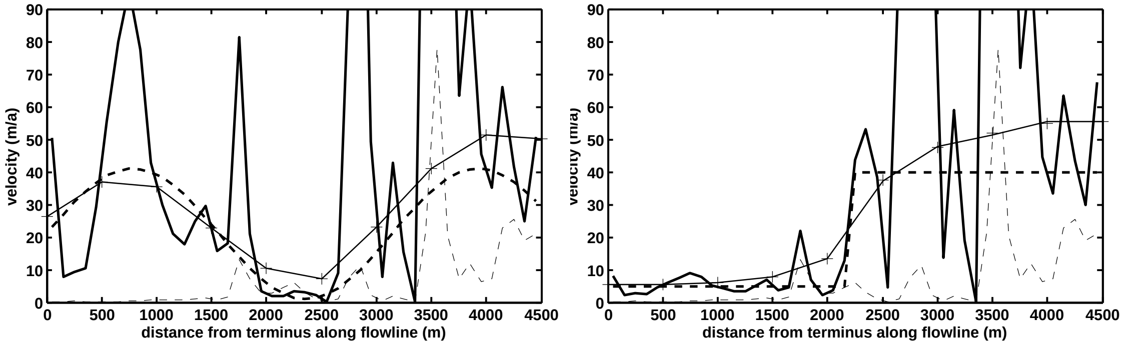

(e) Test5: real geometry/sinusoidal basal velocity (f) Test6: real geometry/step basal velocity

Figure 4.16: Control test results using a spectral approach without a reference model. For each of the six tests (a) to (f), ice velocity is plotted against the distance from the glacier terminus along the flowline. The thick dashed line and the thick full line are respectively the synthetic and recovered basal velocity profiles. The crosses are the synthetic perturbed velocities, the thin full line is the predicted velocity profile and the thin dashed line represents the deformational velocity.

arbitrary basal velocity models are not necessarily physically consistent with the glacier geometry or the method of inversion. For example, the step in the rectangular basal velocity model cannot be recovered properly by inverting for a smoothest model. This can be seen in the results of tests 2, 4 and 6, where the basal velocity is not reproduced accurately with any of the four methods presented. Moreover, methods of inversion are not equivalent in quality. As mentioned above, both deterministic and spectral methods trigger spatial oscillations in the recovered model when used without a reference model. It thus appears that using a reference model suppresses unrealistic structure. A reference model is therefore used in all subsequent experiments. In addition, visual assessment of the results of control tests using the spectral method shows that these are more successful than control tests using the deterministic method. Although inversions of real data are performed with both methods, spectral decomposition inversion which also has the advantage of being computationally more efficient, is judged to be a better method for this application. The results of the control tests are discussed further in Section 4.4.

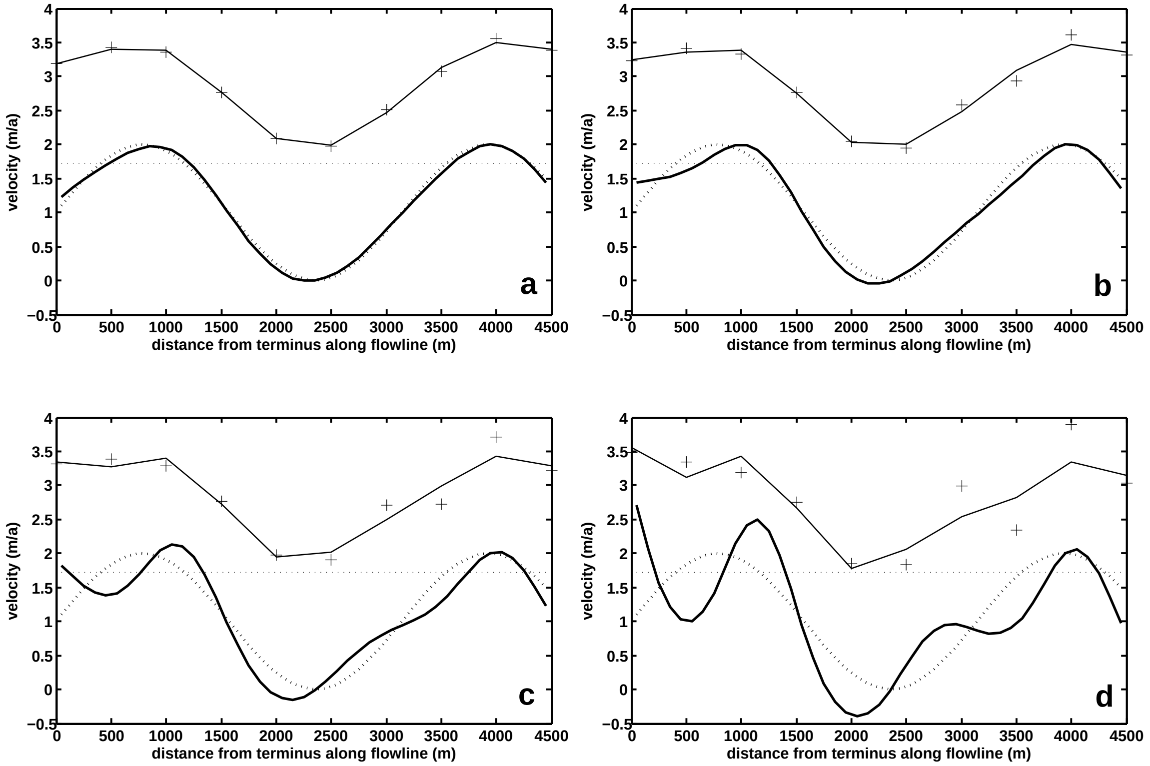

Figure 4.17: Control test results using variable amounts of noise. Control test is run for a slab-like glacier with a sinusoidal synthetic basal velocity profile (test 1) and using the spectral decomposition method and a reference model. Noise accounts for (a) 2%, (b) 5%, (c) 10% and (d) 20% of the mean synthetic surface velocity. For each of the four profiles, ice velocity is represented as a function of the distance from the glacier terminus along the flowline. The thick dashed line and the thick full line are respectively the synthetic and recovered basal velocity profiles. The crosses are the synthetic perturbed velocities, the thin full line is the predicted velocity profile and the thin dashed line represents the deformational velocity

4.3.3 Inversion of real data

The inversion algorithms for both deterministic and spectral approaches have been evaluated by control tests. We can now proceed to inverting real surface velocity data to obtain basal velocity profiles. A reference model is used, since the control tests have shown that results greatly deteriorate when no reference model is used and that using a realistic reference model helps in suppressing unrealistic model structure. The algorithm thus attempts to minimize the difference between the computed model and a reference model, taken as the difference between measured surface velocity and calculated deformational velocity, with the simple assumption that creep and basal motion sum to the local observed surface velocity (Kamb and Echelmeyer (1986) have shown that it is not in fact true, as we saw in the beginning of this chapter). This reference model is chosen because it results from a simplified calculation of the basal velocity profile and is thus expected to show some similarity to the real basal velocity profile.

Input data for the inversion are presented in Section 4.1. Using the local slope, ice thickness and shape factor profiles, presented in Figure 3.34, and following Equation 4.2, the deformational velocity is calculated. The slope and ice thickness, along with the resulting creep velocity are presented in Figure 4.18. The four sets of surface velocities are presented in Chapter 2 and again in Figure 4.2 in section 4.1.

An inversion is run for each of the four datasets, corresponding to four periods: summer 2006 (dataset 1), summer 2007 (dataset 2), year 2006-2007 (dataset 3) and year 2007-2008 (dataset 4). The main steps of the inversion procedure, similar to those outlined for the control tests, are the following:

1. A set of surface velocities (dataset 1, 2, 3 or 4) is chosen
2. the data are computed from the measured surface velocities using the relationship of Equation 4.10,
3. the data are run through the inversion algorithm and a recovered basal velocity profile is extracted,
4. the basal velocity profile resulting from the inversion is again run through the forward model to generate a set of predicted surface velocities.

Table 4.5 presents constants and parameters used in both inversion methods.

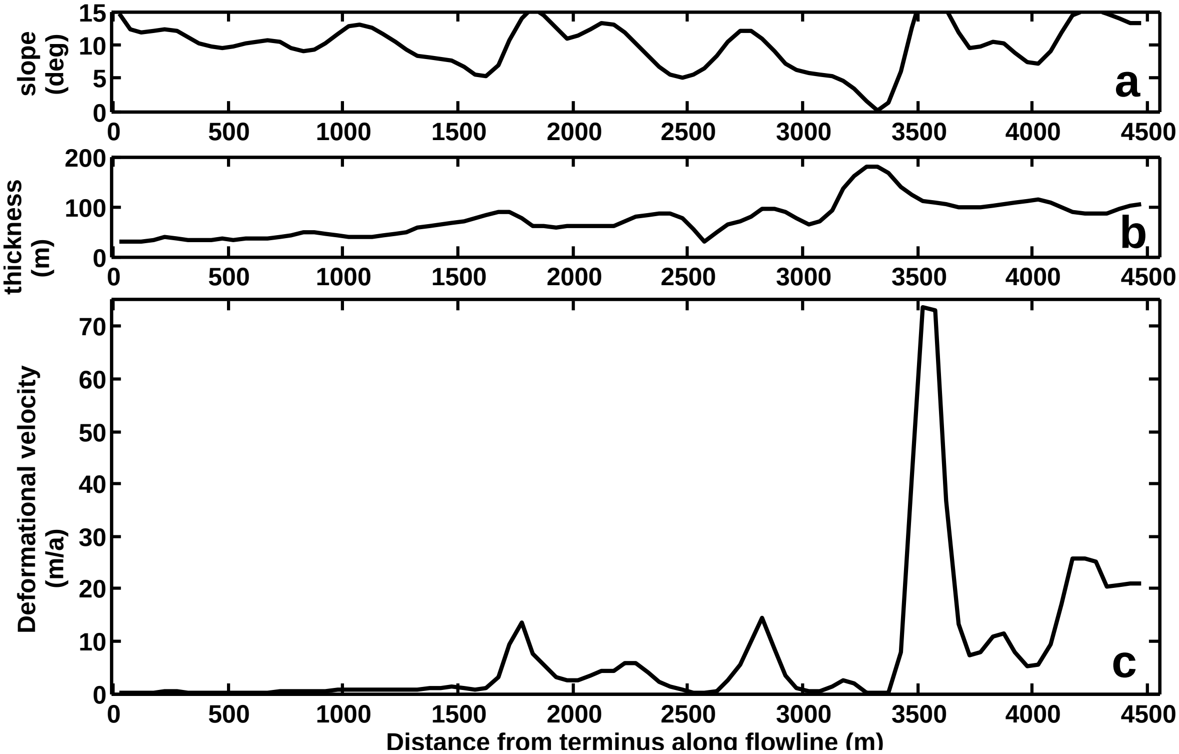

Figure 4.18: Input data for inversion. (a) Surface slope, (b) ice thicknesses and (c) calculated deformational velocity. All quantities are flowline profiles plotted as a function of distance from glacier terminus along the flowline.

Symbol	Name	Value	Units
ρ	ice density	917	$\mathrm{kg\,m^{-3}}$
g	gravitational acceleration	9.81	$\mathrm{m\,s^{-2}}$
n	flow-law exponent	3	–
A	flow-law coefficient	2.24×10^{-24}	$\mathrm{Pa^{-3}\,s^{-1}}$
dx	model grid spacing	50	m
L	length of flowline	4500	m
l	longitudinal averaging length	$3\,\mathrm{h}$	m

Table 4.5: Constants and parameters used in the inversion of real data for both deterministic and spectral methods.

Deterministic approach

We start with the deterministic approach, inverting the full matrix system and using Tikhonov regularisation. Details pertaining to this method are presented in section 4.2.3. Parameters and numerical results specific to this method are outlined in Table 4.6 and graphical results, for each of the four datasets considered, are shown in Figure 4.19 and 4.20.

	Summer 06	**Summer 07**	**Annual 06-07**	**Annual 07-08**
Number of data N	11	11	8	11
Size of model M	80	90	56	84
Full inversion (or deterministic) method				
Original range for β	10^{-25} to 10^{+25} with increments of 10^4			
Tolerance	0.1 (about 1% of N)			
β^*	2.035×10^{10}	9.970×10^{11}	2.076×10^{-2}	5.111×10^9
Misfit Φ^*	10.92	10.94	8.05	10.96
Spectral decomposition inversion method				
Number of p	11	11	8	11
J	6	3	8	10
Misfit Φ^*	10.31	2.15	0	2.07

Table 4.6: Parameters and numerical results of the inversion of real data using both deterministic and spectral methods. β is the Tikhonov regularisation parameter and β^* the specific value chosen for the inversion. J is the number of singular values p kept after truncation.

Spectral decomposition method

Inversion of the same four datasets using the spectral decomposition method, also called singular value decomposition, is then performed. Details pertaining to this method are presented in Section 4.2.4. Since control tests have shown that this method appears more reliable than the deterministic inversion method, I emphasize the results of this method by presenting them in more detail.

For each dataset considered, two figures are presented. The first figure consists of three plots, representing the misfit and the model norm as a function of the rank of singular values and the misfit as a function of the model norm. Note that I use the word rank here to refer to the index of a specific singular value p in the progression of singular values (first, second,

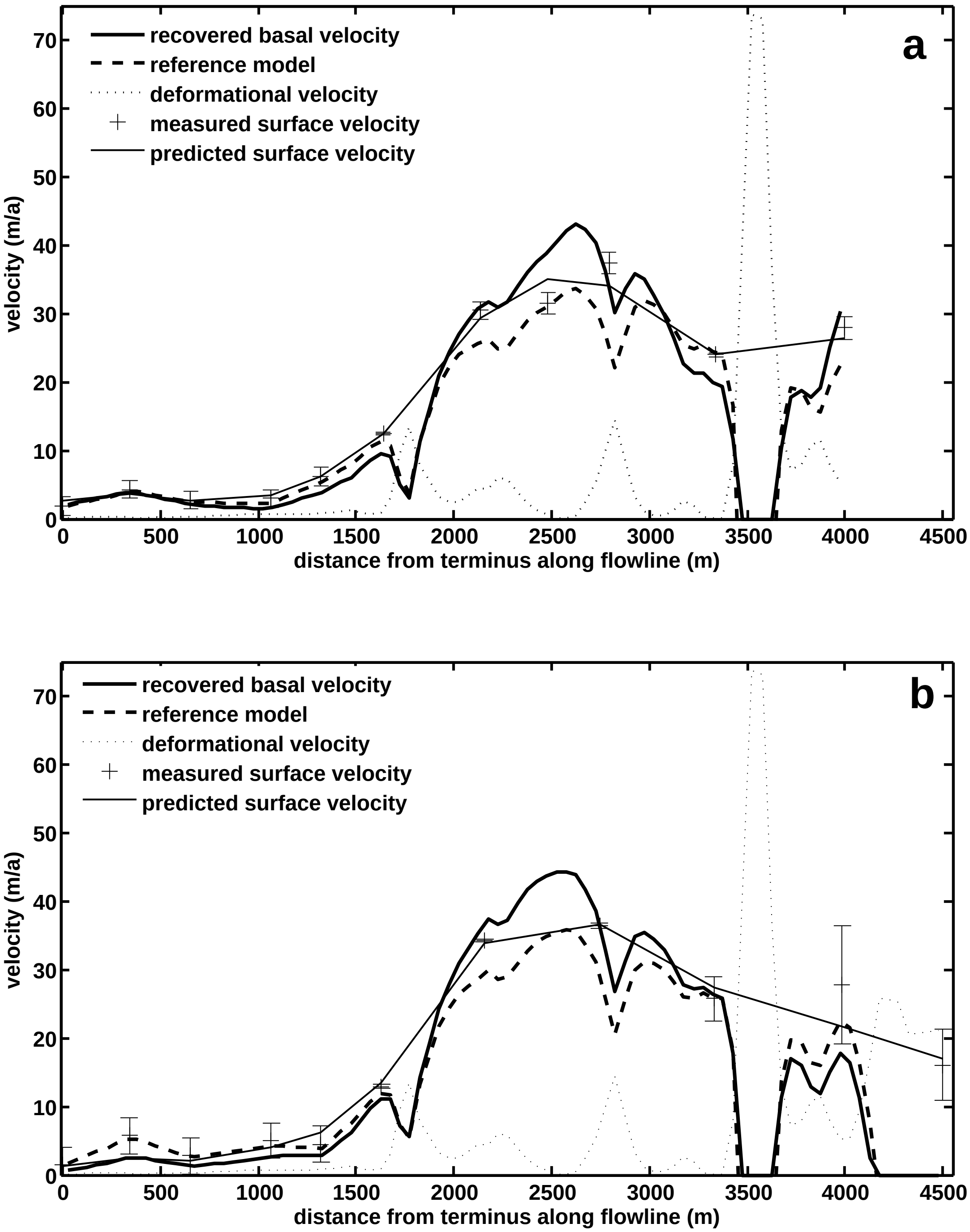

Figure 4.19: Results of the inversion of real data using a deterministic approach. (a) Summer 2006 dataset and (b) summer 2007 dataset. Ice velocities are expressed as a function of distance from the glacier terminus along the flowline.

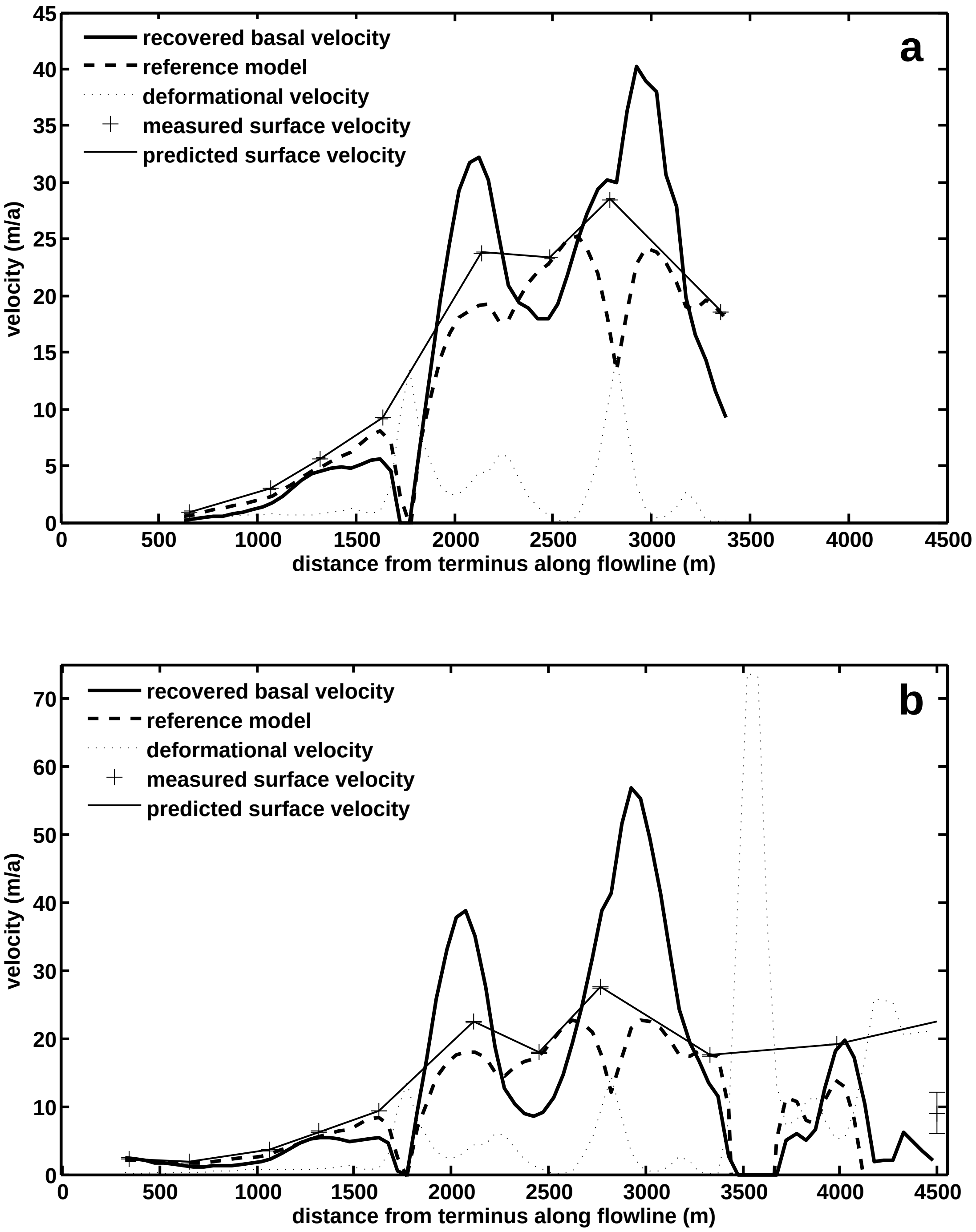

Figure 4.20: Results of the inversion of real data using a deterministic approach. (a) 2006-2007 annual dataset and (b) 2007-2008 annual dataset. Ice velocities are expressed as a function of distance from the glacier terminus along the flowline.

third, ...). In the second figure, a plot of ice velocities (surface, basal and creep velocities) as a function of distance along the flowline is presented at the top, and a plot of the variation of the contribution of basal motion, or slip ratio, is shown at the bottom. The contribution of basal motion is defined as

$$P = 100\,\frac{v_b}{v_b + v_c}, \tag{4.47}$$

and expressed as a percentage of the total motion. Numerical results, including the number of singular values J kept after truncation of the decomposition (J can be seen as a sort of regularisation parameter) and the corresponding misfit, are presented in Table 4.6. Results from inversion of the four datasets using both spectral and deterministic methods are summarized in Appendix C.

Datasets 1 and 2: summer 2006 and summer 2007: Graphical results are presented in Figures 4.21 and 4.22 for the summer 2006 dataset and in Figures 4.21 and 4.23 for the summer 2007 dataset. The results for these datasets are very similar and the description below applies to both datasets. In Figures 4.22a and 4.23a, various ice velocities are plotted as a function of distance from the glacier terminus along the flowline. The measured surface velocity, represented as crosses along with errorbars, varies between 0 and about 15 m/a over the lower 1500 m of the glacier. These values are relatively low compared to the 20 to 40 m/a recorded over the upper 3000 m of the glacier. The recovered basal velocity is close to the reference model and follows the pattern of the surface velocity: it is relatively low over the lower 1500 m of the glacier and much higher over the upper reaches of the glacier. The predicted surface velocity is computed by running the basal velocity profile through the forward model. Although it is represented by a continuous line in Figures 4.22a and 4.23a, the predicted surface velocity is defined in the data space, at the same locations as the measured surface velocity along the flowline. The predicted surface velocity is plotted as a continuous line to avoid confusion with the measured surface velocity but should not be interpreted as a continuous profile. Figure 4.22a and 4.23a show that the predicted surface velocity falls within the range of error of the measured surface velocity for all locations (except the last pole location for the summer 2006 dataset), indicating that the basal velocity profile resulting from the inversion is consistent with the measured surface velocity. Figures 4.22b and 4.23b show that basal motion accounts for 60 to 90% of the total motion of the glacier over most of its length.

Datasets 3 and 4: annual 2006-2007 and annual 2007-2008: Graphical results are shown in Figures 4.24 and 4.25 for the 2006-2007 dataset and in Figures 4.24 and 4.26 for the 2007-2008 dataset. Since the results obtained with these two datasets are very similar, the description below is valid for both 2006-2007 and 2007-2008 annual datasets. The measured surface velocity exhibits the same two-zone pattern (slow ice flow downglacier and substantially faster ice flow upglacier) as in the summer datasets. The surface velocities are between 0 and 10 m/a over the lower 2000 m of the glacier and between 15 and 30 m/a over the upper 2500 m. The predicted surface velocities fit the measured data very closely, since the errors are very small (too small to appear in the figures). The basal velocity profile follows the pattern of the surface velocity, but shows unrealistic oscillations between 2000 and 3500 m from the terminus along the flowline. The basal velocity exceeds the measured surface velocity over two sections within this area and, from a glaciological point of view, is unrealistic. This issue, along with other inversion-related issues will be discussed at the end of this chapter. Figures 4.25b and 4.26b show that basal motion accounts for 50 to 90% of the total motion over most of the glacier.

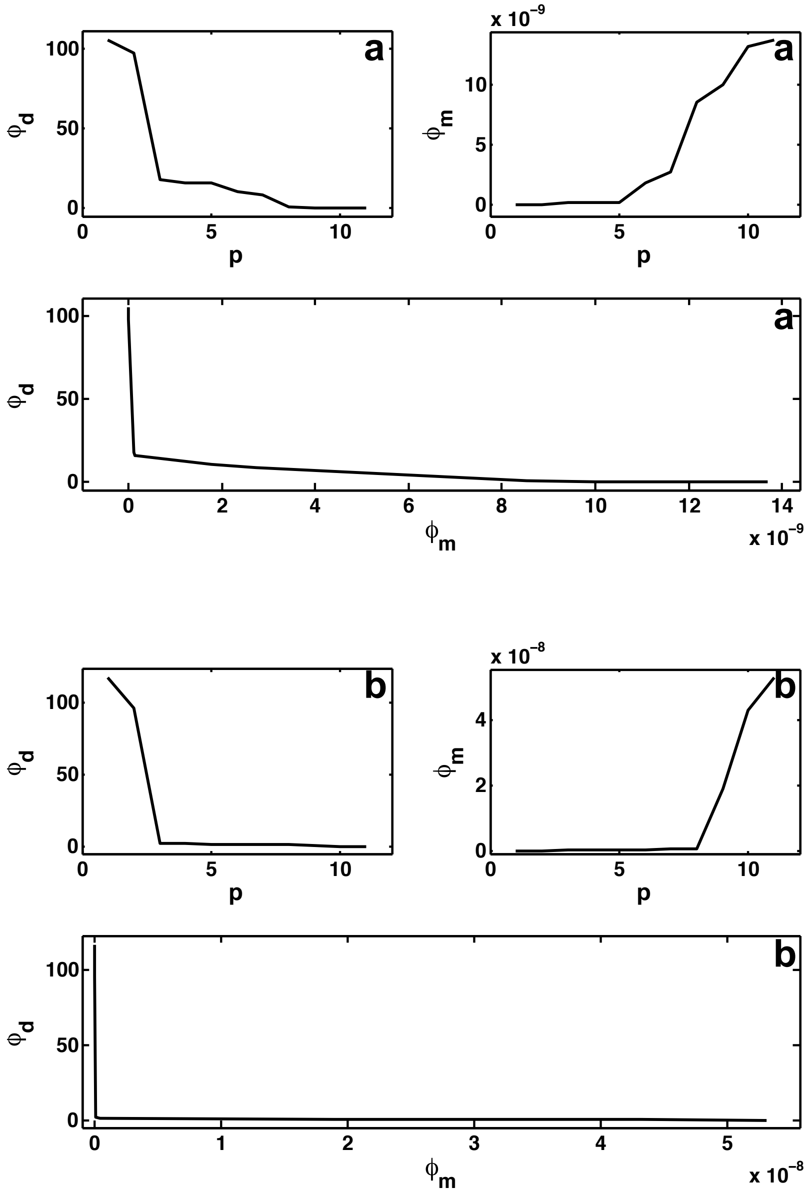

Figure 4.21: Tikhonov curves obtained using regularisation with the spectral approach for the (a) summer 2006 and (b) summer 2007 datasets. For both (a) and (b): *Top left:* misfit ϕ_d versus rank of singular values p; *top right:* model norm ϕ_m versus p; *bottom:* misfit ϕ_d versus model norm ϕ_m. The regularization parameter is determined for a value of misfit close to the number of data N (here $N = 11$ for both datasets).

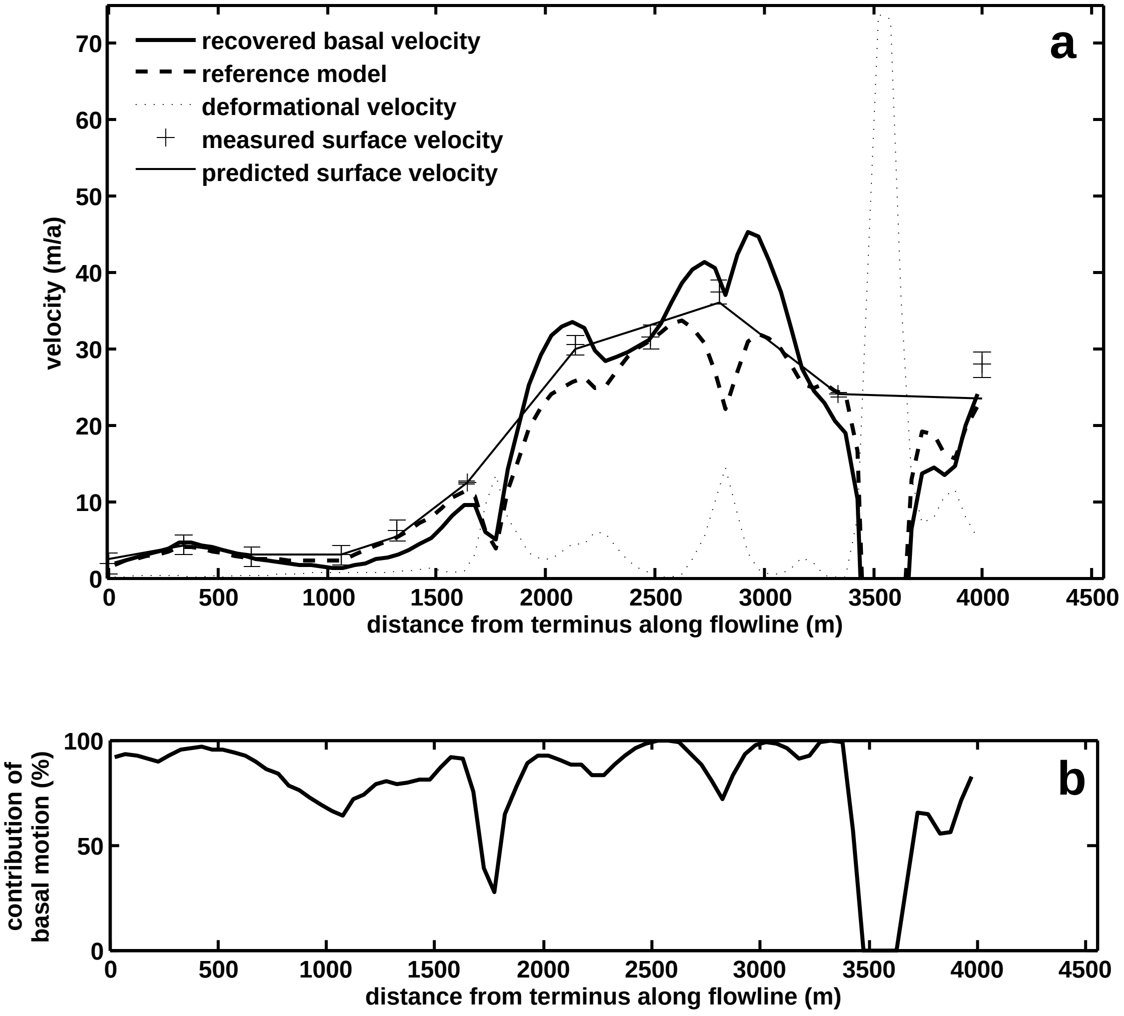

Figure 4.22: Results of the inversion of real data using a spectral approach for the summer 2006 dataset. (a) Ice velocities as a function of the distance from terminus along the flowline. (b) contribution of basal motion, expressed as a percentage, as a function of the distance from terminus along the flowline.

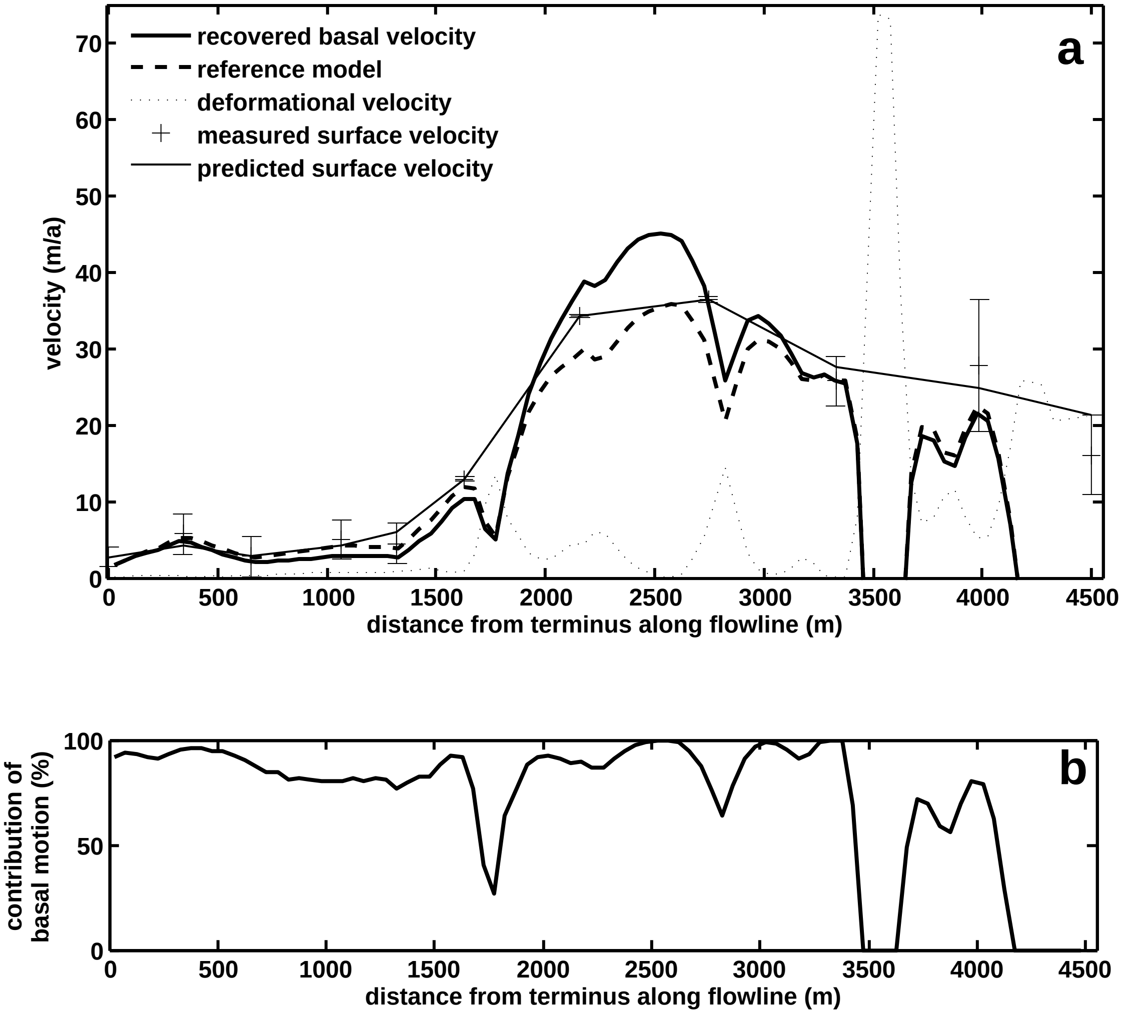

Figure 4.23: Results of the inversion of real data using a spectral approach for the summer 2007 dataset. (a) Ice velocities as a function of the distance from terminus along the flowline. (b) contribution of basal motion, expressed as a percentage, as a function of the distance from terminus along the flowline.

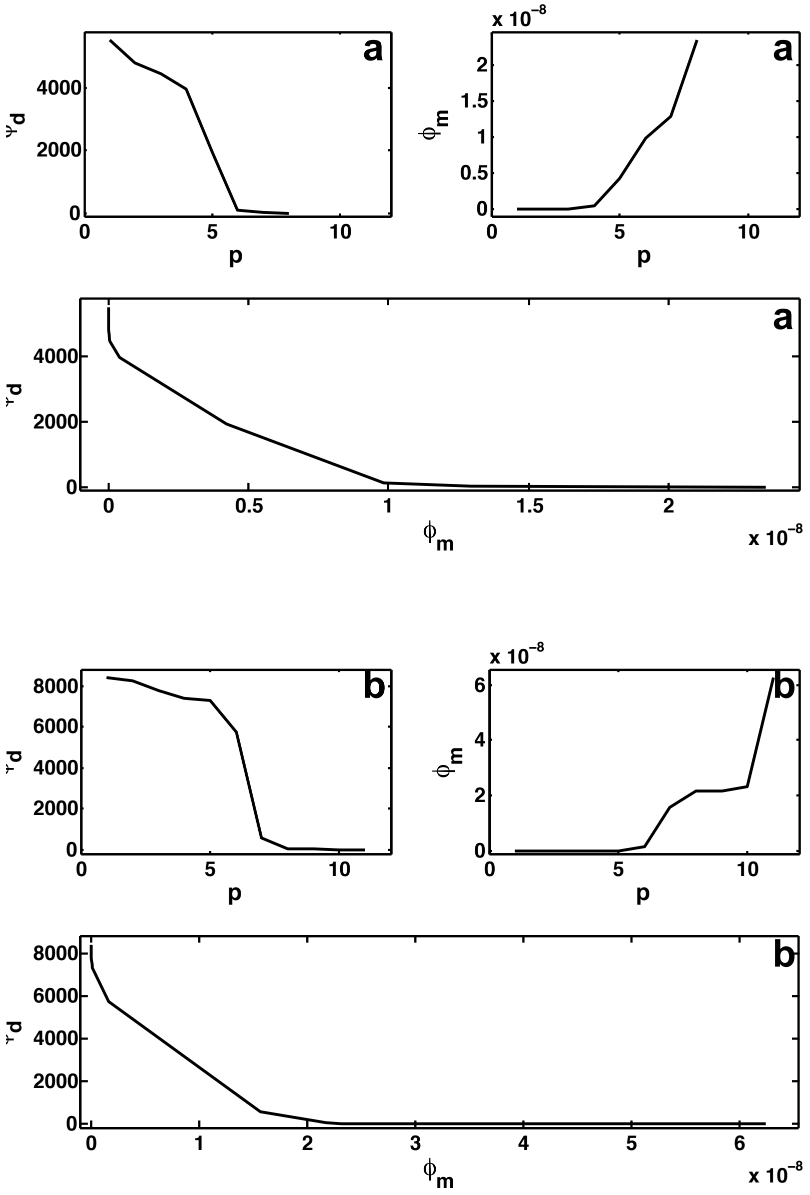

Figure 4.24: Tikhonov curves obtained using regularisation with the spectral approach for the (a) annual 2006-2007 and (b) annual 2007-2008 datasets. For both (a) and (b): *Top left:* misfit ϕ_d versus rank of singular values p; *top right:* model norm ϕ_m versus p; *bottom:* misfit ϕ_d versus model norm ϕ_m. The regularization parameter is determined for a value of misfit close to the number of data N (here $N = 8$ for (a) and $N = 11$ for (b)).

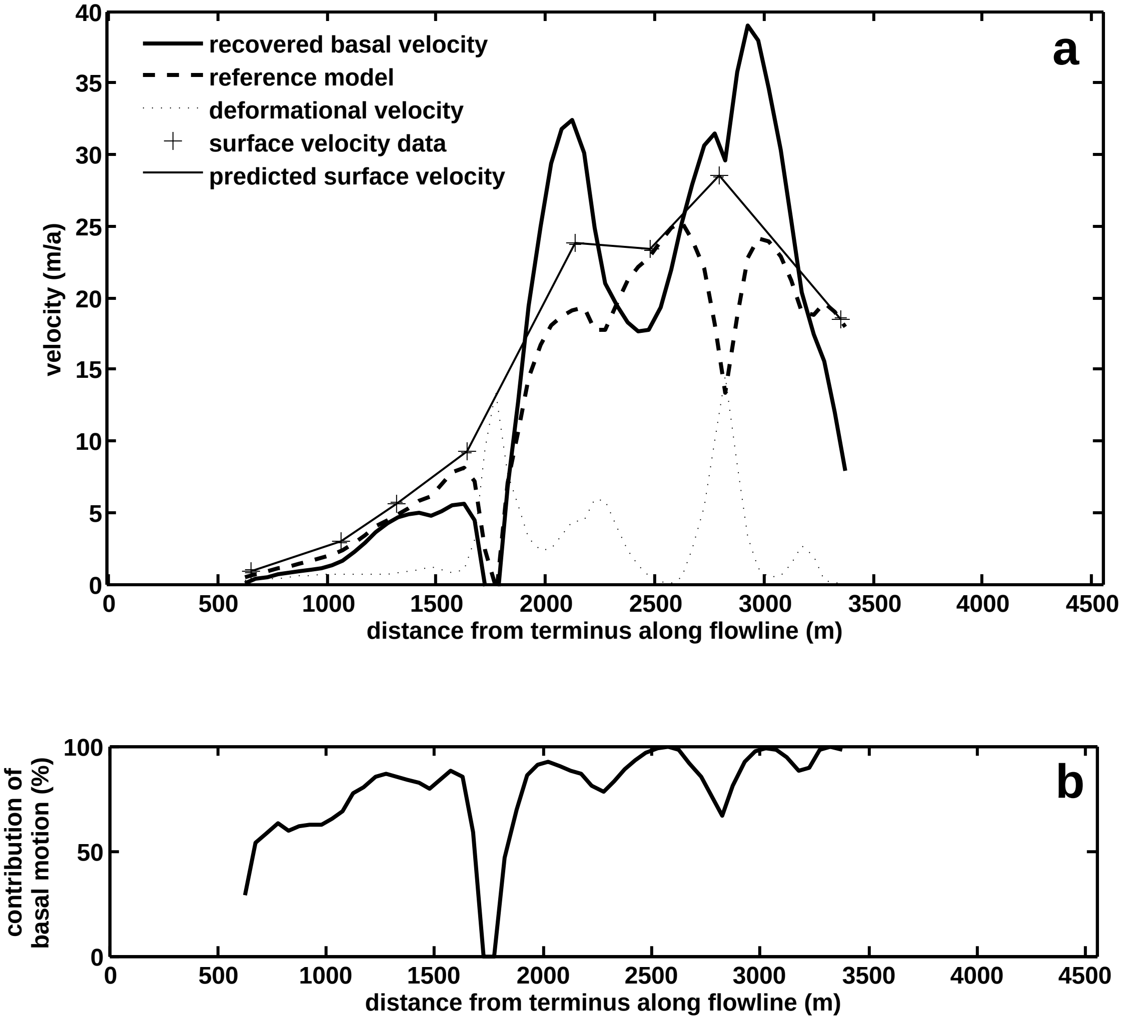

Figure 4.25: Results of the inversion of real data using a spectral approach for the annual 2006-2007 dataset. (a) Ice velocities as a function of the distance from terminus along the flowline. (b) contribution of basal motion, expressed as a percentage, as a function of the distance from terminus along the flowline.

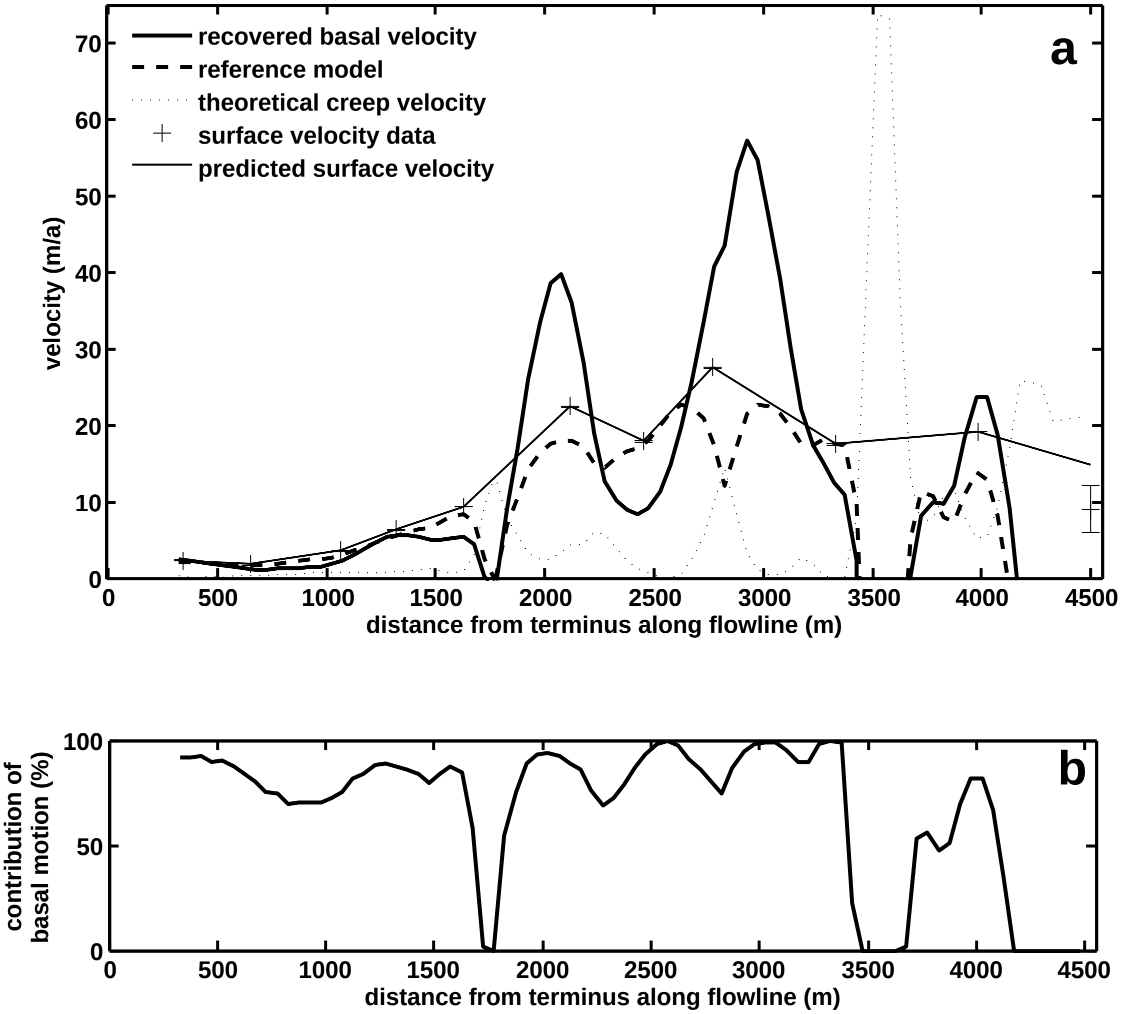

Figure 4.26: Results of the inversion of real data using a spectral approach for the annual 2007-2008 dataset. (a) Ice velocities as a function of the distance from terminus along the flowline. (b) contribution of basal motion, expressed as a percentage, as a function of the distance from terminus along the flowline.

4.3.4 Sensitivity tests

Several quantities and parameters used in the inversion are subject to uncertainty that cannot be eliminated with the available field measurements. In these cases, I use values qualitatively consistent with the study glacier environment or values prescribed by the literature. This is the case for the shape of the bed, assumed to be a semi-ellipse, and for the longitudinal coupling length, taken as three times the local ice thicknesses. The ice temperature was calculated from field measurements, but modelling and averaging were necessary to include it in the inversion as an effective temperature (a detailed explanation for this is provided in section 4.2.5). As a result, the temperature of the ice, leading to the choice of an appropriate flow-law coefficient, is only an approximation and is thus uncertain.

For these reasons, it is important to quantify the sensitivity of the inversion results to parameters that are uncertain. To this end, three tests are conducted to outline the impact on modelled basal motion of the shape factor, the flow-law coefficient and the longitudinal coupling length. In each experiment, I vary the value of the parameter of interest, while keeping other parameters constant and equal to the default values used previously. Since the spectral decomposition method has been judged to be the most reliable of the two methods tested according to results of the control tests, only the spectral approach is used in the sensitivity tests. The same reference model as for the inversion of real data is also used for all tests. Each experiment was run for each of the four surface velocity datasets, leading to four sets of results for each sensitivity test. An additional test was conducted on two datasets to test the sensitivity of the inversion results to uncertainty in the data.

Sensitivity to the shape factor f

In control tests and inversion using real data, the bed was assumed to have the shape of a semi-ellipse. This choice was motivated by the geometry of the valley and the bed DEM. In reality however, the shape of the bed deviates from the model of a semi-ellipse at a few locations along the flowline. In addition, non-uniform basal motion in a transverse direction can have an influence on the value of the shape factor (Truffer et al., 2001). It is thus of interest to quantify how such deviations affect the modelled basal motion.

The routine designed to test the sensitivity of the inversion to the shape factor is therefore run for beds having a rectangular or parabolic shape in addition to the default semi-elliptical shape. The shape of the bed is quantified by the shape factor, whose derivation is explained in section 3.5.3. Values of shape factors advocated by Paterson (1994), presented in Table 3.8, were used to derive shape factor profiles for elliptical, rectangular and parabolic beds. The averaged shape factor values are presented in Table 4.7.

From these values, three shape factor profiles are derived, which correspond to the three

W	Parabola	Semi-ellipse	Rectangle
1	0.445	0.500	0.558
2	0.646	0.709	0.789
3	0.746	0.799	0.884
4	0.806	0.849	1.000
∞	1.000	1.000	1.000

Table 4.7: Values of shape factors for three bed types. Values for elliptical, parabolic and rectangular beds were taken from Paterson (1994). For each particular bed type, the shape factor is determined using the ratio W of the glacier half-width by the ice thickness.

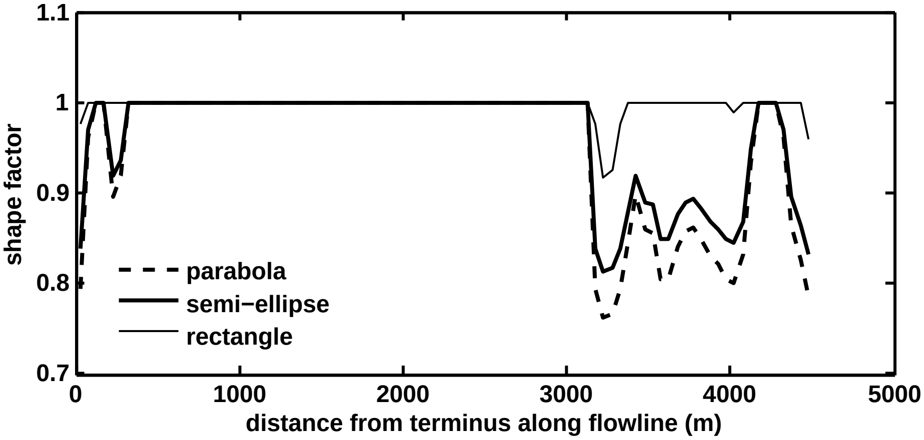

Figure 4.27: Three shape factor profiles. The thick full line, used for the shape factor of a semi-elliptical bed, represents the default used for control tests and inversion with real data.

glacier bed shapes mentioned above. These profiles, presented in Figure 4.27, are then used as input in the sensitivity tests. The profiles are used to calculate the deformational velocity (Equation 4.2). This results in three creep velocity profiles, presented in Figure 4.28. These profiles are identical over most of the length of the glacier, but differ slightly from each other over the upper part of the glacier, from 3400 m to 4500 m along the flowline. The effect of these differences on the inversion results is illustrated in Figure 4.29 and Figure 4.30. For all four datasets, the slip-ratio profiles computed with the three bed shapes are identical over most of the length of the glacier and differ slightly for the upper part of the glacier (∼3400-4500 m). In this area, the difference in the contribution of basal motion obtained with semi-elliptical and parabolic bed shapes is less than 10% of the total motion. With the rectangular bed shape, the slip-ratio profile in this area differs from the profile obtained with a semi-elliptical bed shape by up to 30% of the total motion. This pattern is observed for the four datasets (except for dataset 3, as there are no data in this area). These results are discussed in Section 4.4.

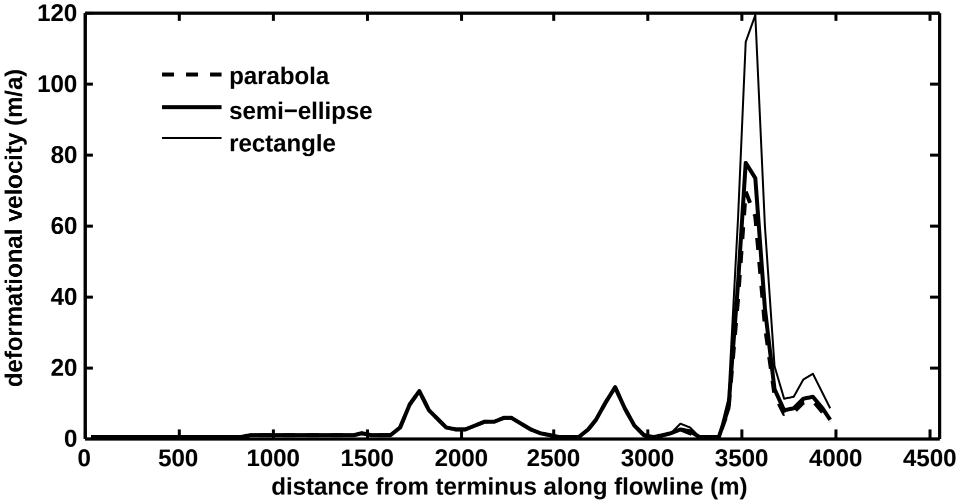

Figure 4.28: Sensitivity of the deformational velocity to the shape factor. The deformational velocity is plotted as a function of the distance from the glacier terminus along the flowline.

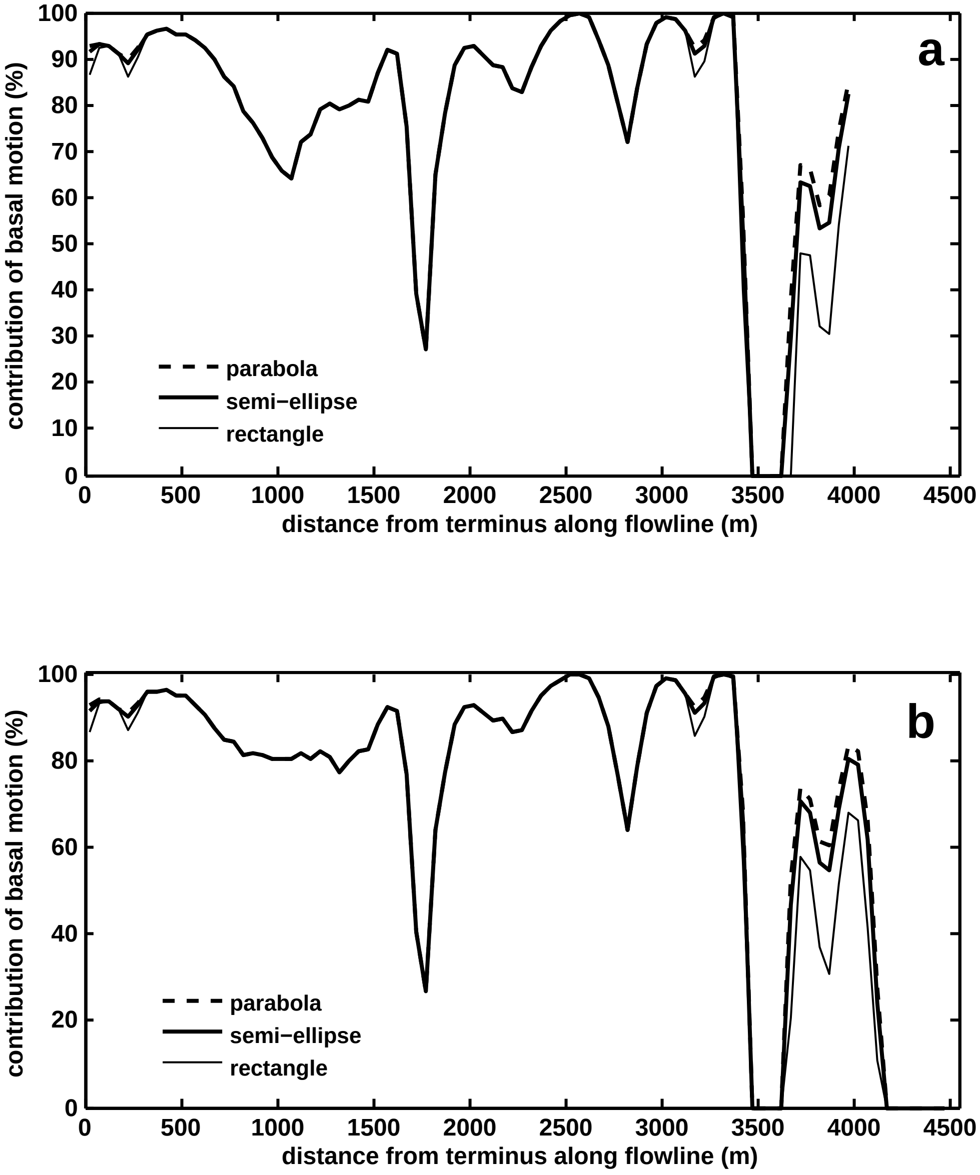

Figure 4.29: Sensitivity of the contribution of basal motion to the shape factor. (a) Summer 2006 dataset, (b) summer 2007 dataset. For each panel, the contribution of basal motion, expressed as a percentage, is plotted as a function of the distance from the glacier terminus along the flowline.

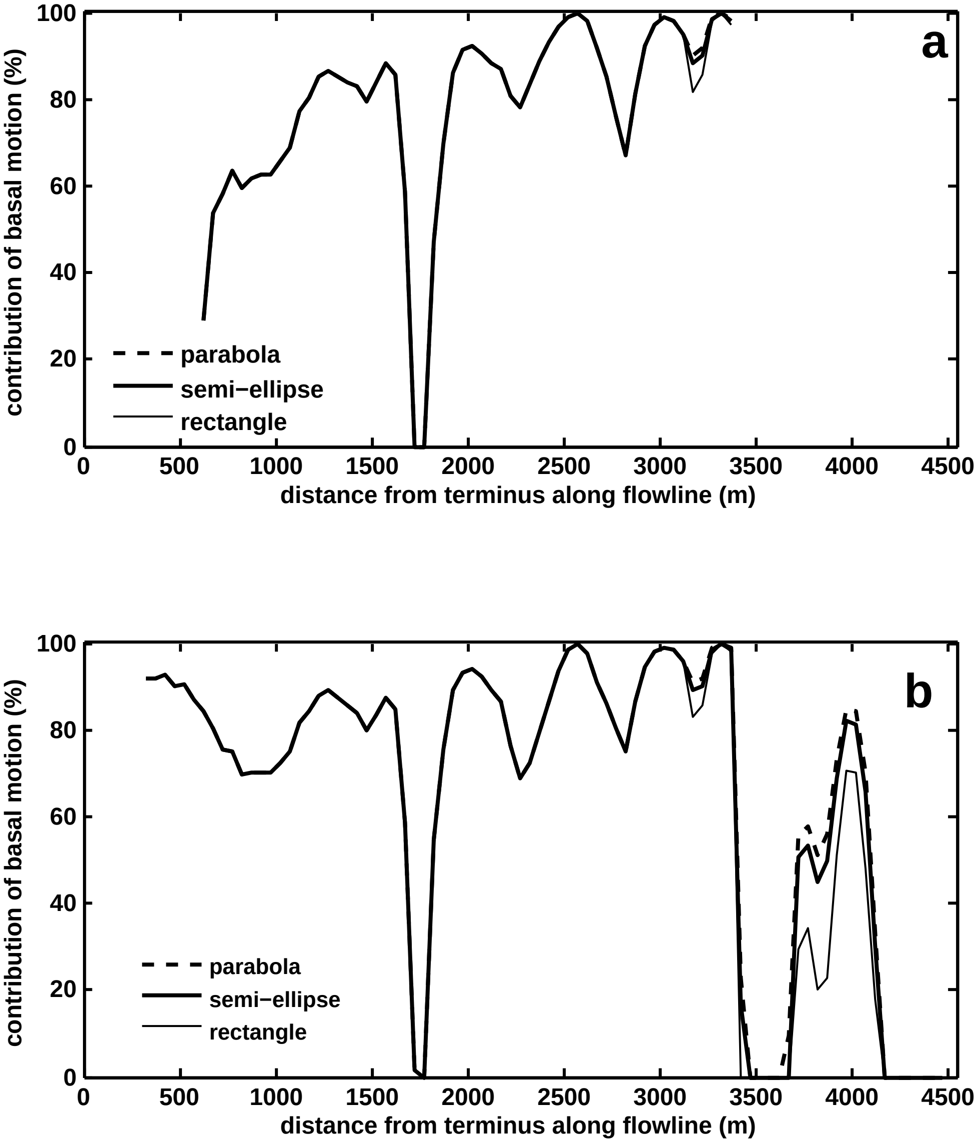

Figure 4.30: Sensitivity of the contribution of basal motion to the shape factor. (a) 2006-2007 annual dataset, (b) 2007-2008 annual dataset. For each panel, the contribution of basal motion, expressed as a percentage, is plotted as a function of the distance from the glacier terminus along the flowline.

Sensitivity to the flow-law coefficient A

The rheology of ice, and hence the deformation velocity, is strongly dependent on ice temperature through the flow-law coefficient A. As a consequence, uncertainty in the ice temperature translates into uncertainty in the flow-law coefficient. Importantly, temperature varies with depth in the glacier, a dimension that is not accounted for in the 1-D model. Therefore, effective values of the temperature must be used. These values are derived in section 4.2.5 by modelling temperature, and a value of the flow-law coefficient corresponding to an effective temperature of $-2°$C is adopted.

A simple sensitivity test is conducted to illustrate the effect of various effective temperatures on the modelled basal velocity. Inversions are run with flow-law coefficients corresponding to different effective temperatures, while all other parameters are kept constant. The range of temperatures considered, along with values of the corresponding flow-law coefficients is presented in Table 4.8.

The four flow-law coefficients presented in Table 4.8 were used to calculate four creep velocity profiles, shown in Figure 4.31. These velocity profiles were in turn used as input in the four inversions run for this sensitivity test. Results of the four runs, expressed as the contribution of basal motion or slip ratio, are presented in Figure 4.32 and Figure 4.33. For the four datasets, the overall contribution of basal motion increases as the effective temperature, and therefore the deformational velocity, decreases. The deviation from the profile obtained using the default effective temperature of $-2°$C is not significant for an effective temperature of $-5°$C, but becomes significant when using flow-law coefficients corresponding to effective temperatures of 0°C and $-10°$C. The overall contribution of basal motion rises to between 80 and 100% when an effective temperature of $-10°$C is used, and drops

Temperature (°C)	**flow-law coefficient** A ($\mathrm{Pa}^{-3}\mathrm{s}^{-1}$)
0	6.8×10^{-24}
-2	2.4×10^{-24}
-5	1.6×10^{-24}
-10	4.9×10^{-25}

Table 4.8: Values of temperatures and associated flow-law coefficients used in the flow-law coefficient sensitivity tests, taken from Paterson (1994). $A = 2.4 \times 10^{-24}\,\mathrm{Pa}^{-3}\mathrm{s}^{-1}$ was used in the control tests and inversion of real data.

to between 10 and 70% of the total motion when an effective temperature of 0°C is used. For comparison, the overall contribution of basal motion ranges between 60 and 100% with the default effective temperature. These results are discussed in Section 4.4.

An additional experiment is carried out concerning the flow-law coefficient. Since all previous inversion experiments show a relatively high contribution of basal motion, and thus a considerable amount of sliding, I test whether or not it is possible to obtain a basal profile with no sliding at all, and what value of the flow-law coefficient A would be required to produce such a profile. To accomplish this, I run successive inversions with increasing values of A. The previous sensitivity test indeed shows that the contribution of basal motion decreases when the flow-law coefficient (and the associated effective temperature) increases. For the purpose of illustration, this experiment is only performed with the summer 2006 dataset.

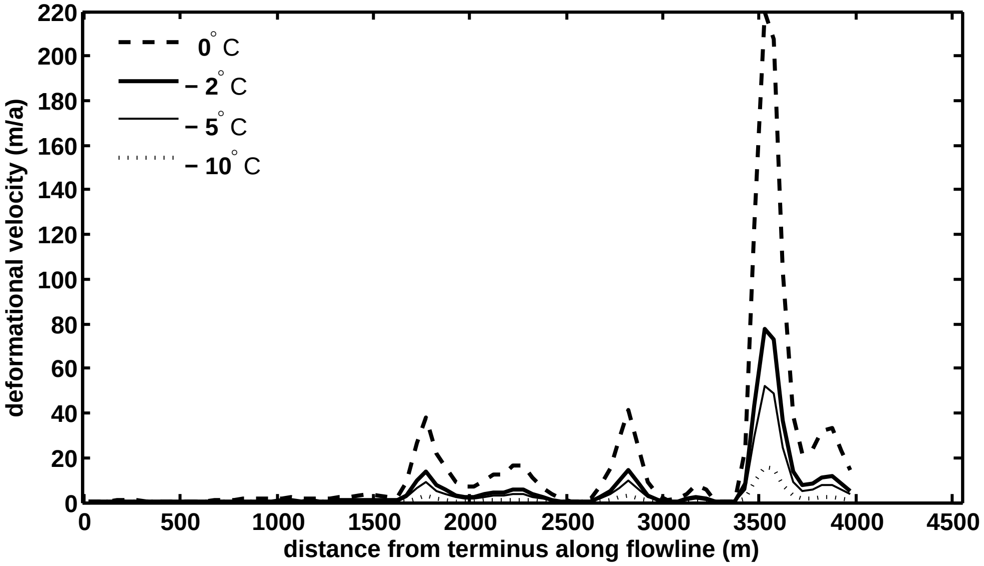

Figure 4.31: Sensitivity of the deformational velocity to the flow-law coefficient. The deformational velocity is plotted as a function of distance from the terminus along the flowline for four effective temperatures: 0°C, −2°C (default), −5°C and −10°C. The deformational velocity is computed using values of the flow-law coefficient corresponding to effective temperatures outline in the legend. These values are presented in Table 4.8.

Experiments with the flow-law coefficient show that:

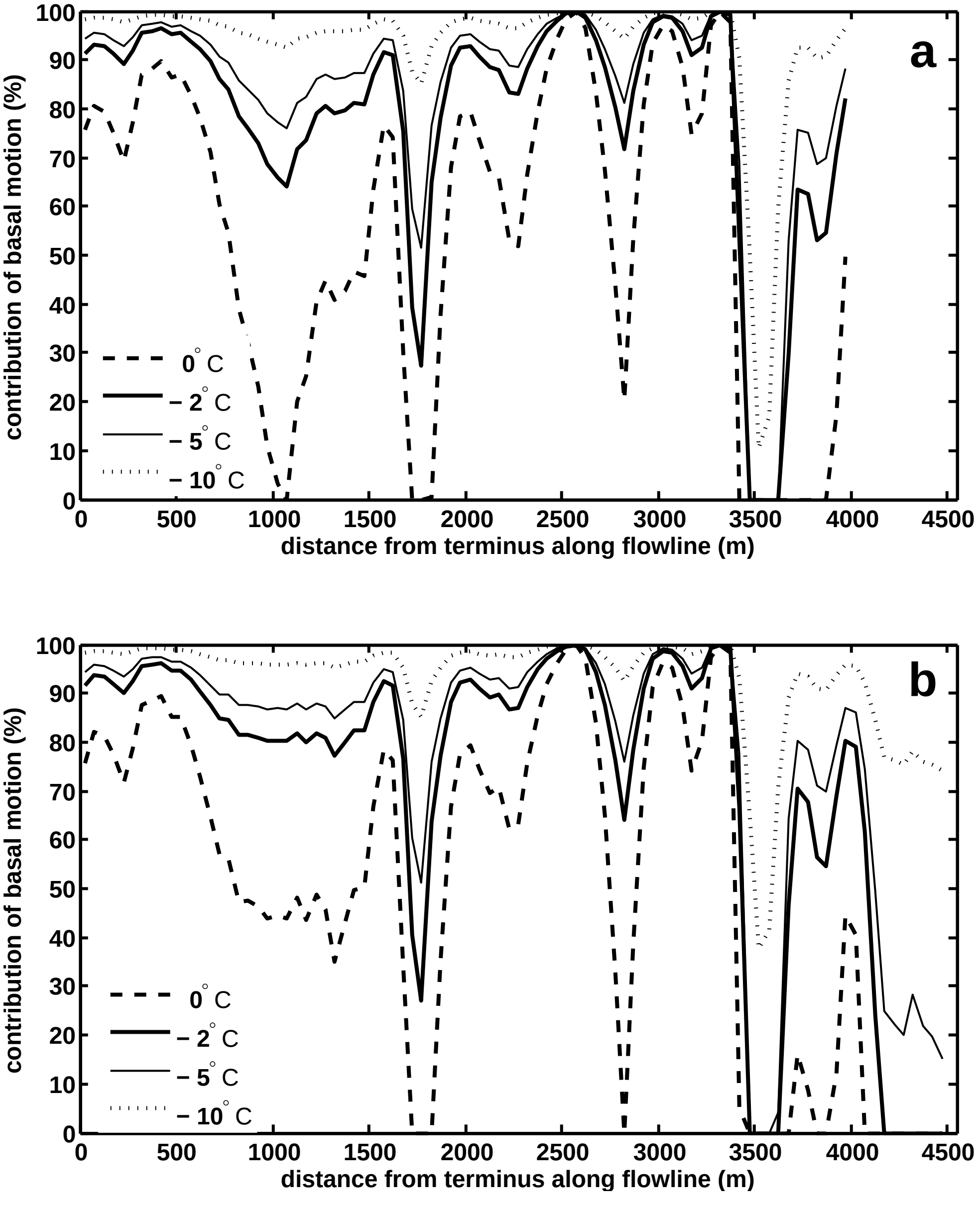

Figure 4.32: Sensitivity of the contribution of basal motion to the flow-law coefficient. (a) Summer 2006, (b) summer 2007. The contribution of basal motion, expressed as a percentage, is plotted against the distance from terminus along the flowline for four effective temperatures: 0°C, −2°C (default), −5°C and −10°C. The contribution of basal motion for each dataset is calculated from inversions run using flow-law coefficients associated with the effective temperatures considered.

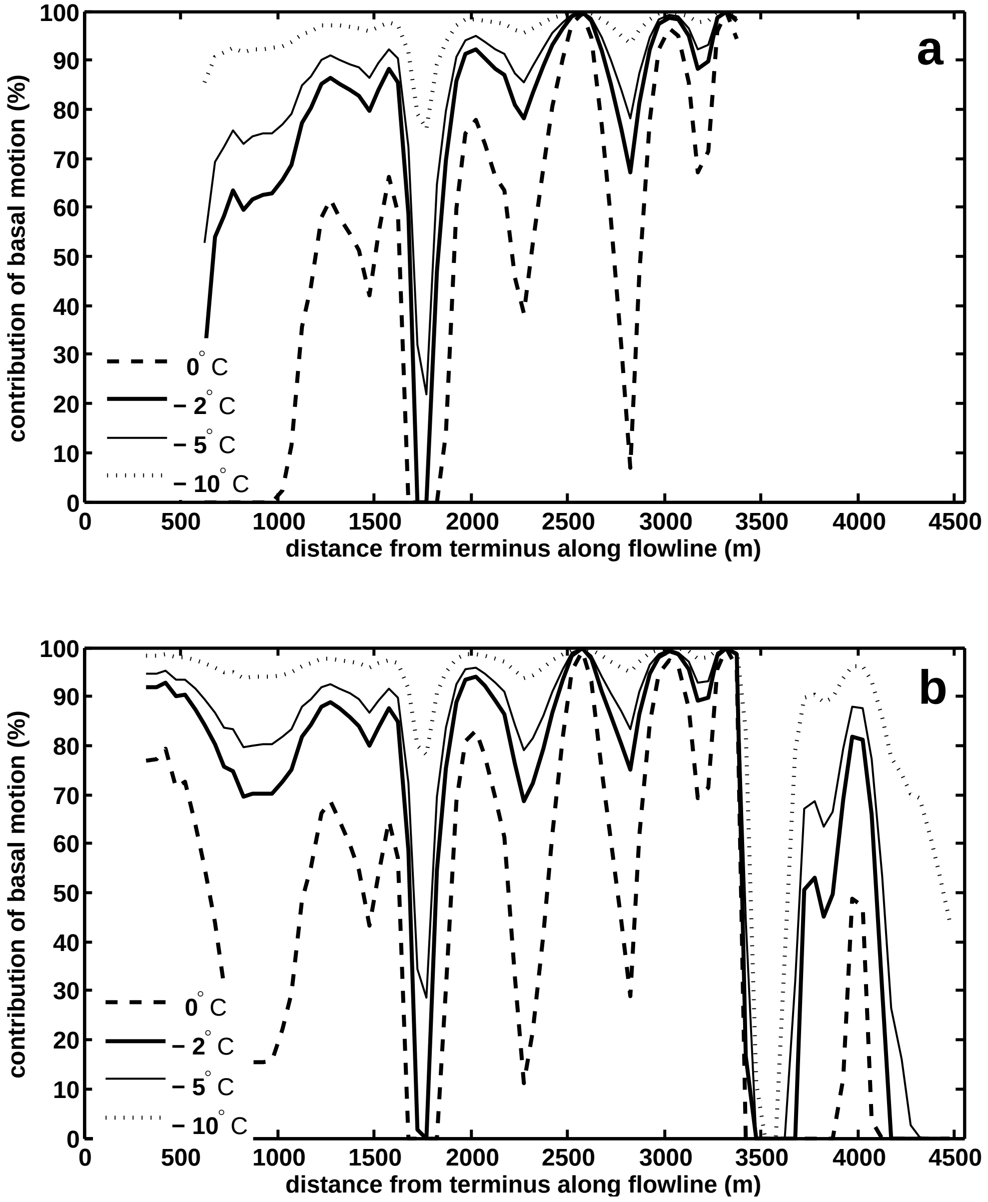

Figure 4.33: Sensitivity of the contribution of basal motion to the flow-law coefficient. (a) 2006-2007 annual dataset, (b) 2007-2008 annual dataset. The contribution of basal motion, expressed as a percentage, is plotted against the distance from terminus along the flowline for four effective temperatures: 0°C, −2°C (default), −5°C and −10°C. The contribution of basal motion for each dataset is calculated from inversions run using flow-law coefficients associated with the effective temperatures considered.

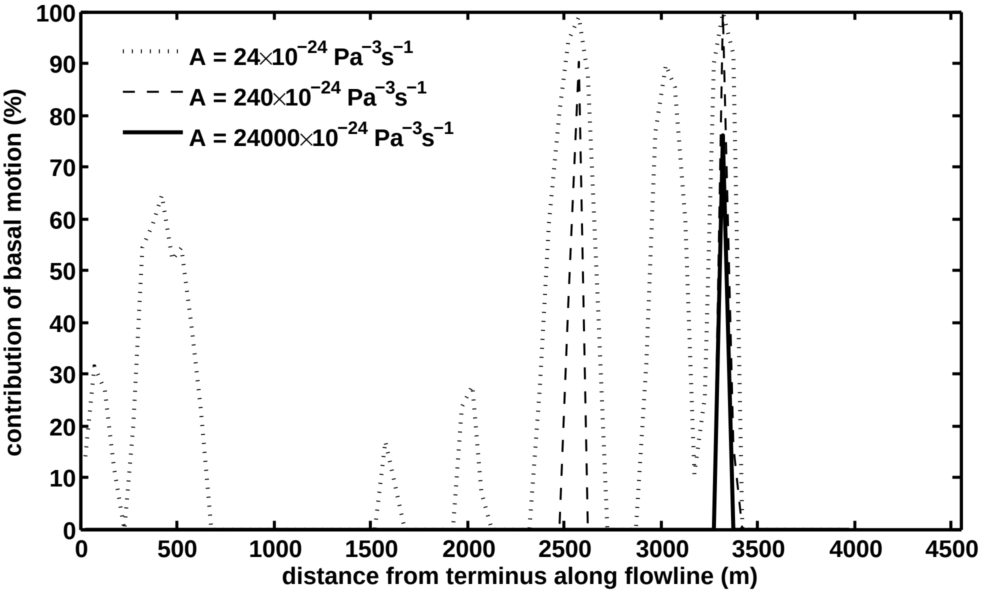

Figure 4.34: Effects of a high flow-law coefficient on the contribution of basal motion. The contribution of basal motion is plotted against the distance from the glacier terminus along the flowline to illustrate the effect of a high flow-law coefficient. The dotten and dashed lines represent, respectively, a 10-fold and 100-fold increase in the value of the flow-law coefficient A. The thick full line represents a 10000-fold increase in A, with which basal motion is restricted to a narrow zone (~100 m long) along the flowline

- an increase in A by less than one order of magnitude, for example from $6.8 \times 10^{-24}\,\mathrm{Pa}^{-3}\mathrm{s}^{-1}$ to $10 \times 10^{-24}\,\mathrm{Pa}^{-3}\mathrm{s}^{-1}$, has very little effect on the contribution of basal motion,
- a 10-fold increase in A (from the default value) is required to decrease the contribution of basal motion below 50% over most of the flowline (except for a few major peaks in slip ratio seen in Figure 4.32),
- a 100-fold increase in A suppresses all peaks except the two largest peaks,
- a 10000-fold increase in A suppresses all basal motion along the flowline, except for a narrow zone at ~3300–3400 m along the flowline.

These findings are illustrated in Figure 4.34 and discussed in Section 4.4.

Sensitivity to the longitudinal coupling length l

The longitudinal coupling length controls the distance over which the influence of local slope and ice thickness is averaged in the forward model and is usually expressed as a multiple of the local ice thickness. Kamb and Echelmeyer (1986) advocate a value of one to four ice thicknesses, and Truffer (2004) states that the typical value of the longitudinal coupling length is three ice thicknesses. The value of three ice thicknesses ($l = 3\,h$) was thus used in the control tests and inversion of real data.

The value of the longitudinal coupling length depends on glacier characteristics. Kamb and Echelmeyer (1986) have developed an expression to calculate the longitudinal coupling length along the flowline as a function of the rheology of ice, the vertically integrated velocity, the basal shear stress and the ice thickness. However, for simplicity, a typical value of three ice thicknesses was used here. The calculation of a more precise longitudinal coupling length using the expression of Kamb and Echelmeyer would be an interesting improvement to this work. Because the value of l was not calculated but assumed, it is uncertain and therefore submitted to a sensitivity test.

In this experiment the value of the longitudinal coupling length l was varied from 1 to 5 multiples of the ice thickness. Results, presented in Figure 4.35 and Figure 4.36, show how the contribution of basal motion is affected. For the four datasets, the profile illustrating the contribution of basal motion is similar for all l over most of the length of the glacier, but localized deviations from the profile obtained with $l = 3\,h$ (thick full line in Figure 4.35 and 4.36) are observed in the four the datasets. Significant deviations are observed in one zone for the summer 2006, summer 2007 and annual 2006-2007 datasets and in two zones for the annual 2007-2008 dataset. For the summer 2006 dataset, there is significant deviation from the default profile for $l = 4\,h$ and $l = 5\,h$ only. These results are discussed in Section 4.4.

Sensitivity to uncertainty in the measured data

Two final sets of tests are conducted to evaluate the sensitivity of the inversion result to the errors in the measured data. The purpose of these tests is to attempt to explain the unrealistic oscillations observed in the inversion of the annual velocity datasets. Inversion of the measured surface velocity data is carried out using the spectral decomposition method and a reference model.

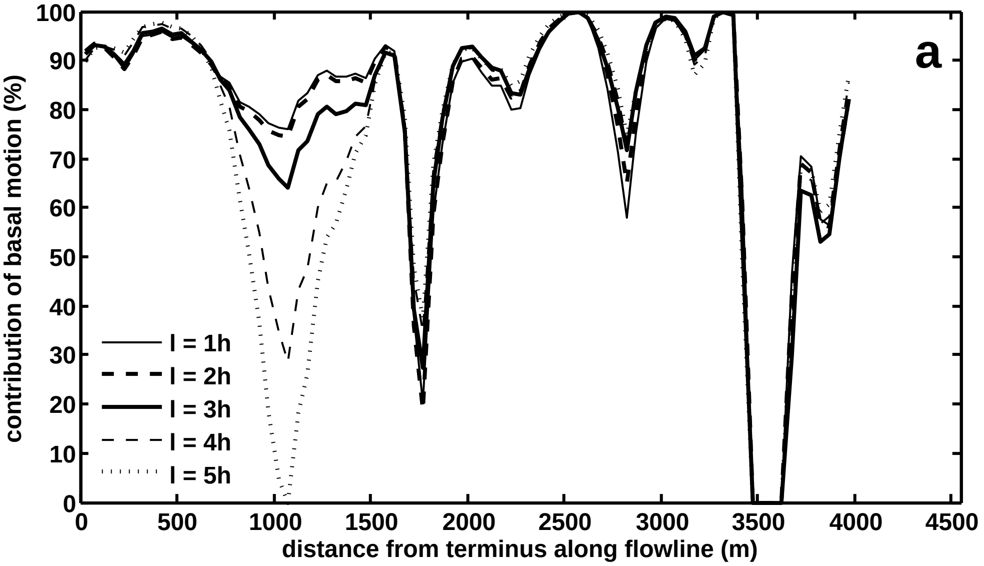

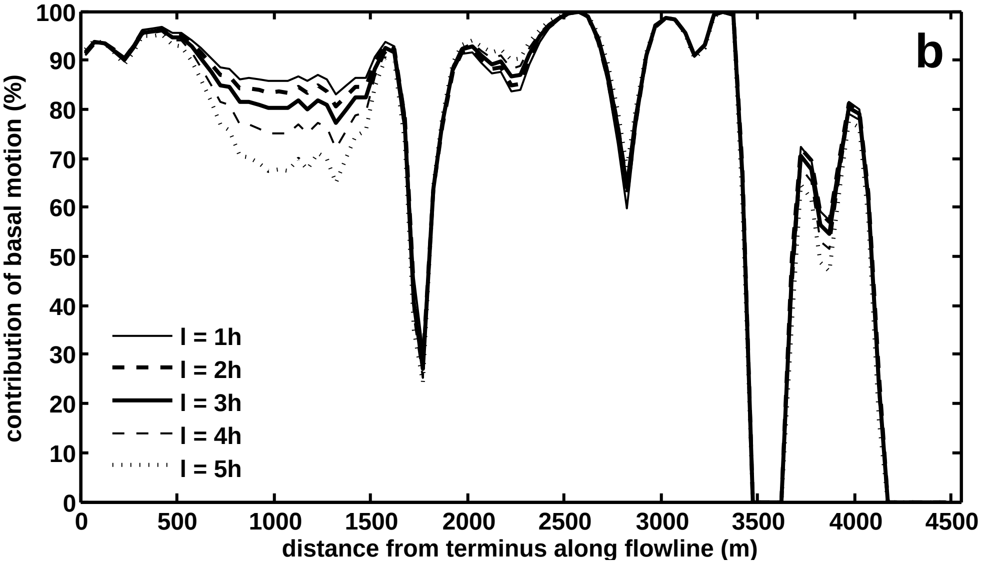

Figure 4.35: Sensitivity of the contribution of basal motion to the longitudinal coupling length l. (a) Summer 2006 dataset, (b) summer 2007 dataset. The contribution of basal motion to the total ice motion is plotted as a function of the distance from the glacier terminus along the flowline for longitudinal coupling lengths varying from 1 to 5 ice thicknesses. The default value $l = 3\,h$ was used for all previous results.

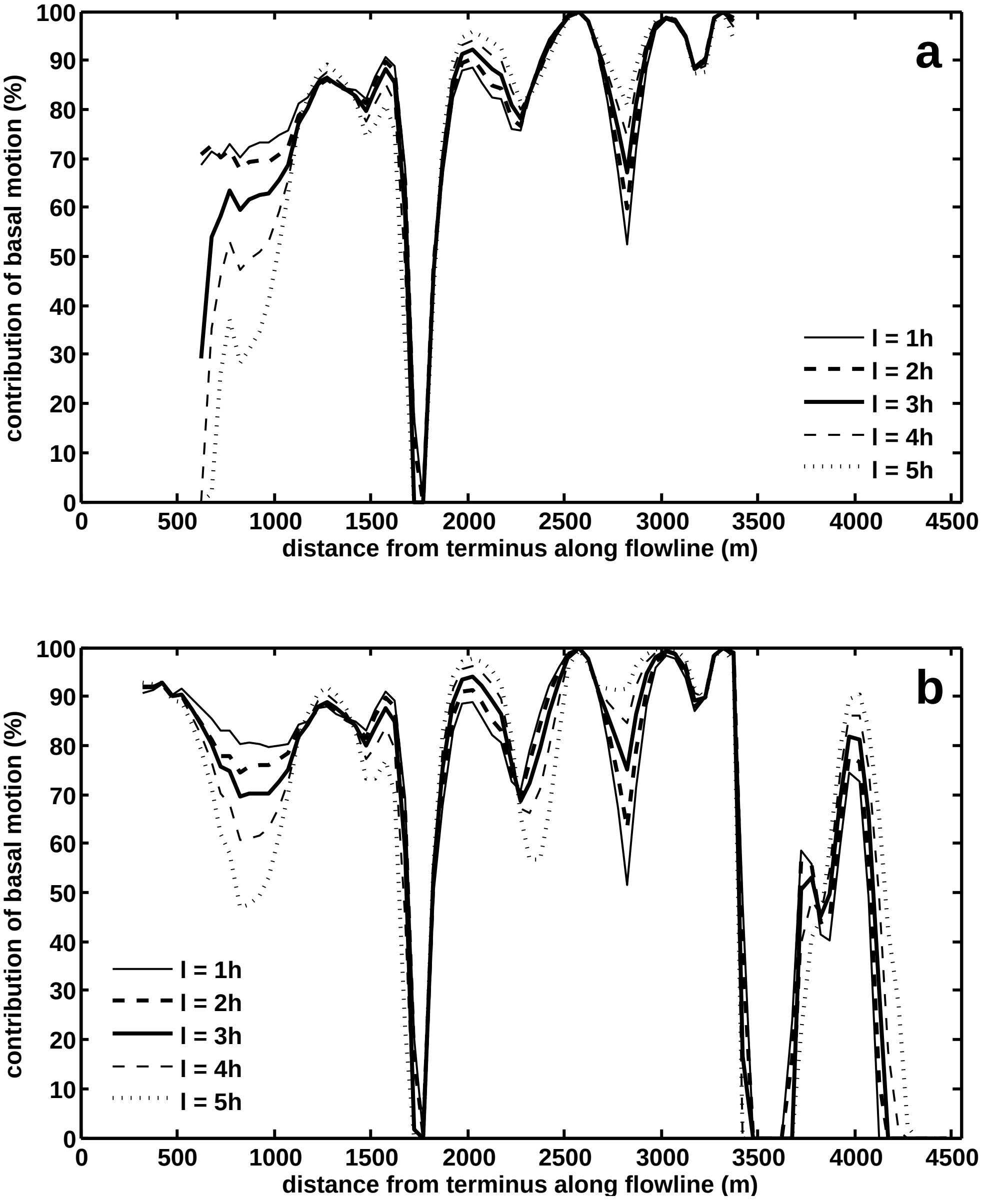

Figure 4.36: Sensitivity of the contribution of basal motion to the longitudinal coupling length l. (a) 2006-2007 annual dataset, (b) 2007-2008 annual dataset. The contribution of basal motion to the total ice motion is plotted as a function of the distance from the glacier terminus along the flowline for longitudinal coupling lengths varying from 1 to 5 ice thicknesses. The default value $l = 3\,h$ was used for all previous results.

In a first set of tests, errors associated with the summer 2007 surface velocities (dataset 2) are gradually decreased. Inversions of the measured data are run with errors of 0.50, 0.25, 0.10 and 0.01 of the default errors. The resulting basal velocity profiles are presented in Figure 4.37. For comparison, Figure 4.23 shows the results of inversion of the same dataset with the default error values and the same inversion method. The basal velocity profile obtained with the errors reduced by half (Figure 4.37a) is identical to the profile obtained with the full errors. Dividing the error on the measured surface velocity by two has thus no effect on the basal velocity profile. When the default errors are scaled by 0.25 (Figure 4.37b), the basal velocity profile is identical to the profile obtained with the full errors over the lower 1500 m of the glacier. Over the upper 3000 m, the divergence of the basal velocity profile from the reference model is greater than for the inversion run with the default errors. When the errors on the data are decreased to 0.10 of the their default values, the basal velocity profile presents oscillations of small amplitude over the lower 2800 m of the glacier. The basal velocity profile remains unchanged when errors are further decreased to 0.01 of the default values or lower, as shown in Figure 4.37d. Tests also show that the basal velocity profile remains unchanged when the errors on the measured surface velocity are increased to two to ten times the default errors.

In a second set of tests, errors associated with the 2007-2008 annual dataset (dataset 4) are gradually increased to up to 20 times the default values. Basal velocity profiles resulting from the inversion of surface velocity data with errors 10, 16, 17 and 20 times the default errors are presented in Figure 4.38. Results are shown for these multiples of the default errors because they best illustrate the evolution of the basal velocity profile. When the errors are increased to up to 16 times their default values (Figure 4.38a and b), the basal velocity profile remains identical to that obtained with the default values. When the errors reach 17 times the default errors (Figure 4.38c), the basal velocity profile suddenly changes to a form that is similar in shape to that obtained for the summer datasets (see Figures 4.22 and 4.23). The unrealistic oscillations of the basal velocity profile, observed in the area between 2000 m and 3000 m along the flowline when smaller errors are used, are no longer present and the basal velocity is lower than the measured surface velocity over the whole length of the glacier (except for a small section around 2700 m). When errors are increased to 20 times the default values and above, the basal velocity profile remains similar to that obtained with 17 times the default errors. Results of inversions run with decreased errors show no changes in the basal velocity profile.

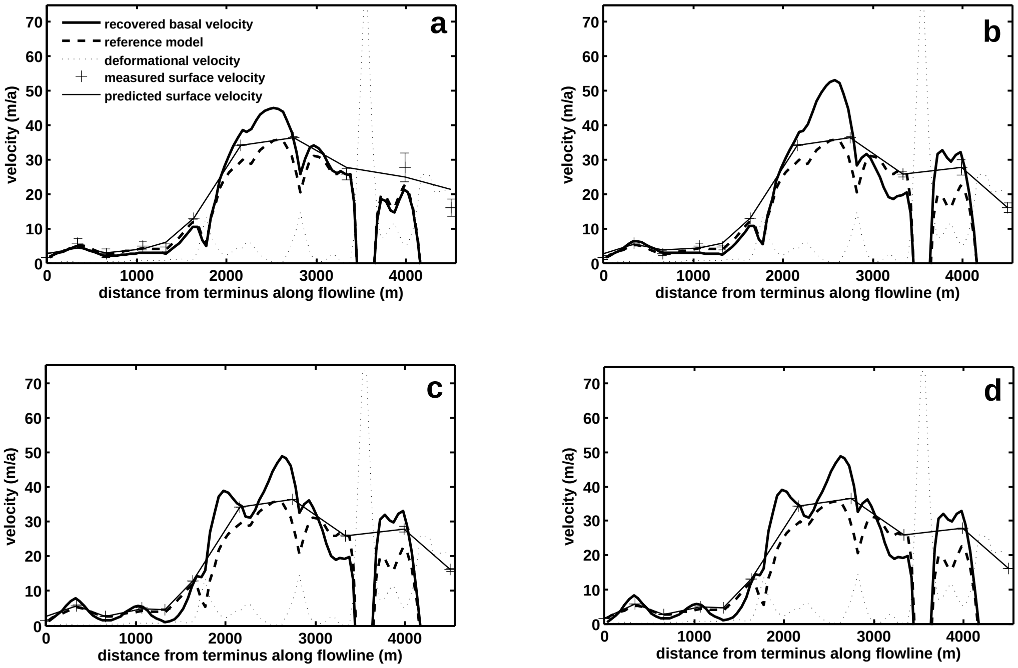

Figure 4.37: Sensitivity of the basal velocity profile to uncertainty in the measured data for the summer 2007 dataset. Basal and surface velocities are presented as a function of distance from the glacier terminus along the flowline. The errors associated with the measured data used in this inversion are (a) 0.50, (b) 0.25, (c) 0.10 and (d) 0.01 of the default values.

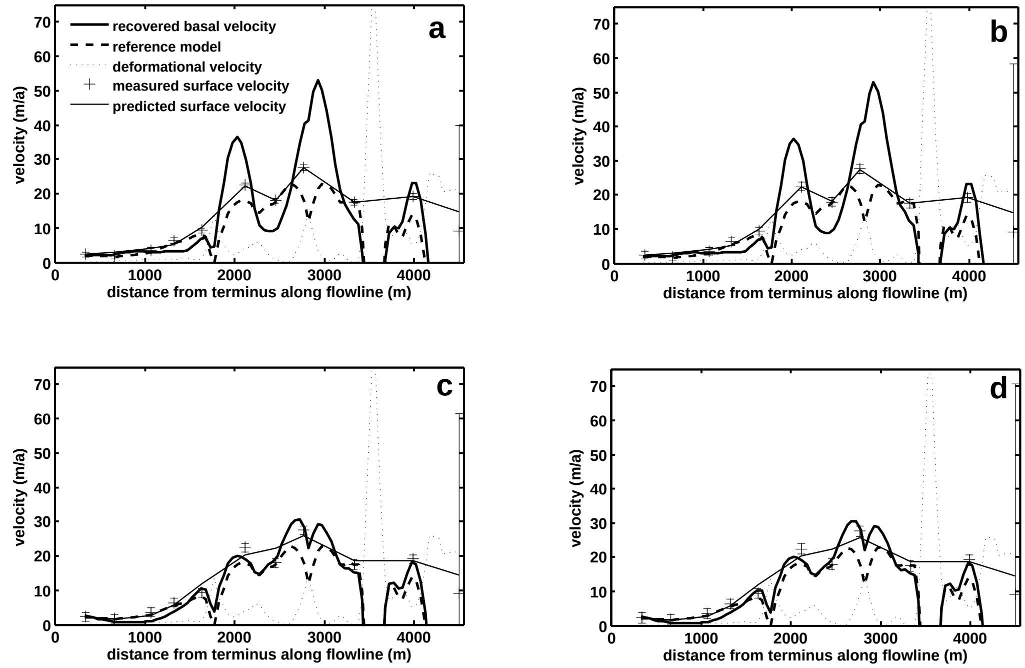

Figure 4.38: Sensitivity of the basal velocity profile to uncertainty in the measured data for the 2007-2008 annual dataset. Ice velocities are plotted against the distance from the glacier terminus along the flowline. Default errors associated with the measured data were multiplied by (a) 10, (b) 16, (c) 17 and (d) 20.

4.4 Discussion of inversion results

This discussion is confined to inversion-related issues, while a more general discussion of the results from a glaciological point of view is postponed until Chapter 5. Sections 4.4.1 and 4.4.2 deal with the results of the control tests and of the inversion of real data, respectively. The sensitivity of the inversion to diverse factors is discussed in Section 4.4.3.

4.4.1 Control tests

Control tests of the inversion were performed and results are shown is Section 4.3.2. Synthetic data were derived from a synthetic basal velocity model and a given glacier geometry using the forward model (Equation 4.11), and then inverted in order to recover a basal velocity profile. Two types of synthetic basal velocity profile (sinusoidal and rectangular) and three types of glacier geometry (slab, wedge and real geometry) were used in a set of six tests (see Table 4.4). These tests were performed using both deterministic and spectral approaches with and without a reference model. The results of these four sets of six control tests are presented in Figures 4.13, 4.14, 4.15 and 4.16. The quality of each inversion method is assessed by comparing the synthetic and recovered basal velocity profiles.

Effect of glacier geometry and synthetic basal velocity model

As mentioned in Section 4.3.2, arbitrary basal velocity models are not necessarily consistent with the glacier geometry or the inversion method. Of the 12 control tests performed using a rectangular basal velocity profile, none succeeds in recovering the basal velocity as well as in the tests using a sinusoidal basal velocity profile. In the control tests performed using the spectral decomposition method, a reference model, and a sinusoidal basal velocity profile (Figure 4.14a), a close match between the synthetic and recovered basal velocity profiles is obtained. However, when comparing this to the results obtained using the same method with a rectangular basal velocity profile (Figure 4.16b), the synthetic model is less well recovered, and the recovered model presents velocity oscillations where the synthetic model does not. This can be explained by the fact that, regardless of the performance of the method used for inversion, a synthetic model presenting a discontinuity or step cannot be accurately recovered using a method that selects the smoothest model.

The type of glacier geometry considered, synthetic or real, also has an impact on the quality of the results. In the four sets of control tests, the quality of the recovered model deteriorates when the glacier geometry is changed from a simple slab glacier (tests 1 and 2), to a more complex wedge-shaped glacier (tests 3 and 4), to the geometry of the study glacier (tests 4 and 6). It is important to note that this effect is also linked to an increase in the amplitude of the synthetic basal velocity profile. Indeed, the peak-to-peak amplitude of the synthetic basal velocity profiles is 2 m/a in the tests run with slab and wedge geometries (tests 1 and 3), and 40 m/a in the tests run with real geometry (tests 5). The amplitude of the step function similarly increases from 1 m/a with the slab and wedge geometries to 35 m/a with the real geometry. Large amplitudes were chosen for the control tests on real geometry to make the contributions from deformation and sliding of similar magnitude. The synthetic surface velocity data depend on both the synthetic basal velocity profile and the glacier geometry (through the deformational velocity). We note that by looking at the results of tests 1, 3 and 5, the range of values of the synthetic surface velocity over the length of the glacier increases from test 1 to test 5 (these values are the same for the four sets of tests conducted, only the recovered basal velocity changes). This is also true for the tests conducted with a rectangular synthetic model (tests 2, 4 and 6). The large range of values in the data produces matrices with higher condition numbers and that are sometimes close to singular. The high condition numbers make the matrices numerically more difficult to invert, resulting in unrealistic structure and deviations from the synthetic model.

Effect of the reference model

Comparison of control tests conducted with (Figures 4.13 and 4.14) and without (Figures 4.15 and 4.16) a reference model shows a significant improvement in the quality of the recovered model when a reference model is used. The quality of the inversion is partly a function of choosing a good reference model. In the control tests, the use of a reference model suppresses unrealistic structure in the recovered basal velocity profile. Experimentation shows that the resulting system of equations is more difficult to invert, producing matrices that are close to singular, when no reference model is used.

Performance of the deterministic and spectral decomposition methods

In addition to examining the effect of the glacier geometry, synthetic models and the use of a reference model on the quality of the recovered basal velocity profile, the control tests allow one to compare the performance of the spectral and deterministic approaches. Figures 4.13

and 4.14 present results of the set of six control tests conducted using the deterministic method and the spectral decomposition method, respectively (both using a reference model). As mentioned above in Section 4.3.2, the synthetic basal velocity profile is better recovered by the spectral decomposition method than by the deterministic method. The spectral decomposition method involves decomposing the matrix to be inverted into a product of invertible matrices containing eigenvectors and eigenvalues (Section 4.2.4). In the deterministic method, the inverse of a matrix is directly computed to recover the model (Section 4.2.3). The success of the deterministic method therefore depends on the condition number of the matrix whose inverse is computed. When running inversions using the deterministic method, this matrix was often found to be close to singular or to have especially high condition numbers. The high-frequency oscillations seen in the control tests of the deterministic method can be related to high condition numbers. For example, oscillations are present in the control test number 5 (deterministic method with a reference model, Figure 4.13e), and the condition number of the matrix to be inverted is 2.67×10^{15}, a very high value. Conversely, there are no high-frequency oscillations in the inversion of real data using this method and the condition number of the matrix to be inverted is only 1.69×10^{6} (Figure 4.19b). The spectral decomposition method is designed to avoid issues related to high condition numbers through singular value decomposition of the matrix to be inverted. Since the spectral decomposition method avoids these singularity issues, its performance is better in this application.

Effect of noise

An additional control test, designed to illustrate the influence of the amount of noise on the quality of the inversion, is described in Section 4.3.2. In this test, synthetic data generated from a sinusoidal synthetic model are perturbed with variable amounts of noise and inverted. The test was performed for a slab-like glacier with a sinusoidal synthetic basal velocity profile (test 1) using the spectral decomposition method and a reference model. Profiles resulting from inversions using amounts of noise of 2%, 5%, 10% and 20% of the mean of the synthetic surface velocity are presented in Figure 4.17. This figure shows that the quality of the recovered model deteriorates as the amount of noise increases. The main pattern of the synthetic model is recovered for amounts of noise less than about 20%.

4.4.2 Results of the inversion of real data

Results of the inversion of real data, using real glacier geometry, are presented in Section 4.3.3. The results obtained using the deterministic method are presented in Figures 4.19 and 4.20, and those obtained using the spectral decomposition method are presented in Figures 4.22, 4.23, 4.25 and 4.26. Results obtained using the spectral decomposition method are discussed here, but all comments made in this section are also valid for the results obtained with the deterministic approach, since results obtained using both methods are very similar.

Significance of the deviation of the basal velocity profile from the reference model

The results of the inversion of the summer 2006 and summer 2007 datasets using the spectral decomposition method are presented in Figures 4.22 and 4.23, respectively. In these figures, the recovered basal velocity profile differs from the reference model (taken as the difference between the measured surface velocity and the deformational velocity) by up to 20 m/a. This divergence is significant and triggers the question of whether or not the recovered basal velocity profile can be trusted to this level of detail. The control test examining the effect of noise can help answer this question. The introduction of random noise in the synthetic data is replaced in the inversion of real data by estimates of uncertainty in the measured data.

For the annual datasets (datasets 3 and 4), the uncertainty accounts for up to 5% of the magnitude of the measured surface velocities over the lower 1500 m of the glacier and for less than 1% over the upper 3500 m of the glacier (except for the last point on the flowline in the 2007-2008 annual dataset which has an error of 3% of the measured datum). In the control tests, these values correspond to noise amounts resulting in good model recovery. However, the reliability of the results is called into question by the oscillations in the recovered basal velocity profile observed for the annual datasets and by the fact that the basal velocity exceeds the measured surface velocity in several areas along the flowline. These issues are discussed further below. For the summer datasets (datasets 1 and 2), the errors amount to less than 5% of the measured data over the upper 3500 m of the glacier, but are 22% to 94% of the measured data over the lower 1500 m. These errors are too large to provide reasonable constraint, which suggests that the recovered basal velocity profile cannot be trusted in the lower part of the glacier. However, the errors are proportionately higher over the lower part of the glacier because the measured velocities are much lower. With such low values of surface velocity, there are few possibilities for the basal velocity profile. This increases the reliability of the basal velocity profile over the lower 1500 m of the glacier, despite the high proportion of uncertainty in the data.

Sensitivity tests conducted to examine the influence of uncertainty in the data can shed light on the reliability of the results. Inversions are run for the summer 2007 dataset using the spectral decomposition method and fractions of the default errors associated with the measured data. Figure 4.37 presents results obtained using errors of 0.50, 0.25, 0.10 and 0.01 of the default errors. The results, described in Section 4.3.4, show that the basal velocity profile obtained with half errors is identical to the profile obtained with the default errors. The profile obtained with errors of 0.25 of the default errors is also identical to the profile obtained with the default errors for the lower 1500 m of the glacier. In this area, the default errors range from 22% to 94% of the measured data. The fact that the basal velocity profile remains the same in this area when errors are divided by four weighs in favour of a reliable result.

Oscillations in the basal velocity profile for the annual datasets

The basal velocity profiles generated from inversion of the two annual datasets present suspicious oscillations in the area between 2000 m and 3000 m along the flowline. In this area, the recovered basal velocity exceeds the measured (and predicted) surface velocity by up to 20 m/a in two locations. The forward model is defined so that the surface velocity may not be the sum of the basal and deformational velocity at each location along the flowline, but rather over a certain distance (the averaging length). However, such an excess seems unrealistic from a glaciological point of view.

Truffer (2004) reported that inverting the surface velocity data without taking into account the associated error by using a misfit condition (ie: fitting the data exactly) results in a basal velocity profile presenting oscillations. The errors associated with the annual datasets are indeed so small that inversion attempts to fit the data almost exactly. The oscillations observed in the annual datasets are therefore probably associated with the particularly small errors on the data.

The tests conducted to assess the sensitivity of the basal velocity profile to the uncertainty in the data are meant to help verify this hypothesis. First, it is interesting to note that when the inversion is run with errors of 0.10 and 0.01 of the default errors associated with the summer 2007 dataset, the resulting basal velocity profile presents oscillations of small amplitude over most of the length of the glacier. These oscillations are not present when higher errors are used and must therefore be caused by the particularly small errors. An additional set of tests is conducted on the 2007-2008 annual dataset. The errors associated with the data are multiplied by factors of up to 20. Results are described in Section 4.3.4 and shown in Figure 4.38. The recovered basal velocity profile remains unchanged for errors up to 16 times the default errors. For errors of 17 times the default errors and higher, the basal velocity presents no oscillations and does not exceed the surface velocity (except for a very small area). The switch between the two basal velocity profiles is not gradual, suggesting that oscillations are triggered when the errors on the data drop below a given threshold. The basal velocity profile obtained with errors higher than 17 times the default errors is very similar to the profile obtained for the summer 2006 dataset using the same inversion method. Moreover, the increased errors are of the same order of magnitude as the errors associated with the summer 2007 surface velocities.

Decreasing errors on the data triggers small-amplitude oscillations in the summer 2007 dataset and increasing errors suppresses the oscillations in the 2007-2008 annual dataset. This strongly suggests that the oscillations are indeed caused by the especially small uncertainties in the measured data. Moreover, the fact that the basal velocity profile obtained with increased errors from the 2007-2008 annual dataset is similar in shape to both summer datasets suggests that the basic structure of the recovered basal velocity is not an artefact produced by specific inversion settings.

Effect of pole locations and other sources of error

The location of poles controls the distribution of data along the flowline and influences the resulting basal velocity profile. The inverse problem is underdetermined, and thus there are many more locations at which the basal velocity profile is estimated than data points. As a consequence, the recovered basal velocity profile may not be accurate in areas between pole measurements. The influence of pole location on the recovered basal velocity can be illustrated by comparing the results obtained for the summer 2006 dataset (Figure 4.22) and the summer 2007 dataset (Figure 4.23). In Figure 4.23, the basal velocity profile exceeds the measured surface velocity in the area between the poles located at 2150 m and 2750 m along the flowline. Because there are no measured data between these two poles, it is difficult to assess the reliability of the basal velocity profile in this section of the flowline. In the summer 2006 dataset, there is a surface velocity datum in this section, as a pole is located at 2500 m along the flowline between the 2150 m and the 1750 m poles. The resulting basal velocity profile, shown in Figure 4.22, is therefore different in this section and the basal velocity only exceeds the surface velocity measurements by a few meters per year. The additional datum thus has a constraining effect on the basal velocity in this area and thus makes the resulting profile more reliable.

Additional sources of error limit the reliability of the basal velocity profile as a true flowline profile. First, the flowline itself is uncertain. An approximate flowline was theoretically identified from the map 115 B/14 covering the area around Kluane Glacier, produced from aerial photographs taken in 1977, by identifying the direction of steepest slope. The locations of surface velocity measurements were subsequently chosen so that poles were distributed along the approximate flowline. Because not all locations along the approximate flowline are easily accessible, some poles are slightly off the approximate flowline, introducing an additional source of error. Moreover, it is assumed in this work that the ice flow at each pole location is tangential to the flowline. However, some poles are installed on steep slopes that are not orthogonal to the flowline, which may give rise to flow that is not tangential to the flowline. These additional sources of error affect the representativeness of the data and, therefore, the reliability of the recovered basal velocity profile.

Note on the results obtained with the annual datasets

As mentioned above, a factor of 17 was shown to suppress oscillations in the basal velocity model for the annual datasets and the increased errors used to generate the annual basal velocity profiles are of the same order of magnitude as the uncertainty in the summer datasets. Increasing the magnitude of the errors can be justified by the fact that the original calculated errors do not account for uncertainties in the position of the flowline itself, nor do they account for the fact that some poles are slightly off the flowline and may not have velocities tangential to it. For the two annual datasets, the contribution of basal motion obtained with the increased errors is therefore used to interpret and discuss the results from a glaciological point of view (Chapter 5).

4.4.3 Sensitivity tests

The sensitivity of the inversion results to the shape factor, the flow-law coefficient, the longitudinal coupling length and the uncertainty in the data is tested in Section 4.3.4. The results of these tests, presented in Section 4.3.4, are discussed in the present section, with the exception of the sensitivity to uncertainty in the data which has already been discussed above.

Sensitivity to the shape factor

The shape-factor profile used as input in both the control tests and the inversion of real data is computed from ice thickness and glacier width data for a semi-elliptical bed. In view of the bed DEM, the semi-elliptical shape is judged to be representative of the overall bed shape. However, subsequent inspection of glacier cross-sectional profiles indicates that the bed shape is closer to a rectangle in the north-eastern reaches of the glacier and closer to a parabola at a few locations in the north-west and near the terminus of the glacier. It is thus of interest to quantify how such a deviation from the semi-elliptical bed shape affects the contribution of basal motion to the total glacier motion. Shape-factor profiles computed for rectangular, semi-elliptical, and parabolic bed shapes are presented in Figure 4.27. The profiles obtained with all three bed shapes are identical over most of the length of the glacier and differ only over the upper $\sim$1000 m of the flowline. In this area, the difference in the contribution of basal motion to the total glacier motion is only significant for a rectangular bed shape (as compared to the semi-elliptical bed shape used as default throughout this work). The contribution of basal motion obtained with the rectangular bed shape in the upper reaches of the glacier is lower than the contribution obtained with the default semi-elliptical bed shape in the same area. The sensitivity of the inverse model to the shape of the bed is thus negligible over most of the length of the glacier. In light of this sensitivity test, a lower contribution of basal motion over a small section (a few hundred meters long) of the flowline in the north-eastern reaches of the glacier due to a rectangular bed shape is possible. The argument developed in Chapter 5 relies on the fact that the contribution of basal motion is especially high. This argument remains valid in regard of the results of this sensitivity test, since the proportion of basal motion is important over most of the length of the glacier, regardless of the bed shape used in the inverse model.

Sensitivity to the flow-law coefficient

The transient temperature-depth model used in Section 4.2.5 to calculate effective values of ice temperature has limitations and is based on several assumptions. Because this model is not thermomechanically coupled, feedback between the dynamics and the temperature of the ice mass is not modelled. Thus advection of heat to deeper ice layers is not accounted for in the model. The refreezing heat pump mechanism is neglected as well. Meltwater percolating through the ice during the day often refreezes over night in the accumulation zone of alpine glaciers, thus releasing latent heat and warming the surrounding ice (Paterson, 1994). For alpine glaciers, this mechanism is thought to contribute to warming the ice over the accumulation area in summer. Neglecting the effect of heat advection and meltwater refreezing can introduce errors in the effective temperature.

In Section 4.3.4, the contribution of basal motion is computed for flow-law coefficients corresponding to effective ice temperatures of 0°C, -2°C, -5°C and -10°C. The default effective temperature used in the control tests and inversion of real data is -2°C. Figures 4.32 and 4.33 illustrate the effect of such a variation in the flow-law coefficient on the contribution of basal motion. Results show that there is no significant change in the contribution of basal motion for an effective temperature of -5°C, but that the contribution of basal motion increases significantly for an effective temperature of -10°C and decreases significantly for an effective temperature of 0°C. Modelling of temperature with depth and derivation of depth-integrated effective temperatures, presented in Table 4.3, showed that an effective temperature of -10°C is not realistic for the study glacier. However, the temperature of 0°C is closer to the effective temperatures obtained by considering a glacier bed at the pressure melting point and is thus a more plausible situation than the -10°C effective temperature. In this case, the contribution of basal motion is lower over the whole length of the glacier, but still accounts for over 50% of the total glacier motion over most of the length of the flowline. In addition, Paterson's value of the flow law coefficient at 0°C has been found to be too high for temperate ice by several authors (e.g. Hooke, 1981; Hubbard et al., 1998; Gudmundsson, 1999). Truffer et al. (2001) use a value of A that is about half of the value recommended by Paterson to calculate flow through a glacier cross-section using a finite-element ice-flow model. If the value of the flow-law coefficient used for 0°C here is indeed excessive, then the contribution of basal motion for this temperature may be higher than modelled.

An additional test was run to determine what magnitude of the flow-law coefficient is required to explain the surface velocity entirely in terms of deformation. It was found that an increase in A of less than an order of magnitude has little impact on the contribution of basal motion, but a 10-fold increase decreases the contribution of basal motion below 50% over most of the length of the glacier, with the exception of a few peaks (see Figure 4.34). The flow-law coefficient depends not only on the ice temperature, but also on many other factors such as the effect of impurity content and crystal orientation. Values of A describing the rheology of actual glacial ice may thus be higher than the value of $6.8 \times 10^{-24}\,\mathrm{Pa}^{-3}\mathrm{s}^{-1}$ advocated by Paterson (1994) for an ice temperature of 0°C. For example, Budd and Jacka (1989) measured a value of $A = 9.3 \times 10^{-24}\,\mathrm{Pa}^{-3}\mathrm{s}^{-1}$ in the laboratory. Marshall (2005) states that for a given temperature, the flow-law coefficient can vary by up to a factor 10 due to the factors mentioned above. It could thus be possible that the proportion of basal motion is indeed lower than modelled. However, a situation in which the flow-law coefficient varies by a factor of 10 from the value advocated by Paterson seems extreme and deformation is most certainly not responsible for all glacier motion. The uncertainty associated with the rheology of ice could be lowered by experimentally constraining the flow-law coefficient using borehole inclinometry measurements.

Sensitivity to the longitudinal coupling length

A final set of tests was conducted to explore the sensitivity of the inversion results to the longitudinal coupling length l. The longitudinal coupling length was varied from the default value of three ice thicknesses ($l = 3\,h$) to 1, 2, 4 and 5 ice thicknesses. The results, presented in Figures 4.35 and 4.36, show that the effect of the value of l on the contribution of basal motion is only significant when l is increased to four or five ice thicknesses (from the default value of three ice thicknesses). The deviations are visible for the four datasets and are restricted to short sections of the flowline in each case. Therefore, sensitivity of the inversion results to the longitudinal coupling length is low. The longitudinal coupling length depends on the geometry of the glacier and on the basal velocity itself. Iterative calculation of this quantity within the inversion scheme would help estimate and possibly improve the reliability of the modelled basal velocity profile.

4.4.4 Uncertainty in the forward model

Finally, it is important to note that the forward model itself offers no guarantee to be a good model of reality and should not be used to predict surface measurement with a high accuracy. The forward model is therefore uncertain in itself, although errors are difficult to assess. One way to qualitatively assess these errors would be to generate a set of synthetic data using a more accurate model (such as a full Stokes model taking into account all stresses) and then invert these data using the forward model used in this work.

Chapter 5

Interpretation and discussion

In this chapter, the results from the inversion of surface velocity data, presented in Chapter 4, as well as results from upstream area calculations (Appendix D) and balance velocity modelling (Appendix E) are discussed from a glaciological point of view. Arguments are synthesized in Section 5.6.

5.1 Spatial structure of the glacier flow regime

Based on observations made between 2006 and 2008 and our modelling results, the study glacier can be divided in three zones, each dynamically and morphologically distinct. This three-zone pattern is reflected in surface features, surface velocities and basal motion. The first zone spans the lower ∼1700 m of the glacier, the second zone spans ∼1700–3300 m from the terminus, and the third zone covers the upper part of the glacier, from ∼3300 m to 5000 m along the flowline.

The lower ∼1700 m of the glacier are free of crevasses and present a less variable surface slope than the rest of the glacier. The zone between 1700 and 3300 m exhibits surface undulations about 20 to 30 m high. The upper zone also presents variable surface slopes and undulations, but the undulations are associated with two prominent icefalls. Both central and upper zones are crevassed, with many areas of extensive crevassing in the central zone. Several crevasses in both the central and upper zones appear to have formed very recently. Moulins are present in the lower zone, but not in the central or upper zones. While the transition between central and upper zones is visually subtle, the transition between the lower and central zones is well defined and plainly visible on aerial photographs (Figure 5.1).

This three-zone structure is reflected in the annual and summer surface velocity measurements, with the lowest velocities (3–20 m/a) over the lowermost ~1700 m of the flowline, velocities from 20 to 40 m/a in the central region (~1700–3300 m), and from 10 to 30 m/a in the upper region. It can be argued that the refreezing heat pump mechanism may contribute to the relatively high summer velocities observed over the central and upper zones of the glacier. Sensitivity tests show that considering ice at an effective temperature of 0°C results in a significant decrease of the contribution of basal motion over the upper 1000 m of the flowline only (Figures 4.32 and 4.33). The refreezing heat pump mechanism is therefore not sufficient to explain the observed surface velocity over the central zone of the glacier. The very low surface velocities measured over the lower glacier suggest that this ice is nearly stagnant and may be a remainder of the last surge. A surface flowline profile generated from 1977 map data (before the reported surge in the 1980s) indeed shows that the glacier terminus was located ~800 m further up-valley (Figure 5.2).

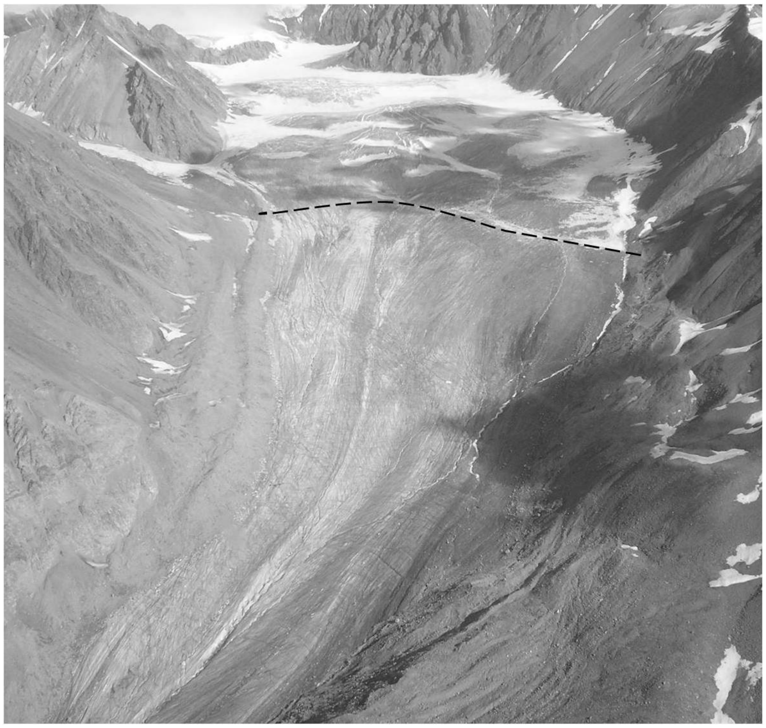

Figure 5.1: Photograph of the study glacier in August 2005 showing the transition (dashed line) between the slow-flowing ice over the lowermost ~1700 m of the glacier and the faster-flowing ice characterized by surface undulations ~20–30 m high above. Credit: G. Flowers.

The contribution of basal motion (shown in Figure 5.4) and the basal velocity (shown in Figure 5.3) also exhibits a three-zone pattern. The basal velocities are low, between 2 m/a and 10 m/a both in summer and annually, in the lower zone, and much higher, up to 30 m/a annually and up to 45 m/a in summer, over most of the central zone. Basal velocities range from zero to ∼15–20 m/a in the upper zone. The contribution of basal motion is high in the lower zone, between ∼70% and 90% in the summer, and slightly lower, between ∼50% and 90% annually. In the central zone, with the exception of a short distance along the flowline at ∼1700–1800 m, the contribution of basal motion is high (70–100%) over most of the year. In the upper zone, the contribution of basal motion ranges between 0% and 80%. Both the surface velocity and the contribution of basal motion show seasonal variability over the lower zone (0–1700 m), although the difference in the surface velocity is smaller than the measurement errors in general. The surface and basal velocities show substantial seasonal variability over the central zone (1700–3300 m). Because the water pressure at the interface between ice and bed directly influences basal motion, we expect that the seasonal variation in the contribution of basal motion over the lower zone of the glacier is related to a seasonal variation in basal water pressure. The relationships between surface velocity, basal motion and subglacial hydrology are discussed in more detail in Section 5.3.

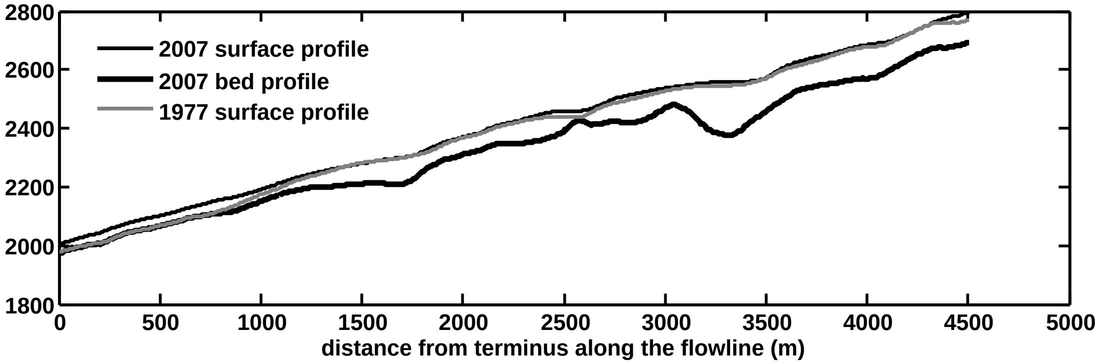

Figure 5.2: Glacier surface profiles in 1977 and 2007. The 2007 surface profile is derived from the surface DEM in Chapter 3 and the 1977 surface profile is derived from a surface DEM constructed from the map of the area of Kluane Glacier.

The extensive crevassing observed in the central zone (∼1700–3300 m) is consistent with the high velocities over this area. Fast flow indeed leads to higher longitudinal stresses, which in turn promote crevassing. In addition, the surface undulations observed between

1700–3300 m from the terminus are consistent with the high contribution of basal motion modelled over this area for all datasets. Such a flow regime is expected to enhance the transmission of basal topography to the glacier surface as demonstrated by Gudmundsson et al. (2003). The arguments presented in this section are summarized in Table 5.1.

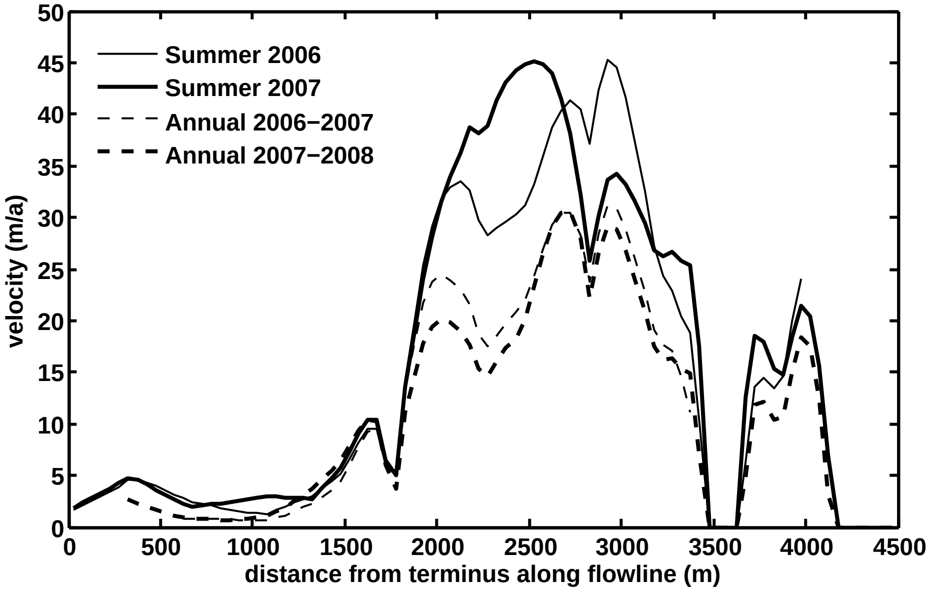

Figure 5.3: The modelled basal velocity for each of the four datasets is plotted as a function of distance along the flowline. Increased errors (see Section 4.4) are used for the two annual datasets.

5.2 A peculiar flow regime

The measured surface velocities over the upper 3500 m of the glacier, especially between ~1700 and 3300 m along the flowline, are higher than expected for a surge-type glacier of this size in its quiescent phase. The theoretical deformational velocities, calculated in Chapter 4, are below 10 m/a over most of the length of the glacier, except for a few locations where the surface slope is steep (the peak at ~3500 m along the flowline is associated with an icefall) or where the ice is thick. Basal motion is usually responsible for only a small fraction of the total motion of a surge-type glacier in its quiescent phase, and thus annual quiescent-phase surface velocities for a glacier of this size, slope and thickness are expected to be relatively low. Examples of reported quiescent phase surface velocities are given

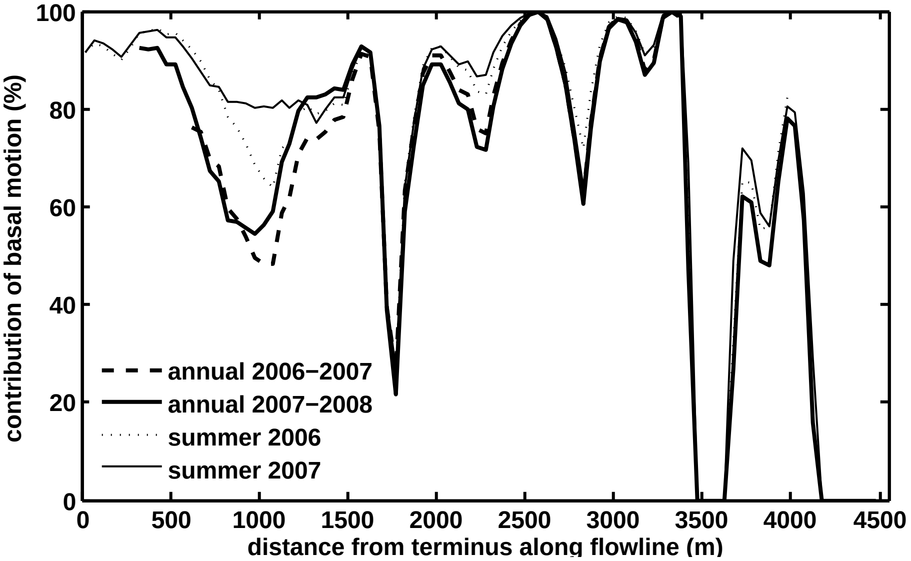

Figure 5.4: The contribution of basal motion for each of the four datasets is plotted as a function of distance along the flowline. Increased errors (see Section 4.4) are used for the two annual datasets.

Approximate distance from terminus along the flowline (m)	**0–1700**	**1700–3300**	**3300–5000**
Surface profile	slope variations of small amplitude	undulations	undulations (associated with icefalls)
Moulins present	yes	no	no
Crevasses present	no	yes	yes
Fresh crevasses	N/A	yes	yes
Annual surface velocity (m/a)	∼3–10 (low)	∼10–30 (high)	∼10–20 (medium)
Summer surface velocity (m/a)	∼3–20 (low)	∼20–40 (high)	∼10–30 (medium)
Seasonal cycle in surface velocity	?	yes	weak
Contribution of basal motion	high in summer, medium annually?	high	medium
Inferred summer subglacial drainage system	efficient	less efficient	less efficient

Table 5.1: Summary of observations and model results for the three zones

in Chapter 1, Section 1.1.3. Surface velocities typically undergo a 10- to 100-fold increase during a surge, with average surge velocities ranging from 100 m/a to over 1000 m/a for small glaciers in Alaska and south-western Yukon (Meier and Post, 1969). The surface velocities measured on the study glacier are therefore much lower than typical surge velocities for the Alaska/Yukon region.

Inverse modelling reveals that basal motion is responsible for 50 to 100% of the total glacier motion for both summer and annual velocity datasets. The high contribution of basal motion is characteristic of surging glaciers and is the result of high basal water pressures, themselves thought to be caused by persistent inefficient subglacial drainage (e.g. Kamb et al., 1985).

5.3 Subglacial hydrology

The distribution of upstream subglacial drainage area, presented in Appendix D, suggests a propensity for channelization along the flowline over the lower 750 m of the glacier and east of the flowline from ∼1000 m to ∼3000 m. The surface hydrology of the lower ∼1700 m of the glacier is characterized by supraglacial streams that terminate in moulins, several of which are close to the flowline. One of the most prominent streams originates from a pond that forms in an overdeepening at 1700 m along the flowline. Water also accumulates in an overdeepening at ∼2600 m, but this is the only supraglacially stored water found in the central and upper zones of the glacier. Although surface streams and moulins are absent above ∼1700 m, it is still possible for water to reach the bed through crevasses.

Given the predisposition to a channelized subglacial drainage system suggested by the upstream area calculation, it seems likely that the concentrated water sources over the lowermost 1700 m of the glacier (water flowing from the supraglacial streams into moulins) would contribute to efficient channelized drainage in this area. Moreover, the very thin ice (30–50 m) over the lowermost 750 m of the flowline leads to very low deformation rates, which would contribute to keeping the subglacial channels open. If interpretable, the seasonal variations in the contribution of basal motion over the lower zone, showing a higher contribution for the summer datasets than for the annual datasets, suggest that the contribution of basal motion may be low throughout the fall and winter seasons and only peak in summer when the water fluxes are higher.

The high flow speeds and high fraction of basal motion over the central zone (~1700–3300 m) are suggestive of generally high basal water pressures and an inefficient drainage system. These results seem incompatible with the suggestion of channelized drainage from the upstream area calculation, and indicate that topography is not the primary control on the current subglacial hydrology in the central zone of the glacier. The relatively distributed injection of water through crevasses in the central reaches of the glacier would not promote channelized drainage as strongly as the injection of water through moulins as found over the lower reaches of the glacier. Moreover, the fast basal velocities modelled in this area would contribute to the closure of subglacial hydraulic pathways. Evidence is thus in favour of a relatively inefficient drainage system over the central zone (~1700–3300 m) of the glacier, causing meltwater to accumulate at the bed and thus raising the basal water presssure. This would in turn enhance sliding of the glacier over its bed and deformation of any underlying sediments.

In addition, the seasonal variation of the drainage system in the central zone is most likely not as strong as in the lower zone, as evidenced by its high annual basal motion contribution. Because fast flow may inhibit the development of channels in the summer, some of the surface meltwater produced in summer may remain at the glacier bed throughout the season and into the following winter. This would lead to relatively high basal water pressures persisting throughout the winter, even in the absence of substantial water injection.

5.4 Balance velocity calculations

Jóhannesson et al. (1989) predict a characteristic time-scale of 10 to 100 years for the adjustment of typical mountain glaciers (of length 1-20 km and velocity at the teminus of 1-10 m/a) to changes in mass balance. A glacier is therefore not expected to be in equilibrium with each balance year, thus a long-term mass balance record is required to make a valid comparison between measured and balance velocities. However, mass balance data for the study glacier are only available for the year 2006-2007. I nevertheless derive a 2006-2007 balance velocity profile from these data (Appendix E) and find that the balance velocity is zero over the lower ~3500 m (lower and central zones) of the glacier and <5 m/a over the upper ~1500 m. This result can only be interpreted if the 2006-2007 mass balance reflects the longer-term mass balance.

An additional experiment shows that with a fictitious net balance distribution similar in shape to the 2006-2007 measured net balance distribution, a total net balance of -0.03 m.w.e. is required to generate surface velocities of the same magnitude as the measured surface velocities (Appendix E). This mass balance does not seem unrealistically high, however there is little evidence that mass balance has been close to zero any time recently in the St. Elias Mountains. Using repeat airborne laser altimetry, Arendt et al. (2002) calculate rates of thinning of (∼1.8 m/a) for the nearby Kaskawulsh Glacier from the mid-1950s to the mid-1990s, and somewhat lower rates of thinning (>0.5 m/a) for the period ∼1995 to 2001. More recently, Arendt et al. (2008) found the St. Elias Mountains to have the highest rates of ice mass loss in Alaska/north-western Canada for 2003–2007 based on data from the Gravity Recovery and Climate Experiment (GRACE). Measured surface velocities are therefore probably substantially higher than the recent glacier balance velocities.

The balance velocity calculations described in Appendix E assume a constant glacier profile, and thus a rate of thickness change that is equal to zero. The rate of thickness change is likely negative in reality, as the glacier appears to have thinned substantially over the past decades. Balance velocity calculations suggest that the glacier flow regime is out of balance with climate and is unsustainable. Mass balance has likely been more positive some time in the past, and the flow regime may have yet to adapt to the recent negative mass balance. Alternatively, the current flow regime may be characteristic of a surge. Evidence in favour of one or the other of these hypotheses could be provided by calculating the rate of thickness change along the glacier flowline. A delay in the glacier response to changes in mass balance would result in thinning of the ice over the whole length of the glacier. A surge would modify this profile by redistributing ice from the reservoir to the receiving area.

5.5 The slow surge of Trapridge Glacier and the surging history of the study glacier

Frappé and Clarke (2007) recently reported on the last surge of Trapridge Glacier, a small polythermal glacier located in the St. Elias Mountains, Yukon Territory, Canada. Trapridge Glacier is located about 80 km from our study glacier and is of similar size. The evolution of ice flow and glacier geometry between 1951 and 2005 was monitored using a combination of air photographs and ground-based optical surveys. Pole survey measurements, available for most of the 1969-2005 period, suggest that the glacier was surging from ∼1977 until ∼2000, but surging surface velocities were only about four times higher than quiescent phase velocities (in constrast to the 10- to 100-fold increase reported by Meier and Post (1969) for glaciers in this region). The terminus advanced by 450 m over the surge period, a much shorter distance than the ∼1 km advance of the previous 1930s surge. Based on a ∼60 m advance of the terminus between 1939 and 1941 reported by the expedition geologist R. P. Sharp and on photographic evidence showing that the glacier terminus occupied a similar position in 1941 as at the end of the last surge in 2000, the authors suggest that the previous surge of Trapridge Glacier may have proceeded in two phases, with a period of slow advance initiated before 1939, followed by a presumably short period of fast surging some time after 1941. Such periods of slow advance are usually classified as periods of flow acceleration, taking place at the end of the quiescent phase, rather than as part of a surge. Because of its slow flow regime and especially long active phase, the 1977–2000 surge is likened to the slow advance phase that is thought to have taken place before 1941. The authors hypothesize the existence of a different model of surge evolution with multiple switching events rather than one single switch from slow to fast flow. The multiple-switch model would explain the proposed evolution of the 1930s Trapridge Glacier surge, in which the first switching event would terminate the quiescent phase and initiate a period of "slow surging" of unknown duration and a second switching event would trigger a shorter period of fast, typical Alaskan-type surging. The authors suggest that a decrease in net accumulation over the past few decades prevented the build-up of sufficient mass in the reservoir area to allow Trapridge Glacier to reach the fast-flow phase of the surge. The 1977-2000 surge of Trapridge Glacier reported by Frappé and Clarke (2007) is the only detailed account of a so-called "slow surge" in western North America.

The peculiar dynamics currently exhibited by the study glacier are reminiscent of the 1977-2000 surge of Trapridge glacier. However, unlike for Trapridge Glacier, little is known about the surging history of the study glacier. An aerial photograph taken around 1951 (Figure 5.5) shows the glacier during what has been interpreted as a surge (P. G. Johnson, personal communication, 2006), with the terminus located about 1km further down-valley than at present. Another surge in the late 1980s has also been reported (P. G. Johnson, personal communication, 2006). For lack of further information, this might suggest a surge period of 30–40 years, a value within the range established by Meier and Post (1969) for surge-type glaciers in the St. Elias Mountains.

Figure 5.5: Photograph of the study glacier taken around 1951 (J. O. Wheeler Collection). The glacier is interpreted to be surging, with the terminus about 1 km.

5.6 Synthesis

The dynamics and morphological characteristics of our study glacier lead to the identification of three distinct zones: thin, nearly stagnant ice in the lower zone (0–1700 m), thicker, crevassed, faster-flowing ice with a high fraction of basal motion and pronounced surface undulations in the central zone (1700–3300 m) and less active, but relatively fast-flowing ice in the upper zone (3300–5000 m). Characteristic features usually observed during glacier surges, such as a propagating bulge, lateral shear margins and extensive chaotic crevassing, are not evident on the study glacier. However, the relatively high surface velocities and the high proportion of basal motion, combined with the observation of newly formed crevasses in the upper 3500 m of the glacier suggest that the glacier is not in a state of quiescence.

The study glacier is shown surging around 1951 in Figure 5.5, according to P. G. Johnson (personal communication, 2006). The terminus is located about 1 km further down-valley than at present, and the surface of the lower and central zones is clearly crevassed, though not as heavily as one might expect for a surge. This suggests that the study glacier may have undergone fast Alaskan-type surges in the past. Another surge was reported in the late 1980s, and thus a surge period of ∼30–40 years can be hypothesized, in which case a new surge might be expected to begin in the period ∼2010–2030. Given that surge periods can vary with time, the present flow regime could be indicative of a peculiar surge. In Figure 5.5, the upper ∼2000 m of the glacier show less evidence of crevassing than the lower ∼3000 m. This may indicate that only the central and lower zones (<3300 m) of the glacier surge, which is not unusual for valley glaciers of any size. Meier and Post (1969) report that only the lower half of Kluane Glacier surges. The hypothesis that only the central and lower zones of the glacier may surge is consistent with the fact that both the velocity and the contribution of basal motion are highest in the central zone.

Upstream area calculations and field observations suggest that water is drained through an efficient channelized system in the lower 1700 m of the glacier. Above 1700 m, the high modelled contribution of basal motion and the observation of many crevasses, which allow water to reach the bed in a distributed manner, argue against a topography-controlled channelized drainage system and suggests that the current drainage system is strongly influenced by other processes.

Balance velocity calculations suggest that the current flow regime is not in equilibrium with the recent negative mass balances of the region. Lefauconnier and Hagen (1991) link the consistently negative mass balance in Svalbard to surges that are released with less ice mass, and that are thus weaker, slower surges. If the strongly negative mass balance recorded for 2006-2007 is characteristic of a longer period (e.g. Arendt et al., 2002, 2008), then the current surface velocities are not characteristic of a sustainable quiescent flow regime and it seems possible that the glacier has been unable to accumulate sufficient mass to support a vigourous surge. These arguments lead us to conclude that the study glacier may be undergoing a “slow surge” as described by Frappé and Clarke (2007) for Trapridge Glacier.

Hewitt (2007) reports on an unprecedented sudden concentration of surges at Panmah

Glacier, Karakoram, Himalaya. Four tributaries of Panmah Glacier surged in the same decade at times that are not consistent with known surge periods. The author suggests that recent changes in climate might have triggered this unusual concentration of surges. If changes in glacier mass balance are having a significant effect on the nature of glacier surges, this challenges the traditional notion of surges being independent of climate (e.g. Meier and Post, 1969; Paterson, 1994) and this relationship may need to be reconsidered.

5.7 Limitations and outlook

The present work sheds light on the peculiar dynamics of the study glacier. However, there are several limitations to our analysis, some of which could be eliminated with further data or an improved model. The various limitations associated with the one-dimensionality of the forward model used in this study and possible strategies to upgrade the one-dimensional flowline model to a two- or three-dimensional ice-flow model are discussed in the first two paragraphs. In the third and fourth paragraphs, simple adaptations to the current model that could improve the quality of the inversion results are discussed.

The forward model of glacier flow used in combination with geophysical inversion methods to compute basal velocities is a one-dimensional flowline model and thus yields a one-dimensional basal velocity profile. Because the model is one-dimensional, ice flow that is not tangential to the flowline is not taken into account, and the effect of lateral shear stresses on the ice mass is approximated using the shape factor. Moreover, as mentioned in Chapter 4, the temperature of the ice varies with depth, which causes the rheology of the ice to also vary with depth. The flow-law coefficient is used to calculate the velocity due to deformation at the surface of the glacier, which is a major input to the inversion routine. However, the one-dimensional model does not account for variations of the flow-law coefficient with depth. This problem was circumvented by using a one-dimentional thermal model to calculate an effective temperature for the glacier. More reliable results would likely be achieved by (1) calculating or measuring effective temperatures at many locations along the flowline, or (2) adapting the forward model to take into account vertical variations in ice rheology.

In addition, the fact that the model is one-dimensional restricts our knowledge of basal motion to the area along the glacier flowline. It would therefore be very useful to adapt the forward model and inversion methods to allow modelling of basal motion over the whole glacier area. The transformation of our 1-D flowline model to a two- or three-dimensional model is indeed not straightforward and cannot be carried out using the forward model in this work (see Chapter 4). However, 2-D and 3-D ice-flow models exist that take into account longitudinal stress gradients (e.g. Muller, 1991; Colinge and Blatter, 1998; Pattyn, 2002; DePonti et al., 2006) and can possibly be adapted to our purpose. Such models usually require information about basal conditions as input, such that inversion of surface velocities should therefore be carried out by iteration, and the parameters describing the basal boundary condition adjusted at each iteration. Another possibility is a forward model in which basal and deformational velocities are solved for simultaneously, using a Coulomb-type friction law to parameterize the basal boundary condition (e.g. Schoof, 2005). Models of ice flow in which longitudinal stress gradients are accounted for are usually non-linear. Since neither of the two methods used in Chapter 4 can be used to solve non-linear inverse problems, a different inversion method would be required. Upgrading the one-dimensional flowline model used in this study to a two- or three-dimensional ice-flow model would therefore require the use of a completely different methodology and the design of a new forward model.

Simpler adaptations to the current model and inversion method could be made to incrementally improve the quality of the results. The sensitivity tests performed in Chapter 4 indicate that the inversion scheme is fairly robust with respect to the longitudinal coupling length, the flow-law coefficient and the shape factor. However, the basal velocity profile would be better constrained if these parameters were known. Kamb and Echelmeyer (1986) showed that the longitudinal averaging length is a function of glacier geometry and basal velocity. This parameter could be better constrained by iteration. A first-guess averaging length could be computed using the reference model as a basal velocity profile, then this first-guess could be refined by using the output of the inversion to calculate a new averaging length to use as input in the inversion. The iteration process would then be continued until basal velocities stabilize.

A shape factor profile is used to calculate a deformational velocity profile, which is itself used as input of the inversion. The value of the shape factor depends on the bed-shape model used. In this study, a semi-elliptical bed shape was used over the whole length of the flowline, but inspection of glacier cross-sectional profiles reveals that the bed shape differs slightly from a semi-ellipse at several locations along the flowline. Generating a shape-factor profile that takes into account local bed shapes would improve the reliability of the inversion results. The robustness of the inversion algorithm with respect to the flow-law coefficient was also tested in Chapter 4. As mentioned in Section 4.4, factors such as ice fabric or impurity content can produce variations of up to a factor of 10 in the flow-law coefficient (e.g. Marshall, 2005). To help improve the reliability of the inversion results, the value of the flow-law coefficient could be constrained with borehole inclinometry on the study glacier.

A simple way to assess the reliability of the inversion result is to calculate resolving functions. This can be done by running a point perturbation (a Dirac delta distribution) through the forward model to generate a set of synthetic data, which are subsequently inverted. The result is a bell-shaped curve whose half-width gives a measure of the maximum spatial resolution that can be resolved in the inversion. Resolving functions are useful to determine the level of detail to which inversion results should be interpreted.

The morphology and dynamics of the study glacier have only been investigated for three years, and no significant changes in flow regime or glacier geometry have been recorded over this three-year period. Careful recording of the evolution of both surface and basal dynamics over a longer period, as well as a longer mass balance record, would be required to confirm or invalidate the hypothesis of a slow surge, and relate the overall dynamics of the study glacier to the regional climate.

Chapter 6

Conclusion

Glaciers of the Yukon/Alaska region are currently undergoing substantial mass loss and are making major contributions to sea level (Arendt et al., 2002). Glacier-climate sensitivity studies that take glacier dynamics into account are needed to assess and understand the response of these glaciers to climate, especially tidewater and surge-type glaciers. The work presented in this thesis is a contribution to a study aimed at evaluating the sensitivity of glaciers to climate in the Donjek Range of the St. Elias Mountains. I have focused on the dynamics of a small unnamed surge-type glacier with an emphasis on its basal flow regime.

Surface elevation data, ice-penetrating radar soundings and pole displacement data were collected between 2006 and 2008 on the study glacier. These data helped characterize both the geometry and the dynamics of the study glacier. Annual (2006-2007 and 2007-2008) and seasonal (July/August 2006 and July/August 2007) surface velocity estimates along an approximate flowline, derived from the pole survey, revealed that surface velocities over the upper 3500 m of the 5000 m-long glacier are higher than expected for a surge-type glacier in its quiescent phase, but much lower than typical surge velocities. The velocity distribution along the flowline shows a distinct three-zone pattern, with very low velocities over the lower 1500 m of the glacier, especially high velocities over a zone ~1700–3300 m from the terminus and medium to high velocities above 3300 m along the flowline. This velocity pattern is reflected in the morphology of the glacier surface, and in the distribution of moulins and crevasses.

Digital elevation models (DEMs) of the glacier surface and bed are constructed by statistical kriging from the surface GPS and radar sounding data, respectively. The surface and bed DEMs are used to derive flowline profiles of the surface slope, ice thickness and shape factor, which are geometrical inputs required for the inverse model.

Geophysical inverse methods are used to constrain the contribution of basal motion to overall glacier motion. A one-dimensional flowline inverse model is developed to reconstruct basal velocities from the measured surface velocities. The forward model is defined by an analytical relationship between the basal, deformational and surface velocities of a simplified ice body flowing in a channel, and is subsequently linearized using a method of longitudinal averaging for variable ice thickness and surface slope. Two different methods (a deterministic inversion method and a singular value decomposition method) are used to invert the data. These methods are tested through a set of control tests using synthetic input data prior to the inversion of real data. The spectral decomposition method (SVD), identified as the most accurate, is found to generally yield good model results for the amounts of noise corresponding the errors on the measured data, and is used preferentially to derive subsequent results. Inversion of measured surface velocity data is then performed using the SVD method for four surface velocity datasets. Sensitivity of the inverse model to uncertain quantities such as the flow-law coefficient, the shape factor, the longitudinal averaging length and the errors on the data is quantified through a series of tests. The especially small uncertainties associated with the annual datasets trigger unrealistic oscillations in the recovered basal velocity profile for these datasets, but these oscillations can be suppressed by increasing the errors. The inversion routine is found to be otherwise relatively robust with respect to the four parameters tested.

Inversion of the measured surface velocities produced results that are similar for the four datasets, with the contribution of basal motion accounting for at least 50% and up to 100% of the total measured surface motion along most of the flowline. Measured surface velocities and the modelled proportion of basal motion are especially high over a zone ~1700–3300 m from the terminus. Such a high proportion of basal motion persisting throughout the year is unusual for a surge-type glacier in its quiescent phase. However, the characteristic features of a typical surge are not evident, which suggests that the study glacier is not undergoing a typical Alaskan-type surge. Upstream area calculations suggest a predisposition for efficient drainage over a zone above 1700 m from the terminus, whereas the high proportion of basal motion persisting throughout the year suggests a less efficient drainage system. This indicates that the subglacial hydrology is not strictly controlled by topography over this area and is strongly influenced by other processes. It seems probable that the subglacial drainage system is not efficient enough in this region to evacuate summer meltwater as fast as it is produced, leading to increased basal water pressures and high rates of basal motion throughout the year. Balance velocity calculations indicate that the current flow regime would require a more positive mass balance than the 2006-2007 net mass balance to be sustained. If mass balance has been consistently negative over the past few decades, it seems possible that the glacier has been unable to accumulate sufficient mass to sustain a vigourous surge, and the glacier may instead be undergoing a “slow surge” as described by Frappé and Clarke (2007) for Trapridge Glacier. The present climate trends may be influencing the surge vigour of the study glacier. I speculate that a continuing such trend could compromise the glacier’s future ability to surge entirely. Although a longer period of study would be required to validate the hypothesis of a slow surge, this possibility calls for renewed efforts to better understand the relationship between climate, mass balance and glacier surges.

Appendix A

Propagation of errors

This appendix presents the methods used to propagate errors for the displacement and velocity data presented in Chapter 2.

A.1 Four main rules to propagate errors

The following rules used to propagate errors are taken from Taylor (1982). For two independent variables x and y, with associated respective uncertainties δx and δy, we have:

$$(\delta f)^2 = \left(\frac{\delta f}{\delta x}\right)^2 (\delta x)^2 + \left(\frac{\delta f}{\delta y}\right)^2 (\delta y)^2. \tag{A.1}$$

The following rules are special cases of Equation A.1:

1. The error of the sum $z = x + y$ is given by:

$$\delta z = \sqrt{\delta x^2 + \delta y^2}; \tag{A.2}$$

2. The error of the product $z = x * y$ is:

$$\frac{\delta z}{|z|} = \sqrt{\left(\frac{\delta x}{x}\right)^2 + \left(\frac{\delta y}{y}\right)^2}; \tag{A.3}$$

3. The error associated with the product $z = B * x$, where B is known exactly, is:

$$\delta z = |B|\, \delta x; \tag{A.4}$$

4. Finally, the error associated with the function of one variable $z = f(x)$ is:

$$\delta z = \left| \frac{\mathrm{df}}{\mathrm{dx}} \right| \delta x. \tag{A.5}$$

A.2 Displacement errors

The horizontal displacement between two pole location measurements (N_1,E_1) and (N_2,E_2) is

$$d = \sqrt{(N_1 - N_2)^2 + (E_1 - E_2)^2}, \tag{A.6}$$

with $\delta N = \delta E = \delta$, since errors associated with Northing (N) and Easting (E) coordinates are the same. Using a simple change of variables, the displacement can be written

$$d = \sqrt{x^2 + y^2}, \tag{A.7}$$

where $x = N_1 - N_2$ and $y = E_1 - E_2$. From this, errors for x and y are easily calculated with Equation A.2:

$$\delta x = \delta y = \sqrt{\delta^2 + \delta^2} = \sqrt{2\delta^2} = \delta\sqrt{2}, \tag{A.8}$$

Displacement can also be written as a function of one variable: $d = f(z)$, with $z = x^2 + y^2$ and f a function such that $f(z) = z^{1/2}$. Following this and applying the error propagation rule presented in Equation A.4, we have:

$$\delta d = \left| \frac{\mathrm{df}}{\mathrm{dz}} \right| \delta z. \tag{A.9}$$

Inserting $f(z)$ leads to

$$\delta d = \left| \frac{\mathrm{d}}{\mathrm{dz}} (z^{1/2}) \right| \delta z, \tag{A.10}$$

and finally,

$$\delta d = \frac{1}{2} \left| z^{-1/2} \right| \delta z. \tag{A.11}$$

Let us now derive the error δz associated with the variable z. Since we have $z = x^2 + y^2$, the first rule for propagating errors (Equation A.2) applies and we obtain

$$\delta z = \left[\delta(x^2)^2 + \delta(y^2)^2 \right]^{1/2}. \tag{A.12}$$

Considering that $\delta(x^2) = \delta(f(x))$, where f is a function, and invoking the propagation rule for a function of one variable (Equation A.5), we have

$$\delta(x^2) = \left| \frac{\mathrm{d}}{\mathrm{dz}}(x^2) \right| \delta x, \tag{A.13}$$

which reduces to

$$\delta(x^2) = 2\,|x|\,\delta x. \tag{A.14}$$

In a similar fashion we obtain that $\delta(y^2) = 2\,|y|\,\delta y$. Incorporating these results in Equation A.12, factoring and using the expressions for δx and δy derived in Equation A.8, we find that

$$\delta z = 2\sqrt{2}\,\delta\,(x^2 + y^2)^{1/2}. \tag{A.15}$$

Substituting δz into Equation A.11, we obtain

$$\delta d = \delta\sqrt{2}. \tag{A.16}$$

A.3 Velocity errors

Velocity is linked to pole displacement by the relation

$$v = \frac{d}{n}, \tag{A.17}$$

where n is the length of the measurement period, in days (for our purpose both velocity and errors must be subsequently converted to m/a). Assuming there is no error associated with n, the propagation rule cited in Equation A.5 leads to

$$\delta v = \left| \frac{1}{n} \right| \delta d. \tag{A.18}$$

Appendix B

Basic glacier physics

This appendix presents the governing equations describing ice flow. These are basic principles, but the notation and development closely follows unpublished course notes from G.K.C. Clarke, "Theoretical Glaciology" (EOSC 554, UBC). Three governing equations are derived from conservation laws in the first section and a constitutive law, describing the rheology of ice, is presented in the second section. The temperature and strain rate equations, used in the thermal model (Section 4.2.5), are derived in the third section.

Let us first define the coordinate system. An idealized parallel-sided slab glacier of constant thickness h and constant slope θ is considered (Figure B.1). The longitudinal coordinate x is in the direction of the ice flow and parallel to the bed, the transverse coordinate y is perpendicular to the direction of flow, and the third coordinate z is perpendicular to both x and y. The coordinate $z = 0$ at the bed and $z = h$ at the glacier surface.

B.1 Continuity equations

Motion of a physical object within an isolated system occurs with conservation of mass, linear and angular momentum and energy. Glacier flow thus obeys basic laws describing the conservation of these quantities. These laws give rise to three continuity equations, also called balance or conservation equations, when expressed in a mathematical form. It is important to note that continuity equation is often used by glaciologists to refer specifically to the conservation of mass.

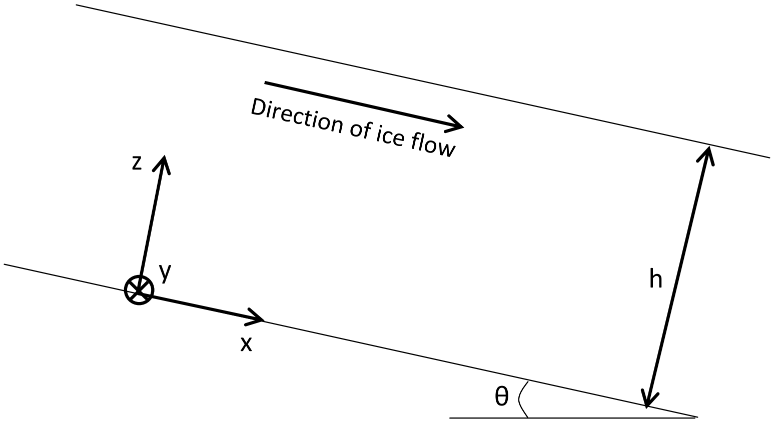

Figure B.1: Coordinate system for a slab glacier. A parallel-sided slab glacier of constant thickness h and slope θ is represented, along with the associated coordinate system. The transverse coordinate y points in the direction perpendicular to the plane formed by x and z.

B.1.1 Conservation of mass

Let us consider a parallel-sided slab glacier of constant thickness h, as described above (Figure B.1). This idealized glacier is of length L, so that $0 \leq x \leq L$. For such a glacier, the total volume V per unit width at the time t can be written

$$V(t) = \int_0^{\mathrm{L}} h(x,t)\,\mathrm{d}x. \tag{B.1}$$

Reynolds transport theorem is a fundamental theorem used in continuum mechanics to calculate the full time derivatives of extensive quantities in terms of their intensive counterparts. It states that the rate of change of an extensive property is equal to the integral of the sum of the time rate of change of its corresponding intensive property within the considered volume and the flux of the property through the surface of the volume. The material derivative is the local form of Reynolds transport theorem and can be written

$$\frac{\mathrm{d}h(x,t)}{\mathrm{d}t} = \frac{\partial h(x,t)}{\partial t} + \frac{\partial}{\partial x}\big(v(x,t)\,h(x,t)\big). \tag{B.2}$$

Applying Reynolds transport theorem:

$$\frac{\mathrm{d}V}{\mathrm{d}t} = \int_0^{\mathrm{L}} \left(\frac{\partial h(x,t)}{\partial t} + \frac{\partial q(x,t)}{\partial x} \right) \mathrm{d}x, \tag{B.3}$$

where the ice flux $q = \bar{v}\, h$ is the product of the depth-averaged ice velocity $\bar{v}$ by the cross sectional area per unit width (ie: the ice thickness). The rate of change of the volume $\frac{\mathrm{d}V}{\mathrm{d}t}$ is zero in the case where the glacier is in equilibrium. When the glacier is not in equilibrium, $\frac{\mathrm{d}V}{\mathrm{d}t}$ is equal to the net volume of ice added to or removed from the glacier, called the net balance. The net balance at a point $\dot{b}_n(x,t)$ is equal to the rate of accumulation ($\dot{b}_n > 0$) or ablation ($\dot{b}_n < 0$). With this notation, the rate of change in ice volume can be written

$$\frac{\mathrm{d}V}{\mathrm{d}t} = \int_0^{\mathrm{L}} \dot{b}_n(x,t)\, \mathrm{d}x. \tag{B.4}$$

The continuity equation for incompressible ice is obtained by equating Equations B.3 and B.4:

$$\dot{b}_n = \frac{\partial h}{\partial t} + \frac{\partial q}{\partial x}. \tag{B.5}$$

Equation B.5 expresses the conservation of mass of ice and is referred to as the mass balance equation or continuity equation by glaciologists. A non-zero net balance $\dot{b}_n$, corresponding to either net accumulation or ablation of ice, thus causes thickening/thinning of the glacier $\left(\frac{\partial h}{\partial t} \neq 0\right)$ or a change in the flow regime $\left(\frac{\partial q}{\partial x} \neq 0\right)$.

B.1.2 Conservation of linear and angular momentum

Linear momentum is another quantity conserved by any closed system. Let us consider an element of volume within the parallel-sided slab glacier represented in Figure B.1. Using the coordinate system defined above, this volume element can be written $\mathrm{d}^3 r = \mathrm{d}x\, \mathrm{d}y\, \mathrm{d}z$ and the mass associated to the element of volume of ice is thus $\rho\, \mathrm{d}^3 r$, where ρ is the density of ice. The velocity of this volume element is denoted $v_k(x,t)$, where k is a vector index such that $v_k = (v_x, v_y, v_z)$.

Newton's second law

Conservation of momentum for a volume element implies that the rate of change of the momentum is either zero, or it is balanced by an external force applied to the volume element. This principle is expressed in Newton's second law as

$$\frac{\mathrm{d}P}{\mathrm{d}t} = F^{\mathrm{net}}, \tag{B.6}$$

where P is the total linear momentum of the ice body and F^{net} is the net external force applied to the ice body.

Linear momentum

Linear momentum is defined as the product of the mass of an object and its velocity. The momentum of the volume element considered is thus $\rho\, v(x,t)\, \mathrm{d}^3 r$, and the total linear momentum of an ice body of volume V can be written

$$P = \int_V \rho\, v_k(x,t) \mathrm{d}^3 r. \tag{B.7}$$

The rate of change of the total linear momentum is thus related to the rate of change of the quantity $\rho\, v_k$ and, using Reynolds transport theorem, the full time derivative of the linear momentum takes the form

$$\frac{\mathrm{d}P}{\mathrm{d}t} = \int_V \left(\frac{\partial}{\partial t}(\rho\, v_k) + \frac{\partial}{\partial x_l}(v_l\, \rho\, v_k) \right) \mathrm{d}^3 r, \tag{B.8}$$

where l is a vector index.

Body and surface forces

The external forces to which the ice body is subjected can be classified as body forces, acting on the whole volume of ice, or contact forces, acting on the external surface of the ice mass. The total body force acting on the volume V of ice is

$$F^{\mathrm{body}} = \int_V \rho\, f_k\, \mathrm{d}^3 r, \tag{B.9}$$

where f_k is the body force per unit mass acting on the volume element $\mathrm{d}^3 r$. The total surface force acting on the external surface S of the ice volume V can be written in terms of stress as

$$F^{\mathrm{surf}} = \int_S \sigma_{lk}\, n_l\, \mathrm{d}S, \tag{B.10}$$

where n_l is the unit vector perpendicular to the element of surface $\mathrm{d}S$ and σ_{lk} is the stress acting on the l-th surface in the k-th direction. Using Gauss's theorem, the surface integral in Equation B.10 can be transformed into a volume integral, and the total force F^{net}, resulting from the sum of the body and surface forces, can be written

$$F^{\mathrm{net}} = F^{\mathrm{body}} + F^{\mathrm{surf}} = \int_V \left[\rho\, f_k + \frac{\partial \sigma_{lk}}{\partial x_l} \right] \mathrm{d}^3 r, \tag{B.11}$$

where x_l is a position vector.

Linear momentum balance equation

The conservation of momentum is expressed by substituting each side of Equation B.6 with the expressions of linear momentum rate and net force obtained in Equations B.8 and B.11, respectively. Equating the expressions within the integrals leads to the local form of the conservation of momentum:

$$\rho\, f_k + \frac{\partial \sigma_{lk}}{\partial x_l} = \frac{\partial}{\partial t}(\rho\, v_k) + \frac{\partial}{\partial x_l}(\rho\, v_l\, v_k). \tag{B.12}$$

Expanding the partial derivatives and recognizing that $\frac{\partial \rho}{\partial t} + \frac{\partial(\rho\, v_l)}{\partial x_l} = \frac{\mathrm{d}\rho}{\mathrm{d}t} = 0$ by conservation of mass and the definition of the material derivative, the following continuity equation is obtained:

$$\rho\, \frac{\mathrm{d}v_k}{\mathrm{d}t} = \rho\, f_k + \frac{\partial \sigma_{lk}}{\partial x_l}. \tag{B.13}$$

Equation B.13 is called the momentum balance equation, and relates the acceleration of an ice body to a body force or a surface traction. In practice, the body force f_k is gravitation, and the acceleration is negligible, so the conservation of linear momentum in an ice body takes the form:

$$\rho g_k + \frac{\partial \sigma_{lk}}{\partial x_l} = 0. \tag{B.14}$$

Conservation of angular momentum

In a similar manner, it can be demonstrated that the tensor representing the distribution of stress in an ice body is symmetric because angular momentum is conserved:

$$\sigma_{ij} = \sigma_{ji}. \tag{B.15}$$

B.1.3 Conservation of energy

The fourth quantity conserved in an isolated system is energy. The conservation of energy is expressed in the first law of thermodynamics that states that the rate of variation of the total energy of a system is equal to the sum of the rate of heating and the rate of work done on the system. The first law of thermodynamics can be stated mathematically as

$$\frac{\mathrm{dU}}{\mathrm{d}t} + \frac{\mathrm{dK}}{\mathrm{d}t} = Q + W, \tag{B.16}$$

where U is the total internal energy, K the kinetic energy, Q the rate of heating and W the work done on the system per unit time. As in the previous section, an element of volume $\mathrm{d}^3 r$ having a density ρ and a velocity v_k is considered.

Internal and kinetic energies

The total internal energy of an ice body of volume V is defined as

$$\mathrm{U} = \int_V \rho\, u \, \mathrm{d}^3 r, \tag{B.17}$$

where u is the specific (per unit mass) internal energy. The specific internal energy is related to the specific heat and temperature of ice through a constitutive relationship (see Equation B.47). Since the density of ice is assumed to be uniform, the rate of change of the total internal energy can be written

$$\frac{\mathrm{dU}}{\mathrm{d}t} = \int_V \rho \, \frac{\mathrm{d}u}{\mathrm{d}t} \, \mathrm{d}^3 r. \tag{B.18}$$

In a similar manner, the total kinetic energy of a volume element $\mathrm{d}^3 r$ is defined as $\frac{1}{2}\,\rho\, v_k^2$ and the rate of change of the total kinetic energy of an ice mass of volume V is

$$\frac{\mathrm{dK}}{\mathrm{d}t} = \int_V \rho\, v_k \, \frac{\mathrm{d}v_k}{\mathrm{d}t} \, \mathrm{d}^3 r. \tag{B.19}$$

Heat added to the system

The rate of heating Q of an ice body of volume V is the sum of internal body heating (in the case of an internal source of energy) and heat exchange through the surface S. It can be written in the form

$$Q = \int_V \rho\, a\, \mathrm{d}^3 r + \int_S q_k\, n_k\, \mathrm{d}S, \tag{B.20}$$

where n_k is the unit vector perpendicular to the surface element $\mathrm{d}S$ and pointing outwards, q_k is the conductive energy flux through the surface element (negative by convention if exiting the element of volume) and a is the energy supply due to an internal heat source, often set to zero in the case of ice. The surface integral in Equation B.20 is transformed into a volume integral using Gauss's theorem, so that

$$Q = \int_V \left(\rho\, a + \frac{\partial q_k}{\partial x_k} \right) \mathrm{d}^3 r. \tag{B.21}$$

Work done on the system

The work W done on a volume element $\mathrm{d}^3 r$ per unit time is, by definition, the product of the net force F_k applied to the element and the velocity v_k of the element itself. The net force F_k can be a combination of a body force, as expressed in Equation B.9, and a surface traction, as expressed in Equation B.10. Using Gauss's theorem to transform the surface integral into a volume integral, the work W done on an volume V of ice per unit time can be written as

$$W = \int_V \left(\rho\, f_k\, v_k + \frac{\partial}{\partial x_l} (\sigma_{lk}\, v_k) \right) \mathrm{d}^3 r. \tag{B.22}$$

Developing the partial derivative and recognizing that $\rho f_k + \frac{\partial \sigma_{lk}}{\partial x_l} = \frac{\mathrm{d} v_k}{\mathrm{d}t}$ through the conservation of momentum (Equation B.13), the work W done on the system per unit time takes the form

$$W = \int_V \left[\rho\, v_k \frac{\mathrm{d} v_k}{\mathrm{d}t} + \sigma_{lk} \frac{\partial v_k}{\partial x_l} \right] \mathrm{d}^3 r. \tag{B.23}$$

The partial derivative $\frac{\partial v_k}{\partial x_l}$ is a rank two tensor and can therefore be expressed as the sum of a symmetric tensor and an antisymmetric tensor. The stress tensor σ_{lk} is symmetric due to the conservation of angular momentum, and the product of a symmetric tensor and an antisymmetric tensor is zero. Thus, only the symmetric part of the $\frac{\partial v_k}{\partial x_l}$ tensor is expressed in the product with the stress tensor. We thus have

$$\sigma_{lk} \frac{\partial v_k}{\partial x_l} = \frac{1}{2} \sigma_{lk} \left(\frac{\partial v_k}{\partial x_l} + \frac{\partial v_l}{\partial x_k} \right) = \sigma_{lk}\, \dot{\epsilon}_{lk}, \tag{B.24}$$

where $\dot{\epsilon}_{lk}$ is the strain-rate tensor. With this notation, the work W done on a volume V of ice is

$$W = \int_V \left[\rho \, v_k \, \frac{\mathrm{d}v_k}{\mathrm{d}t} + \sigma_{lk} \, \dot{\epsilon}_{lk} \right] \mathrm{d}^3 r. \tag{B.25}$$

Energy balance equation

By substituting the four quantities of Equation B.16 by their expressions derived above, a global form for the energy balance is obtained. Both the ice velocity v_k and acceleration $\frac{\mathrm{d}v_k}{\mathrm{d}x_k}$ are small for glaciers and can be neglected. By equating the integrands on both sides of the resulting equation, we arrive at the local form of the energy balance equation:

$$\rho \, \frac{\mathrm{d}u}{\mathrm{d}t} = \sigma_{lk} \, \dot{\epsilon}_{lk} + \rho \, a + \frac{\partial q_k}{\partial x_k}. \tag{B.26}$$

Equation B.26 states that any change in the internal energy of an ice body results from a combination of heat produced by deformation of the ice, called strain heating (first term on the left-hand side of Equation B.26), heat originating from an internal energy source (second term), and exchange of heat through the ice surface (third term).

B.2 The constitutive law for ice

Four quantities are commonly used to characterize glacier dynamics: ice thickness, velocity, temperature and stress. These four quantities are coupled in the conservation laws presented above. Since there are four unknown quantities but only three equations, an additional relationship relating stress to one of the three other quantities is required to determine all of the four quantities mentioned above. Since the physical laws governing the flow of ice have already been exploited to derive the three conservation equations presented above, an additional constitutive relationship is required. Because the strain rate is a function of velocity, a constitutive law relating the stress to the strain rate would link the stress to the velocity and allow calculation of the four quantities mentioned above.

The constitutive relationship for ice commonly used in glaciology, often referred to as Glen's flow law, is an empirically-derived power law relating stress to strain rate (Glen, 1955). The flow-law exponent n describes the rheology of ice. For $n = 1$, the relationship between stress and strain rate is linear and ice would be treated as a very viscous Newtonian fluid. The value $n \to \infty$ corresponds to the assumption of perfect plasticity (Nye, 1951). As a perfectly plastic solid, ice would show little deformation when subjected to stresses lower than a threshold value called yield stress, but the strain rate becomes significant for stresses higher than the yield stress. It is common in glacier studies to consider ice a non-linear viscous fluid for which $n = 3$. This value is adopted on the basis of field and laboratory measurements of strain rates for a given stress. Values of n ranging between 1.5 and 4.have been measured (Weertman, 1973; Glen, 1955; Goldsby and Kohlstedt, 1997).

Strain rate tensor

The strain rate is a symmetric rank two tensor describing the rate of deformation of the ice. It can be expressed in matrix form for the coordinate system described above as:

$$\dot{\epsilon_{ij}} = \begin{pmatrix} \dot{\epsilon}_{xx} & \dot{\epsilon}_{xy} & \dot{\epsilon}_{xz} \\ \dot{\epsilon}_{xy} & \dot{\epsilon}_{yy} & \dot{\epsilon}_{yz} \\ \dot{\epsilon}_{xz} & \dot{\epsilon}_{yz} & \dot{\epsilon}_{zz}. \end{pmatrix}, \tag{B.27}$$

The strain rate is defined in terms of velocity as

$$\dot{\epsilon}_{ij} = \frac{1}{2}\left(\frac{\partial v_i}{\partial x_j} + \frac{\partial v_j}{\partial x_i}\right), \tag{B.28}$$

where i and j are indices such that $i, j = (x, y, z)$. With this notation, x_x is equivalent to the coordinate x while x_y and x_z are equivalent to y and z respectively.

Stress tensor and deviatoric stress

Stress is a measure of the intensity of the internal forces acting within an ice body as a reaction to contact forces and body forces. It is a symmetric rank two tensor that can be written as

$$\sigma_{ij} = \begin{pmatrix} \sigma_{xx} & \sigma_{xy} & \sigma_{xz} \\ \sigma_{xy} & \sigma_{yy} & \sigma_{yz} \\ \sigma_{xz} & \sigma_{yz} & \sigma_{zz}. \end{pmatrix}, \tag{B.29}$$

Stress is usually written in a non-matrix form using indices in the same manner as for the strain rate. The diagonal components σ_{ii} are called normal stresses (tensile stress if positive, compressive stress if negative) and the components σ_{ij}, with $i \neq j$, located off the diagonal of the matrix, are called shear stresses.

The stress tensor can be written as the sum of two tensors: the mean hydrostatic stress tensor $P\,\delta_{ij}$, depending on the pressure P of the overlying ice and acting on the volume of the ice body, and the deviatoric stress tensor, denoted σ'_{ij}, which is the stress primarily responsible for deformation. The deviatoric stress tensor thus differs from the full stress tensor in that the hydrostatic component is subtracted from the normal stress components. The ice overburden pressure P can be defined as a function of stress as $P = -\frac{1}{3}(\sigma_{xx} + \sigma_{yy} + \sigma_{zz})$, and the deviatoric stress tensor can be written in a matrix form as

$$\sigma = \begin{pmatrix} \frac{2}{3}\sigma_{xx} - \frac{1}{3}(\sigma_{yy} + \sigma_{zz}) & \sigma_{xy} & \sigma_{xz} \\ \sigma_{xy} & \frac{2}{3}\sigma_{yy} - \frac{1}{3}(\sigma_{xx} + \sigma_{zz}) & \sigma_{yz} \\ \sigma_{xz} & \sigma_{yz} & \frac{2}{3}\sigma_{zz} - \frac{1}{3}(\sigma_{xx} + \sigma_{yy}). \end{pmatrix}, \tag{B.30}$$

Use of the deviatoric stress tensor is appropriate for defining the relationship between stress and strain rate. Indeed, laboratory experiments and field observation show that the deformation of ice is nearly independent of the hydrostatic pressure. Therefore, we seek to establish a relationship between the strain rate and the deviatoric stress.

Relationship between stress and strain rate

The relationship between the deviatoric stress and the strain rate can be written in the form

$$\dot{\epsilon}_{ij} = A\,F(\sigma'_{ij})\sigma'_{ij}, \tag{B.31}$$

where F is a function of the deviatoric stress σ'_{ij} and A is a factor independent of σ'_{ij}. It is also desirable that the relationship be independent of the coordinate system. The function F must therefore depend on one of the three invariants of the deviatoric stress tensor. The first invariant of the deviatoric stress is the sum of the diagonal components and is equal to zero (see Equation B.28), thus not a suitable option. The second invariant of the deviatoric stress tensor is defined as $I_2 = \frac{1}{2}\sigma'_{ij}\,\sigma'_{ij}$. Since experiments have shown that the relationship between stress and strain rate is not linear, the function F is defined as a power of the second invariant: $F = I_2^{\frac{n-1}{2}}$. The relationship of Equation B.31 thus takes the form

$$\dot{\epsilon}_{ij} = A\,(\frac{1}{2}\sigma'_{ij}\,\sigma'_{ij})^{\frac{n-1}{2}}\sigma'_{ij}. \tag{B.32}$$

This relationship between strain rate and deviatoric stress is called the generalized flow law.

Special case of simple shear

In most cases a simpler version of the generalized flow law is used, commonly referred to as Glen's flow law. It is assumed that the glacier deforms by simple shear, a stress regime in which the stress tensor is

$$\sigma = \begin{pmatrix} 0 & 0 & \sigma_{xz} \\ 0 & 0 & 0 \\ \sigma_{zx} & 0 & 0. \end{pmatrix}, \tag{B.33}$$

Since the hydrostatic pressure acts only on the normal stress components, the deviatoric stress tensor is identical to the stress tensor presented in Equation B.33. The product $\sigma'_{ij}\,\sigma'_{ij}$ can thus be developed into

$$\sigma'_{ij}\,\sigma'_{ij} = \sigma_{xz}\,\sigma_{zx} + \sigma_{zx}\,\sigma xz = 2\,\sigma_{xz}^2, \tag{B.34}$$

since the stress tensor is symmetric. Substituting this expression into Equation B.33, it follows that the flow law can be written

$$\dot{\epsilon}_{xz} = A\,\sigma_{xz}^n. \tag{B.35}$$

The previous expression is the form of the constitutive law for ice used throughout this work. The value $n = 3$ is commonly used for the flow law exponent and the flow law coefficient A depends mainly on the ice temperature, and to a lesser extent on several other factors such as crystal size and orientation or impurity content (Paterson, 1994). It is usually written as $A = A_0 \exp\big(-\frac{Q}{RT}\big)$, where A_0 is a temperature-independent coefficient, Q is the activation energy for ice, R is the universal gas constant and T is the ice temperature. These parameters are constant in this study and their values can be found in Table 4.2 in Section 4.2.5.

B.3 Derivation of the velocity, strain-rate and temperature equations

In this section, the equation describing the velocity profile in a slab glacier is derived. The derivations of the temperature and strain rate equations used in the thermal model (Section 4.2.5) are also presented in detail.

B.3.1 Vertical velocity profile in a slab glacier and strain rate equation

The vertical distribution of velocity can be derived directly from Glen's flow law, using the momentum balance and the definition of strain rate. A parallel-sided slab glacier of infinite length and width, and of uniform thickness and slope, is considered in the coordinate system defined above (see Figure B.1). The only non-zero velocity component for this glacier is the velocity v_x and v_x varies only in z. This corresponds to a simple-shear stress regime and the only non-zero component of the strain rate, defined in Equation B.28, is thus

$$\dot{\epsilon}_{xz} = \dot{\epsilon}_{zx} = \frac{1}{2}\left(\frac{\partial v_x}{\partial z} + \frac{\partial v_z}{\partial x}\right) = \frac{1}{2}\frac{\partial v_x}{\partial z}. \tag{B.36}$$

Replacing the strain rate in Equation B.36 by its expression in Glen's flow law (Equation B.35), the partial derivative of the velocity with respect to z takes the form

$$\frac{\partial v_x}{\partial z} = 2\,A\,\sigma_{xz}^{n}. \tag{B.37}$$

The shear stress at a depth z within the ice mass is balanced by the force causing the glacier to flow under its own weight, called the driving stress. The expression for the shear stress can be obtained by integrating the momentum balance. Indeed, in the case of simple shear the conservation of momentum (Equation B.14) can be expressed by two equations:

$$\frac{\partial \sigma_{xz}}{\partial x} = -\rho g_z = -\rho g \cos\theta, \tag{B.38}$$

$$\frac{\partial \sigma_{zx}}{\partial z} = -\rho g_x = -\rho g \sin\theta, \tag{B.39}$$

where g_x and g_z are the x- and z-components of the vertical acceleration of gravity, respectively. Integrating Equation B.39 with respect to z and recognizing that the shear stress is zero at the surface for $z = h$ leads to the following expression for the shear stress at a distance z above the glacier bed:

$$\sigma_{xz} = \rho g(h - z)\sin\theta, \tag{B.40}$$

where ρ is the density of the ice, g the acceleration of gravity and θ the glacier slope. Substituting the expression for the shear stress of Equation B.40 into Equation B.37 and integrating both sides over z, Equation B.37 becomes:

$$v_x = \frac{2A}{n+1}(\rho g \sin\theta)^n\,[h^{n+1} - (h-z)^{n+1}]. \tag{B.41}$$

On the surface of the glacier, where $z = h$, the ice velocity can thus be written

$$v_x(z = h) = \frac{2A}{n+1}(\rho g \sin\theta)^n\, h^{n+1}. \tag{B.42}$$

Combining the flow law of ice, expressed in Equation B.35, and the expression for the shear stress (Equation B.40), the strain rate profile takes the form

$$\dot{\epsilon}_{xz}(z) = A_0 \exp\left(-\frac{Q}{RT}\right)[\rho g\,(h - z)\,\sin\theta]^n\,. \tag{B.43}$$

B.3.2 The temperature equation

We start with the energy balance equation (Equation B.26), derived in Section B.1:

$$\rho\frac{du}{dt} = \sigma_{xz}\dot{\epsilon}_{xz} + \rho a - \frac{\partial q_k}{\partial x_k}, \tag{B.44}$$

where u is the internal energy, ρ the ice density, σ_{xz} the shear stress, $\dot{\epsilon}_{xz}$ the strain rate, a the energy supply term and q_k the energy flux. This equation means that the internal energy of the glacier is a function of three terms: the heat production by deformation of the ice, the energy supply and the loss of heat by conduction. We neglect internal heat sources, so the energy supply term a is zero. We can transform the left hand side of equation (B.44) by developing the full time derivative into partial time and space derivatives:

$$\rho\frac{du}{dt} = \rho\left(\frac{\partial u}{\partial t} + v_x\frac{\partial u}{\partial x} + v_y\frac{\partial u}{\partial y} + v_z\frac{\partial u}{\partial z}\right). \tag{B.45}$$

We have already specified that there is no y- or z-component of ice velocity. It is also assumed that the bed-normal component of flow is zero. This is consistent with the forward model presented in Section 4.2.1. We thus have the condition: $v_y = v_z = 0$. As a consequence, equation B.45 simplifies as follows:

$$\rho\frac{du}{dt} = \rho\left(\frac{\partial u}{\partial t} + v_x\frac{\partial u}{\partial x}\right). \tag{B.46}$$

We consider the following constitutive relation for the internal energy:

$$u = \int_0^{\mathrm{T}} c(T')dT', \tag{B.47}$$

where the heat capacity $c(T)$ can be written

$$c(T) = c_1 + c_2 T \tag{B.48}$$

and the constants c_1 and c_2 can be determined empirically and are presented in Table 4.2 in Section 4.2.5. We can then write the internal energy as a function of temperature

$$u = \int_0^{\mathrm{T}} (c_1 + c_2 T')dT' = c_1 T + \frac{1}{2}c_2 T^2. \tag{B.49}$$

With this notation, the temporal and spatial derivatives of u can be written respectively as:

$$\frac{\partial u}{\partial t} = \frac{\partial}{\partial t}\big(c_1 T + \frac{1}{2}c_2 T^2\big) = c_1\frac{\partial T}{\partial t} + c_2 T\frac{\partial T}{\partial t} = c(T)\frac{\partial T}{\partial t}, \tag{B.50}$$

$$\frac{\partial u}{\partial x} = \frac{\partial}{\partial x}\big(c_1 T + \frac{1}{2}c_2 T^2\big) = c_1\frac{\partial T}{\partial x} + c_2 T\frac{\partial T}{\partial x} = c(T)\frac{\partial T}{\partial x}. \tag{B.51}$$

It follows that equation B.46 can now be written

$$\rho\frac{du}{dt} = \rho c(T)\left[\frac{\partial T(z,t)}{\partial t} + v_x(z,t)\frac{\partial T(z,t)}{\partial x}\right]. \tag{B.52}$$

The temperature depends only on depth and time, thus the partial derivative of temperature with respect to x is zero and equation B.52 reduces to

$$\rho\frac{du}{dt} = \rho c(T)\frac{\partial T(z,t)}{\partial t}. \tag{B.53}$$

Let us now consider the right hand side of equation B.44. The energy supply term is assumed to be zero, so the second term disappears. We can expand the third term, transforming Equation B.44 to

$$\rho\frac{du}{dt} = \sigma_{xz}\dot{\epsilon}_{xz} - \frac{\partial q_x}{\partial x} - \frac{\partial q_z}{\partial z}. \tag{B.54}$$

Another constitutive relation links the heat flux q_k to the thermal conductivity $K(T)$:

$$q_k = -K(T)\frac{\partial T}{\partial x_k}. \tag{B.55}$$

Like the heat capacity, the thermal conductivity can be written as a polynomial function of temperature,

$$K(T) = c_3 + c_4 T + c_5 T^2, \tag{B.56}$$

and the values of constants c_3, c_4 and c_5 can be found experimentally and are presented Table 4.2 in Section 4.2.5. Equation B.56 allows the thermal conductivity to be introduced in Equation B.54, which leads to the following equations after expansion of the partial derivatives:

$$\rho\frac{du}{dt} = \sigma_{xz}\,\dot{\epsilon}_{xz} - \frac{\partial}{\partial x}\left(- K(T)\frac{\partial T}{\partial x}\right) - \frac{\partial}{\partial z}\left(- K(T)\frac{\partial T}{\partial z}\right), \tag{B.57}$$

then,

$$\rho\frac{du}{dt} = \sigma_{xz}\,\dot{\epsilon}_{xz} + \frac{\partial K(T)}{\partial x}\frac{\partial T}{\partial x} + \frac{\partial K(T)}{\partial z}\frac{\partial T}{\partial z} + K(T)\left(\frac{\partial^2 T}{\partial x^2} + \frac{\partial^2 T}{\partial z^2}\right). \tag{B.58}$$

The term $\sigma_{xz}\,\dot{\epsilon}_{xz}$, called strain heating, is linked to the shear stress σ_{xz} by the constitutive relation characterizing the rheology of ice (Glen's flow law, see Equation B.35)

$$\sigma_{xz}\,\dot{\epsilon}_{xz} = 2A_0 \exp\left[-\frac{Q}{RT}\right]\sigma_{xz}^{n+1}. \tag{B.59}$$

Because temperature does not depend on the x-coordinate in our simplified model, the first and second derivatives of temperature with respect to x are zero: $\dfrac{\partial T(z,t)}{\partial x} = 0$ and $\dfrac{\partial^2 T(z,t)}{\partial x^2} = 0$. The derivative $\dfrac{\partial K(T)}{\partial x_k}$ can then be written as the product of two partial derivatives by the chain rule: $\dfrac{\partial K(T)}{\partial T}\dfrac{\partial T}{\partial x_k}$. It follows that the thermal equation can be written

$$\rho c(T)\frac{\partial T(z,t)}{\partial t} = \sigma_{xz}\,\dot{\epsilon}_{xz} + \frac{\partial K(T)}{\partial T}\left(\frac{\partial T(z,t)}{\partial z}\right)^2 + K(T)\frac{\partial^2 T(z,t)}{\partial z^2}. \tag{B.60}$$

By dividing both sides by $\rho c(T)$, Equation B.60 takes the form

$$\frac{\partial T}{\partial t} = \frac{1}{\rho c(T)}\left[K(T)\frac{\partial^2 T}{\partial z^2} + \frac{\partial K(T)}{\partial T}\left(\frac{\partial T}{\partial z}\right)^2 + \sigma_{xz}\,\dot{\epsilon}_{xz}\right]. \tag{B.61}$$

Equation (B.61) is a non-linear second order partial differential equation (first order in time and second order in space) governing the transient diffusion of heat through the ice.

Appendix C

Summary of inversion results

This appendix summarizes results of the inversion of the four surface velocity datasets using both spectral and deterministic methods. The results, presented in a graphical form, are all gathered to make comparison easier. The plots presented in Figures C.1 and C.2 can be found in larger version in Section 4.3.3. In Figure C.3, results of the inversion of real data using the deterministic and spectral methods are presented on the same plot.

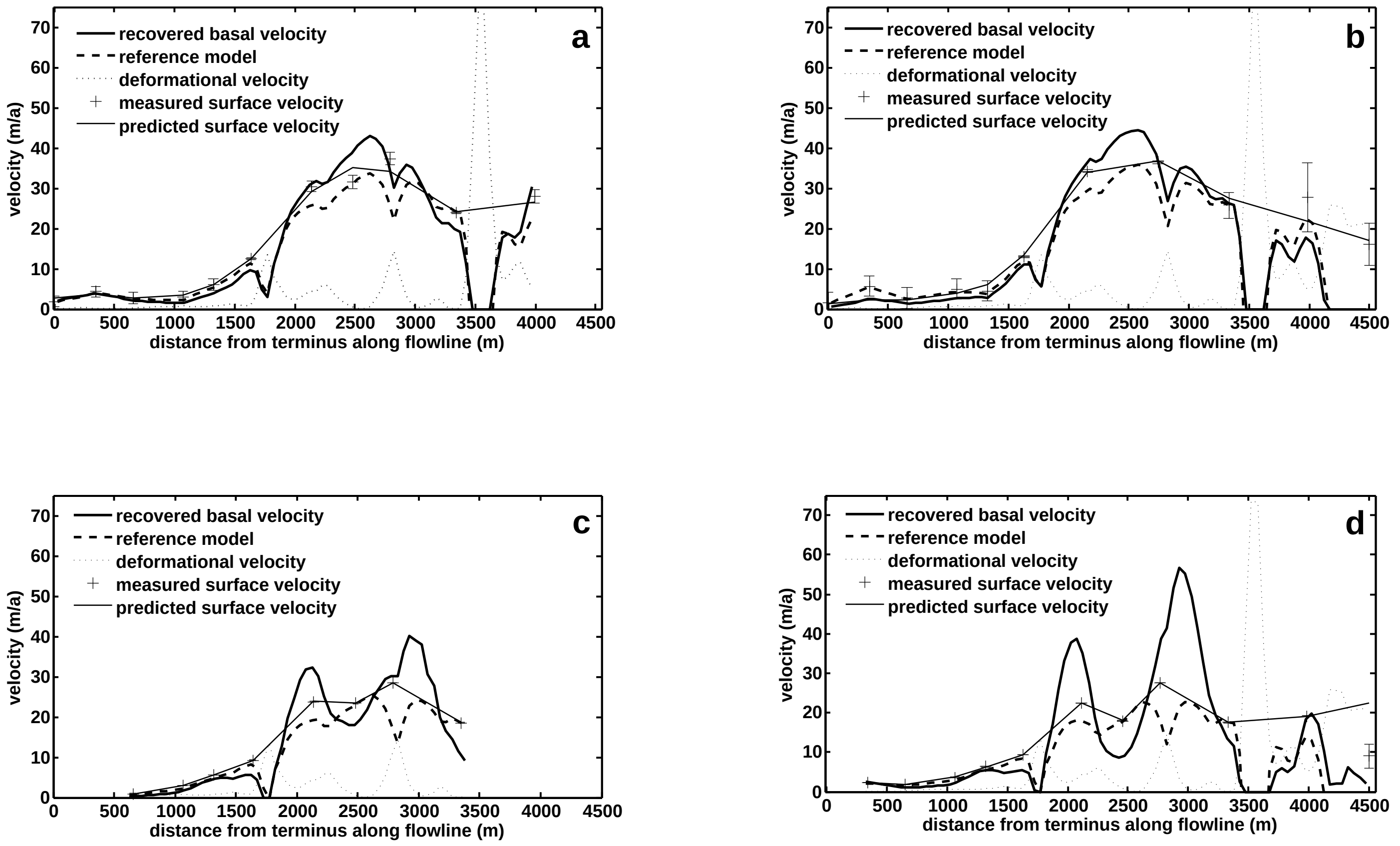

Figure C.1: Results of the inversion of real data using a deterministic approach. (a) Summer 2006 dataset, (b) summer 2007 dataset, (c) 2006-2007 annual dataset and (d) 2007-2008 annual dataset. Ice velocities are expressed as a function of distance from the glacier terminus along the flowline

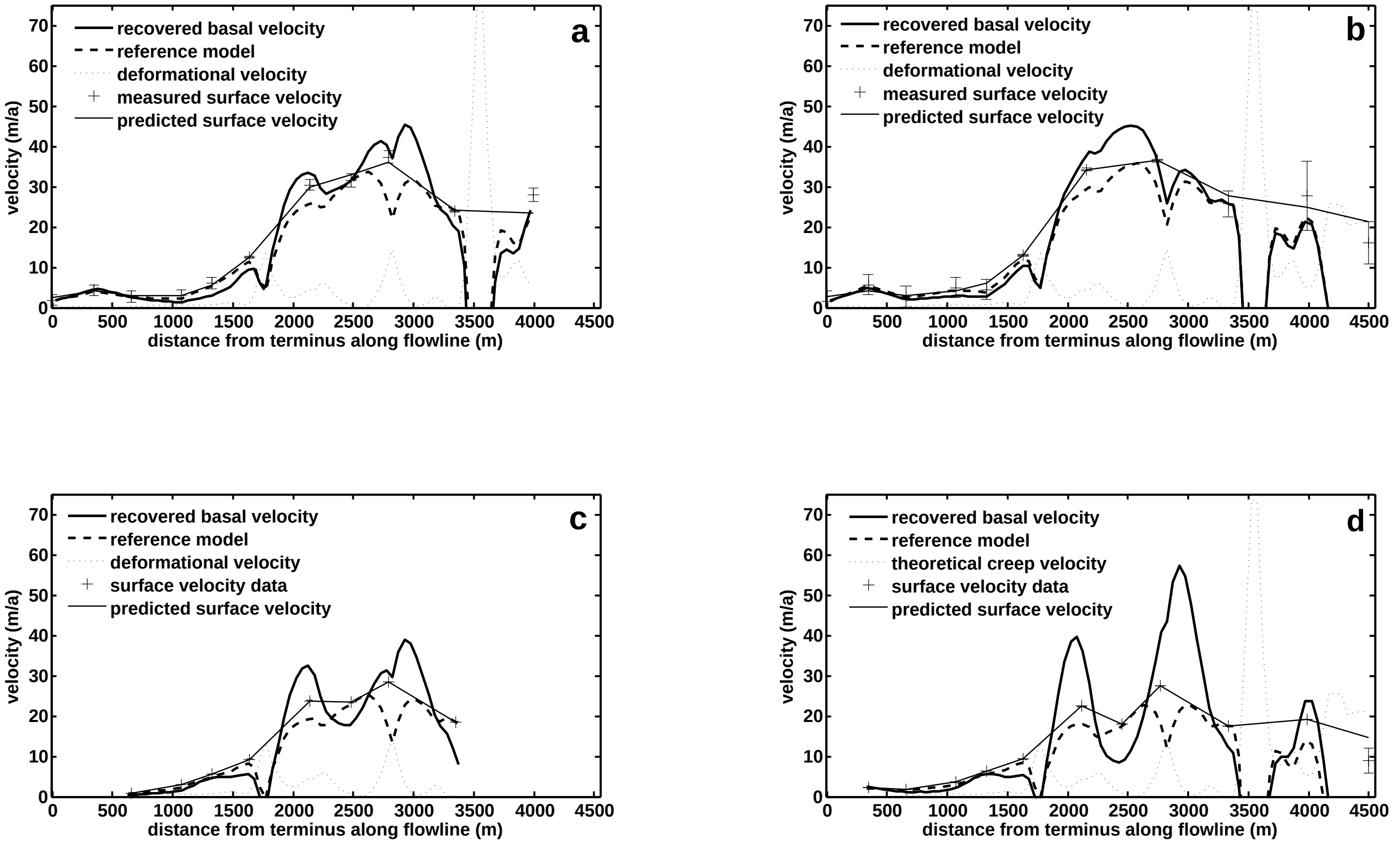

Figure C.2: Results of the inversion of real data using the spectral decomposition method. (a) Summer 2006 dataset, (b) summer 2007 dataset, (c) 2006-2007 annual dataset and (d) 2007-2008 annual dataset. Ice velocities are expressed as a function of distance from the glacier terminus along the flowline

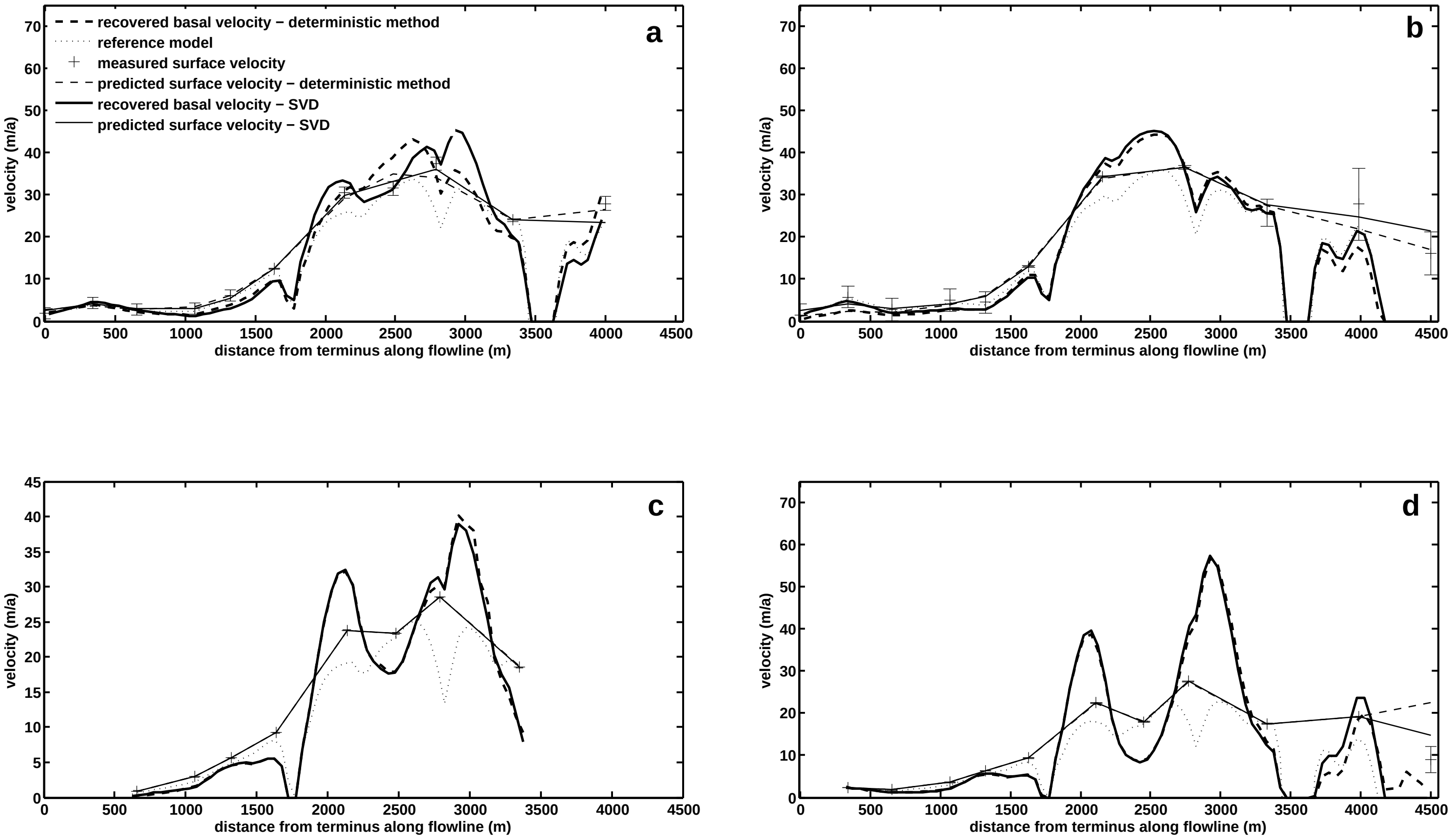

Figure C.3: Comparison of the results of inversion of real data using the deterministic and spectral decomposition methods. (a) Summer 2006 dataset, (b) Summer 2007 dataset, (c) 2006-2007 annual and (d) 2007-2008 annual dataset. Ice velocities are expressed as a function of distance from the glacier terminus along the flowline

Appendix D

Upstream area calculation

Upstream drainage area calculations are conducted in an attempt to link our model results and field observations to subglacial hydrology. For a given gridcell, upstream area is defined as the sum of the areas of all gridcells that have a higher hydraulic potential (and therefore that are "upstream" according to our metric of hydraulic potential) and that are connected through a drainage path. When upstream area is computed for all gridcells in a DEM, preferred drainage paths can be identified.

D.1 Method

Upstream area is computed by applying a method presented by Quinn et al. (1991) and previously used, for example, by Flowers and Clarke (1999). Subglacial water flow is controlled by both bed topography and ice thickness, and the direction of water flow depends on the fluid potential, expressed as (Shreve, 1972)

$$\Phi = \rho_w g z_b + f \rho_i g h_i, \tag{D.1}$$

where ρ_w and ρ_i are the densities of water and ice respectively, g is the acceleration due to gravity, z_b is the bed elevation and h_i the ice thickness. The second term on the right hand side of Equation D.1 is the water pressure and is usually expressed as a fraction of the ice overburden pressure $\rho_i g h_i$, with f a coefficient ranging from zero to one called the flotation ratio. In Chapter 4, geophysical inversion of measured surface velocity data reveals that basal sliding and bed deformation are responsible for 50% to over 90% of the total glacier motion. Because such a high contribution of basal motion is most certainly caused by high subglacial water pressures, the basal water pressure is assumed to be equal to the ice overburden pressure. A flotation fraction $f = 1$ is therefore thought to represent the best current subglacial conditions and is used to derive the main result, although the distribution of upstream area is also calculated for $f = 0.5$ and $f = 0.9$ for comparison. The gradient of hydraulic potential can be expressed mathematically as

$$\nabla \Phi = \rho_i g \nabla z_s + (\rho_w - \rho_i) g \nabla z_b, \tag{D.2}$$

where z_s is the surface elevation. Hydraulic potential gradients are calculated numerically between each gridcell and the eight neighbouring gridcells.

As a precursor to calculating upstream area for a given gridcell, the preferential drainage direction(s) of each gridcell must be determined. As water flows from high to low potential, water will flow in the directions where fluid potential gradients are positive in a given cell. The method presented by Quinn et al. (1991) allows for multiple drainage directions for a given cell and partitions upstream area according to the fluid potential gradients between the neighbouring cells. Upstream area for one cell is computed in the same algorithm as drainage directions, by propagating cell areas down the path of decreasing potential and summing the areas of all "upstream" cells that are connected to a given gridcell.

D.2 Results

The distribution of the logarithm of upstream area, computed using the method above and the surface and bed DEM (see Chapter 3), is presented in Figure D.1. Results are plotted as logarithms to highlight variation over the dominant downslope trend. Upstream area is a purely geometrical calculation that takes no account of water sources or sinks or variations in subglacial water pressure. However, high values of upstream area have been successfully used to infer locations of preferential subglacial drainage (e.g. Sharp et al., 1993). If interpreted this way, Figure D.1 shows evidence for channelization (preferential flow) along the flowline over the lowermost 750 m of the glacier and east of the flowline for about 2000 m above this. Figure D.2 shows preferential drainage paths for flotation ratios of $f = 0.5$ and $f = 0.9$. The subglacial drainage configurations obtained for $f = 0.5$ and $f = 0.9$ are very similar to that obtained for $f = 1$ (Figure D.1), which suggests that the drainage configuration suggested in Figure D.1 is robust with respect to the flotation fraction f. The significance of these results is discussed in Chapter 5.

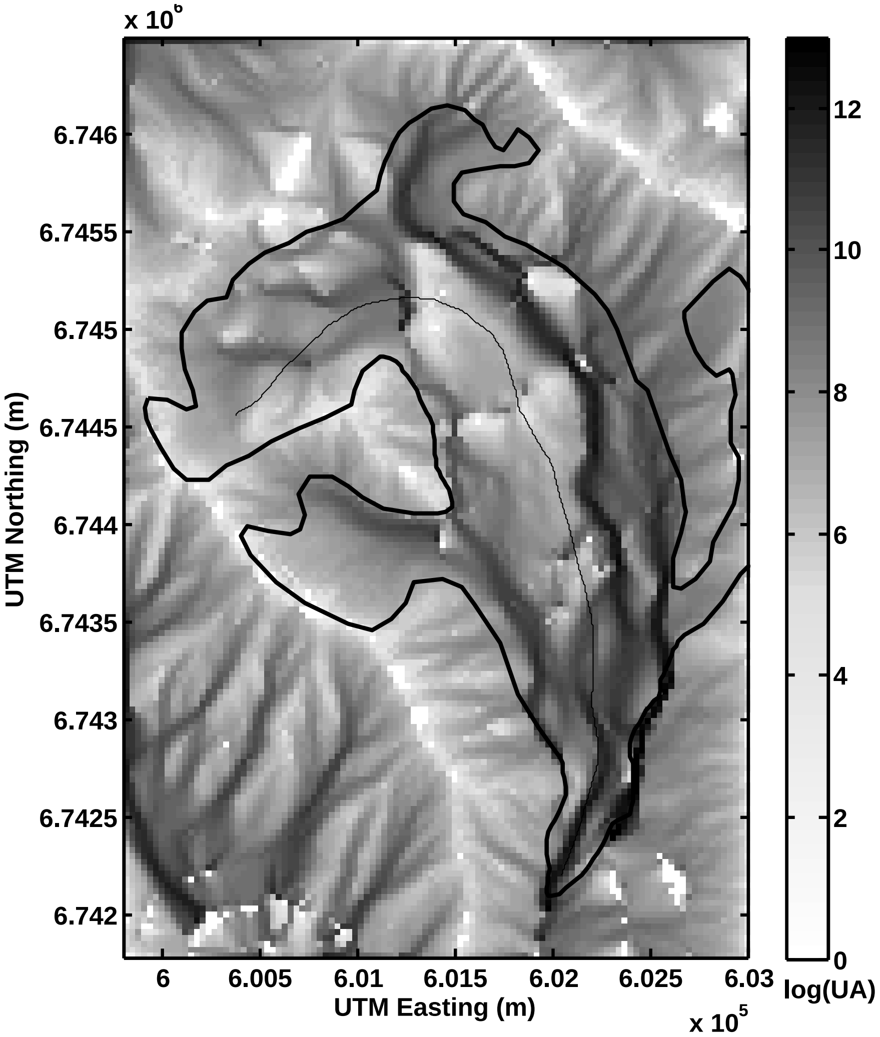

Figure D.1: Logarithm of upstream area for a flotation ratio f=1. Dark areas represent possible subglacial drainage channels.

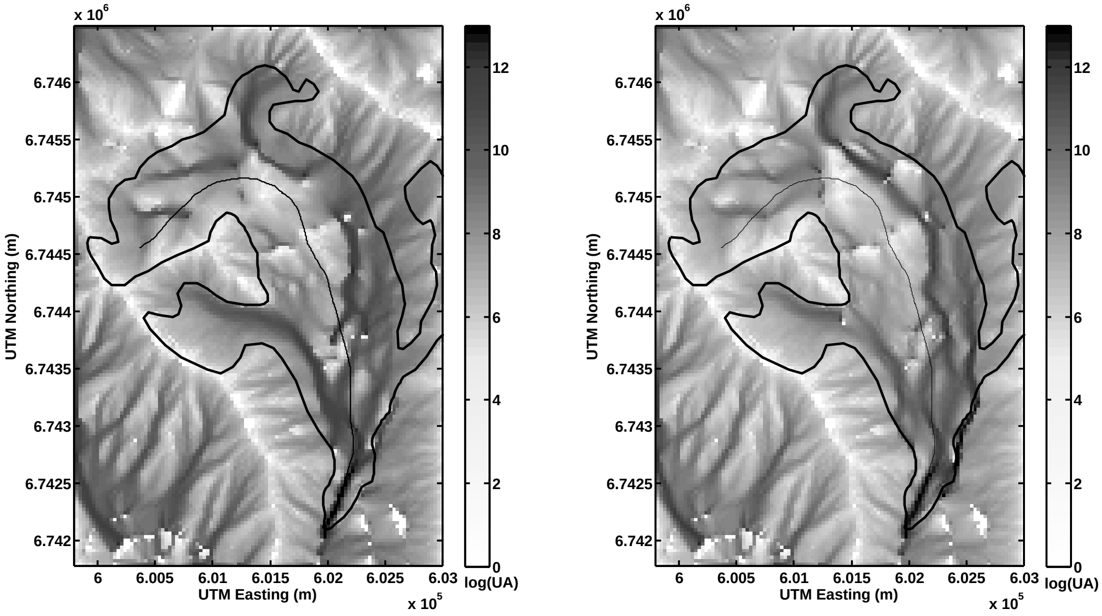

(a)

(b)

Figure D.2: Logarithm of upstream area for (a) f=0.5 and (b) f=0.9. Dark areas represent possible subglacial drainage channels.

Appendix E

Balance velocity calculations

A comparison of measured surface velocities and calculated balance velocities is made to assist in evaluating the current glacier flow regime. Balance velocity is defined as the glacier velocity required to maintain a constant surface profile, given a particular mass balance distribution (e.g. Budd and Allison, 1975; Budd and Warner, 1996). Balance velocity depends on the net mass balance and on the glacier geometry, such that a glacier flowing at the theoretical balance velocity is in equilibrium with climate. An analytical relationship between balance velocity and net mass balance can be derived from the conservation of mass (see Appendix A):

$$\frac{\partial h}{\partial t} + \frac{\partial q}{\partial x} = \dot{b}_n, \tag{E.1}$$

where t and x are the temporal and spatial coordinates, respectively, h is the ice thickness, q the ice flux, and $\dot{b}_n$ the net mass balance rate. Assuming a constant surface profile is equivalent to setting $\frac{\partial h}{\partial t} = 0$, and the flux q at a position x can then be defined from Equation E.1 as

$$q(x) = \int_0^x \dot{b}_n(x) \mathrm{d}x'. \tag{E.2}$$

The ice flux can be written as $q = \bar{u}h$, where $\bar{u}$ is the vertically averaged velocity, and thus the balance velocity can be written as a function of the ice thickness and the net mass balance

$$\bar{u}(x) = \frac{1}{h} \int_0^x \dot{b}_n(x) \mathrm{d}x'. \tag{E.3}$$

E.1 Methods

E.1.1 2006-2007 balance velocity

Net mass balance data for the year 2006-2007 (Wheler, 2009) are used to calculate balance velocities. Glacier response to climate is a slow process, spanning years to decades (Jóhannesson et al., 1989), such that the glacier is not expected to be in equilibrium with climate on a yearly basis. A longer mass balance record would therefore be required to make a valid comparison between climate and the current flow regime, however mass balance data are only available for the year 2006-2007 at this time.

Balance velocities are estimated at pole locations, marked as crosses in Figure E.1, along the glacier flowline. The glacier is divided into sections whose boundaries are defined by fictitious flux gates perpendicular to ice flow and passing through the locations of the velocity survey poles. Calculation of the balance velocity requires glacier geometry and net mass balance data as input. The surface and bed DEMs generated in Chapter 3 are used to calculate the vertical cross-sectional area of each gate as well as the surface area of each section. Mass balance data have been collected at many locations on the study glacier for the year 2006-2007 (winter 2006-2007, summer 2007), and interpolated onto $30 \times 30\,\mathrm{m}$ grids (Wheler, 2009). The interpolated values are plotted against elevation in Figure E.2a. The distribution of net mass balance is used to calculate the volume of accumulation (or ablation) over each section.

Any change in volume of a given section, either by flow through the upstream boundary or local accumulation/ablation, must be compensated by flow through the downstream boundary. The total volume V_{OUT} that must flow out of a given section in order to maintain a constant surface profile is the sum of the volume V_{UPSTREAM} that flows through the upstream boundary and the local volumetric net balance V_{NB} over the given section. The balance velocity at the downstream boundary is then defined as

$$u_{\mathrm{BAL}} = \frac{V_{\mathrm{UPSTREAM}} + V_{\mathrm{NB}}}{A_{\mathrm{CROSS}}}, \tag{E.4}$$

where A_{CROSS} is the glacier cross-sectional area along the gate defining the downstream boundary of the section considered.

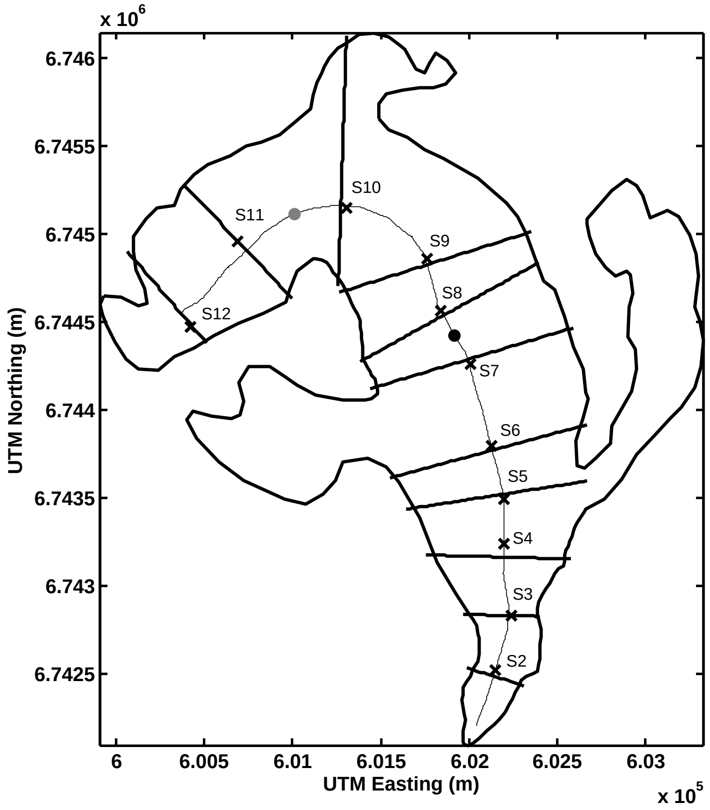

Figure E.1: Flux gates, survey poles and ELA position. The crosses indicate the positions of the surface velocity survey poles and the black lines are fictitious gates perpendicular to the flowline defining glacier sections for balance velocity calculations. The gray dot (between S10 and S11) indicates the position of the ELA inferred from the 2006-2007 net mass balance data. The black dot (between S7 and S8) indicates the position of the ELA corresponding to the modelled balance velocity profile that is most similar to the measured surface velocity profile.

E.1.2 Hypothetical balance velocity

An additional experiment is carried out to determine what net mass balance is required to explain the magnitude of the measured surface velocities. A best-fit curve describing the measured net balance data as a function of elevation is computed (Figure E.2a), and is then shifted incrementally toward increasing net balance (to the right in Figure E.2a, by increments of 0.1 m.w.e.). A balance velocity profile is then derived for each hypothetical net balance curve. This process is repeated until balance velocities of the same magnitude as the measured annual surface velocities for the year 2007-2008 are generated (the annual

2007-2008 dataset is chosen instead of the 2006-2007 dataset because it covers a longer distance along the flowline).

E.2 Results

The measured net balance for 2006-2007 is negative over most of the glacier area, with positive values of net balance confined to the four upper sections shown in Figure E.1. The total net balance is -0.69 m.w.e. and the equilibrium line altitude (ELA), at which the net balance is zero, is 2620 m. This corresponds to an equilibrium line passing between poles S10 and S11, as shown by the gray dot in Figure E.1. The calculated volumetric net balance over each section and the cross-sectional area at each pole are recorded in Table E.1, along with the balance velocities computed at each pole using the method presented above. The resulting balance velocities are negative for 8 of the 11 glacier sections. Because negative velocities are not physically meaningful (ice does not flow upstream), negative balance velocities are set to zero (these corrected velocities are subsequently referred to as “capped” balance velocities). The capped balance velocities are plotted as a function of the distance from the glacier terminus along the flowline in Figure E.2b, along with the measured surface velocities.

Because conclusions cannot be drawn from one year of mass balance data, a second set of calculations, described in Section E.1.2 is carried out. The thin black lines in Figures E.2a and E.2b show the best-fit curve describing the mass balance distribution and the balance

Pole	**Volumetric net balance** ($\times 10^5\,\mathrm{m}^3$)	**Cross-sectional area** ($\times 10^3\,\mathrm{m}^2$)	**Balance velocity (m/a)**
S2	-2.77	1.9	-1854.8
S3	-3.37	11.8	-264.4
S4	-4.55	45.8	-61.6
S5	-6.02	72.0	-32.9
S6	-3.94	82.8	-21.3
S7	-9.40	73.2	-18.7
S8	-2.79	65.3	-6.6
S9	-1.84	106.6	-1.4
S10	-1.14	65.0	0.5
S11	0.35	76.4	1.9
S12	1.12	68.0	1.7

Table E.1: Balance velocity results

velocity profile, respectively, for each increment. The balance velocity profile plotted in Figures E.2a and E.2b as a bold black line most resembles the measured velocity profile. The total mass balance associated with this curve is -0.03 m.w.e. and leads to an ELA of 2431 m. This corresponds to an equilibrium line passing between poles S7 and S8, as shown with a black dot in Figure E.1. The results presented in this appendix are discussed in Chapter 5.

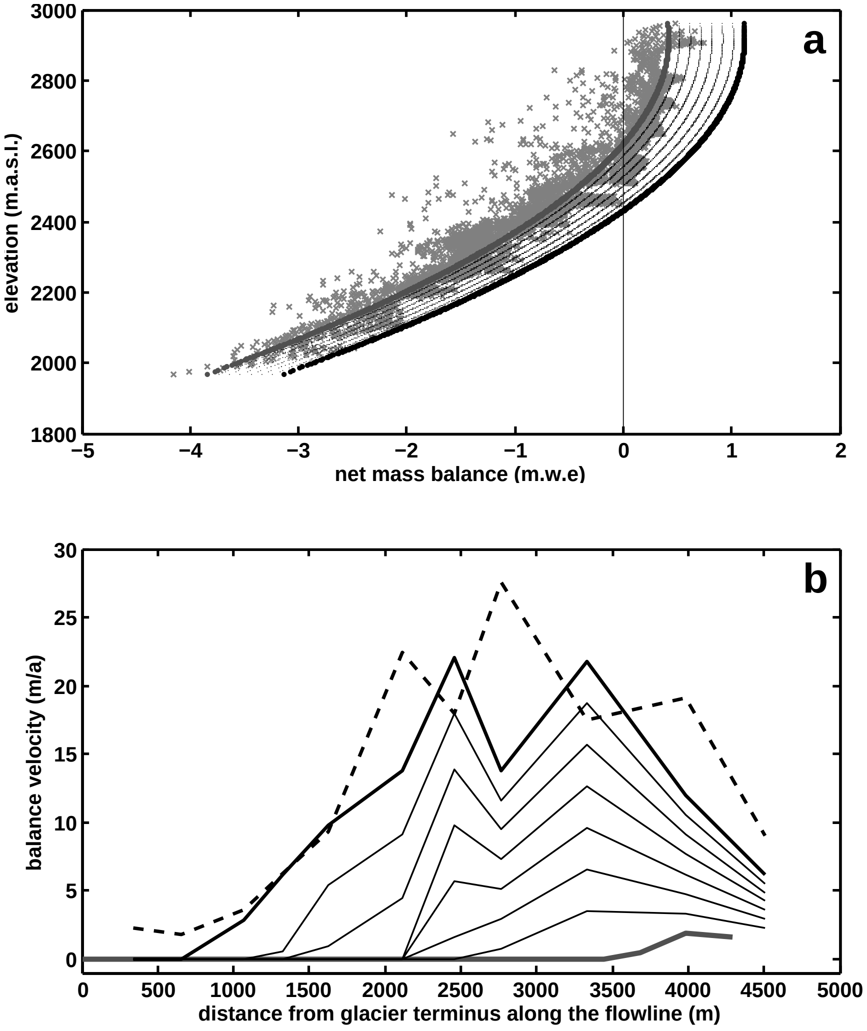

Figure E.2: (a) Measured net balance (gray crosses) as a function of elevation. The the best-fit curve (dark gray) is incrementally shifted to the right (thin black curves) until the generated balance velocities are of the same magnitude as the measured surface velocities (bold black curve). (b) Balance velocity as a function of the distance from glacier terminus along the flowline. The gray line is the current balance velocity profile with negative values set to zero, the thin black lines are the profiles obtained by incrementally increasing the net balance, and the bold black line represents the balance velocity profile that most resembles the measured annual surface velocity profile for the year 2007-2008 (dashed line).

Bibliography

Arendt, A., Luthcke, S., Abdalati, W., Larsen, C., Lingle, C., Echelmeyer, K., Rowlands, D., Krabill, W., 2008. Estimates of Glacier Mass Change in the St. Elias Mountains of Alaska, USA and Yukon Territory, Canada: a Strategy for Combining GRACE and Aircraft Laser Altimetry Data.

Arendt, A. A., Echelmeyer, K. A., Harrison, W. D., Lingle, C. S., Valentine, V. B., 2002. Rapid wastage of Alaskan glaciers and their contribution to rising sea level. Science 297, 382–386.

Bamber, J., Payne, T., 2004. The mass balance of the cryosphere: observations and modelling of contemporary and future changes. Cambridge University Press.

Barrand, N. E., Murray, T., 2006. Multivariate controls on the incidence of glacier surging in the Karakoram Himalaya. Arctic, Antarctic and Alpine Research 38, 489–498.

Bartholomaus, T. C., Anderson, R. S., Anderson, S. P., 2008. Response of glacier basal motion to transient water storage. Nature Geoscience 1, 33–37, doi:10.1038/ngeo.2007.52.

Bindschadler, R., Harrison, W. D., Raymond, C. F., Crosson, R., 1977. Geometry and dynamics of a surge-type glacier. Journal of Glaciology 18, 181–194.

Björnsson, H., 1998. Hydrological characteristics of the drainage system beneath a surging glacier. Nature 395, 771–774.

Björnsson, H., Pálsson, F., Sigurdsson, O., Flowers, G. E., 2003. Surges of glaciers in Iceland. Annals of Glaciology 36, 82–90.

Blackwell, D. D., Richards, M., 2004. Geothermal Map of North America - Alaska insert. American Association of Petroleum Geologist (AAPG). 1 sheet, scale 1:6,500,000.

Braithwaite, R. J., Raper, S. C. B., 2002. Glaciers and their contribution to sea level change. Phys. Chem. Earth 27, 1445–1454.

Budd, W. F., Allison, I. F., 1975. An empirical scheme for estimating the dynamics of unmeasured glaciers. International Association of Hydrological Sciences 104, 246–256.

Budd, W. F., Jacka, T., 1989. A review of ice rheology for ice sheet modelling. Cold regions science and technology 16, 107–144.

Budd, W. F., Warner, R. C., 1996. A computer scheme for rapid calculations of balance-flux distributions. Annals of Glaciology 23, 21–27.

Carr, J. R., 1995. Numerical Analysis for the Geological Sciences. Prentice Hall: Englewood Cliffs, NJ 07632.

Clarke, G. K. C., 2005. Subglacial processes. Annual Review of Earth and Planetary Science 33, 247–276.

Clarke, G. K. C., Collins, S. G., Thompson, D. E., 1984. Flow, thermal structure, and subglacial conditions of a surge-type glacier. Canadian Journal of Earth Sciences 21, 232–240.

Clarke, G. K. C., Schmok, J. P., Ommaney, C. S. L., Collins, S. G., 1986. Characteristics of a surge-type glacier. Journal of Geophysical Research 91, 7156–7180.

Colinge, J., Blatter, H., 1998. Stress and velocity fields in glaciers: Part I. Finite-difference schemes for higher-order glacier models. Journal of Glaciology 44, 448–456.

Constable, S. C., Parker, R. L., Constable, C. G., 1987. Occam's inversion: A practical algorithm for generating smooth models from electromagnetic sounding data. Geophysics 52, 289–300.

David, M., 1977. Geostatistical Ore Reserve Estimation. Amsterdam: Elsevier.

De Woul, M., Hock, R., 2005. Static mass-balance sensitivity of Artic glaciers and ice caps using a degree-day approach. Annals of Glaciology 42, 217–224.

DePonti, A., Pennati, V., De Biase, L., Maggi, V., Berta, F., 2006. A new fully three-dimensional numerical model for ice dynamics. Journal of Glaciology 52, 365–376.

Dept of Energy, Mines and Resources Canada, 1987. Map of Kluane Glacier area, Yukon Territory, Canada. 115 B/14 1st Edition. 1 sheet, scale 1:50,000. Produced from aerial photographs taken in 1977.

Dowdeswell, J. A., Hamilton, G. S., Hagen, J. O., 1991. The duration of the active phase on surge-type glaciers–Contrasts between Svalbard and other regions. Journal of Glaciology 37, 388–400.

Dyurgerov, M. B., Aizin, V. B., Buynitskiy, A. B., 1985. Nakopleniyemassy v oblasti pitaniya lednikaMedvezhyegoza periodymezhdu yegopodvizhkami [Mass accumulation in the accumulation area of Medvezhiy Glacier during its quiescence periods]. Mater. Glyatsiol. Issled. 54, 131–135.

Eisen, O., 2008. Inference of velocity pattern from isochronous layers in firn, using an inverse method. Journal of Glaciology 54, 613–630.

Eisen, O., Harrison, W. D., Raymond, C. F., 2001. The surges of Variegated Glacier, Alaska, U.S.A., and their connection to climate and mass balance. Journal of Glaciology 47, 351–358.

Flowers, G. E., Clarke, G. K. C., 1999. Surface and bed topography of Trapridge Glacier, Yukon Territory, Canada: digital elevation models and derived hydraulic geometry. Journal of Glaciology 45 (149).

Fountain, A. G., Walder, J. S., 1998. Water flow through temperate glaciers. Reviews of Geophysics 36, 299–328.

Fowler, A. C., Murray, T., Ng, F. S. L., 2001. Thermally controlled glacier surging. Journal of Glaciology 47, 527–538.

Frappé, T.-P., Clarke, G. K. C., 2007. Slow surge of Trapridge Glacier, Yukon Territory, Canada. Journal of Geophysical Research 112, F03S32.

Gardner, J. S., Hewitt, K., 1990. A surge of Bualtar Glacier, Karakoram Range, Pakistan - a possible landslide trigger. Journal of Glaciology 36, 159–162.

Glen, J. W., 1955. The creep of polycrystalline ice. Proceedings of the Royal Society of London, series A 228 (1175), 519–538.

Goldsby, D. L., Kohlstedt, D. L., 1997. Grain boundary sliding in fine-grained ice I. Scripta Materiala 37, 1399–1406.

Gudmundsson, G. H., 1999. A three-dimensional numerical model of the confluence area of Unteraargletscher, Bernese Alps, Switzerland. Journal of Glaciology 45, 219–230.

Gudmundsson, G. H., Að̄algeirsdóttir, G., Björnsson, H., 2003. Observational verification of predicted increase in bedrock-to-surface amplitude transfer during a surge. Annals of Glaciology 36, 91–96.

Gudmundsson, G. H., Raymond, M., 2008. On the limit to resolution and information on basal properties obtainable from surface data on ice streams. The Cryosphere 2, 167–178.

Harrison, W. D., Post, A. S., 2003. How much do we really know about glacier surging? Journal of Glaciology 36, 1–6.

Hewitt, K., 2007. Tributary glacier surges: an exceptional concentration at Panmah Glacier, Karakoram Himalaya. Journal of Glaciology 53, 181–188.

Hock, R., Jensen, H., 1999. Application of kriging interpolation for glacier mass balance computations. Geografiska Annaler 81 A (4).

Hooke, R. L., 1981. Flow law for polycrystalline ice in glaciers: comparison of theoretical predictions, laboratory data and field measurements. Reviews of Geophysics and Space Physics 19, 664–672.

Hubbard, A., Blatter, H., Nienow, P., Mair, D., Hubbard, B., 1998. Comparison of a three-dimensional model for glacier flow with field data from Haut Glacier d'Arolla, Switzerland. Journal of Glaciology 44, 368–378.

Iken, A., 1981. The effect of the subglacial water pressure on the sliding velocity of a glacier in an idealized numerical model. Journal of Glaciology 97, 407–421.

Iverson, N. R., Hooyer, T., Baker, R. W., 1998. Ring-shear studies of till deformation: Coulomb plastic behavior and distributed strain in glacier beds. Journal of Glaciology 44, 634–642.

Jiskoot, H., Murray, T., Boyle, P., 2000. Controls on the distribution of surge-type glaciers in Svalbard. Journal of Glaciology 46, 412–422.

Jóhannesson, T., 1997. The response of two Icelandic glaciers to climatic warming computed with a degree-day glacier mass-balance model coupled to a dynamic glacier model. Journal of Glaciology 43, 321–327.

Jóhannesson, T., Raymond, C. F., Waddington, E. D., 1989. Time-scale for adjustment of glaciers to changes in mass balance. Journal of Glaciology 35, 355–369.

Journel, A. G., Huijbregts, C. J., 1978. Mining Geostatistics. New York, Academic Press.

Kamb, B., 1987. Glacier surge mechanism based on linked cavity configuration of the basal water conduit system. Journal of Geophysical Research 92, 9083–9100.

Kamb, B., Echelmeyer, K. A., 1986. Stress-gradient coupling in glacier flow: I. longitudinal averaging of the influence of ice thickness and surface slope. Journal of Glaciology 32, 267–284.

Kamb, B., Raymond, C. F., Harrison, W. D., Engelhardt, H., Echelmeyer, K. A., Humphrey, N., Brugman, M. M., Pfeffer, T., 1985. Glacier Surge Mechanism: 1982-1983 Surge of Variegated Glacier, Alaska. Science 227, 469–479.

Kaser, G., Cogley, J. G., Dyurgerov, M. B., Meier, M. F., Ohmura, A., 2006. Mass balance of glaciers and ice caps: Consensus estimates for 1961-2004. Geophysical Research Letters 33, L19501, doi:10.1029/2006GL027511.

Kaser, G., Georges, C., Juen, I., Mölg, T., 2004. In: Huber et al. (Eds), Global Change and Mountain Regions.

Lefauconnier, B., Hagen, J. O., 1991. Surging and calving glaciers in eastern Svalbard. Nor. Polarinst. Medd., 116 pp.

Lingle, C. S., Fatland, D. R., 2003. Does englacial water storage drive temperate glacier surges? Annals of Glaciology 36, 14–20.

Marshall, S. J., 2005. Recent advances in understanding ice sheet dynamics. Earth and Planetary Science Letters 240, 191–204.

Matheron, G., 1963. Principles of geostatistics. Econ. Geol. 58, 1246–1266.

Maxwell, D., Truffer, M., Avdonin, S., Stuefer, M., 2008. An iterative scheme for determining glacier velocities and stresses. Journal of Glaciology 54, 888–898.

Meier, M. F., Dyurgerov, M. B., Rick, U. K., O'Neel, S., Pfeffer, W. T., Anderson, R. S., Anderson, S. P., Glazovsky, R. S., 2007. Glaciers dominate eustatic sea-level rise in the 21st century. Science 317, 1064–1067.

Meier, M. F., Post, A., 1969. What are glacier surges? Canadian Journal of Earth Sciences 6, 807–817.

Melvold, K., Hagen, J. O., 1998. Evolution of a surge-type glacier in its quiescent phase: Kongsvegen, Spitsbergen, 1964–95. Journal of Glaciology 44, 394–404.

Muller, H. C., 1991. Une méthode itérative simple pour résoudre les équations du mouvement d'un glacier. Mémoire de Diplome en Mathématique, Université de Genève.

Murray, T., Strozzi, T., Luckman, A., Jiskoot, H., Christakos, P., 2003. Is there a single surge mechanism? Contrasts in dynamics between glacier surges in Svalbard and other regions. Journal of Geophysical Research 108, 2237, doi:10.1029/2002JB001906.

Narod, B. B., Clarke, G. K. C., 1994. Miniature high-power impulse transmitter for radio-echo sounding. Journal of Glaciology 40, 190–194.

Nienow, P., Sharp, M., Willis, I., 1998. Seasonal changes in the morphology of the subglacial drainage system, Haut Glacier d'Arolla, Switzerland. Earth Surface Processes and Landforms 23, 825–843.

Nye, J. F., 1951. The flow of glaciers and ice-sheets as a problem in plasticity. Proceedings of the Royal Society of London, series A 207, 554–572.

Nye, J. F., 1952. The mechanics of glacier flow. Journal of Glaciology 2, 82–93.

Nye, J. F., 1953. The flow law of ice from measurements in glacier tunnels, laboratory experiments and the Jungfraufirn borehole experiment. Proceedings of the Royal Society of London, Series A 219, 477–489.

Nye, J. F., 1965. The flow of a glacier in a channel of rectangular, elliptic or parabolic cross section. Journal of Glaciology 5, 661–690.

Nye, J. F., 1976. Water flow in glaciers: jökulhlaups, tunnels and veins. Journal of Glaciology 17, 181–207.

Oerlemans, J., Dyurgerov, M. B., van de Wal, R. S. W., 2007. Reconstructing the glacier contribution to sea-level rise back to 1850. Cryosphere 1, 59–65.

Parker, R. L., 1994. Geophysical Inverse Theory. Princeton University Press.

Parrenin, F., Jouzel, J., Waelbroeck, C., Ritz, C., Barnola, J.-M., 2001. Dating the vostok ice core by an inverse method. Journal of Geophysical Research 106, 31,837–31,851.

Paterson, W. S. B., 1994. The Physics of Glaciers, 3rd Edition. Pergamon Press, Elsevier Science Ltd.

Pattyn, F., 2002. Transient glacier response with a higher-order numerical ice-flow model. Journal of Glaciology 48, 467–477.

Post, A. S., 1969. Distribution of surging glaciers in western North America. Journal of Glaciology 8, 229–240.

Quinn, P., Beven, K., Chevallier, P., Planchon, O., 1991. The prediction of hillsplope flow paths for distributed hydrological modeling using digital terrain models. Hydrological Processes 5, 59–80.

Raymond, C. F., 1987. How do glacier surge? A review. Journal of Geophysical Research 92, 9121–9134.

Raymond, C. F., Benedict, R. J., Harrison, W. D., Echelmeyer, K. A., Sturm, M., 1995. Hydrological discharges and motion of Fels and Black Rapids Glaciers, Alaska, USA: Implications for the structure of their drainage systems. Journal of Glaciology 41, 290–304.

Röthlisberger, H., 1972. Water pressure in intra- and subglacial channels. Journal of Glaciology 11, 177–203.

Schoof, C., 2005. The effect of cavitation of glacier sliding. Proceedings of the Royal Society of London, Series A 461, 609–627.

Sharp, M., Richards, K., Willis, I., Arnold, N., Nienow, P., Lawson, W., Tison, J. L., 1993. Geometry, bed topography and drainage system structure of the Haut Glacier d'Arolla, Switzerland. Earth Surface Processes and Landforms 18, 557–571.

Shreve, R. L., 1972. Movement of water in glaciers. Journal of Glaciology 11, 205–214.

Sidler, R., 2003. Kriging and conditional geostatistical simulation based on scale-invariant covariance models. Diploma Thesis published in the Institute of Geophysics, Department of Earth Science, Swiss Federal Institute of Technology, Zurich.

Solomon, S., Quin, D., Manning, M., Marquis, M., Averyt, K., Tignor, M. M. B., Miller, H. L., Zhenlin, C., 2007. Climate change 2007: the physical science basis. Contribution of Working Group I to the Fourth Assessment Report of the Intergovernmental Panel on Climate Change. Cambridge University Press.

Taylor, J. R., 1982. An Introduction to Error Analysis. University Science Books, Oxford University Press.

Truffer, M., 2004. The basal speed of valley glaciers: an inverse approach. Journal of Glaciology 50 (169).

Truffer, M., Echelmeyer, K. A., Harrison, W. D., 2001. Implications of till deformation on glacier dynamics. Journal of Glaciology 47, 123–133.

Waddington, E. D., Neumann, T. A., Koutnik, M. R., Marshall, H.-P., Morse, D. L., 2007. Inference of accumulation-rate patterns from deep layers in glaciers and ice sheets. Journal of Glaciology 53, 694–712.

Weertman, J., 1973. Creep of ice. *In* Whalley, E., Jones, S.J. and Gold, L. W. *(eds.)*, Physics and Chemistry of Ice, Royal Society of Canada, Ottawa , 320–337.

Wheler, B. A., 2009. Melt modelling of glaciers in the Donjek Range, southwest Yukon Territory, Canada. Master's thesis, Simon Fraser University.

Zevenberger, L. W., Thorne, C. R., 1987. Quantitative analysis of land surface topography. Earth Surface Processes and Landforms 12, 47–56.